

① LEVEL II

AGARD-AG-243

AGARD-AG-243

AGARD

ADVISORY GROUP FOR AEROSPACE RESEARCH & DEVELOPMENT

7 RUE ANCELLE 92200 NEUILLY SUR SEINE FRANCE

AD A 076315

AGARDograph No. 243

Fluid Dynamic Aspects of Wind Energy Conversion

DISTRIBUTION STATEMENT A

Approved for public release;
Distribution Unlimited

DDC
RECEIVED
NOV 9 1979
B

DDC FILE COPY

NORTH ATLANTIC TREATY ORGANIZATION



DISTRIBUTION AND AVAILABILITY
ON BACK COVER

BEST AVAILABLE COPY

79-11-08 085

NORTH ATLANTIC TREATY ORGANIZATION
ADVISORY GROUP FOR AEROSPACE RESEARCH AND DEVELOPMENT ✓
(ORGANISATION DU TRAITE DE L'ATLANTIQUE NORD)

6 AGARDograph No. 243
FLUID DYNAMIC ASPECTS OF WIND ENERGY CONVERSION

by
10 O. de Vries

National Aerospace Laboratory NLR
Anthony Fokkerweg 2
1059 CM Amsterdam
The Netherlands

11 Jul 79

12 154

DDC
RECEIVED
NOV 9 1979
B

DISTRIBUTION STATEMENT A
Approved for public release;
Distribution Unlimited

400 043

The AGARDograph has been produced at the request of the Fluid Dynamics Panel of AGARD.

7/10

THE MISSION OF AGARD

The mission of AGARD is to bring together the leading personalities of the NATO nations in the fields of science and technology relating to aerospace for the following purposes:

- Exchanging of scientific and technical information;

Continuously stimulating advances in the aerospace sciences relevant to strengthening the common defence posture;

- Improving the co-operation among member nations in aerospace research and development,

Providing scientific and technical advice and assistance to the North Atlantic Military Committee in the field of aerospace research and development;

Rendering scientific and technical assistance, as requested, to other NATO bodies and to member nations in connection with research and development problems in the aerospace field;

Providing assistance to member nations for the purpose of increasing their scientific and technical potential,

Recommending effective ways for the member nations to use their research and development capabilities for the common benefit of the NATO community.

The highest authority within AGARD is the National Delegates Board consisting of officially appointed senior representatives from each member nation. The mission of AGARD is carried out through the Panels which are composed of experts appointed by the National Delegates, the Consultant and Exchange Programme and the Aerospace Applications Studies Programme. The results of AGARD work are reported to the member nations and the NATO Authorities through the AGARD series of publications of which this is one.

Participation in AGARD activities is by invitation only and is normally limited to citizens of the NATO nations.

The content of this publication has been reproduced directly from material supplied by AGARD or the author.

Published July 1979

Copyright © AGARD 1979
All Rights Reserved

ISBN 92-835-1326-6



*Printed by Technical Editing and Reproduction Ltd
Harford House, 7-9 Charlotte St, London, W1P 1HD*

FLUID DYNAMIC ASPECTS OF WIND ENERGY CONVERSION

by

O. de Vries

National Aerospace Laboratory NLR,
Anthony Fokkerweg 2
1059 CM AMSTERDAM
The Netherlands

SUMMARY

A review is made of the fluid dynamic aspects of wind energy conversion. A short survey of the total framework of wind energy conversion is given to bring the fluid dynamics aspect in its proper dimensions. Next, the several wind concentrator concepts are discussed, while the main body of the report is formed by a discussion of the theory of wind-driven turbines, including both the horizontal-axis and the vertical-axis turbines.

The report concludes with a survey of inhomogeneous flow and turbulence effects, turbine control and wake interference effects.

FOREWORD

There has been in recent years a dramatic revival of interest in harnessing the energy contained in terrestrial winds. Wind energy conversion systems are being developed now in many countries, meetings and symposia are being organized at an ever increasing frequency, and hundreds of journal articles, company reports, papers in conference proceedings and official government publications are being issued all over the world. Scattered among all these sources are various bits and pieces of information about the most fundamental aspects of wind energy conversion, the prime force that makes it all work, THE FLUID DYNAMICS of such a process. At the present time no single, generally accessible source exists that could provide a comprehensive summary of the fluid dynamics foundations of the great variety of wind turbines that now are being constructed or proposed. To fill this gap, the Fluid Dynamics Panel of AGARD has decided to sponsor the preparation of the present review. Since the fluid dynamics processes involved in wind energy conversion are not too dissimilar from those occurring in flight of various types of aerospace vehicles, it was considered particularly appropriate that such a review be undertaken under the auspices of an aerospace advisory group and that it be performed by an aerospace organization. In this regard the Panel was most fortunate to secure the cooperation of the National Aerospace Laboratory of The Netherlands, one of the best known aerospace research organizations in the world, which kindly undertook to perform this work. It is hoped that this volume will find its way into the hands of the many designers of modern wind turbines and that it will facilitate their difficult task by providing a comprehensive review of the fluid dynamics methods and data on which their designs have to be based.

Ottawa, 8 December 1978

Kazimierz J. Orlik-Rückemann,
Deputy Chairman,
Fluid Dynamics Panel.

ACCESSION for		
NTIS	White Section	<input checked="" type="checkbox"/>
DDC	Buff Section	<input type="checkbox"/>
UNANNOUNCED		<input type="checkbox"/>
JUSTIFICATION _____		
BY _____		
DISTRIBUTION/AVAILABILITY CODES		
Dist.	AVAIL.	and/or SPECIAL
A		

TABLE OF CONTENTS

	Page
1 GENERAL INTRODUCTION	1-1
1.1 Wind energy development in the past	1-1
1.2 Recent developments	1-1
1.3 Scope of the present report	1-1
1.4 Acknowledgement	1-2
1.5 List of references	1-2
2 SURVEY OF ASPECTS PERTAINING TO WIND ENERGY CONVERSION	2-1
List of symbols	2-1
2.1 Introduction	2-2
2.2 Available amount of wind energy	2-2
2.2.1 Data from weather stations	2-2
2.2.2 Wind shear	2-3
2.2.3 Wind energy flux	2-4
2.3 Useable amount of wind energy	2-5
2.3.1 Design power, cut-in speed	2-5
2.3.2 Turbine characteristics	2-5
2.4 Structural aspects	2-7
2.4.1 Shape of the rotor blade	2-7
2.4.2 Aerodynamic loads on a wind turbine	2-8
2.4.3 Aeroelastic effects	2-9
2.5 Conversion, storage and distribution to the consumer	2-10
2.6 Cost analyses	2-11
2.7 Environmental effects	2-12
2.8 List of references	2-12
Figures (2.1 through 2.11)	2-14
3 WIND CONCENTRATORS	3-1
List of symbols	3-1
3.1 Introduction	3-3
3.2 The Betz limit	3-3
3.2.1 Derivation of the formula	3-3
3.2.2 Discussion	3-4
3.3 The diffuser augmentor	3-5
3.3.1 Simple diffuser	3-5
3.3.2 Shrouded turbine	3-6
3.4 The tip-vane concept	3-8
3.4.1 The basic idea	3-8
3.4.2 Discussion	3-8
3.5 Vortex-augmentor concepts	3-10
3.6 Concluding remarks	3-11
3.7 List of references	3-11
Figures (3.1 through 3.17)	3-12
4 THEORY OF WIND-DRIVEN TURBINES	4-1
List of symbols	4-1
4.1 Introductory remarks	4-4
4.2 Drag-driven turbine	4-5
4.3 Flutter machine used as a wind turbine	4-6
4.3.1 General remarks	4-6
4.3.2 Energy extracted by a plain aerofoil	4-6
4.3.3 Energy extracted by an aerofoil with plain flap	4-7
4.3.4 Estimation of power output	4-8
4.4 Horizontal-axis turbine	4-9
4.4.1 General remarks	4-9
4.4.2 Theory for an infinite number of blades	4-9
4.4.3 Tip correction theories	4-12
4.4.3.1 Linearized correction	4-12
4.4.3.2 Theory of Wilson and Lissaman	4-13
4.4.3.3 High-order correction	4-14
4.4.4 Linearized vortex wake theory	4-15
4.4.5 Extended numerical methods	4-16
4.4.6 Aerodynamic optimization	4-16
4.4.7 Calculation method for a given blade geometry	4-18
4.4.7.1 Description of the method	4-18
4.4.7.2 The ideal rotor shape	4-18
4.4.7.3 More practical blade shapes	4-19
4.4.8 Concluding remarks	4-19
4.5 Vertical-axis turbines	4-20
4.5.1 General remarks	4-20
4.5.2 Two-dimensional momentum theory	4-21
4.5.3 Two-dimensional vortex theory	4-23
4.5.4 Stream-curvature effects	4-26
4.5.5 Unsteady effects	4-27
4.5.6 Two-dimensional vertical-axis rotor with variable pitch	4-28
4.5.7 Three-dimensional turbines	4-31
4.5.7.1 Straight or curved blades	4-31
4.5.7.2 Momentum theories	4-31
4.5.7.3 Vortex theories	4-33
4.5.7.4 Experimental results	4-36
4.5.8 Concluding remarks	4-36
4.6 List of references	4-37
Figures (4.1 through 4.57)	4-38

5 MISCELLANEOUS TOPICS	5-1
List of symbols	5-1
5.1 Effects of flow inhomogeneity and turbulence	5-4
5.1.1 Introductory remarks	5-4
5.1.2 Effect of wind shear	5-4
5.1.3 Effect of turbulence and unsteadiness of the wind	5-8
5.2 Turbine control	5-13
5.2.1 Introductory remarks	5-13
5.2.2 Starting and stopping	5-13
5.2.3 Control during normal operation	5-15
5.2.4 Safety aspects	5-16
5.3 Wind turbine "farms"	5-17
5.3.1 Introductory remarks	5-17
5.3.2 Wake interaction theories	5-17
5.3.2.1 Surface roughness theory	5-17
5.3.2.2 Wake-decay theory	5-20
5.3.3 Experimental results	5-21
5.3.3.1 Wake behind a single turbine	5-21
5.3.3.2 Wake interaction in a finite array	5-22
5.3.3.3 Practical applications	5-22
5.4 Short note on literature and bibliographies	5-23
5.5 List of references	5-24
Figures (5.1 through 5.36)	5-25
APPENDIX A	
STREAM FUNCTION AND VELOCITY DISTRIBUTION DUE TO AN ANNULAR WING WITH A TRIANGULAR CHORDWISE VORTICITY DISTRIBUTION IN AXISYMMETRIC FLOW	A1
A.1 Introduction	A1
A.2 Induced axial velocities	A1
A.3 Estimation of section lift coefficient	A2
A.4 List of references	A4
Figures (A.1 through A.6)	A4
APPENDIX B	
ENERGY EXTRACTION FROM AN INCOMPRESSIBLE STEADY FLOW	B1
B.1 The Bernoulli constant H	B1
B.2 Choice of the reference frame	B2
APPENDIX C	
DETERMINATION OF THE INDUCED VELOCITIES IN AXISYMMETRIC FLOW	C1
C.1 Introduction	C1
C.2 The vortex structure; general formulation	C1
C.3 The cylindrical wake	C3
C.4 Momentum considerations	C4
C.5 Concluding remarks	C8
C.6 List of references	C8
Figures (C.1 through C.5)	C9
APPENDIX D	
SOME CONSIDERATIONS ABOUT THE ROTOR BLADE SHAPE	D1
D.1 Introduction	D1
D.2 Bending stresses due to centrifugal loading for a drum-type vertical-axis turbine	D1
D.3 The troposkien blade shape for a vertical-axis turbine	D1
D.4 Centrifugal stresses in the blades of a horizontal-axis turbine	D2
D.5 Possible reduction of bending moments due to the aerodynamic load on the blade of a horizontal-axis turbine	D3
Tables (D.1 and D.2)	D5
Figures (D.1 through D.4)	D6

1 GENERAL INTRODUCTION

1.1 Wind energy development in the past

The very idea to make use of the power of the wind flowing over the earth surface is a very old one. It was put into practice already in ancient times for ship propulsion, but also the conversion of wind energy into mechanical energy (grinding, wood cutting, water pumping) was used centuries ago. One has only to recall the well-known satirical romance by Miguel de Cervantes (1605), where Don Quixote, the hero of this romance, once fought windmills.

Windmills were extensively used up to the beginning of the industrial era, which started with the invention of the steam engine, soon followed by the invention of the electric motor/generator and the internal combustion engine. Because of the ready availability of coal, oil and natural gas (improved transport systems) and because of the capacity of engines to generate a large amount of power in a small volume at any required instant, the windmills soon became obsolete.

During the Second World War and shortly afterwards, there was a relatively short-lived revival of interest in wind power, with an emphasis on the generation of electricity by a large-scale wind turbine.

Without the intention to be complete, some names and projects may be mentioned here, such as Ulrich Hütter (Refs 1.1, 1.2 and 1.3) in Germany, the studies and practical experience of the Électricité de France (EDF, Ref. 1.4) and Neyrpic (Ref. 1.5) in France, Golding (Refs 1.6, 1.7 and 1.8) in the UK, the Gedser windmill in Denmark and, last but not least, the Putnam turbine at Grandpa's Knob (Ref. 1.9) in the USA.

The decline of interest in wind power in the post-war years was mainly due to the abundance of low-priced oil, the growing insight that wind energy is a relatively expensive form of energy, and the technical problems with some of the turbines (fatigue).

1.2 Recent developments

The energy-crisis of 1973-1974 and the growing acceptance of the idea that fossil fuel resources are not unlimited ended the euphoric era of rapid industrial expansion and increasing rates of economic growth, and led to a renewed and probably lasting interest in alternative energy resources, such as solar energy and wind power.

The wider acceptance of studying alternative energy sources led to long-term research projects sponsored by government agencies, in contrast with the more limited wind energy projects in the post-war years. In this respect, the Energy Research and Development Administration (ERDA) and their Biennial Workshops on Wind Energy Conversion Systems (1st in June 1973) in the USA, have to be mentioned first. Also Sweden made an early start with their National Program on Wind Energy Conversion (Swedish Board for Technical Development, STU) and organized a Workshop in Stockholm (29-30 August 1974). The Netherlands started a National Program in March 1976, while research programs were started also in Germany and Denmark. These last two countries do not yet have an official National Program; neither does the UK, where general studies are carried out at several universities and institutions, such as e.g. the Central Electricity Generating Board (CEGB). Canada stands out with its vertical-axis turbine project and allied studies of the National Research Council (NRC, Refs 1.10 and 1.11), whereas in several other countries in the world investigations are under way in universities and other institutions.

Moreover, in 1973/1974, the then US Foreign Minister Dr. Kissinger convened an energy conference in Washington D.C., which was continued in the so-called "Energy Co-ordinating Group" and resulted in an "Agreement on an International Energy Program" (IEP), in which 18 countries participated. To execute IEP, the "International Energy Agency" (IEA) was founded with its residence in Paris at the Organization for European Economic Co-operation (OECE).

The Governing Board of IEA is assisted by 4 Standing Groups. Each Standing Group set up a number of Sub-Groups. The Sub-Group for Energy R&D set up a number of so-called "Working Parties". The Working Party on Wind Power was inaugurated in March, 1976, with The Netherlands as "lead country".

Other landmarks of the growing interest in wind power are the International Symposia on Wind Energy Systems (1st ISWES, 7-9 Sept. 1976, 2nd ISWES, 3-6 Oct. 1978) organized by the British Hydromechanics Research Association (BHRA), the growing number of articles on wind power in the "Journal of Energy" (USA), the establishment of a journal devoted to a large extent to wind power, viz. "Wind Engineering" (UK) and the establishment of the "Wind Energy Society of America" (USA).

1.3 Scope of the present report

The entire field of Wind Energy Conversion Systems (WECS) is a very extensive one. Most National Programs are devoted to large-scale applications of wind turbines to generate electricity which could be fed into the public grid, but there is a growing tendency to consider also decentralized application of wind power (each farm its own turbine, possibly combined with solar energy), especially in scarcely populated areas.

Furthermore, the application of wind power in developing countries has problems of its own, ranging from rather simple approaches (Ref. 1.12) to the more fundamental ones, as covered by the "Dutch Steering Committee for Wind Energy in Developing Countries" (SWD, Refs 1.13 and 1.14).

Finally, there is the already well-established field of small-scale wind turbines for pumping water in rural areas and for special purposes, such as radio and light beacons that have to operate unattended for very long periods (Ref. 1.15).

Giving an overview of the entire field of wind energy conversion systems is only possible by forming a staff of contributors. Therefore, it was decided to limit the study to fluid dynamics aspects only, which still is an extensive field to discuss, due to the rather exponential growth of the number of

publications of recent years.

In order to put the rather extensive aerodynamic discussions in its proper perspective, it was decided to start with a short survey of the different aspects of wind energy conversion (Chapter 2). The discussion being far from complete, an emphasis is laid on large-scale turbines.

Since the discovery of the Betz limit (Ref. 1.16; 1926 and Section 3.2), which states that an isolated wind turbine of a given size can extract only a part of the energy flux offered by the wind stream, there have been many proposals for so-called "wind concentrators", to get more power from a turbine with given diameter than indicated by the Betz limit. A number of these proposals is discussed in Chapter 3. Although it can be shown that the power output of a turbine with a given diameter can indeed be increased above the Betz limit by several of the proposed devices, it is the belief of the author that the cost-increase due to the added structures outweighs the power-increase, with the exception of some special cases (e.g. Trade-wind areas).

Chapter 4 discusses the aerodynamic theory of the wind-driven turbines. It constitutes the main body of the report and is limited to the discussion of a turbine in a steady, non-turbulent homogeneous flow. One of the most intriguing results is that, though a wind turbine is subjected to large aerodynamic lift forces, only a small component of that lift force is used to drive the turbine. Most of the existing theories are based on momentum considerations and a blade element theory, but more elaborate computer codes including trailing vortex wake calculations and lifting surface theory are under way. Although the more complicated computer codes give a better prediction of the induced velocities in the plane of rotation of the rotor, it might be questioned whether they could predict the small components of the lift force (leading-edge suction peak) with a significantly greater accuracy. This applies especially for the vertical-axis (Darrieus) turbine, where higher accuracy probably cannot be achieved without including effects due to unsteady aerodynamics and stream curvature. Furthermore, a wind turbine is submerged in a non-homogeneous, unsteady and turbulent flow (atmospheric boundary layer), the effect of which on the turbine performance is difficult to assess. This is also the reason why the feasibility of developing very extensive turbine-performance computer codes is still questionable.

The inhomogeneous flow and turbulence effects are briefly discussed in Chapter 5, together with a short discussion of the aerodynamic aspects of turbine control and the effect of putting a large number of turbines together in a so-called wind turbine "farm" (wake interference effects).

In the discussion of the subjects in this report the basic assumptions are stronger underlined than specific results obtained with the theory. The choice of the subjects to be discussed and the depth of exposition of some details reflect the author's prejudice, which seems inevitable in such a new field of research.

It is hoped that this review summarizes the present state-of-the-art to such an extent that it will have a function in the dialogue with respect to the feasibility of using wind power to alleviate future energy shortages.

1.4 Acknowledgement

The constant encouragement during the preparation of this report by Dr. K.J. Orlik-Rückemann (NRC, Canada) and Dr. B.M. Spee (NLR, The Netherlands) is gratefully acknowledged.

The author also wishes to express his gratitude to his colleague Mr. R.A. Maarsingh for doing the difficult job of reviewing the technical arguments involved.

1.5 List of references

- 1.1 Hütter, U.: Beitrag zur Schaffung von Gestaltungsgrundlagen für Windkraftwerke. Dissertation TH Wien (1942)
- 1.2 Hütter, U.: Windkraftmaschinen. Hütte, des Ingenieurs Taschenbuch, Band IIA (Berlin, 1954) pp. 1030-1044.
- 1.3 Hütter, U.: Optimum Design Concept for Windelectric Converters. Proc. Workshop on Advanced Windenergy Systems (Stockholm 29-30 Aug. 1974).
- 1.4 Bonnefille, R.: Les Réalisations d'Électricité de France Concernant l'Énergie Éolienne. d'Électricité de France, Rapport F 40/74 No.4 (Avril 1974).
- 1.5 -- : Aerogenerateurs Neyrpic de Grande Puissance. (Etablissements Neyrpic, Grenoble, France; Oct. 1961).
- 1.6 Golding, E.W.: Electricity from the Wind. Discovery (March 1950) pp. 97-99.
- 1.7 Golding, E.W.: Harnessing the Wind. Discovery (Dec. 1953) pp. 373-377.
- 1.8 Golding, E.W.: The Influence of Aerodynamics in Wind Power Development. AGARD Report 401 (1961).
- 1.9 Putnam, P.C.: Power from the Wind. (V. Nostrand Cy., N.Y., 1948).
- 1.10 Rangi, R.S., South, P., Templin, R.J.: Wind Power and the Vertical-Axis Wind Turbine Developed at the National Research Council. NRC Canada Quart. Bull. Report No. DME/NAE 1974(2) (Ottawa, 1 April to 30 June 1974) pp. 1-14.
- 1.11 Templin, R.J., South, P.: Some Design Aspects of High-Speed Vertical-Axis Wind Turbines. Proc. Intern. Symp. on Wind Energy Systems (St. John's College, Cambridge, England; 7-9 Sept. 1976).
- 1.12 Parkes, M.E.: The Use of Windmills in Tanzania. Univ. of Dar es Salaam, Res. Paper No.33 (June 1974).

- 1.13 Jansen, W.A.M.: Literature Survey; Horizontal-Axis Fast Running Wind Turbines for Developing Countries.
TNO-IWECO Rep. No. 11663/2 (The Netherlands, March 1976).
- 1.14 Jansen, W.A.M.: Horizontal-Axis Fast Running Wind Turbines for Developing Countries.
TNO-IWECO Rep. No. 11663/3 (The Netherlands, June 1976).
- 1.15 Hinsley, A.J.A., Smith, D.A.D.: The Application of Small Wind Powered Generators in Telecommunication and Other High Reliability Systems.
(Pye Telecommunications Ltd.) Symp. on Wind Power in the United Kingdom (London, 13 July 1978).
- 1.16 Betz, A.: Windenergie und ihre Ausnutzung durch Windmühlen.
(Vandenhoeck und Ruprecht, Göttingen, 1926).

List of symbols

a	axial induction factor (-)
B	number of rotor blades (-)
c	chord length of rotor blade (m)
C_l	lift coefficient of aerofoil section (-)
C_p	$= P / \frac{1}{2} \rho U^3 S_{ref}$ = power coefficient (-)
$C_{p, ideal}$	$= P_{ideal} / \frac{1}{2} \rho U^3 S_{ref} = 16/27$ = theoretical maximum power coefficient according to Betz (-)
C_Q	$= Q / \frac{1}{2} \rho U^2 S_{ref} R_o = C_p / \lambda$ = torque coefficient (-)
g	acceleration of gravity (m/s^2)
H	height above the ground (m)
H	height of rotor (m)
H_{ref}	height at which the reference wind velocity is measured (m)
P	power (W)
$P_{average}$	annual average power based on wind statistics (W)
P_{design}	design power or installed power (W)
P_{ideal}	theoretical maximum power according to Betz (W)
$P(U_j)$	probability of occurrence of a wind velocity in the velocity class U_j (-)
$P(E, U_j)$	$= \frac{\text{annual energy at wind velocity class } U_j}{\text{total wind energy in a year}}$ (-)
Q	torque (Nm)
r	local radius (m)
R_o	maximum radius or tip radius (m)
s	arc length of rotor blade (m)
S_{ref}	reference area of the turbine; area swept by the rotor perpendicular to the wind velocity (m^2)
t	time (s)
t	profile thickness (m)
T	integration time for determination of average (s)
U	wind velocity or undisturbed velocity (m/s)
\bar{U}	average wind velocity, depending on integration time T (m/s)
u	$= U - \bar{U}$ = wind velocity fluctuation (m/s)
U_i, U_j	average wind velocity in wind velocity class i or j, e.g. $U_j = 10$ m/s when $9.5 \leq U_j \leq 10.5$ m/s
U_{ref}	average wind velocity at reference height H_{ref} (m/s)
U_{500}	average wind velocity at a height of 500 m (m/s)
$\sqrt{u^2}/\bar{U}$	root-mean-square value of wind fluctuation divided by the average wind velocity; turbulence intensity (-)
x	axial deflection of rotor blade (m)
α	exponent of power-law wind-velocity distribution (-)
λ	$= \Omega R_o / U$ = tip speed ratio (-)
ρ	air density (kg/m^3)
ρ_m	density of rotor blade material (kg/m^3)
σ	$= Bc/R_o$ = solidity ratio of Darrieus turbine or a drum-type vertical-axis turbine (-)
σ	$= B/S_{ref} \int_0^s c \, ds$ = solidity ratio definition valid for both horizontal and vertical-axis turbines (-)
σ_b	bending stress (N/m^2 or N/mm^2)
σ_t	tensile stress (N/m^2 or N/mm^2)
ϕ	$= \frac{\text{material area of blade cross-section}}{\text{blade thickness times chord length}}$ (-)
Ω	angular velocity of the rotor (radians/s)

2.1 Introduction

When the discussion of wind energy conversion is restricted to fluid dynamics aspects, only the top of an iceberg is revealed. A complete study should include a large number of aspects, some of which are listed below:

- Meteorology
- Aerodynamics
- Structures (aeroelasticity)
- Energy conversion (e.g. mechanical energy to electricity or heat)
- Energy storage
- Distribution of energy to the consumer
- Economy
- Environmental effects.

An authoritative review of all these areas is beyond the scope of this report, but some background information about these areas is indispensable to appreciate a discussion of the fluid dynamics aspects.

The practicability of small-scale conversion systems is already fully recognized. On the other hand, large-scale systems that may have significant economic potential are now being studied in many countries, but their feasibility has not yet been fully demonstrated. In order to assist in such studies, the emphasis of the present review is placed on large-scale rather than small-scale systems.

The kinetic energy of the atmosphere of the earth is enormous. Although it is an open question at which rate this energy can be extracted from the atmosphere without changing the weather system, it is evident that a very interesting amount of energy is present for this purpose.

A possible optimistic prognosis that might be based on this precognition is changed drastically by the fact that, on practical grounds, direct energy conversion is only possible up to heights from 50 to 150 m above the ground (the maximum height of wind turbines that can be envisaged). A further reduction is caused by the vertical wind gradient. Due to the friction with the surface of the earth, the wind velocity above the surface is reduced and an atmospheric "boundary layer" is formed. The height of this boundary layer ranges up to several hundreds of metres, depending on the "roughness" of the surface of the earth. The energy conversion, therefore, takes place in the lower part of the boundary layer with a correspondingly reduced energy content.

Geographical factors and practical limitations on the height of the turbines are, however, not the only factors that limit the usable amount of wind energy. There is a kind of implicit economic reasoning, which leads to converting only a part of all available wind energy (cut-in speed, design speed). Also the choice of the type of turbine and its mode of operation is strongly connected with economic considerations.

The structural lay-out of a wind turbine is determined by a large number of factors, of which static strength, fatigue lifetime and cost-efficiency are the main points. They depend strongly on the total wind energy conversion system considered, i.e. the type of turbine, the conversion system, the mode of operation, etc. It is impossible to reveal in brief all the interrelations between the several factors in a proper way. The discussion of structural aspects will, therefore, be restricted to the effect of the shape of the rotor blade for HA (horizontal-axis propeller type) and vertical-axis (VA) Darrieus*) wind turbines. Also the aerodynamic loads and the aeroelastic instabilities (divergence, flutter) will be discussed briefly. Structural aspects of wind concentrators (shrouds, vortex augmentors, etc.) are little studied up till now and will, therefore, not be discussed. The cost-effectiveness of a structural design will also not be discussed explicitly.

The above-mentioned aspects were all connected with the technical feasibility to build a wind turbine, although some cost-effectiveness aspects were implicitly involved. A next important item is, however, how one wants to use this energy, because this has a strong feed-back to the lay-out of the complete wind energy conversion system. Short comments will be given on the type of conversion (i.e. to mechanical energy, to heat, or to electricity), on the storage, and on the distribution of energy to the consumer.

The survey of aspects pertaining to wind energy conversion will be concluded by a short survey of cost analyses found in the literature, and of environmental effects.

2.2 Available amount of wind energy

2.2.1 Data from weather stations

Most studies on the available amount of wind energy start with a kind of wind energy "prospecting" close to the ground, based on available meteorological data. In most countries, weather stations possess wind velocity recordings over a number of years. From such recordings, a first order-of-magnitude estimate of the available amount of wind energy can be made. In such a survey, the distribution of the velocity over the wind directions is neglected, because this aspect can only be considered by taking the characteristics of the wind turbine into account.

In the interpretation of the meteorological data, a number of factors has to be considered.

The first factor is the height above the ground where the wind velocity is measured. The present-day meteorological standard height is 10 m, but various heights may occur due to local circumstances. For a

*) The reader must notice, that in this report the term "Darrieus turbine" denotes a curved-blade VA wind turbine. Darrieus actually invented several types of wind turbines and in his 1931 US patent he covered both curved and straight-bladed configurations.

proper site selection, it is necessary to compare wind velocity data at the same height (e.g. 30 or 60 m). The translation of the weather-station data to a larger height (wind shear) will be discussed in Sect. 2.2.2.

When wind data of different stations are compared, it is necessary to correct the data for local effects. These local effects may be due to a kind of "wind shadow" from neighbouring obstacles at certain wind directions or due to locally different surface roughnesses at some distance from the station.

In corrugated terrain, a kind of wind energy "concentration" might be possible (see e.g. Ref. 2.1), but this will not be discussed here.

Another factor is the influence of the wind velocity sampling method on the estimation of the annual average energy flux. This will be discussed here at some length, because some confusion can be observed in the literature.

The variation of the wind velocity due to a variation of the weather system is relatively slow (except in case of a thunderstorm). The wind velocity is measured, however, in the lower part of a turbulent boundary layer, and the instantaneous wind velocity fluctuates strongly. The meteorological wind velocity is, therefore, measured as an average over a certain time interval, say half an hour or one hour. When the time interval is denoted by T , the average wind velocity is defined as:

$$\bar{U} = \frac{1}{T} \int_0^T U dt. \quad (2.2.1)$$

When the velocity fluctuation within that interval is denoted by:

$$u = U - \bar{U},$$

the average of the fluctuation in that interval is zero:

$$\bar{u} = \frac{1}{T} \int_0^T (U - \bar{U}) dt = 0. \quad (2.2.2)$$

The average energy flux in that interval is proportional to:

$$\bar{U^3} = \frac{1}{T} \int_0^T (\bar{U} + u)^3 dt = \bar{U}^3 + 3\bar{U}^2\bar{u} + 3\bar{U}\bar{u}^2 + \bar{u}^3. \quad (2.2.3)$$

Some remarks can be made about the right-hand terms of Eq. (2.2.3), viz.:

$$3\bar{U}^2\bar{u} = 0, \text{ because } \bar{u} = 0.$$

$$3\bar{U}\bar{u}^2 \neq 0, \text{ because } \bar{u}^2 \neq 0.$$

$$\bar{u}^3 \begin{cases} = 0, & \text{if the probability distribution of } u \text{ is symmetrical,} \\ \neq 0, & \text{if the probability distribution of } u \text{ is skew.} \end{cases}$$

Eq. (2.2.3) can, therefore, be written as:

$$\bar{U^3} = \bar{U}^3 \left(1 + 3 \frac{\bar{u}^2}{\bar{U}^2} + \frac{\bar{u}^3}{\bar{U}^3} \right). \quad (2.2.4)$$

The difference between $\bar{U^3}$ and \bar{U}^3 , i.e. the difference between the true average energy flux and the energy flux estimated from the average wind velocity, depends strongly on the integration time T .

At small time intervals, e.g. $T = 1$ or 2 minutes, the contribution to u comes from the high-frequency turbulent fluctuations of the atmospheric boundary layer. In that case, the skewness of the probability distribution is small and the last term in Eq. (2.2.4) can be neglected. The turbulence intensity ($\sqrt{\bar{u}^2}/\bar{U}$) in the lower part of the atmospheric boundary layer (referred to as the local wind velocity) may be of the order of 20 percent. In that case, the difference $\bar{U^3}$ and \bar{U}^3 is 12 percent, viz.:

$$\bar{U^3} = \bar{U}^3 [1 + 3(0.2)^2] = 1.12 \bar{U}^3.$$

At very large time intervals, e.g. $T = 1$ year, the fluctuations from the average become very large and the probability distribution becomes skew, so that the third term in Eq. (2.2.4) is significant. In such a case, the ratio of $\bar{U^3}$ and \bar{U}^3 may amount to a factor 3 or 4.

When hourly averages ($T = 1$ hour) are used, the value of the factor is between the two values quoted above. In most cases, the contribution of the skewness is no large, and the factor does not differ significantly from the factor quoted for the small time intervals (1.12).

The data gathered at weather stations contain much more relevant information, e.g. the frequency distribution of the duration of a calm (no wind energy available) or the frequency distribution of the duration of a wind velocity within a certain velocity interval (duration of a certain energy production). This information is important in the discussion on energy storage.

2.2.2 Wind shear

The wind velocity increases with height. Greater heights possibly mean larger rotor diameters and, in that case, the wind velocity varies across the rotor area and the annual energy flux has to be averaged also over a certain height (Ref. 2.2).

The increase of the wind velocity with height (wind shear) can be described in two different ways, viz. with a power-law formula or with a logarithmic formula. Meteorologists often prefer the logarithmic formula, because it can be derived theoretically. The power-law description is used in this Section because of its simplicity and because it is used in Ref. 2.3.

The effect of the wind shear has been rather extensively studied in Sweden (Ref. 2.3). The wind shear depends on the wind direction, the wind velocity, and the stability condition of the atmosphere. The instantaneous velocity profile can be defined by an exponent α (see also Fig. 2.1):

$$U/U_{\text{ref}} = (H/H_{\text{ref}})^{\alpha} \quad (2.2.5)$$

Table 2.1 shows some results of Ref. 2.3.

Site	U (m/s) H = 50 m	α	Remarks
Oskarshamn	2.3	0.87	night wind from sea
	5.5	0.63	ditto
	9 - 10	0.31	wind from land
	10 - 15	0.12	wind from sea
Marviken	2.0	1.6	night wind from sea
	3.5	0.9	ditto
	4.5	0.38	wind from land
	7 - 12	0.36	ditto
	7 - 12	0.13	wind from sea

Table 2.1: Instantaneous wind shear data (Ref. 2.3)

The difference in measured wind shear between wind from land or from sea is caused by the difference in "surface roughness". Large differences in wind shear at low wind velocities are possibly due to different stability conditions of the atmosphere. Because wind velocities below 4 or 5 m/s are negligible with respect to their contribution to the annual average energy flux (cf. Sect. 2.3), these large variations in wind shear are not too interesting from the point of view of wind energy conversion.

In a statistical-average sense, the wind shear at the higher wind velocities depends only on the "surface roughness" in the wind direction. When a measured wind velocity at a small height is translated into a velocity at larger height, the wind direction has to be taken into account, when the surface roughness varies appreciably between the various wind directions.

In a sense Fig. 2.1 is somewhat misleading, because the wind profiles are given at the same U_{ref} (velocity measured by weather station). Under the same weather conditions, the wind velocity at a large height is almost independent of the surface roughness; since the effect of the surface roughness is a slowing down of the wind approaching the ground. At the other hand, Fig. 2.1 shows clearly how important it is to correct the wind velocity data measured in inland weather stations for the effective height of the wind turbine. Table 2.2 shows the influence of the wind shear on the energy flux $\frac{1}{2}\rho U^3$ (W/m²).

height (m)	10	20	30	40
	energy flux (W/m ²) $U_{500 \text{ m}} = 15 \text{ m/s}$			
wind from sea $\alpha = 0.12$	507	651	753	836
wind from land $\alpha = 0.31$	54	104	151	198

Table 2.2: Influence of wind shear on energy flux at low level with a constant velocity at large height (500 m)

2.2.3 Wind energy flux

In the literature, many estimations of the annual average energy flux have been given. The magnitudes depend strongly on the geographical location, but the factors discussed in the Sects 2.2.1 and 2.2.2 certainly also affect the values given.

Without starting an extensive survey of the literature, it seemed useful to give at least some figures, to illustrate the low density of wind energy and the consequently large turbine areas necessary to obtain a reasonable amount of energy from the wind.

Country	Ref.	Conditions		Annual average	
		height (m)	site	velocity (m/s)	energy flux (kW/m ²)
Canada	2.4	33	coastal	?	0.3 - 0.4
			inland	?	0.1 - 0.2
France	2.5	40	coastal	?	0.35 - 0.55
			inland	?	0.34
The Netherlands	2.6	14	coastal	6-7	0.47
Sweden	2.3	50	coastal	7.7	0.43
			inland	5.6	0.22
USA	2.7	?	coastal	6-7	0.15 - 0.2
			inland*)	7.8-8.6	0.3 - 0.4

*) Great Plains

Table 2.3: Average annual energy flux at several countries

There are, of course, large climatological differences between the countries listed, but in general coastal areas reveal higher energy fluxes than inland areas, with the Great Plains in the USA as a noticeable exception.

The wind energy flux above sea might be interesting, but information is scarce, and there are additional problems connected with wind energy "harvesting" on sea (platforms, maintenance).

2.3 Useable amount of wind energy

2.3.1 Design power, cut-in speed

It seems advantageous, from the point of view of economics, to limit the wind energy conversion at a certain maximum wind velocity (see e.g. Ref. 2.8). This (maximum) design power determines the costs (investments) of the WECS (Wind Energy Conversion System) to a large extent. In rural applications, such as pumping of water, it is often desirable that the wind turbine starts its operation at a wind velocity as low as possible. From the point of view of the annual energy production, such a low "cut-in" speed is not necessary, as is easily demonstrated by considering a wind velocity probability curve (Fig. 2.2).

When the probability of occurrence of a wind velocity within a certain interval is denoted by $P(U_i)$, the dimensionless distribution of energy, corresponding to a wind velocity interval U_j , can be calculated from

$$P(E, U_j) = \frac{U_j^3 P(U_j)}{\sum_i U_i^3 P(U_i)} \quad (i \text{ ranging over all classes}) \quad (2.3.1)$$

The denominator corresponds to the area below the $P(E, U)$ -curve in Fig. 2.2 and is, except a numerical factor, equal to the annual wind energy flowing through an area of 1 m^2 . The example given in Fig. 2.2 corresponds to an annual energy of $4.37 \text{ MWh/m}^2/\text{year}$.

It follows directly from Fig. 2.2, that low wind velocities have such a low energy flux that, notwithstanding their high probability, the contribution to the annual energy is negligible (shaded area at the left-hand side).

Very high wind velocities have a high energy flux, but, due to the low probability, their contribution to the annual energy is also low. When the excess power is destroyed partially (e.g. by blade-pitch control), in order to continue the energy production at wind velocities above the design speed, the corresponding power loss is even smaller than the shaded area at the right-hand side of Fig. 2.2.

The arguments for accepting a reduced annual energy production in order to reduce the design power (costs) are demonstrated more clearly in Fig. 2.3.

When a power coefficient

$$C_p = \frac{P}{\frac{1}{2} \rho U^3 S_{\text{ref}}} = 0.4$$

is assumed at wind velocities below the design speed, and a constant power above the design speed, it is possible to calculate the annual energy production, using the wind statistics of Ref. 2.6 as an example.

Fig. 2.3 shows, that the annual energy production increases very slowly at design speeds above say 15 m/s . Also shown in Fig. 2.3 is the ratio of the design power to the average annual power, which is a kind of "costs benefit"-ratio. The figure reveals a rapid increase of this ratio with design speed, which emphasizes the choice of a lower design speed.

2.3.2 Turbine characteristics

The useable amount of wind energy is further restricted by some characteristics of the wind turbine, viz. the performance characteristics and the effect of the operating mode (control).

One aspect pertaining to the performance characteristics of the wind turbine in connection with the useable amount of energy, is the possibility to convert also the energy from the turbulent component of the wind into mechanical energy. As mentioned in Sect. 2.2.1, this turbulent energy could possibly amount up to 12 percent of the energy, calculated from half-hourly or hourly mean values.

The possibility to convert turbulent energy with a wind turbine depends on the scale of the turbine with respect to the "scale" of the atmospheric turbulence. A very small turbine reacts on almost every fluctuation, but a large wind turbine only reacts on low-frequency (large-scale) fluctuation. The high-frequency (small-scale) fluctuations are "integrated" along the rotor blade span and possibly contribute nothing to (or even deteriorate) the driving force on the rotor blade, in the same way as there is no turbulence signal from a very long hot-wire. In Sect. 5 these effects will be discussed in more detail.

It is still questionable whether the development of a special large-scale quick-responding turbine is feasible, because the whole Wind Energy Conversion System (WECS) has to be attuned to it, and the extra amount of energy obtained is not very large.

In this context, it is perhaps worthwhile to mention the difference between Horizontal-Axis (HA) and Vertical-Axis (VA) turbines. The HA turbine has to be set into the wind direction to operate at maximum efficiency, whereas the VA turbine operates independently of the wind direction. Because a large HA turbine can only be yawed slowly, it is impossible to follow quick variations in wind direction, which possibly results in a reduction in energy production.

Betz (Ref. 2.9) showed long ago, that any wind turbine cannot extract more than a certain amount of energy from a given (steady) wind energy flux (see also Section 3.2.1), viz.:

$$C_{p_{\text{ideal}}} = \frac{P_{\text{ideal}}}{\frac{1}{2} \rho U^3 S_{\text{ref}}} = \frac{16}{27} \approx 0.59, \quad (2.3.2)$$

with

- P_{ideal} = theoretical maximum power of turbine (W)
 $\frac{1}{2}\rho U^3$ = wind energy flux (W/m²)
 ρ = air density (kg/m³)
 U = steady or average wind velocity (m/s)
 S_{ref} = area perpendicular to the wind stream, swept by the rotor of the turbine (m²).

The actual power coefficients of existing wind turbines are still lower than the ideal power coefficient given by Betz, because of rotation (vortices) left in the wake behind the rotor and because of viscous losses (profile drag). These aerodynamic losses depend on the type of wind turbine considered and will be discussed extensively in Sect. 4. Suggestions to increase the power coefficient above this Betz limit by so-called "wind concentrators", will be discussed in Sect. 3.

The variation of the power coefficient C_p with the operating conditions of a given turbine also plays an important role. The performance characteristics of a wind turbine are described by the variation of the power coefficient C_p and the torque coefficient C_Q with the tip-speed ratio λ . These quantities are defined as follows:

$$\lambda = \Omega R_0 / U, \quad (2.3.3)$$

with Ω = angular velocity of the rotor (rad/s)
 R_0 = maximum radius of the rotor (m);

$$C_p = \frac{P}{\frac{1}{2}\rho U^3 S_{ref}}, \quad (2.3.4)$$

$$C_Q = \frac{Q}{\frac{1}{2}\rho U^2 S_{ref} R_0}, \quad (2.3.5)$$

with P = aerodynamically generated power (W)
 Q = aerodynamic torque (Nm).

Because of the relation between power and torque

$$P = \Omega Q,$$

there is a relation between the power and torque coefficients, viz.:

$$C_p = \lambda C_Q. \quad (2.3.6)$$

Therefore, when the C_p -vs- λ curve is given, C_Q -vs- λ can easily be calculated by Eq. (2.3.6).

Figure 2.4 gives examples of the characteristics of HA and VA turbines, which, however, are perhaps not fully representative of a modern design. An important parameter that determines the λ -range in which the turbine operates is the so-called solidity ratio, i.e. the ratio of the total rotor blade area to the area swept by the rotor blades.

In case of the VA turbines one also often applies a solidity ratio defined by:

$$\sigma = B c / R_0, \quad (2.3.7)$$

with B = number of blades of the rotor (-),
 c = chord or the rotor blade (m).

The general definition of the solidity ratio is

$$\sigma = B / S_{ref} \int_0^s c \, ds, \quad (2.3.8)$$

with ds = blade-element length, measured along the span (m);
 s = total blade length, measured along the span (m).

For a constant C_p , a high solidity ratio means a low λ (Fig. 2.4) and, because of Eq. (2.3.6), a relatively high C_Q . Sometimes a high torque is wanted at a relatively low angular velocity (e.g. when a water pump is to be driven). In such a case, a multi-bladed HA turbine (so-called American windmill) or a Savonius turbine (VA turbine, $\sigma \geq 2$) can be applied. Both types are also "self-starting", i.e. they start rotating from standstill at a sufficiently high wind velocity.

A low solidity ratio means a high λ and a relatively low C_Q . In most WECS designs, the low-solidity turbines are preferred because of the higher angular velocity and the lower torque, which reduces the costs of the gear-box.

The VA Darrieus turbines are only weakly self-starting, with the torque being slightly positive for most parked positions. Usually, they have to be started by using the generator as a driving electric motor or by combining them with a Savonius rotor (see Ref. 2.7).

A low- σ HA turbine shows a rather flat-topped C_p -vs- λ curve. Therefore, the turbine can be operated at almost constant C_p over a rather large range of λ . This range of λ at almost constant C_p can even be increased by giving the blades a pitch control, i.e. by changing the blade setting angle during operation.

The Darrieus turbines show a much stronger variation of C_p with λ . However, the effect of the turbine characteristics on the annual energy production also depends on the operating mode, together with the wind statistics (Fig. 2.2). The choice of the operating mode of the turbine, viz. operating at λ = constant or Ω = constant, has important consequences, which will be discussed below. Little is found in the literature about matching the torque vs angular velocity curves of turbine and generator. This will, therefore, not be included in the discussion below.

λ = constant

It is clear from the outset, that a maximum amount of energy is extracted from the wind at every wind velocity, when the turbine always operates at the value of the tip-speed ratio λ corresponding with the

optimum power coefficient. In that case the angular velocity of the turbine Ω is proportional to the wind velocity U , the torque Q is proportional to U^2 , and the power P is proportional to U^3 . When the case of converting mechanical power P of the turbine into electric power is considered, it is often suggested to operate the generator at constant RPM, which requires much from the gear-box (variable gear-ratio).

$\Omega = \text{constant}$

When the turbine operates at constant angular velocity, λ varies proportional to $1/U$ and the generated power P and torque Q depend on the C_p -vs- λ curve, which is determined by the type of wind turbine considered.

Figure 2.5 shows idealized C_p -vs- λ curves for a HA and a VA turbine, together with corresponding C_p -vs- U curves for $\Omega = \text{constant}$.

A careful choice of Ω in case of a HA turbine results in a large range of wind velocities with an almost constant C_p equal to the optimum of C_p . The decrease of C_p at high and low U does not affect the annual energy production appreciably (cf. Sect. 2.3.1 and Fig. 2.2). It is also clear from Fig. 2.5, that special aerodynamic means are necessary to limit the power at high wind velocities to the design power (pitch control or spoilers for a HA turbine).

At $\Omega = \text{constant}$ the Darrieus (VA) turbine shows some favourable features. The choice of Ω determines automatically the cut-in speed by $C_p = 0$ at high λ . Even more important is the decrease of C_p at high wind velocities (low λ), at which the generated power (proportional to $C_p U^3$) shows a maximum, i.e. the design power can be fixed by choosing a proper value of Ω . When the Darrieus turbine is optimized by selecting a value for Ω and a value for the solidity ratio σ , also using a given wind velocity probability distribution, the annual energy production will be found to be not much lower than the same turbine operating at $\lambda = \text{constant}$ and at the same design power. The loss in annual energy production has to be balanced against a reduction in costs by using a simpler (less expensive) gear-box (see also the discussion in Ref. 2.10).

2.4 Structural aspects

2.4.1 Shape of the rotor blade

The large-scale wind turbine tends to be of a low-solidity type (higher angular velocity, lower torque) with relatively slender blades (small chord with respect to blade span). The bending stiffness of the blade is limited because the thickness-chord ratio of the profile has to be small (profile drag). To alleviate the bending stresses in the blade, special blade shapes have been developed. A typical example is the Darrieus turbine, where the bending stresses due to centrifugal forces have been avoided entirely (see also Appendix D).

From an aerodynamic point of view, a vertical-axis turbine with straight blades is advantageous, because the full span of the blade is aerodynamically active in generating power, whereas the extreme parts of the curved blades of a Darrieus turbine are aerodynamically less active. On the other hand, the Darrieus turbine has a structural advantage (shown in Fig. 2.6) when it is compared with the straight-bladed vertical-axis turbine. In addition, the Darrieus turbine can operate at substantially higher circumferential velocities than the straight-bladed vertical-axis turbine at an equal stress level, which is advantageous in view of the lower torque and lower gear-ratio of the gear-box.

The rather simple estimate of the stress in the blades of a Darrieus turbine due to centrifugal forces is possible when a constant chord and mass distribution along the span is assumed, because the blade mass is proportional to the material cross-section of the blade, which cross-section is also used to calculate the stress and, therefore, drops out of the formula. For the calculation of the bending stress in a straight-bladed vertical-axis turbine, however, a t/c -value has to be assumed and the radius of gyration of the section is chosen equal to $\frac{1}{2}t$ (Appendix D).

Figure 2.6 shows the large influence of the blade support on σ_b for a straight-bladed vertical-axis turbine, but even the multiple-supported blade is inferior to the curved Darrieus rotor blades. Details about the so-called "troposkien" blade shape of the Darrieus turbine can be found in the Refs 2.11 and 2.12 (the name troposkien was coined by Blackwell and Reis as a greek transliteration of "skipping rope", i.e. "tropos" = turn and "schoinion" = rope).

The centrifugal acceleration exerts pure tensile forces in the blades of a horizontal-axis turbine. The tensile stress is a function of the tip speed (λU) and the taper ratio of the blades, when a mass per unit length is assumed that is proportional to chord times thickness ($t c$). Results of such an estimation are shown in Fig. 2.7 (for details see App. D). Comparison between the Figs 2.6 and 2.7 reveals that the horizontal-axis turbine can withstand even higher tip speeds than a Darrieus turbine at an equal stress level.

The shape of the aerodynamic load distribution on a curved-bladed vertical-axis turbine differs slightly from the shape of the centrifugal load distribution. Therefore, small bending moments may remain in a troposkien-shaped rotor blade. It should be possible to modify the troposkien in such a way, that the bending moments due to a given aerodynamic loading would be exactly zero, but this has little practical significance.

In the case of a horizontal-axis turbine, the blade shape can be chosen in such a way that the bending moments due to the combined action of centrifugal and aerodynamic load are exactly zero. This can only be realized, however, at one value of $\lambda = \Omega R_0 / U$.

Figure 2.8 shows an estimation of the required shape of the blade, i.e. such a shape that the resultant of the centrifugal and the aerodynamic load is always parallel to the blade span. The aerodynamic load is estimated for an optimum turbine according to the theory of Glauert (Ref. 2.13), neglecting tip losses. Therefore, the displacement (x/R_0) at the tip is slightly over-estimated. The data of Fig. 2.8 apply to a rather heavy rotor-blade construction; light-weight constructions are not considered here, because such constructions lead to large displacements and thus to unrealistic blade shapes (for details see App. D).

So far, the influence of gravity was neglected in the discussion of the blade shape. It can be shown, that the influence of gravity on a troposkien depends on the ratio of centrifugal acceleration to the acceleration of gravity, thus $\Omega^2 R_0 / g$. Darrieus turbines of similar shapes but different sizes operate at equal tip speed ratios $\lambda = \Omega R_0 / U$. The above-mentioned ratio can, therefore, be written as $\lambda^2 U^2 / g R_0$. This ratio decreases with increasing size of the turbine, which suggests that the weight of the rotor blades may not be neglected when a large-scale Darrieus turbine is considered. The ratio of the maximum tensile force in the rotor blade due to the centrifugal load and the weight of the rotor blade is a good indicator whether gravity can be neglected. This ratio is shown in Fig. 2.9.

In case of a large-scale Darrieus turbine, the weight will cause bending moments in the blade. It is possible to modify the troposkien in such a way, that bending moments due to weight are avoided too. This is, however, only possible at one chosen value of $\Omega R_0 / g$, i.e. only when the turbine operates at $\Omega = \text{constant}$.

The influence of the weight on the blade loading of a horizontal-axis turbine is somewhat more complicated. The load varies during a revolution of the rotor and can, therefore, not be compensated by a modification of the shape of the rotor blade. The variation in tensile force depends on the ratio between maximum centrifugal force and weight of the blade. For a blade with taper ratio 0.5, this amounts to

$$\frac{\text{centrifugal force}}{\text{weight}} \approx 0.2 (\Omega R_0)^2 / g R_0,$$

which differs from the values given in Fig. 2.9 for the Darrieus vertical-axis turbine by not more than a factor 0.6.

When the blade of a horizontal-axis turbine is in a horizontal position, the bending moments due to the weight will be maximal. Because of the blade twist, there will be a component of the bending-moment vector parallel to the blade chord at the blade root. The blade thickness is always smaller than the chord, and the bending stresses due to weight at the blade root may, therefore, become significant.

From the preceding discussion, it can be concluded that a careful consideration of the shape of the rotor blade is helpful in alleviating blade stresses.

In case of a vertical-axis turbine, bending moments due to centrifugal forces can be avoided by applying a troposkien blade shape. Under operation at $\Omega = \text{constant}$, the bending moments due to weight can also be avoided by modifying the troposkien. Bending moments due to the aerodynamic load cannot be avoided completely, but are of little practical significance.

In case of a horizontal-axis turbine, centrifugal forces only induce tensile stresses. When the turbine operates at $\lambda = \text{constant}$, the rotor blade can be bent in such a way, that bending moments due to the aerodynamic load are avoided. Variation in tensile and bending stresses due to weight cannot be alleviated by changing the shape of the rotor blade.

2.4.2 Aerodynamic loads on a wind turbine

In the preceding Section, the aerodynamic load on a rotor blade was already mentioned. That load was thought to be due to a steady homogeneous wind stream. An actual wind turbine is immersed, however, in a highly turbulent wind stream with a more or less steady vertical wind gradient or wind shear.

A detailed discussion of the aerodynamics of rotors will be given in Section 4, whereas the influence of wind shear and turbulence will be discussed in Section 5.

It seems adequate to point out here the importance of the scale of the wind turbine with respect to the "scale" of the turbulence of the atmospheric boundary layer. A small-diameter turbine (say, 1 m), responds to more or less rapid variations of wind velocity and wind direction, whereas a large diameter turbine (say 50 m) responds only to relatively slow variations in wind velocity and direction and does not respond to rapid variations, because they act only on a part of the whole rotor. The quintessence of this remark is the change in character of the fluctuating aerodynamic load due to turbulence with the scale of the wind turbine.

Also important to notice is the different behaviour of a VA and a HA turbine in wind shear and turbulence.

A wind shear induces a stationary load distribution along the span of the blade in case of a VA turbine, but in case of a HA turbine, a wind shear induces aerodynamic load variations during a revolution. With other words, wind shear contributes to the fatigue load in the case of a HA turbine. Variations in wind direction that are slow with respect to the time needed for one revolution of the rotor do not affect a VA turbine, whereas such variations lead to fluctuating aerodynamic loads in case of a HA turbine, because it cannot be yawed fast enough to follow the variations in wind direction. The faster variations in wind velocity and direction contribute to the aerodynamic fatigue load for both the HA and the VA turbine.

Another important fluctuating load source stems from the aerodynamic blade-tower interference, i.e. a load variation due to moving the rotor blade through the wake of the tower. Such an interference is always present in case of a VA turbine, but the interference is relatively mild, because the effective part of the rotor blade is at a relatively large distance from the tower. In case of a HA turbine, such an interference is only present with a rotor downstream of the tower. The interference is strong in that case, because of the short distance between blade and tower.

A significant static load case is the stopped rotor during a heavy storm. In such a case, the pre-stressing action of the centrifugal forces disappears and the bending moments increase strongly.

Templin and South (Ref. 2.14) discuss the blade buckling in case of a Darrieus wind turbine. In case of a HA turbine, it is often proposed to feather the blades in case of a heavy storm.

Banas and Sullivan (Ref. 2.10) discuss the favourable feature of operating a Darrieus VA turbine at $\Omega = \text{constant}$, because of the decrease of the torque above a certain wind velocity (by blade stall), which does not necessitate the stopping of the turbine at a heavy storm. The pre-stressing effect of the centrifugal forces diminishes the danger of blade buckling in that case.

Since the rotor blades are connected to the tower in one way or another, the aerodynamic loads on the blades are transferred to the tower. In case of a HA turbine in a steady wind, this results in a constant force downstream, the so-called "rotor drag" force. A VA turbine in a steady wind also experiences this rotor drag in a time-average sense, but the instantaneous force varies during a revolution in case of a one- or two-bladed rotor. In case of a three- or more-bladed rotor, the rotor drag is almost time-independent.

When we sum up this Section, it can be stated that a wind turbine is subject to varying loads, which determine the fatigue lifetime of the structure, especially that of the rotor blades.

Turbulence of the atmospheric boundary layer contributes to the fatigue load in case of both the VA and the HA turbine. An additional fatigue load comes from the periodic lift variation during a revolution in case of a VA turbine, but also a HA turbine shows additional fatigue loads due to wind shear, due to the fact that it is not properly aligned with the wind direction, and due to blade-tower interference in case of a downstream-placed rotor.

Notice, that the gravity forces cause fluctuating blade forces in case of a HA turbine also (cf. Sect. 2.4.1).

2.4.3 Aeroelastic effects

In the preceding Sections, external loads and their relation with the turbine configuration have been mentioned. The severity of the loads can only be judged by calculating the stresses induced in the structure by these loads.

From the more or less steady external loads, the stresses in the structure can be estimated in a rather straightforward way, although in case of a statically indeterminate structure, it might be necessary to apply a finite-element computation method.

The estimation of fluctuating stresses due to fluctuating external loads is often less straightforward. Only in the case of low-frequency fluctuations, a quasi-steady calculation of the stresses might make sense, but if frequencies occur approaching some of the eigenfrequencies of the structure, this might lead to strong discrepancies. This means, that the wind turbine has to be considered as an elastomechanic structure and that the various responses to fluctuating loads have to be calculated. When these calculations have to be preferred, the specialized field of vibrations and aeroelasticity is entered.

It is obvious that a HA turbine and a helicopter rotor have much in common, and the experience from helicopter industry should be valuable. There are, however, differences which make that these results are not directly applicable to a wind turbine, and that the aeroelastic modeling of a wind turbine has to be formulated from the basis, as is discussed in Ref. 2.15. The VA turbine reveals some characteristics differing from the HA turbine, which necessitate an alternative formulation (see e.g. the discussion in Ref. 2.16). The flutter boundary for a VA turbine, using a blade flutter and a mass parameter, has been discussed in Ref. 2.14.

In general terms, the aeroelastic modeling of a wind turbine starts with setting up the equations of motion of the rotating elastomechanic structure. Solving these equations of motion is largely facilitated by choosing such a co-ordinate system, that the coefficients of the differential equation are time-independent. In that case, the solution procedure boils down to a system of linear eigenvalue equations, from which the stability of the system can be studied more easily. Some remarks have to be made on the choice of the co-ordinate system, in order to obtain time-independent coefficients in the differential equation.

A rotating three- or more-bladed rotor described in a co-ordinate system fixed to "earth" reveals a kind of polar symmetry, which leads to time-independent coefficients. This is no longer true for a one- or two-bladed rotor. In that case, the co-ordinate system has to be fixed to the rotor instead of to earth. It is here that an important difference appears between VA and HA turbines. A one- or two-bladed turbine with a co-ordinate system fixed to the rotor describes the "tower" or "base" as a structure rotating in the co-ordinate system, and time-independent coefficients can only be obtained when the tower or base has a polar symmetry with respect to the "rotor-fixed" co-ordinate system. Such a polar symmetry can only be expected with a VA turbine, not with a HA turbine. With a view to the cost-effectiveness, there is a preference for a two-bladed HA turbine, which leads to differential equations with time-dependent coefficients and a correspondingly increased computational labor to solve these equations (Ref. 2.15).

When only inertial forces are considered, the stability calculations reveal the dynamic stability of the wind turbine (e.g. the existence of a "critical" RPM).

When so-called "self-induced" aerodynamic forces are included, i.e. aerodynamic forces due to vibratory motions, important flutter cases can be disclosed. Because of the rotation of the rotor, even in still air a high velocity relative to the rotor blade exists and small angle-of-attack variations due to the vibratory motion induce appreciable aerodynamic force variations. This explains why the flutter boundaries of Ref. 2.14 are almost independent of the wind velocity.

The aerodynamic forces due to a steady wind velocity are almost constant for a HA rotor and periodically varying for a VA rotor. These aerodynamic forces might induce flutter in case of a VA turbine, but such a behaviour has not been reported at present.

The calculation of the response of the elastomechanic structure to fluctuating external loads, such as blade-tower interference, turbulence (gusts), non-harmonic aerodynamic forces due to the wind, and weight (HA turbine), is more complicated than a stability calculation and it is necessary to obtain reliable estimations of the fatigue loading. The main problem is the estimation of the external load fluctuations (Sect. 2.4.2).

Rather simple considerations can lead to the advice to design the rotor blade cross-section in such a way, that elastic axis, centre of gravity and aerodynamic centre almost coincide, in order to decouple bending and torsion modes of the rotor blade (Ref. 2.10). In Ref. 2.17, however, only a minor effect of blade cross-section mass balancing on the presence of instabilities is mentioned. It is not clear whether

such a conclusion is also valid for a HA turbine.

In reference 2.14 it is stated that sufficient bending and torsional stiffness of the curved rotor blade of a Darrieus turbine is necessary to avoid instabilities, together with sufficient torsional stiffness of the tower.

Sufficient bending stiffness seems sometimes only obtainable by bracing the blades to the tower with struts. The bending stiffness of the tower is increased by guy-wires. In reference 2.17 information is given about the static and dynamic behaviour of guyed masts, together with a reference to the literature.

A two-bladed VA turbine shows a large variation of the torque during a revolution of the rotor, similar to the variation of the rotor drag mentioned in Sect. 2.4.2. In reference 2.14, however, it is stated that this torque "ripple" is largely attenuated by the elasticity of the rotor and the slip characteristics of the induction-type generator, which lead to a tolerable output voltage ripple. The study of the transfer function between the aerodynamic torque (input) and the generator voltage (output) seems, therefore, an interesting subject.

In the case of a HA turbine, a flexible blade hinge is effective in reducing fluctuating blade stress levels (see e.g. Ref. 2.18; hingeless, teetering, coning, gimbaled, or fully articulated). The minimum clearance between blade and tower depends on the coning angle and the dynamic response of the blade on sudden gusts (bending). This clearance is a larger problem in case of a rotor upstream of the tower, but might be reduced by tilting the rotor (Fig. 2.10).

The downstream rotor has the disadvantage of the fatigue load due to blade-tower interference, whereas the tilted rotor shows the disadvantage of fluctuating loads due to the fact that it is not aligned with the wind direction. A tilted rotor might, however, alleviate the fluctuating loads due to wind shear (vertical wind gradient). Sufficient blade-tower clearance in case of an upstream rotor is also obtained by using a swept-forward tower, with the additional advantage of lower bending moments in the tower (Fig. 15 of Ref. 2.19), but the disadvantage of yawing a large part of the tower, together with the rotor into the wind direction.

The problem of calculating the aeroelastic response of a wind turbine to external load variations, in order to estimate fluctuating stress levels (fatigue), is related to the problem of the dynamic response of the whole wind energy conversion system to "gusts". Such a dynamic response can, for instance, be used to estimate fluctuations in electric output (voltage ripple).

Reference 2.20 suggests the use of aeroelastic effects of the rotor blades in the conversion of the energy contained in gusts by a quick aeroelastic response, instead of using a slower mechanical pitch-regulating device.

An interesting problem is the question whether aeroelastic problems increase with increasing scale of the wind turbine. In case of geometrically similar wind turbines, the reduced (dimensionless) eigenfrequencies of the structure are almost independent of scale, which is also the case with the stresses due to aerodynamic and centrifugal forces (Refs 2.14 and 2.18). This seems to indicate that aeroelastic instabilities are almost independent of scale, but the assumption of a geometrically similar structure is probably not valid when the size of the turbine increases drastically.

Such a change in the structure might be due to the increase of stresses with an increase of the scale of the turbine, caused by gravity (Ref. 2.18, see also Sect. 2.4.1). The change in the stress levels, caused by a change of the ratio between the rotor diameter and the "scale" of the atmospheric turbulence (cf. Sect. 2.4.2), might also give rise to different structural designs for large-scale turbines.

Moreover, from cost-effectiveness considerations, the tower and blade structure of a small-scale wind turbine is relatively rigid, because it becomes expensive to develop a special light-weight structure at a small scale. On the other hand, such a development becomes a must at large scale, and the relative stiffness of the structure will be correspondingly reduced.

2.5 Conversion, storage and distribution to the consumer

The kind of conversion chosen for the wind energy conversion system has a strong influence on the choice of the type of wind turbine and gear-box (speed increaser). The direct use of the mechanical energy of the wind turbine can be envisaged in small-scale rural applications, such as pumping water for irrigation. For that purpose often a low- λ type of wind turbine is chosen (large torque, low RPM); the RPM regulation is then of minor importance.

Using the mechanical energy for driving machinery, as in ancient times, does not seem feasible any more.

Conversion of the mechanical energy into a lower-graded kind of energy, e.g. heat, seems feasible when the distance between turbine and consumer is not too large, but even in that case it is often proposed to produce electricity as an intermediate step. Also electrolysis is proposed to produce hydrogen gas, but, as a matter of fact, almost every proposal today is directed towards the production of electricity.

Conversion of the mechanical energy into electric energy, which has to be fed directly into the public utility network, puts a high demand on the output frequency and voltage, and it is often suggested that an almost constant generator RPM facilitates this task appreciably. This implies using a gear-box with a variable gear-ratio or operating the wind turbine at constant RPM. Reference 2.21 gives an appealing but not searching review of possible applications.

Considerations about pros and cons of DC or AC conversion are too specialized to be mentioned here. Some related information is given in the Refs 2.22 through 2.28.

A disadvantage of wind energy is the variance between supply and demand. Energy storage seems a logical answer to this problem, but the feasibility of storing a large amount of energy is still questionable, apart from some special applications.

Storage of electric energy in batteries is only feasible in small- to medium-scale applications, and the high costs of a battery bank are only acceptable when no alternative energy sources are available.

(e.g. in remote areas).

Energy storage by electrolysis of water and recuperation in a fuel cell or by mixing the hydrogen gas with natural gas, is sometimes proposed (Refs 2.29 through 2.31).

Storage of pumped water depends on local conditions: see e.g. Ref. 2.32, where it is reported that water is pumped out of a cavity in a salt layer and the energy is recuperated by dumping the water into the cavity via a hydro-turbine.

Storage by compressed air is proposed in Ref. 2.33, whereas energy storage in flywheels is also studied (e.g. Ref. 2.34). Energy storage in heated water is a possibility in case of space heating (Ref. 2.21).

It is characteristic for the change in attitude towards energy storage, however, that six papers dealing with energy storage were presented at the First Workshop on Wind Energy Conversion Systems in the USA in 1973, whereas only one paper was presented at the Second Workshop in 1975.

The distribution of the energy to the consumer is no direct problem when the wind turbine and consumer are nearby, as is mostly the case in small-scale applications. For large-scale applications with an extensive array of wind turbines, the energy production can be so large, that the energy has to be transported over hundred kilometers or more.

The distribution of energy from an array of wind turbines to a number of dispersed consumers is made possible by converting the energy into electricity or hydrogen gas. To by-pass the high costs of a distribution network of power-lines or pipe-lines, it is frequently proposed to use existing public utility networks.

In case of electricity, because storage is difficult in large-scale applications, the electric power has to be fed directly into the public utility network (standard voltage and frequency). To overcome losses at larger transport distances, the output voltage has to be transformed into higher values before putting it on the power line.

In existing networks and power stations, special measures have to be taken to balance demand and supply. Because of the fluctuating supply in case of wind power, these measures become more complicated. In reference 2.35 it is suggested to couple several arrays of wind turbines across a whole country in order to smoothen out the fluctuations in wind power supply. When wind energy delivers only a fraction of the total electric power in the network, the circulating energy fluxes in the coupled networks remain small and are perhaps acceptable.

Studies about these operational problems are progressing in several countries today, but results have not yet appeared in the open literature.

2.6 Cost analyses

When the wind statistics of a country, or a part of it, look promising, when the industrial capability is sufficiently developed to design and construct a wind energy conversion system, and when there is a market for wind-generated power by selecting a suitable conversion, storage and distribution system, a very difficult question remains to be answered, viz. what is the price of wind energy in that particular case.

It is certainly true that the wind energy price (e.g. US dollar cents/kWh) is not an absolute criterion for the feasibility. In remote and isolated regions, the prices for the traditional forms of energy are much higher, and a wind energy price that was too high for a densely populated and industrialized region might be acceptable there (Refs 2.36 and 2.37). Moreover, when diversification of energy sources is considered in order to become less dependent upon fossil fuel imports in the long run, it might be a policy to accept a relatively high price for wind energy. The feasibility of wind energy with respect to the wind energy price is also intimately connected with the future development of the price of fossil fuels.

It takes an expert to judge the results of several cost analyses appearing in the literature. A direct comparison is often difficult, due to various assumptions about inflation and interest rates and about that part of the system that had to be included into the cost calculation (R&D costs, costs of adaptation to public utility network, etc.). Furthermore, a comparison of the calculated wind energy prices is hindered by differences in the assumed amount of wind energy (wind climate) and other external factors. In order to compare the cost effectiveness of different wind energy conversion systems, it has been suggested to formulate standard data as a basis for such a comparative cost analysis.

A breakdown of the costs of a wind energy conversion system is interesting, because it signalizes that part of the system that looks most promising for R&D in low-cost design. In case of the Putnam 1500 kW horizontal-axis wind turbine, the rotor accounted for almost 43 % of the total cost (Ref. 2.38). In reference 2.39 a cost breakdown is given for a 4 kW vertical-axis wind turbine and in reference 2.40 for a 1000 kW horizontal-axis turbine. Both breakdowns, though not fully comparable, are shown below.

Ref. 2.39		Ref. 2.40	
rotor	26 %	rotor	28 %
bearings	11 %	pintle + drive	9 %
tower	23 %	tower	18 %
gear-box, generator, etc.	40 %	electric system	14 %
		controls system	2 %
		installation	4 %
		site + support fac.	4 %

Table 2.4: Cost breakdown of a small-scale VA (Ref. 2.39) and a large-scale HA (Ref. 2.40) wind turbine.

Modern blade-manufacturing concepts seem to have reduced the rotor costs already from 43 % to 28 %. It must be mentioned in this context, that in Ref. 2.39 the conclusion is drawn that above 20 kW a vertical-axis turbine becomes less economic than a horizontal-axis turbine.

In figure 2.11 a number of energy cost estimates found in the literature is compared. There is indeed a tendency that large vertical-axis turbines become less economic than large horizontal-axis turbines. The variance between the several estimations is, however, large.

According to Ref. 2.32, a storage system almost doubles the price of the WECS. Whether the availability of a more regular flow of energy is worth such an extra investment is difficult to assess.

2.7 Environmental effects

When the technological and economical problems are solved, some problems remain in the area of environmental effects and public acceptance.

Although wind energy (and also solar energy) is a non-polluting kind of energy production in a strict sense, there are phenomena that might be unacceptable in some situations, e.g.:

- Visual pollution, i.e. a large array of wind turbines might be harmful to an attractive landscape.
- Interference with FM radio and TV transmission due to large rotating metal rotor blades. When fibre glass and epoxy are used as constructing materials, these problems might be overcome.
- Interference with bird migratory routes, which might cause an unacceptable high rate of bird collisions.
- Deterioration of the climate due to a reduction of the wind velocities. A variation in the weather system due to an increased "surface roughness" caused by large arrays of wind turbines seems improbable, but an influence on the "micro" climate might be possible.
- Land use. Due to the necessary spacing of the turbines, and due to the safeguarding and access roads, a substantial area will be needed for a wind turbine array.

The above-mentioned situations may differ from country to country. In a densely populated country as The Netherlands, visual pollution and land use mean strong limitations to the possible use of wind power (Ref. 2.41), whereas these factors might be less restrictive in other countries with large uninhabited areas.

2.8 List of references

- 2.1 Freeman, B.E., Taft, J.R.: Mathematical Modelling of Topographic Effects on Wind Energy Systems. Proc. Intern. Symp. on Wind Energy Systems (St. John's College, Cambridge, England; 7-9 Sept. 1976).
- 2.2 Ljungström, O.: Large Scale Wind Energy Conversion System (WECS) Design and Installation as Affected by Site Wind Energy Characteristics, Grouping Arrangement and Social Acceptance. Proc. Intern. Symp. on Wind Energy Systems (St. John's College, Cambridge, England; 7-9 Sept. 1976).
- 2.3 Ljungström, O.: Wind Energy Resources Model for Sweden - Summary Report. National Swedish Board for Energy Source Development (STU). Report No. VES-1975: 28E (22 Jan. 1976).
- 2.4 Rangi, R.S., South, P., Templin, R.J.: Wind Power and the Vertical-Axis Wind Turbine Development at the National Research Council. NRC Canada Quart. Bull. Report No. DME/NAE 1974(2) (Ottawa, 1 April to 30 June 1974) pp. 1-14.
- 2.5 Bonnefille, R.: Les Réalisations d'Électricité de France Concernant l'Énergie Éolienne. d'Électricité de France, Rapport F 40/74 No.4 (Avril 1974).
- 2.6 -- : Wind Velocity Data of Den Helder in the Period 1961 up to 1970, Obtained from the Data Files of the Royal Netherlands Meteorological Institute (KNMI).
- 2.7 Blackwell, B.F., Feltz, L.V.: Wind Energy - A Revitalized Pursuit. Sandia Laboratories Report SAND75-0166 (March 1975).
- 2.8 Golding, E.W.: The Influence of Aerodynamics in Wind Power Development. AGARD Report 401 (1961).
- 2.9 Betz, A.: Windenergie und ihre Ausnutzung durch Windmühlen. Vandenhoeck und Ruprecht (Göttingen, 1926).
- 2.10 Banas, J.F., Sullivan, W.N.: Sandia Vertical-Axis Wind Turbine Program Technical Quarterly Report (Oct.-Dec. 1975). SAND76-0036 (April 1976).
- 2.11 Blackwell, B.F., Reis, G.E.: Blade Shape for a Troposkien Type of Vertical-Axis Wind Turbine. Sandia Laboratories Rep. SLA-74-0154 (April 1974).
- 2.12 Swamy, N.V.C., Fritzche, A.A.: Aerodynamic Studies on Vertical-Axis Wind Turbine. Proc. Intern. Symp. on Wind Energy Systems (St. John's College, Cambridge, England; 7-9 Sept. 1976).
- 2.13 Glauert, H.: Windmills and Fans. Aerodynamic Theory (ed. W.F. Durand), Chapter XI, Div. L. (Dover Publ. Inc., N.Y., 1963).
- 2.14 Templin, R.J., South, P.: Some Design Aspects of High-Speed Vertical-Axis Wind Turbines. Proc. Intern. Symp. on Wind Energy Systems (St. John's College, Cambridge, England; 7-9 Sept. 1976).
- 2.15 Friedmann, P.P.: Aeroelastic Modelling of Large Wind Turbines. Journ. Am. Hel. Soc. 21 (Oct. 1976) pp. 17-27.
- 2.16 Ham, N.D.: Aeroelastic Analysis of the Troposkien-Type Wind Turbine. Proc. Vertical-Axis Wind Turbine Techn. Workshop (Albuquerque, New Mexico; 18-20 May 1976). Sandia Laboratories Report SAND76-5586 (July 1976).
- 2.17 Reuter Jr., R.G., Sheldahl, R.E. (editors): Sandia Vertical-Axis Wind Turbine Project Technical Quarterly Report (April-June 1976). SAND76-0581 (Jan. 1977).
- 2.18 Ormiston, R.A.: Rotor Dynamic Considerations for Large Wind Power Generator Systems. Proc. Workshop on Wind Energy Conversion Systems (Washington D.C.; 11-13 June 1973). NSF/RA/W-73-006 (Dec. 1973).

- 2.19 Hütter, U.: Optimum Wind-Energy Conversion Systems.
Ann. Rev. Fluid Mech. 9 (1977) pp. 399-419.
- 2.20 Jordan, P.F.: Improved Rotors through Utilization of Aeroelastic Effects.
Proc. Second Workshop on Wind Energy Conversion Systems (Washington D.C.; 9-11 June 1975).
The Mitre Corp. MTR-6970 (Sept. 1975).
- 2.21 Eldridge, F.R.: Wind Machines.
The Mitre Corp. MTR-6971 or NSF-RA-N-75-051 (Oct. 1975).
- 2.22 Reitan, D.K.: Wind-Powered Asynchronous AC/DC/AC Converter System.
Proc. Workshop on Wind Energy Conversion Systems (Washington D.C.; 11-13 June 1973).
NSF/RA/W-73-006 (Dec. 1973).
- 2.23 Reitan, D.K.: A Progress Report on Employing a Non-Synchronous AC/DC/AC Link in a Wind Power Application.
Proc. Second Workshop on Wind Energy Conversion Systems (Washington D.C.; 9-11 June 1975).
The Mitre Corp. MTR-6970 (Sept. 1975).
- 2.24 Allison, H.J.: An Electrical Generator with a Variable Speed Input - Constant Frequency Output.
Proc. Workshop on Wind Energy Conversion Systems (Washington D.C.; 11-13 June 1973).
NSF/RA/W-73-006 (Dec. 1973).
- 2.25 Jayadev, T.S.: Novel Electric Generation Schemes for Wind Power Plants.
Proc. Second Workshop on Wind Energy Conversion Systems (Washington D.C.; 9-11 June 1975).
The Mitre Corp. MTR-6970 (Sept. 1975).
- 2.26 Braasch, R.H.: Vertical-Axis Wind Turbine Program.
Proc. Vertical-Axis Wind Turbine Techn. Workshop (Albuquerque, New Mexico; 18-20 May 1976).
Sandia Laboratories Report SAND76-5586 (July 1976).
- 2.27 Veneruso, A.F.: Electrical Power System.
Proc. Vertical-Axis Wind Turbine Techn. Workshop (Albuquerque, New Mexico; 18-20 May 1976).
Sandia Laboratories Report SAND76-5586 (July 1976).
- 2.28 Hirst, P., Rees, D.H.: The Regulation, Storage and Conversion of Wind Produced Electrical Energy at the Level of a Few Hundred Watts.
Proc. Intern. Symp. on Wind Energy Systems (St. John's College, Cambridge, England; 7-9 Sept. 1976).
- 2.29 Hughes, W.L.: Energy Storage Using High-Pressure Electrolysis and Methods for Reconversion.
Proc. Workshop on Wind Energy Conversion Systems (Washington D.C.; 11-13 June 1973).
NSF/RA/W-73-006 (Dec. 1973).
- 2.30 Hausz, W.: Use of Hydrogen and Hydrogen-Rich Components as a Means of Storing and Transporting Energy.
Proc. Workshop on Wind Energy Conversion Systems (Washington D.C.; 11-13 June 1973).
NSF/RA/W-73-006 (Dec. 1973).
- 2.31 Titterton, W.A.: Status and Applicability of Solid Polymer Electrolyte Technology to Electrolytic Hydrogen and Oxygen Production.
Proc. Workshop on Wind Energy Conversion Systems (Washington D.C.; 11-13 June 1973).
NSF/RA/W-73-006 (Dec. 1973).
- 2.32 Fekete, G.I.: A Self-Contained 5,000 kW Capacity Wind Energy Conversion System with Storage.
Proc. Intern. Symp. on Wind Energy Systems (St. John's College, Cambridge, England; 7-9 Sept. 1976).
- 2.33 Szego, G.C.: Energy Storage by Compressed Air.
Proc. Workshop on Wind Energy Conversion Systems (Washington D.C.; 11-13 June 1973).
NSF/RA/W-73-006 (Dec. 1973).
- 2.34 Rabenhorst, D.W.: Superflywheel Energy Storage System.
Proc. Workshop on Wind Energy Conversion Systems (Washington D.C.; 11-13 June 1973).
NSF/RA/W-73-006 (Dec. 1973).
- 2.35 Molly, J.P.: Balancing Power Supply from Wind Energy Converting Systems.
Proc. Intern. Symp. on Wind Energy Systems (St. John's College, Cambridge, England; 7-9 Sept. 1976).
- 2.36 Dodge, R.: Economic Considerations of Utilizing Small Wind Generators.
Proc. Workshop on Wind Energy Conversion Systems (Washington D.C.; 11-13 June 1973).
NSF/RA/W-73-006 (Dec. 1973).
- 2.37 VanSant, J.H.: Wind Utilization in Remote Regions - An Economic Study.
Proc. Workshop on Wind Energy Conversion Systems (Washington D.C.; 11-13 June 1973).
NSF/RA/W-73-006 (Dec. 1973).
- 2.38 Wilson, R.E.: The Oregon State University Wind Studies.
Proc. Workshop on Wind Energy Conversion Systems (Washington D.C.; 11-13 June 1973).
NSF/RA/W-73-006 (Dec. 1973).
- 2.39 Fritzsche, A.A.: Economics of a Vertical-Axis Wind Turbine.
Proc. Intern. Symp. on Wind Energy Systems (St. John's College, Cambridge, England; 7-9 Sept. 1976).
- 2.40 Meier, R.C.: Concept Selection, Optimization and Preliminary Design of Large Wind Generators.
Proc. Second Workshop on Wind Energy Conversion Systems (Washington D.C.; 9-11 June 1975).
The Mitre Corp. MTR-6970 (Sept. 1975).
- 2.41 Van Essen, A.A., et. al.: Physical Planning Aspects of Large-Scale Wind Energy Exploitation in The Netherlands.
Proc. Second Intern. Symp. on Wind Energy Systems (Amsterdam, 3-6 Oct. 1978).
- 2.42 Weingarten, L.I., Blackwell, B.F.: Sandia Vertical-Axis Wind Turbine Program Technical Quarterly Report (Jan.-March 1976).
SAND76-0338 (Aug. 1976).
- 2.43 Lissaman, P.B.S.: General Performance Theory for Crosswind Axis Turbines.
Proc. Intern. Symp. on Wind Energy Systems (St. John's College, Cambridge, England; 7-9 Sept. 1976).
- 2.44 Divone, L.V.: Federal Wind Energy Program.
Proc. Vertical-Axis Wind Turbine Techn. Workshop (Albuquerque, New Mexico; 18-20 May 1976),
Sandia Laboratories Report SAND76-5586 (July 1976).

- 2.45 Banas, J.: Economic Considerations.
Proc. Vertical-Axis Wind Turbine Techn. Workshop (Albuquerque, New Mexico; 18-20 May 1976).
- 2.46 Killen, R.: G.E. Systems Studies of Large-Scale WECS.
Proc. Second Workshop on Wind Energy Conversion Systems (Washington D.C.; 9-11 June 1975).
The Mitre Corp. MTR-6970 (Sept. 1975).

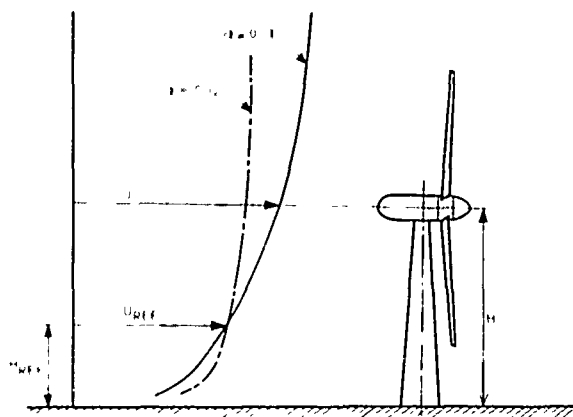


Fig 2.1 Idealized wind shear profiles in relation to a large-scale wind turbine

$\alpha = 0.31$, wind from land (rough)
 $\alpha = 0.12$, wind from sea (smooth)

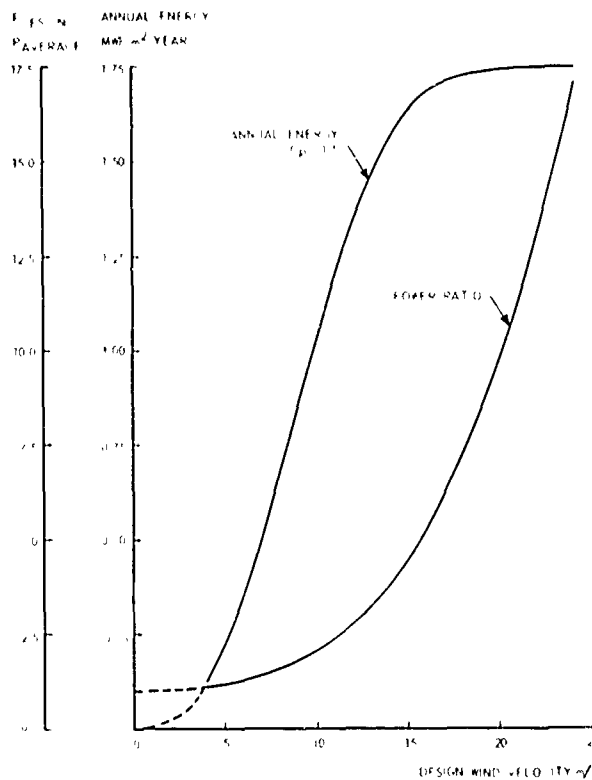


Fig 2.3 Influence of the design wind velocity on annual energy production and on the ratio of the design power to the annual average power, based on wind statistics of Fig 2.2 (power constant at velocities above the design speed)

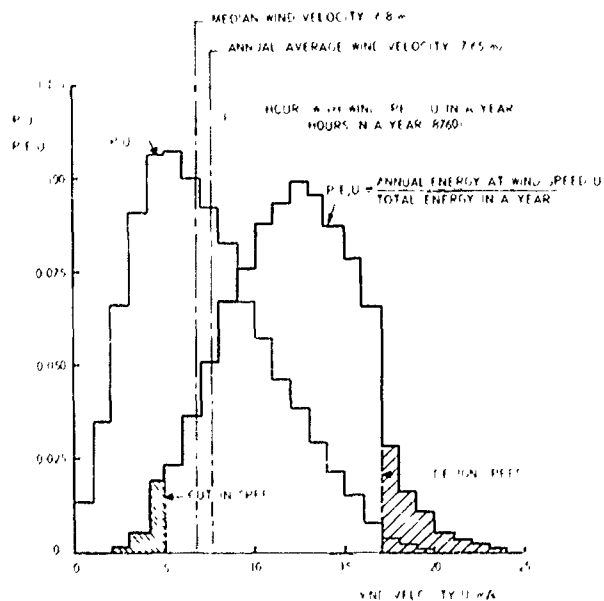


Fig 2.2 Probability distribution of wind velocity $P(U)$ and energy distribution $P(E,U)$ for a location on the Dutch coast at 14 m above the ground (Ref 2.6)

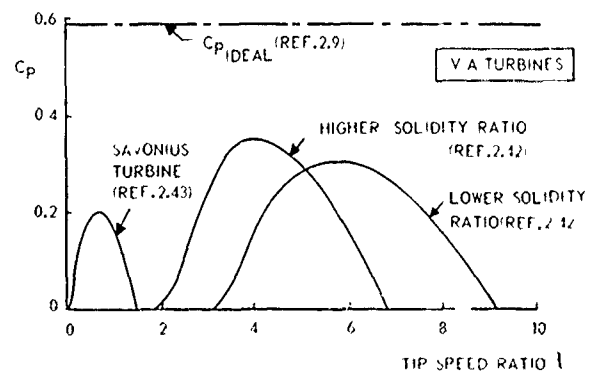
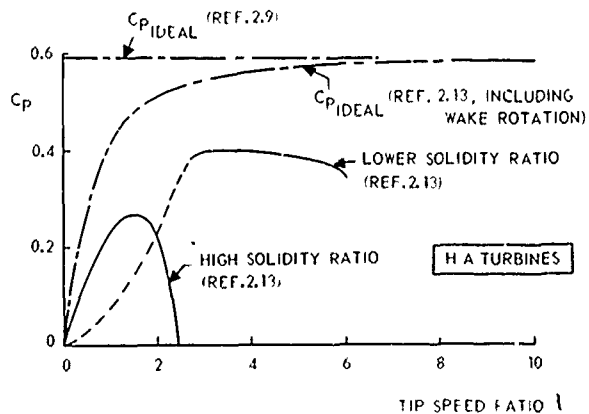


Fig 2.4 Example of wind turbine characteristics

Top: horizontal axis turbines
Bottom: vertical axis turbines

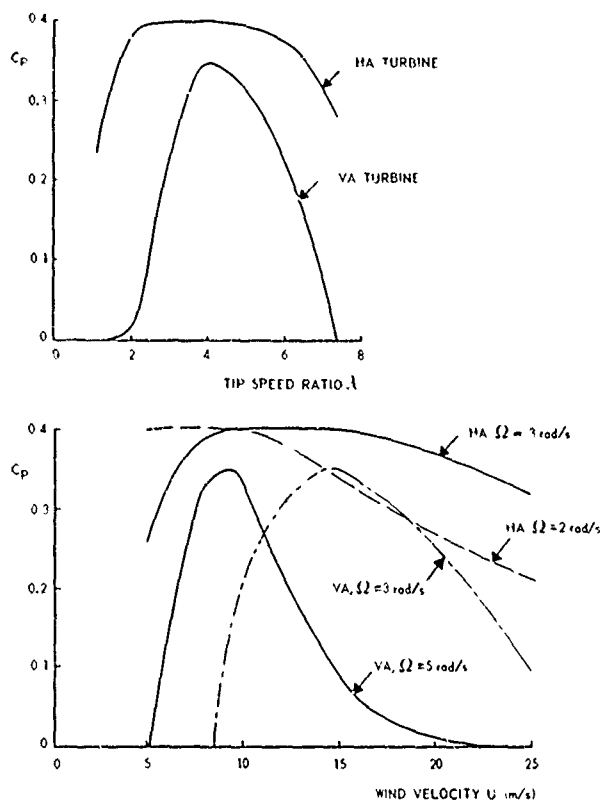


Fig 2.5 Top: typical C_p -vs λ curves for a HA and a VA turbine
Bottom: C_p -vs- U curves, corresponding with the upper diagram for a 25 m diameter turbine operating at Ω constant

'STRAIGHT BLADE' TYPE OF TURBINE

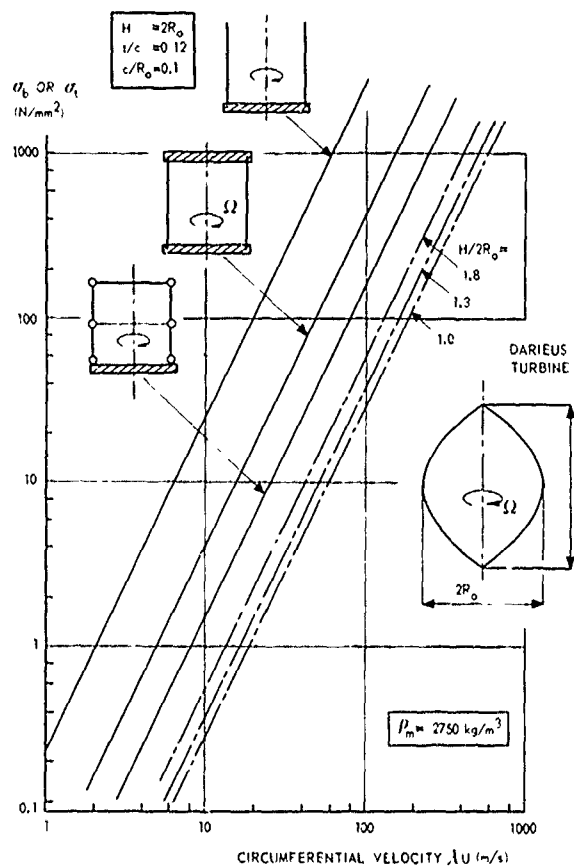


Fig 2.6 Maximum bending stress σ_b in a blade of a vertical-axis turbine with straight blades and the maximum tensile stress σ_t in a blade of a Darrieus turbine as a function of the circumferential velocity (centrifugal forces only)

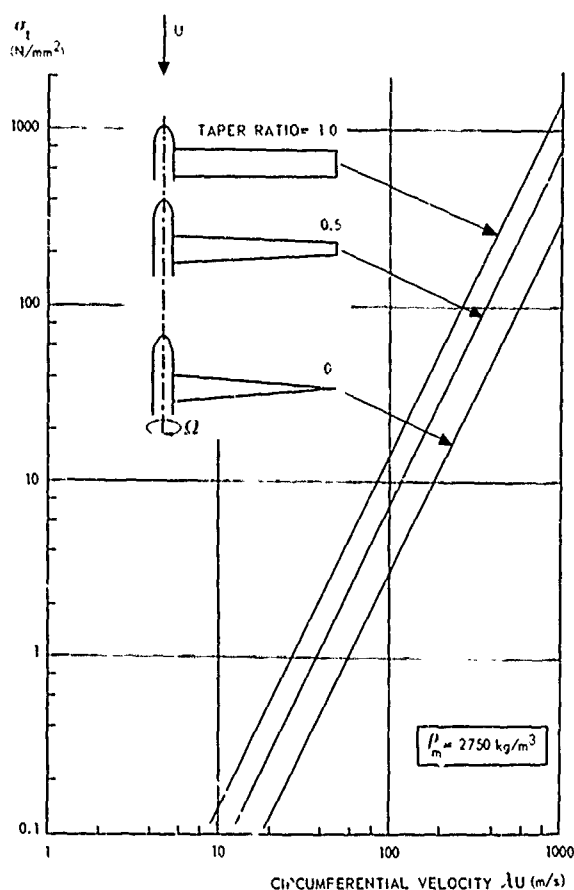


Fig 2.7 Maximum tensile stress σ_t in a blade of a horizontal axis wind turbine due to centrifugal forces only, as a function of the circumferential velocity

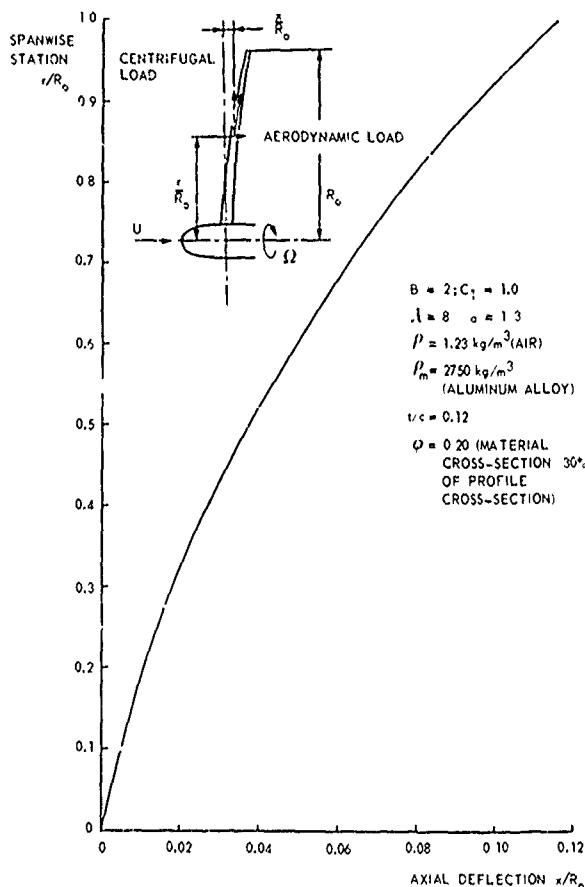


Fig 2.8 Shape of the rotor blade axis of an optimally operating horizontal-axis turbine having zero bending moments in the blade, calculated with a strongly simplified theory (Appendix D)

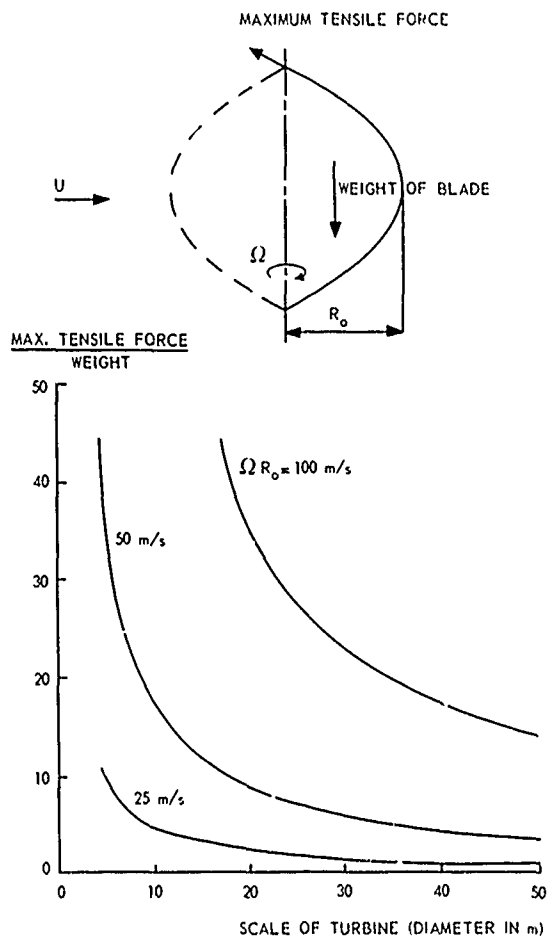


Fig. 2.9 Influence of scale and circumferential velocity on the ratio between maximum tensile force due to centrifugal acceleration and weight of the blade, for a Darrieus turbine with height equal to diameter

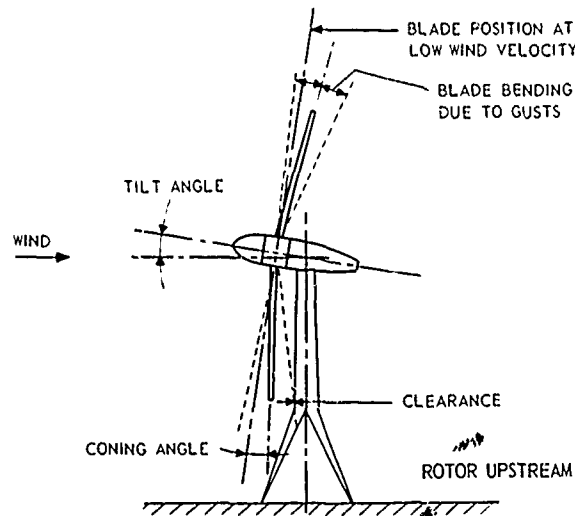
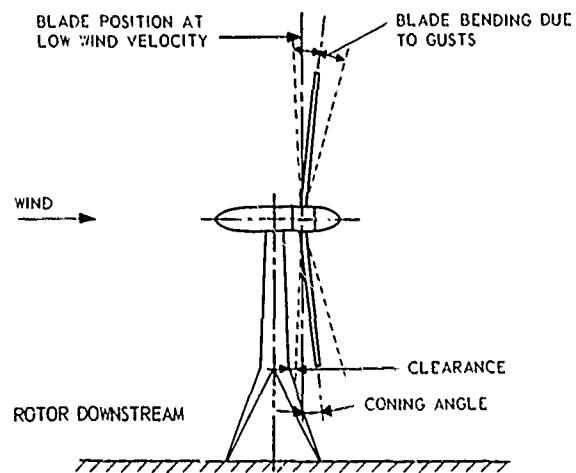


Fig. 2.10 Blade-tower clearance and rotor position

- | | | |
|---|-----------------|-----------|
| 1 | HORIZONTAL AXIS | REF. 2.46 |
| 2 | " | REF. 2.43 |
| 3 | " | REF. 2.40 |
| 4 | VERTICAL AXIS | REF. 2.45 |
| 5 | " | REF. 2.46 |

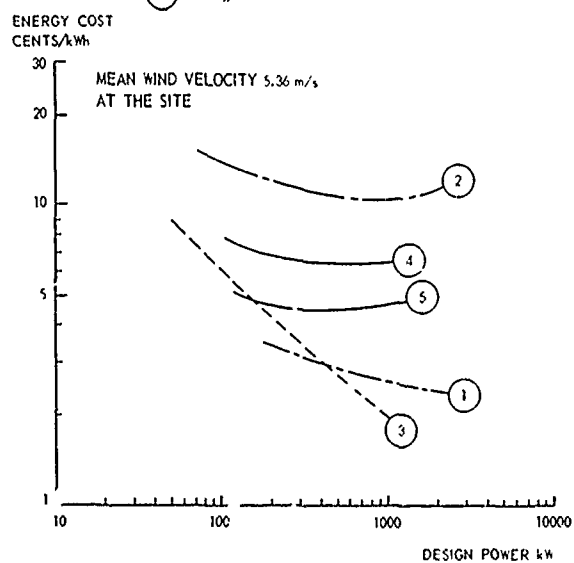


Fig. 2.11 Comparison of several energy cost estimates (US dollar cen's) for a WECS as a function of the design power

List of symbols

A	$= S_e/S_{ref} = \text{diffuser area ratio (-)}$
B	number of blades (-)
B	$= 1 - \eta_d(1 - A^{-2}) = \text{diffuser factor (-)}$
b	span of tip vane (m)
c	chord of rotor blade (m)
C_D	$= D/\frac{1}{2}\rho U^2 S_{ref} = \text{rotor drag coefficient (-)}$
C_d	drag coefficient of aerofoil section (-)
$C_{D_{axial}}$	$= D_{axial}/\frac{1}{2}\rho U^2 S_{ref} = \text{axial force coefficient (-)}$
C_{D_s}	$= D_s/\frac{1}{2}\rho U^2 S_{ref} = \text{axial force coefficient on shroud (-)}$
C_L	lift coefficient of a three-dimensional wing (-)
C_l	lift coefficient of an aerofoil section (-)
C_P	$= P/\frac{1}{2}\rho U^3 S_{ref} = \text{power coefficient (-)}$
C_{pe}	$= (p_o - p_e)/\frac{1}{2}\rho U^2 = \text{pressure coefficient at diffuser exit (-)}$
$C_{P_{ideal}}$	$= P_{ideal}/\frac{1}{2}\rho U^3 S_{ref} = 16/27 = \text{theoretical maximum power coefficient according to Betz (-)}$
c_s	chord length of shroud (m)
c_v	chord length of tip vane (m)
D	drag force (N)
D_{axial}	axial force (N)
D_i	induced drag force of three-dimensional wing (N)
D_r	rotor drag or rotor axial force (N)
D_s	axial force on shroud (N)
k	$= (p_1 - p_2)/\frac{1}{2}\rho U_r^2 = \text{screen resistance factor (-)}$
P	power (W)
P_{ideal}	theoretical maximum power according to Betz (W)
p_e	static pressure at diffuser exit (N/m ²)
p_o	undisturbed or free-stream static pressure (N/m ²)
p_1	static pressure in front of actuator disk (N/m ²)
p_2	static pressure behind actuator disk (N/m ²)
p_{t_o}	free-stream total pressure (N/m ²)
p_{t_1}	total pressure behind actuator disk (N/m ²)
Δp	$= p_1 - p_2 = \text{pressure drop over actuator disk (N/m}^2\text{)}$
r	local radius of rotor blade (m)
R	radius of shroud (m)
R_o	maximum radius or tip radius of rotor (m)
S_e	exit area of diffuser (m ²)
S_{ref}	reference area of the turbine; area swept by the rotor blades (m ²)
U	wind velocity (m/s)
\bar{U}	$= U + \bar{u} = \text{sum of wind velocity and average self-induced velocity inside shroud (m/s)}$
\bar{u}	average induced velocity inside shroud (m/s)
U_e	velocity in exit area of diffuser (m/s)
U_r	velocity through actuator disk (m/s)
v	induced velocity component in y-direction (m/s)
w	induced velocity component in z-direction (m/s)
Γ	circulation (m ² /s)
Γ_b	circulation around rotor blade; bound circulation (m ² /s)
Γ_s	circulation around shroud or annular wing (m ² /s)
Γ_v	circulation around tip vane (m ² /s)
γ_b	vortex sheet strength at wake boundary (m/s)
γ_{be}	ditto far downstream (m/s)
γ_s	vortex sheet strength at shroud (m/s)
λ	$= \Omega R_o/U = \text{tip speed ratio (-)}$
η_d	$= (p_o - p_2)/[\frac{1}{2}\rho(U_r^2 - U_e^2)] = \text{diffuser efficiency (-)}$

3-2

ρ density of air (kg/m^3)

$\sigma = (B/S_{\text{ref}}) \int_0^{R_0} c \, dr = \text{solidity ratio of turbine (-)}$

ψ angle of wake divergence (degrees)

ψ tilt angle of tip vane (degrees)

Ω angular velocity of the rotor (radians/s)

3.1 Introduction

It was recognized by Betz, as early as 1926 (Ref. 3.1), that there was a theoretical upper limit to the amount of energy that can be extracted from the wind energy flux which is available to a wind turbine of given dimensions.

His simple theory was amended by taking into account the influence of rotation left behind in the wake of the wind turbine (e.g. Glauert in Ref. 3.2), but this reduced the attainable amount of wind energy even further, not to mention the inevitable friction losses (profile drag).

Also due to the low energy density of the wind (Sect. 2.2.3), wind turbines of very large diameters have to be applied to produce a significant amount of energy. In order to get around this limitation, a number of devices have been proposed, with the purpose to concentrate the windstream to a smaller area (increased mass flow). The increased energy output for a given diameter has then to be weighed against the cost increase due to the added structural elements.

The purpose of this Chapter is to discuss the various concepts of increasing the power output. It appeared from Sect. 2.6 that a reliable cost analysis is very difficult. Therefore, the cost-effectiveness of a wind concentrator will not be discussed, but the possible adverse effects of the additional costs on the feasibility of a wind concentrator concept has to be kept firmly in mind.

Because of the vital place of the Betz limit in this discussion, his formula will be deduced in full detail. It must be noticed that the Betz limit applies to horizontal-axis as well as to vertical-axis wind turbines. Most of the wind concentrator concepts are, however, proposed for horizontal-axis turbines.

From the discussion of the Betz limit it follows that the power output of a wind turbine with a given diameter may exceed this limit, when it would be possible to increase the mass flow through the turbine. An increased mass flow can only be realized by a further reduction of the pressure in front of the turbine and a consequently increased pressure recovery towards the free-stream pressure behind the turbine. By a number of investigators it was found that the application of a diffuser behind the wind turbine should have the desired result (Refs 3.3 through 3.8).

The original ideas were concentrated on the conventional diffuser, but it was realized that, in order to limit the size of such a device, an annular wing or "shroud" could operate more efficiently, especially as regards the costs of the structure. In this respect it has to be noticed that a diffuser-type augmentor has to be put into the wind direction, though a "bell-mouth" intake in front of the turbine alleviates this restriction substantially (Refs 3.3 and 3.7).

The diffuser augmentor could be used in combination with a vertical-axis turbine, but, in that case, the wind-direction independence of the vertical-axis turbine is lost and the additional advantages of a shrouded horizontal-axis turbine, such as a reduction of tip losses, cannot be obtained.

The tip-vane concept appeared already some years ago (Refs 3.9 and 3.10), but was first published in the open literature in 1976 (Ref. 3.11).

It seems premature to formulate an opinion about the feasibility of the tip-vane concept because a joint Netherlands-USA research program on the subject (Delft Univ. of Techn. and the Aero Vironment Inc.) has been started in the end of 1976. Therefore, only the basic idea will be discussed in this Chapter. For a more mathematical approach to the concept, the references mentioned before may be consulted.

Finally, the vortex-augmentor concept will be briefly discussed. The practicability of the concept seems still questionable and the fluid dynamics processes involved are very complicated.

3.2 The Betz limit

3.2.1 Derivation of the formula

The Betz formula can be derived from three conservation laws, viz. the conservation of energy, axial momentum and mass, which laws are applied to a one-dimensional flow, in order to simplify the calculation.

The wind turbine is replaced by an "actuator disk" (Fig. 3.1), which means that the velocity U_r is continuous through the rotor area (conservation of mass), but that the static pressure shows a drop from p_1 to p_2 (energy absorption by the turbine). It is assumed, that the energy absorption only takes place when air passes through the actuator disk and the pressure drop is constant across the actuator disk (one-dimensional flow). This assumption implies that the total pressure in the wake is constant (differing from the total pressure outside the wake by $p_1 - p_2$) and the Bernoulli equation can also be applied in the wake.

The pressure difference across the actuator disk gives rise to a drag force

$$D = (p_1 - p_2) S_{ref} \quad (3.2.1)$$

Applying the Bernoulli equation in front of and behind the actuator disk leads to

$$D = (p_1 - p_2) S_{ref} = \frac{1}{2} \rho (U^2 - U_e^2) S_{ref} \quad (3.2.2)$$

Applying the axial momentum equation to the situation sketched in Fig. 3.1 leads to

$$D = \rho U_r S_{ref} (U - U_e) \quad (3.2.3)$$

Comparing the Eqs (3.2.2) and (3.2.3) shows that

$$U_r = \frac{1}{2} (U + U_e) \quad (3.2.4)$$

The velocity through the actuator disk is the arithmetic mean of the velocity far in front and far behind the actuator disk.

When energy is absorbed by the turbine, U_e is smaller than U , and it follows from Eq. (3.2.4) that $U_r < U$, which means that the mass flow through the turbine $\rho U_r S_{ref} < \rho U S_{ref}$. The quintessence of the Betz limit is that the absorption of energy from the wind stream is connected with a reduction of the mass flow through the turbine, in that way limiting the maximum amount of energy that could be extracted from the wind.

The power absorbed by the turbine is equal to the energy loss of the mass flow through the turbine, thus

$$P = \frac{1}{2} \rho U_r S_{ref} (U^2 - U_e^2) \quad (3.2.5)$$

Substituting Eq. (3.2.4) into Eq. (3.2.5) and using the definition of the power coefficient (Eq. (2.3.2)) leads to

$$C_p = P / \frac{1}{2} \rho U^3 S_{ref} = 4 (U_r/U)^2 (1 - U_r/U) \quad (3.2.6)$$

It is easily seen that the maximum or ideal power coefficient is obtained when $U_r/U = 2/3$ and $U_e/U = 1/3$, thus

$$C_{p_{ideal}} = \frac{16}{27} \quad (3.2.7)$$

The main source of the power output reduction is due to a reduced mass flow through the turbine (factor 2/3), whereas the influence of incomplete energy absorption is less, viz. a factor $1 - (1/3)^2 = 8/9$.

3.2.2 Discussion

Though the actuator disk suggests a horizontal-axis wind turbine, Eq. (3.2.6) is equally valid for a vertical-axis turbine (within the restrictions of the assumptions applied).

The rotor drag coefficient C_D can be calculated from the rotor drag (Eq. (3.2.2)), viz.:

$$C_D = D / \frac{1}{2} \rho U^2 S_{ref} = 4 (U_r/U) (1 - U_r/U) \quad (3.2.8)$$

Figure 3.2 shows the variation of C_p , C_D and U_e/U with U_r/U , calculated from the Eqs (3.2.4), (3.2.6) and (3.2.8).

An increasing retardation of the flow through the actuator disk increases the rotor drag, decreases the velocity in the far wake, and initially increases the absorbed power.

At $U_r/U = 0.5$, the velocity in the far wake becomes zero, and the absorbed power is already beyond its optimum value. Still lower values of U_r/U lead to negative velocities in the far wake, which violates the continuity equation (mass conservation) in one-dimensional flow.

The simple axial momentum theory cannot cope with $U_r/U < 0.5$. In that range, a real horizontal-axis turbine may operate in the so-called "turbulent wake state" and "vortex ring state", i.e. a return flow exists across a part of the actuator disk, and it is clear that one-dimensional flow theory can be applied (Refs 3.12 and 3.13, see also Ref. 3.14).

Reference 3.15 suggests $C_D = 1.0$ = constant in the range $0 \leq U_r/U < 0.5$, but in view of the very complex flow, where a turbine operates in a turbulent wake state, the simple momentum considerations do not look very convincing (see also Ref. 3.13).

In reference 3.14 it is inferred from helicopter tests that $C_D > 1$ when $U_r/U < \frac{1}{2}$. The question remains also whether modifications in the theory for this part of the operating range of a wind turbine will yield a modified value for the maximum obtainable power coefficient.

Glauert (Ref. 3.2) includes in his discussion of the horizontal-axis wind turbine the rotation left behind in the wake (trailing vorticity of the rotor blades, torque and angular momentum). The tangential velocities due to this rotation, contribute to the kinetic energy left in the wake and decrease the maximum attainable power coefficient. The inclusion of the tangential velocity components has also a small influence on the value of U_r/U at which the optimum C_p is reached (see, however, Appendix C).

Hütter (Ref. 3.12) draws attention to the possibility that the strong diverging streamlines at and behind the actuator disk and also the mixing layer at the wake boundary might lead to a higher optimum value of C_p than that obtained from the simple axial momentum theory.

A large wake divergence might lead to a larger total velocity through the rotor ($U_r/\cos \psi$ instead of U_r ; Fig. 3.3) and thus to a larger kinetic energy at the rotor, but not to a larger mass flow. The wake divergence and turbulent mixing might also result in a lower value of U_e , but this is more difficult to visualize. Farther behind the turbine, U is larger than U_e , due to turbulent mixing (wake decay, Sect. 5.3.2).

Hütter states that the theoretical optimum of C_p might be increased with 4 to 13 % by wake divergence and turbulent mixing.

3.3 The diffuser augmentor

3.3.1 Simple diffuser

The gist of diffuser operation can be shown by one-dimensional flow calculations, almost similar to those leading to the Betz limit.

The axial momentum equation is not convenient in this case, because the external forces on the diffuser are difficult to estimate. The pressure recovery in the diffuser, defined by the diffuser efficiency η_d , can be used instead.

It is assumed that energy losses only take place at the turbine ($p_1 - p_2$) and in the diffuser. It is assumed that the free-stream static pressure p_0 is present at the diffuser exit. A lower pressure at the diffuser exit has an important effect on the mass flow, but complicates the demonstration of the principal action of a diffuser.

The pressure recovery over the diffuser can be calculated from the diffuser efficiency (for notation see Fig. 3.4)

$$p_0 - p_2 = \eta_d \frac{1}{2} \rho (U_r^2 - U_e^2) \quad (3.3.1)$$

It follows from mass conservation in incompressible flow that

$$U_e = (S_{ref}/S_e) U_r = U_r / A \quad (3.3.2)$$

with A = diffuser area ratio.

When it is assumed that the inlet flow towards the turbine is frictionless, thus:

$$p_0 - p_1 = \frac{1}{2} \rho (U^2 - U_r^2) \quad ,$$

then the pressure drop over the turbine can be written as

$$\begin{aligned} p_1 - p_2 &= \frac{1}{2} \rho U^2 - \frac{1}{2} \rho U_r^2 [1 - \eta_d (1 - A^{-2})] \\ &= \frac{1}{2} \rho U^2 [1 - B (U_r/U)^2] \quad , \end{aligned} \quad (3.3.3)$$

with $B = 1 - \eta_d [1 - A^{-2}]$.

The power absorbed by the turbine is

$$P = U_r S_{ref} (p_1 - p_2) = \frac{1}{2} \rho U^2 U_r S_{ref} [1 - B (U_r/U)^2] \quad ,$$

and the power coefficient, defined on the area swept by the turbine blades (S_{ref}), becomes

$$C_p = \frac{P}{\frac{1}{2} \rho U^3 S_{ref}} = (U_r/U) [1 - B (U_r/U)^2] \quad (3.3.4)$$

For a given diffuser (area ratio A and efficiency η_d), i.e. a given value of B , C_p obtains an optimum at a given value of U_r/U , viz.:

$$U_r/U = (3B)^{-\frac{1}{2}} \quad (3.3.5)$$

The corresponding value of U_e/U follows from Eq. (3.3.2), viz.:

$$U_e/U = A^{-1} (3B)^{-\frac{1}{2}} \quad (3.3.6)$$

and the optimum power coefficient is

$$C_{p_{opt.}} = \frac{2}{3} (3B)^{-\frac{1}{2}} \quad (3.3.7)$$

An interesting limit is $\eta_d = 1$, i.e. a frictionless diffuser, which corresponds to a value $B = 1/A^2$. In that case

$U_r/U = A/\sqrt{3}$, thus proportional to the diffuser area ratio,
 $U_e/U = 1/\sqrt{3}$, thus constant and the optimum power coefficient is

$$C_{p_{opt.}} = \frac{2}{9} A\sqrt{3} \quad (3.3.8)$$

The ideal turbine without diffuser, discussed in Sect. 3.2.1, shows in the optimum situation an effective diffusing ratio

$$S_e/S_{ref} = U_r/U_e = 2 \quad ,$$

which diffusion is also assumed to be frictionless.

When both optimum power coefficients are compared at the same value $A = 2$, viz. $16/27 = 0.5926$ with $4\sqrt{3}/9 = 0.7698$, the frictionless solid-wall diffuser shows a larger power output than the wind turbine with a so-called "frictionless free-streamline diffusion".

This difference can be explained by considering the momentum equation, which reveals that the solid-wall diffuser increases the axial drag force, even in case of an inviscid flow ($\eta_d = 1$). An analogous situation is discussed in Sect. 3.3.2 (see Fig. 3.10).

Figure 3.5 shows the optimum power coefficient for the turbine-diffuser combination, according to the simplified theory of Eq. (3.3.7). The deteriorating influence of a low diffuser efficiency is clearly demonstrated. It must be noted, however, that η_d and A are coupled and cannot be freely chosen.

To visualize the relative benefit of the large structure that has to be built around the turbine, the power output of a turbine without diffuser has been plotted in Fig. 3.5 (dotted line) for the case of a turbine with a diameter equal to the exit diameter of the diffuser.

Even an ideal diffuser ($\eta_d = 1$) does not generate a comparable amount of energy. This difference cannot be nullified by taking the tip losses of the turbine without diffuser into account.

The pros & cons of a simple diffuser cannot be weighed objectively without a proper cost analysis, but this figure shows that a simple diffuser is not a panacea for overcoming structural problems in designing large-scale WECS.

Figure 3.6 shows the increased mass flow due to the diffuser (U_r/U), together with the velocity at the diffuser exit (U_e/U). It is clear that the increased mass flow is entirely responsible for the augmentation of the power output.

In wind tunnel experiments on models of wind concentrators, the power absorption is often simulated by a wire screen. The pressure drop over a screen at the plane of the rotor is

$$p_1 - p_2 = k \frac{1}{2} \rho U_r^2, \quad (3.3.9)$$

with k = resistance factor of the screen.

The simulated power absorption is

$$P = (p_1 - p_2) U_r S_{ref} = \frac{1}{2} \rho U_r^3 k S_{ref},$$

and the corresponding power coefficient

$$C_p = k (U_r/U)^3. \quad (3.3.10)$$

It follows from the Eqs (3.3.10), (3.3.5) and (3.3.7) that the optimum C_p can only be simulated with one specific screen, viz. with

$$k = 2B. \quad (3.3.11)$$

Figure 3.7 shows the necessity to use a series of screens in model tests, in order to determine properly the optimum.

Investigation of a diffuser in a wind tunnel revealed an aspect of the influence of the external flow around the diffuser on the internal flow in the diffuser (see e.g. Refs 3.5 and 3.7). The external flow might cause a static pressure at the diffuser exit p_e which is smaller than p_o . Denoting the dimensionless pressure difference at the diffuser exit by

$$C_{pe} = (p_o - p_e) / \frac{1}{2} \rho U^2,$$

the power coefficient becomes (instead of Eq. (3.3.4))

$$C_p = (U_r/U) [1 + C_{pe} - B (U_r/U)^2], \quad (3.3.12)$$

and the optimum power coefficient

$$C_{p_{opt}} = \frac{2}{3} (1 + C_{pe}) [(1 + C_{pe}) / 3B]^{\frac{1}{2}}. \quad (3.3.13)$$

Figure 3.8 shows power coefficients obtained from wind tunnel experiments on models of diffusers, compared with values obtained from Eq. (3.3.13). The calculations can only be used as an illustration, because the values of η_d and C_{pe} obtained at the experiments are not known precisely. The experiments of reference 3.7, designated "with flaps", have been performed with an annular wing (flap) around the diffuser exit, in order to reduce the static pressure at the diffuser exit. When these results are compared with the experimental results "without flaps", the influence of the flaps is shown to be considerable.

These results can also be interpreted in another way (Refs 3.6, 3.7 and 3.8), viz. that using the diffuser behind the turbine to boost the "free-streamline diffusion" is far more effective than using it as a plain solid-wall diffuser. Moreover, it is possible to reduce the dimensions of the diffuser in that way.

When this aspect is elaborated further, it boils down to the long existing idea of a shrouded turbine, which will be discussed in the next Section.

3.3.2 Shrouded turbine

The concept of a shrouded turbine was originally proposed for a propeller (e.g. propeller of a ship), but it is also applicable for a wind turbine. It is based upon the increase of the mass flow through the turbine. An additional advantage is the increased efficiency due to the avoiding of the tip losses, when a small enough tip clearance can be applied.

The increased mass flow due to the shroud can be visualized by considering the shroud as an annular wing in axisymmetric flow (Fig. 3.9). The sectional lift on the annular wing has to be directed towards the axis of symmetry (over-all lift zero), and the corresponding circulatory flow around the wing section of the annular wing induces an increased velocity through the area enclosed by the annular wing (like a vortex ring).

An annular wing in axisymmetric potential flow does not absorb energy from the flow. It follows from the axial momentum equation, that the resultant axial force on the annular wing has to be zero. The only forces on the annular wing then are the purely radial section lift forces (Fig. 3.9).

When an energy-absorbing actuator disk is placed inside this annular wing, the axial momentum is changed, which must be equal to a resultant axial force on the turbine (D_r) and possibly on the shroud (D_s) also.

When assumptions similar to those of Sect. 3.2.1 are used, an expression for the axial momentum can be given:

$$D_r + D_s = \rho U_r S_{ref} (U - U_e) \quad , \quad (3.3.14)$$

and for the drag force on the turbine (cf. Eq. (3.2.2))

$$D_r = \frac{1}{2} \rho (U^2 - U_e^2) S_{ref} \quad . \quad (3.3.15)$$

This gives an expression for U_r (cf. Eq. (3.2.4))

$$U_r = \frac{1}{2} (U + U_e) + \frac{D_s}{\rho (U - U_e) S_{ref}} \quad . \quad (3.3.16)$$

Eq. (3.3.16) shows, that U_r reduces to the value of the turbine without shroud, in the case $D_s = 0$. Although the increased mass flow through the turbine could be calculated from the circulation of the annular wing (see App. A), an increased power output with a shrouded turbine is only possible (within the range of applicability of the simple axial momentum theory), when an axial force on the shroud is present.

The power coefficient for the shrouded turbine can be calculated from the Eqs (3.2.5) and (3.3.16)

$$C_p = \frac{1}{2} [1 - (U_e/U)] [1 + (U_e/U)]^2 + 2 C_{D_s} [1 + (U_e/U)] \quad , \quad (3.3.17)$$

$$\text{with } C_{D_s} = D_s / \frac{1}{2} \rho U^2 S_{ref} \quad .$$

The optimum C_p will be obtained, when

$$(U_e/U) C_{p_{opt}} = -\frac{1}{3} + \frac{2}{3} (1 + 3 C_{D_s})^{\frac{1}{2}} \quad (3.3.18)$$

The optimum is determined with $D_s / \rho U^2 S_{ref} = \text{constant}$.

Figure 3.10 shows C_p and U_r , as a function of U_e and the axial force D_s on the shroud. At $U_e/U = 1$, no energy is absorbed from the wind stream. However, $C_p \neq 0$ when $D_s \neq 0$ in that case. This is caused by $U_r \rightarrow \infty$ when $U_e \rightarrow U$ and $D_s \neq 0$ (see Eq. (3.3.16)), which is physically impossible.

These strongly simplified considerations do not offer a basis for calculating a shrouded wing turbine, but render some insight into the rather large axial forces that have to be created by the shroud, in order to obtain a significant power augmentation.

The calculation of a shrouded wind turbine is very complicated and will not be discussed here. However, it seems possible to get some insight into the problems involved, by considering parts of the complete calculation.

In Appendix A, the mass flow increase through an annular wing has been estimated for a wing section with given circulation. The results described in Appendix A will be summarized below.

Approximating the annular wing by a ring vortex (a kind of lifting line approximation) leads to an infinite mass flow through the annular wing. The infinity can be circumvented by excluding a "vortex core radius" from the calculation of the mass flow, but the choice of such a radius is rather arbitrary.

Distribution of the circulation over a finite chord length results in a finite mass flow. Also the distribution of the axial velocity along the radius becomes more constant (an infinitely long cylinder with a constant strength of the vortex sheet induces a constant velocity inside this cylinder).

The mass flow is proportional to the circulation Γ ; it also depends on the chord/radius-ratio. The circulation cannot be increased arbitrarily ($\Gamma \propto C_l c$). An increasing chord length increases Γ at fixed C_l , but the mass flow decreases with increasing c/R at fixed Γ . This leads to an optimum value of c/R .

The calculation is further complicated by the fact that an annular wing induces an axial velocity along its own chord, which increases the effective velocity, from which the lift coefficient has to be calculated for a given circulation ($C_l \propto \Gamma/\bar{U}$, with $\bar{U} = \text{wind velocity} + \text{self-induced velocity}$).

Figure 3.11 shows the results of the calculations of Appendix A. Though the numerical results given in this diagram are not very accurate, it clearly demonstrates the need for attaining high values of C_l (flapped aerofoil sections, Refs 3.7 and 3.8) and rather large values of c/R (from 2 to 6, depending on C_l). The very large values of the mass flow increase calculated at $C_l \approx 4$ and $c/R \approx 4$ to 6 correspond to extreme high values of Γ . That still acceptable C_l -values are obtained is due to the very strong self-induced velocities along the chord, but it can be questioned whether such a situation is realistically predicted by the approximations used in the calculations (inaccuracies increase at $c/R > 2$).

This discussion of the shrouded wind turbine will be concluded by sketching a method that gives some insight into the shroud-turbine interaction.

Figure 3.12 shows an annular wing with an actuator disk, which absorbs energy from the flow and in that way causes a constant pressure drop Δp across the actuator disk. Behind the disk originates a wake with a constant but lower total head, bounded by a vortex sheet (velocity discontinuity) with zero pressure difference across it.

For a given shape of the annular wing and a given pressure drop Δp , the exercise consists of determining the shape of the discontinuity layer and the vortex strength distribution on wing (γ_c) and discontinuity layer (γ_b) under the following constraints:

- the normal velocity has to be zero on the wing contour and on the surface of the discontinuity layer;
- the tangent to the discontinuity layer at the trailing edge of the wing must coincide with the bisector of the tail angle of the profile;
- the pressure difference across the discontinuity layer has to be zero;
- the pressure in the wake at infinity is equal to p_0 , which determines the constant velocity in the wake at infinity

$$\frac{1}{2} \rho U_e^2 = \frac{1}{2} \rho U^2 - \Delta p \quad , \quad (3.3.19)$$

and the strength of the vortex sheet at infinity

$$\gamma_{be} = U - U_e, \quad (3.3.20)$$

because the flow at infinity is two-dimensional.

The width of the wake at infinity is determined by the mass flow increase through the annular wing (unknown value of γ_s) and the pressure drop Δp and is, therefore, a part of the problem. The existence of the discontinuity layer depends directly on the existence of a pressure drop Δp across the actuator disk and shows the interaction between shroud and turbine.

Due to the difference in total head in the wake, the above sketched problem is not a potential flow problem. However, it can easily be transformed into one by adding a static pressure equal to Δp in the wake area. The discontinuity surface of the actuator disk disappears, the static pressure in infinity in the wake is now equal to $p_0 + \Delta p$, and the pressure difference across the surface of discontinuity is no longer zero but constant and equal to Δp (see Fig. 3.12, bottom).

This second problem can be solved by potential flow methods, in which the shape of the vortex sheet of the wake boundary is calculated by an iteration procedure. The solution of the original problem can be obtained by subtracting Δp from the static pressure in the wake area and from that on the inside area of the annular wing up to the location of the actuator disk.

It must be noticed that such a calculation only refers to a strongly simplified model of a shrouded wind turbine, viz. the representation of the wake of the turbine by a potential flow region enclosed by a surface of discontinuity.

Considering the results of measurements found in the literature and considering the order of magnitude calculations of Appendix A, one can conclude that optimum values of the power coefficient of about $C_p \approx 2$ can be obtained, but a rather large structure around the wind turbine is needed ($c/R > 1$).

It can be concluded that in the literature a number of advantages of a diffuser or shroud has been mentioned, viz.:

- increased energy output at a given turbine diameter, due to an increased mass flow, a small increase of the allowable pressure difference across the turbine, and a higher turbine efficiency (less tip losses);
- less sensitivity of the energy output to yaw;
- lower fluctuating blade loads due to the damping effect of the shroud on the fluctuations of the wind direction;
- higher turbine RPM due to higher mass flow and a consequently reduced gear-ratio of the gear-box.

A disadvantage is:

- Increase of costs due to the large structure around the turbine which has to be put into the wind direction. This last point is less restrictive in areas with a trade wind.

3.4 The tip-vane concept

3.4.1 The basic idea

It was discussed in Sect. 3.3.2, that a vortex ring around a wind turbine could increase the mass flow through the turbine and in that way increases the power output. This "vortex ring" could be created by an annular wing, but this leads to a rather large structure around the turbine, which seems not always practicable.

A tip vane, however, is a relatively small lifting surface, attached to the tip of the turbine blade (Fig. 3.13).

Figure 3.13 tries to clarify how tip-vanes can create a vortex ring. When the tip vane is replaced by a horseshoe-vortex, the tip vane, with a lift force directed towards the axis, generates a pair of tip vortices with a sense of rotation as indicated in Fig. 3.13. At a certain tip speed ratio $\lambda = \Omega R_0/U$, the clockwise and counter-clockwise rotating tip vortices originating from different tip vanes coincide and cancel. The remaining parts of the tip vortices between the tip vanes form a vortex ring with such a sense of rotation, that the mass flow through the turbine increases.

3.4.2 Discussion

That a relatively small tip vane, moving with the turbine blade does the same job as a large fixed shroud around the turbine can be explained along the following lines. The circulation of the shroud (Γ_s) depends on the chord (c_s) and the wind velocity (U), thus

$$\Gamma_s \propto U c_s \quad (\text{neglecting the influence of } c/R).$$

The circulation of the tip vane (Γ_v) depends on the chord (c_v) and the relative velocity, which, at high values of λ , is almost equal to ΩR_0 , thus:

$$\Gamma_v \propto \Omega R_0 c_v.$$

The ratio of these two values is proportional to

$$\Gamma_v/\Gamma_s \propto (\Omega R_0/U)(c_v/c_s) = \lambda(c_v/c_s).$$

At high values of λ , c_v can be made much smaller than c_s and still result in the same value of Γ .

The following relation has to be fulfilled (Fig. 3.13), when the respective tip vortices should cancel:

$$2\pi R_0/B = b/\lambda \quad \text{or} \quad B b/2\pi R_0 = \lambda^{-1},$$

with B = number of turbine blades.

The ratio of the total tip-vane area and the area of the shroud, at equal values of r , is proportional to

$$Bc_v b/(2\pi R_0 c_s) = (B b/2\pi R_0)(c_v/c_s) \propto \lambda^{-2}.$$

This area ratio is small at a high value of λ .

A wing with a finite aspect ratio experiences a drag force that is composed of a profile drag (friction drag) and an induced drag (drag due to the tip vortices). The tip vane is a wing of finite span and, therefore, experiences also a drag, which reduces the power output. Due to the mutual cancelling of the tip vortices (Fig. 3.13), the induced drag is strongly reduced (analogous to drag reduction of airplanes in formation flight). In Ref. 3.9 the possibility to develop a special spanwise loading is considered, which gives the largest induced drag reduction due to vortex cancellation.

The power output reduction due to a drag coefficient (C_d) of the tip vane is easily calculated, viz.:

$$\Delta C_p = -\frac{1}{2} B \rho (\lambda U)^2 C_d c_v b R_0 / (\frac{1}{2} \rho U^3 S_{ref}) = -C_d (B c_v b / S_{ref}) \lambda^3. \quad (3.4.1)$$

This clearly illustrates the necessity to choose the tip-vane area as small as possible and to develop special low-drag aerofoils. The power loss increases with the third power of the tip-speed ratio, which is especially unfavourable, because the mass flow increase of the tip vanes is connected with a high tip-speed ratio.

It was pointed out in Sect. 3.3.2 that a mass flow increase through the turbine requires an extra axial force, which, in case of tip vanes, has to be an axial force on the tip vanes. This axial force can be generated by tilting the tip vane (see Fig. 3.14). This tilt angle is also necessary to let the tip vortices interfere in a favourable way, because of the expanding streamtubes behind the turbine.

The axial force coefficient, which can be compared with the axial force coefficient C_{D_s} of Fig. 3.10 (see also Eq. (3.3.17)), can be calculated for the tip vanes from

$$C_{D_{axial}} = D_{axial} / (\frac{1}{2} \rho U^2 S_{ref}) = \frac{1}{2} B \rho (\lambda U)^2 c_v b C_1 \sin \psi / (\frac{1}{2} \rho U^2 S_{ref}) = C_1 \sin \psi (B c_v b / S_{ref}) \lambda^2. \quad (3.4.2)$$

The axial force is connected with the mass flow increase through the turbine and, therefore, with the power increase (Fig. 3.10), and increases with the tip-speed ratio squared, the sine of the tilt-angle, the lift coefficient, and the tip-vane area. In view of the power loss (Eq. (3.4.1)), the tip-vane area has to be as small as possible, and it follows from Eq. (3.4.2) that the lift coefficient has to be as high as possible (special low-drag-high-lift aerofoils; Liebeck sections) in order to attain sufficient mass flow increase. The velocity through the turbine can now be calculated from Eq. (3.3.16):

$$U_r/U = \frac{1}{2} [1 + (U_e/U)] + \frac{1}{2} C_{D_{axial}} / [1 - (U_e/U)], \quad (3.4.3)$$

and the corresponding power coefficient can be calculated from Eq. (3.3.17):

$$C_p = \frac{1}{2} [1 - (U_e/U)] [1 + (U_e/U)]^2 + \frac{1}{2} C_{D_{axial}} [1 + (U_e/U)]. \quad (3.4.4)$$

The optimum value of C_p at a fixed value of $C_{D_{axial}}$ is attained at a special value of U_e/U (cf. Eq. (3.3.18)):

$$(U_e/U)_{C_p \text{ opt.}} = -\frac{1}{3} + \frac{2}{3} \left[1 + \frac{1}{2} C_{D_{axial}} \right]^{\frac{1}{2}}. \quad (3.4.5)$$

This optimum differs from the one found in Ref. 3.9, because in that case, the velocity increase is assumed to be independent of U_e/U , whereas in Eq. (3.4.3) the velocity increase depends on U_e/U , but $C_{D_{axial}}$ is kept constant. In Ref. 3.9 optimum values of $U_e/U < \frac{1}{3}$ are shown, whereas Eq. (3.4.5) shows optimum values of $U_e/U > \frac{1}{3}$.

It must be noticed that $C_{D_{axial}}$ is a function of ψ (Eq. (3.4.2)) and, because of the yet unknown relation between ψ and U_e/U , $C_{D_{axial}}$ is a function of U_e/U , i.e. the optimum of Eq. (3.4.5) is not an absolute optimum. Furthermore, it is implicitly assumed, that the tip vane induces a constant velocity across the rotor area, which is certainly not true.

The interaction between tip vane and energy-absorbing turbine is included in Eq. (3.3.4) through the tilt angle ψ implicit in $C_{D_{axial}}$. This tilt angle has to be equal to the slope of the streamlines in the tip region of the turbine blades. This slope can only be calculated from vortex wake calculations (cf. Fig. 3.12).

The optimum power output of an ideal wind turbine with tip vanes with a total area equal to 10 % of the turbine reference area and a lift coefficient $C_l = 2$ is given in Fig. 3.15 as a function of the tilt angle and the tip-speed ratio. Also the influence of the profile drag of the tip vane ($C_d = 0.01$) has been calculated from Eq. (3.4.1). The induced drag of the tip vanes is assumed to be zero.

The figure shows that already moderate tilt angles give an appreciable increase of the power output. It is also clear that the turbine has to be designed for a high tip-speed ratio to attain sufficient power increase from the tip vanes. Because U_e/U has to be smaller than 1 (otherwise no energy has been extracted from the flow), $C_{D_{axial}}$ has to be smaller than 4, which is easily observed from Eq. (3.4.5).

The calculations of the Refs 3.9 through 3.11 show rather large tip vanes, viz. a total vane area of the same order of magnitude as the rotor blade area of a low-solidity turbine (which could obtain the high λ values) and a span of the tip vane equal to half the span of the turbine blade has been assumed in the calculations.

In Ref. 3.16 incidentally the T-inducer (tip-vane as discussed above) and the L-inducer are mentioned. The latter is supposed to have no induced drag at all. It will be shown that this assertion is not completely correct. It also brings about an interference effect between tip vane and turbine blade, which has to be

studied carefully in developing the tip-vane concept.

Figure 3.16 shows very schematically the vortex system in the tip region of a turbine blade without inducer and with a T- and L-inducer. For reasons of simplicity, the tip vane is assumed to act like a perfect end-plate, i.e. the circulation of the turbine blade Γ_b is completely carried over to the tip vane. Comparison with Fig. 3.13 shows that the vortex cancellation of the tip-vane contribution to the trailing vorticity Γ_v is not altered in case of an L-inducer. The situation sketched in Ref. 3.16 is obtained in case $\Gamma_v = 0$. There is a downward lift force on the L-inducer (due to Γ_b), but the remaining tip vortex induces only velocities opposite to the wind velocity, and no mass flow increase is generated.

Figure 3.16 also shows the antisymmetric lift distribution superimposed on the lift distribution of the tip vane in case of a T-inducer, caused by the interference with the turbine blade. When the tip vane is not a perfect end-plate, the tip vortex of the turbine blade complicates the vortex system, but basically does not alter the situation.

3.5 Vortex augmentor concepts

Several proposed wind concentrator concepts are based upon the energy-concentrating effect of tip vortices or leading-edge vortices of wings (Refs 3.17 through 3.20).

The different proposals have in common that a wing (rectangular or delta) is placed at an angle of attack to the wind, in that way generating a lift force on the wing. The wing planform is chosen such, that most of the trailing vorticity is concentrated in the tip vortex (rectangular wing) or the leading-edge vortex (delta wing). The axis of the energy-absorbing turbine coincides with the vortex core.

The combination of wing and turbine has to be turned into the wind direction. An example of such a proposal is sketched in Fig. 3.17. Ref. 3.20 proposes a half-model of a rectangular wing placed vertically and the turbine attached to the wing at some distance behind the tip.

There is a connection between the "kinetic" energy of the tip vortex and the "induced" drag D_i of the wing. Usually, drag is connected with a loss of energy of the flow, but the induced drag has a different origin, which is not connected with a loss of flow energy.

In a potential flow model, a vortex sheet is left behind a lifting wing. Far downstream, in the so-called Trefftz-plane, the vortex sheet only induces velocity components perpendicular to the undisturbed velocity U , viz. v and w (in y - and z -direction). The bound vorticity on the wing is so far upstream of the Trefftz-plane that it does not induce any velocity components in the Trefftz-plane and the velocity in the x -direction is equal to the undisturbed velocity U .

Because no energy can be lost in a stationary potential flow (see App. B), the equation of Bernoulli shows, that the vortex sheet induces a static pressure deficit in the Trefftz-plane, viz. (with p_0 = undisturbed static pressure)

$$p - p_0 = -\frac{1}{2}\rho(v^2 + w^2) \quad (3.5.1)$$

Applying the axial momentum equation gives an expression for the induced drag:

$$D_i = - \int_{-\infty}^{+\infty} \int_{\text{Trefftz-plane}} (p - p_0) dy dz = \frac{1}{2}\rho \int_{-\infty}^{+\infty} \int_{\text{Trefftz-plane}} (v^2 + w^2) dy dz \quad (3.5.2)$$

Close behind the wing, the velocity components v and w induced by the vortex sheet are one half of the values induced in the Trefftz-plane, but the bound vortex induces extra w -components.

In a way similar to the diffuser, the vortex sheet also creates kinetic energy at the expense of the static pressure, but the induced velocity components are perpendicular to the main stream and do not increase the mass flow through the turbine.

The kinetic energy of a vortex sheet is spread over still a large area. However, due to boundary layer effects on the wing and due to instability of the vortex sheet behind the wing, a pair of tip vortices are formed which contain already 60 to 80 % of the total trailing vorticity at a small distance behind the wing. It is this rolling-up of the vortex sheet into tip vortices which also concentrates the kinetic energy into a smaller area.

An objection to the tip vortex concept is that boundary layer material is sucked into the vortex core, which decreases the total pressure in the vortex core and thus reduces the energy content of the flow through the turbine. In a leading-edge vortex, the same might take place, but in this case the effect may be compensated by a large axial velocity in the vortex core (see Refs 3.17 and 3.18).

Loth (Ref. 3.20) estimates for a rectangular half-wing with an area of 9 times the rotor area (S_{ref}), a rotor diameter of 0.6 times the wing chord and a lift coefficient of the wing $C_L \approx 4(!)$ and that the kinetic energy flowing through the rotor could be three times $\frac{1}{2}\rho U^3 S_{ref}$, which is the energy flux without concentrator. Such an estimate directly reveals the weakness of such a type of concentrator.

When a rotor solidity $\sigma = 0.05$ is assumed, the above estimate means a stationary wing surface equal to $9/0.05 = 180$ times the rotor blade area. The same amount of energy could be obtained with a free turbine having a $\sqrt{3}$ times larger diameter, which means a three times larger rotor blade area.

The trade-off between a three times larger rotor blade area (to obtain the same increase in power output) or a 180 times larger stationary wing area, which has to be turned into the wind direction and which has to withstand the aerodynamic loads of a storm, is very likely to turn out in favour of the free turbine.

There are more disadvantages connected with the wing-generated vortex augmentors, viz. the very complex oncoming flow to the turbine and the large load fluctuations when the tip vortex is displaced with respect to the turbine axis during a lateral gust.

Moreover, Loth (Ref. 3.21) discusses the change in static pressure deficit in the vortex, when a part of the rotational energy is absorbed by the turbine and the corresponding limitations in energy-absorbing

capacity of the system. Also the question could be raised whether the axial adverse pressure gradient generated by the energy absorbing turbine might induce vortex bursting, with the corresponding adverse effect on the power output.

Ref. 3.22 suggests to use the low pressure in a vortex core to suck air through the turbine. The vortex or "tornado" is generated by the wind flowing through a huge tower with vertical slots (which have to be opened or closed, depending on the wind direction), and the vortex is assumed to be further amplified by thermal effects.

Also in this case, the trade-off between the costs of the structure of the tower with the large movable "Venetian blinds" and the costs of a free turbine with an equal power output is unlikely to be in favour of the "tornado"-type of concentrator. Moreover, sucking air close to the ground surface seems an extra disadvantage, because of the loss of primary wind energy, a flaw that was also contained in the design of the Enfield-Andreau turbine (see Fig. 4.1).

3.6 Concluding remarks

There are several other proposals for increasing the wind energy flux through the turbine disk than those discussed in the preceding sections, e.g. ideas based on the increased velocity near large buildings (Ref. 3.20), or based on the increased velocity due to irregularities in the earth surface (hills, ridges). These proposals are too dependent on local circumstances to become generally applicable.

It seems possible indeed to augment the power output of a wind turbine of a given diameter. However, in most cases the additional structure is so extensive (except possibly the tip-vane concept) and has to be put into the wind direction (except possibly diffuser concepts in trade-wind regions), that it is still questionable whether the increased costs are compensated by the increased power output.

The tip-vane concept seems to be the most promising, because the vanes are attached to the blades and the additional structure possibly needs not be large with respect to the turbine blade area. There are several aspects, however, which have to be studied further before the feasibility of this concept can be shown unequivocally.

3.7 List of references

- 3.1 Betz, A.: Windenergie und ihre Ausnutzung durch Windmühlen. (Vandenhoeck und Ruprecht, Göttingen, 1926).
- 3.2 Glauert, H.: Windmills and Fans. Aerodynamic Theory (ed. W.F. Durand), Chapter XI, Div.L. (Dover Publ. Inc., N.Y., 1963).
- 3.3 Golding, E.W.: The Influence of Aerodynamics in Wind Power Development. AGARD Report 401 (1961).
- 3.4 Iwasaki, M.: The Experimental and Theoretical Investigations of Windmills. Rep. of Res. Inst. Appl. Mech., 2 8 (Dec. 1953) pp. 181-229.
- 3.5 Lilley, G.M., Rainbird, W.J.: A Preliminary Report on the Design and Performance of Ducted Windmills. The Electr. Res. Ass., Techn. Rep. C/T 119 (1957).
- 3.6 Kogan, A., Seginer, A.: Final Report on Shroud Design. Technion, Dept. Aeron. Eng. T.A.E. Rep. No. 32A (1963).
- 3.7 Igra, O.: Shrouds for Aerogenerator. Ben Gurion Univ. of the Negev., Dept. Mech. Eng. Rep. No.2 (1975).
- 3.8 Oman, R.A., Foreman, K.M.: Cost Effective Diffuser Augmentation of Wind Turbine Power Generators. Proc. Second Workshop on Wind Energy Conversion Systems (Washington D.C., 9-11 June 1975). The Mitre Corp. MTR-6970 (Sept. 1975).
- 3.9 Van Holten, Th.: Performance Analysis of a Windmill with Increased Power Output due to Induced Diffusion of the Airstream. Delft Univ. of Techn., Memo M-224 (Nov. 1974).
- 3.10 Van Holten, Th.: Asymptotic Expressions for the Velocity Field due to a Cylindrical Ring Distribution of Vorticity. Delft Univ. of Techn., Memo M-223 (Oct. 1974).
- 3.11 Van Holten, Th.: Windmills with Diffuser Effect Induced by Small Tipvanes. Proc. Intern. Symp. on Wind Energy Systems (St. John's College, Cambridge, England; 7-9 Sept. 1976).
- 3.12 Hütter, U.: Optimum Wind-Energy Conversion Systems. Ann. Rev. Fluid Mech., 9 (1977) pp. 399-419.
- 3.13 Zimmer, H.: The Rotor in Axial Flow. AGARD FDP Specialists' Meeting (Marseille, France; 13-15 Sept. 1972). AGARD-CPP-111 (1972).
- 3.14 Stodard, F.S.: Momentum Theory and Flow States for Windmills. Wind Techn. Journ. 1 1 (Spring 1977).
- 3.15 Rosenbrock, H.H.: An Extension of the Momentum Theory of Wind Turbines. The Electr. Res. Ass., Techn. Rep. C/T 105 (Aug. 1951).
- 3.16 Lissaman, P.B.S.: General Performance theory for Crosswind Axis Turbines. Proc. Intern. Symp. on Wind Energy Systems (St. John's College, Cambridge, England; 7-9 Sept. 1976).
- 3.17 Sforza, P.M.: Vortex Augmentor Concepts for Wind Energy Conversion. Proc. Second Workshop on Wind Energy Conversion Systems (Washington D.C., 9-11 June 1975). The Mitre Corp. MTR-6970 (Sept. 1975).

- 3.18 Sforza, P.M.: Vortex Augmentors for Wind Energy Conversion.
Proc. Intern. Symp. on Wind Energy Systems (St. John's College, Cambridge, England; 7-9 Sept. 1976).
- 3.19 Walters, R.E.: Innovative Vertical Axis Wind Machines.
Proc. Second Workshop on Wind Energy Conversion Systems (Washington D.C., 9-11 June 1975).
The Mitre Corp. MTR-6970 (Sept. 1975).
- 3.20 Loth, J.L.: W.V.U. Wind Energy Concentrators.
Proc. Intern. Symp. on Wind Energy Systems (St. John's College, Cambridge, England; 7-9 Sept. 1976).
- 3.21 Loth, J.L.: Betz Type Limits for Vortex Wind Machines.
Proc. Third Biennial Conf. and Workshop on Wind Energy Conversion Systems (Washington D.C., 19-21 Sept. 1977).
- 3.22 Yen, J.T.: Tornado-Type Wind Energy Systems: Basic Considerations.
Proc. Intern. Symp. on Wind Energy Systems (St. John's College, Cambridge, England; 7-9 Sept. 1976).
- 3.23 Emslie, K.: Industrial Uses of Wind Tunnels with Particular Reference to Wind Machines.
AGARD Report 306 (Oct. 1960).

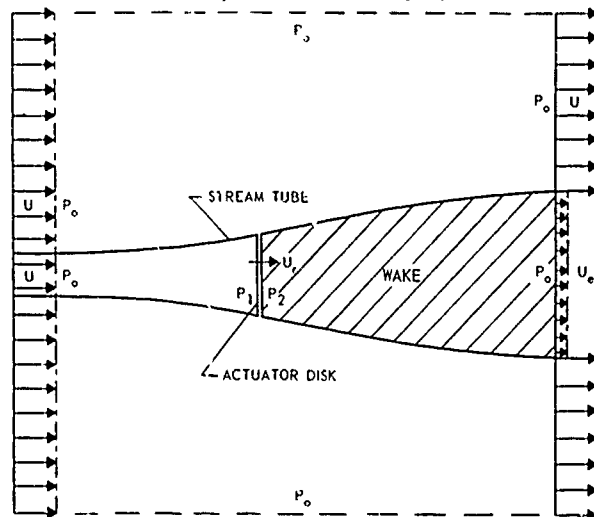


Fig. 3.1 Stream tube containing the actuator disk with area S_{ref} and control surfaces at a large distance from the turbine (actuator disk)

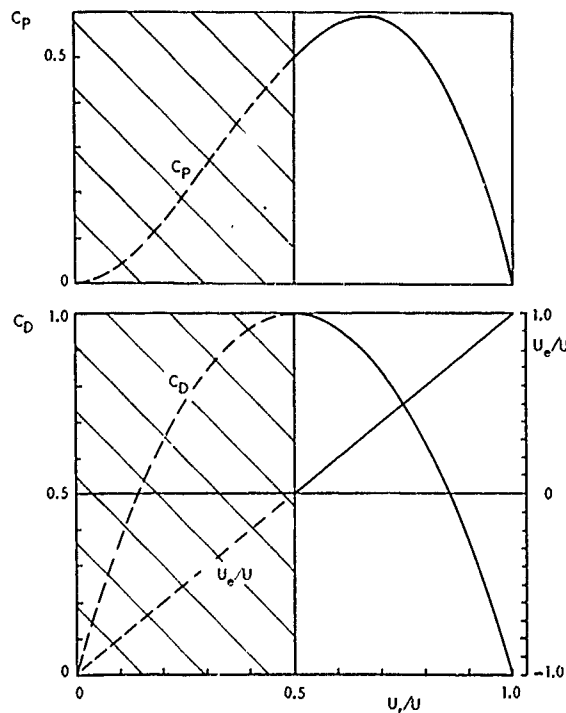
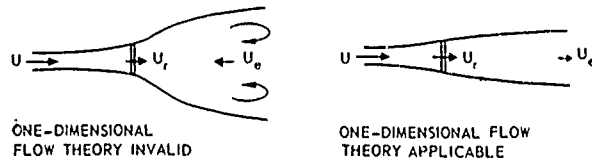


Fig. 3.2 Power coefficient, rotor drag coefficient and velocity in the far wake, predicted by simple axial momentum theory. Range of applicability

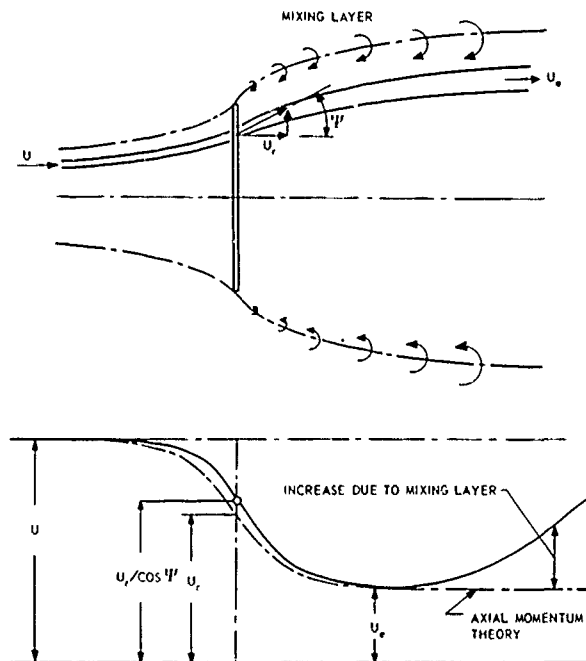


Fig. 3.3 Velocity along a streamline through the actuator disk, according to axial momentum theory and according to Hutter (Ref. 3.12)

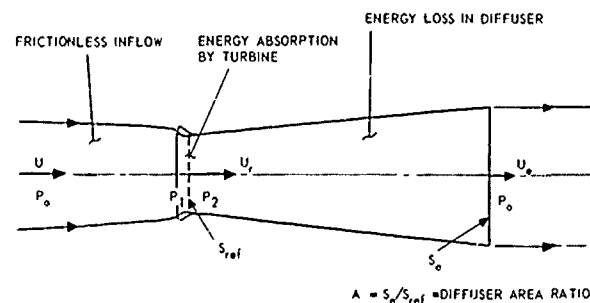


Fig. 3.4 Solid wall diffuser and inlet lip. The turbine is placed in the throat

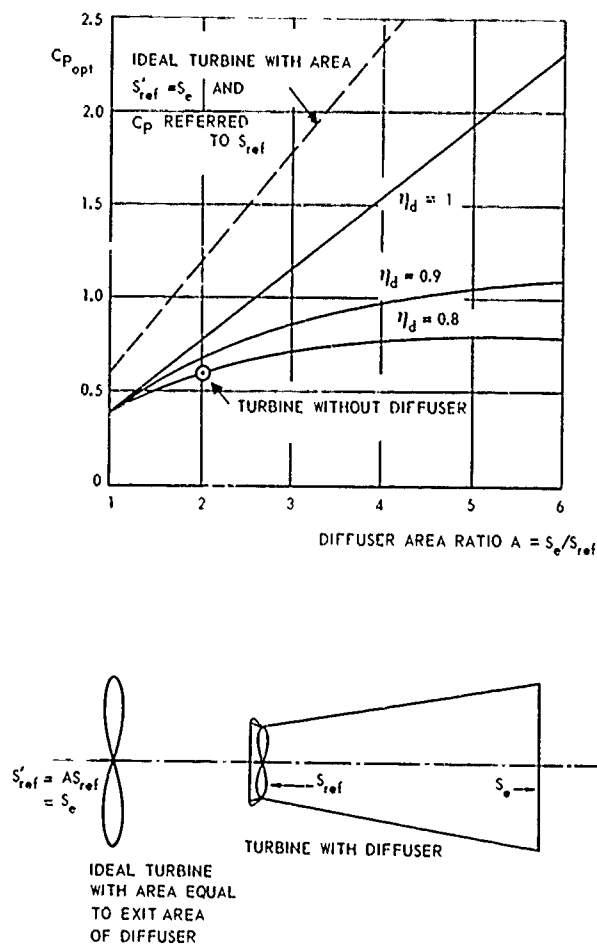


Fig. 35 Influence of diffuser efficiency η_d on optimum power coefficient of a wind turbine with diffuser, compared with the power generated by an ideal turbine with an area equal to the exit area of the diffuser

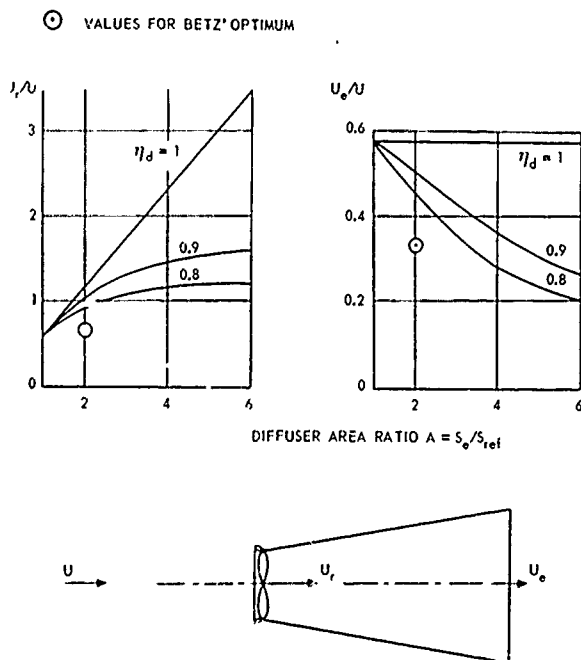


Fig. 36 Influence of the diffuser efficiency η_d on the velocity at the turbine and at the diffuser exit for a simple diffuser, operating at $C_{p_{opt}}$

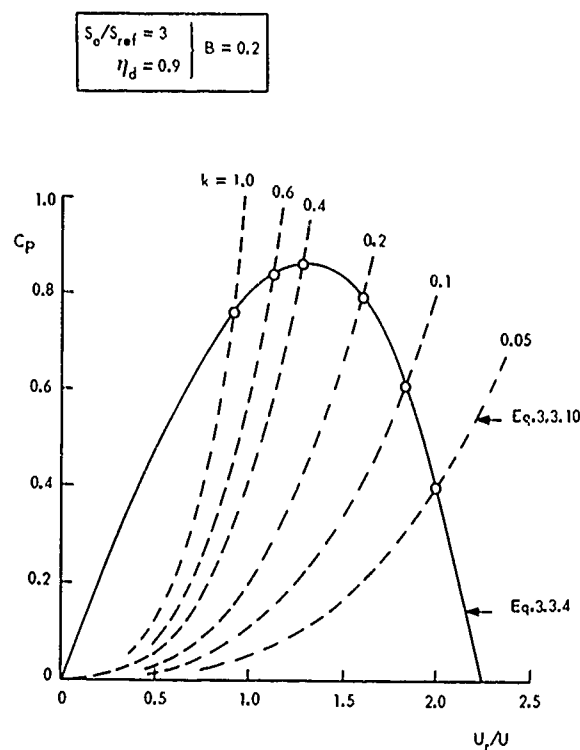


Fig. 3.7 Simulation of various points of the power curve of a turbine diffuser combination by screens, with different screen resistance factors k

WIND TUNNEL EXPERIMENTS

- × Emslie (Ref. 3.23)
- IGRA, WITHOUT "FLAPS" (REF. 3.7)
- IGRA, WITH "FLAPS" (REF. 3.7)

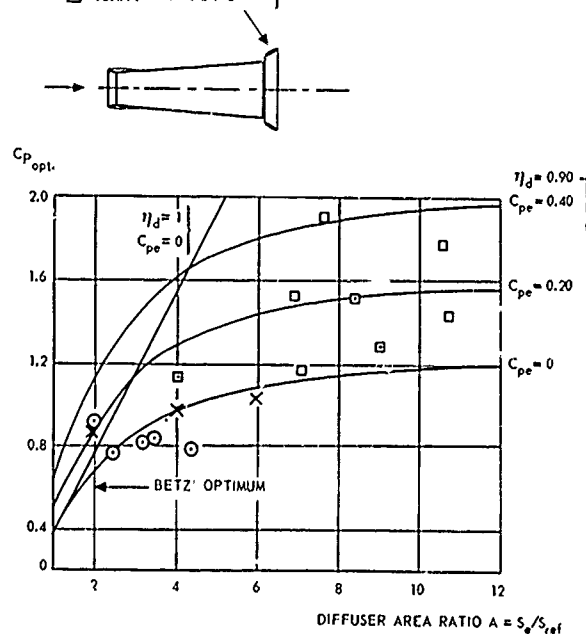


Fig. 3.8 Calculated influence of a reduced pressure at the diffuser exit on the power augmentation (Eq. 3.3.13), compared with results of wind tunnel experiments on models of diffusers

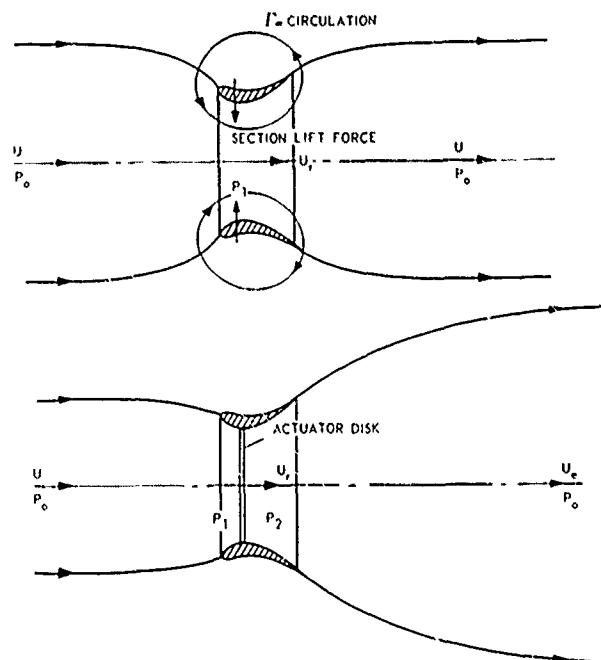


Fig. 3.9 Annular wing in inviscid flow, without and with an actuator disk, representing an energy absorbing turbine

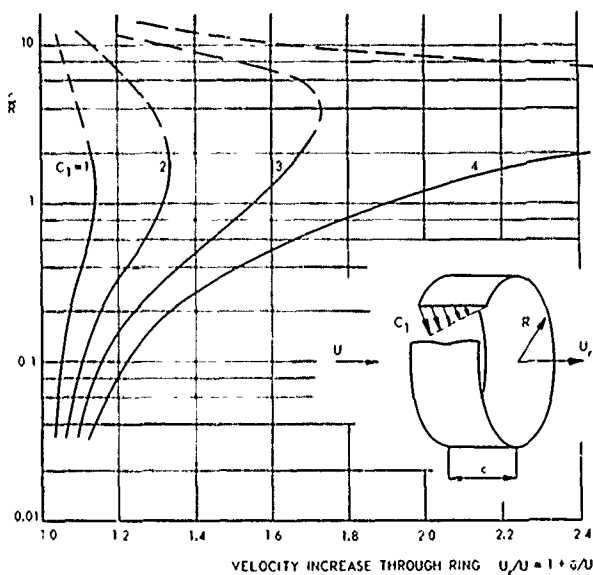


Fig. 3.11 Average mass flow increase through an annular wing with a triangular chordwise vorticity distribution, as a function of c/R and C_x . The lift coefficient C_x is defined, using the average velocity along the chord (sum of wind velocity U and the self-induced axial velocity)

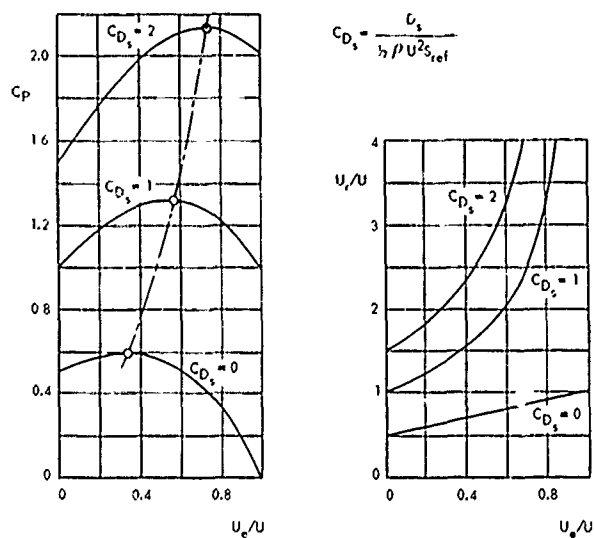


Fig. 3.10 Power coefficient and velocity through the turbine as a function of the velocity far behind the turbine and the axial shroud force, according to the simple axial-momentum theory

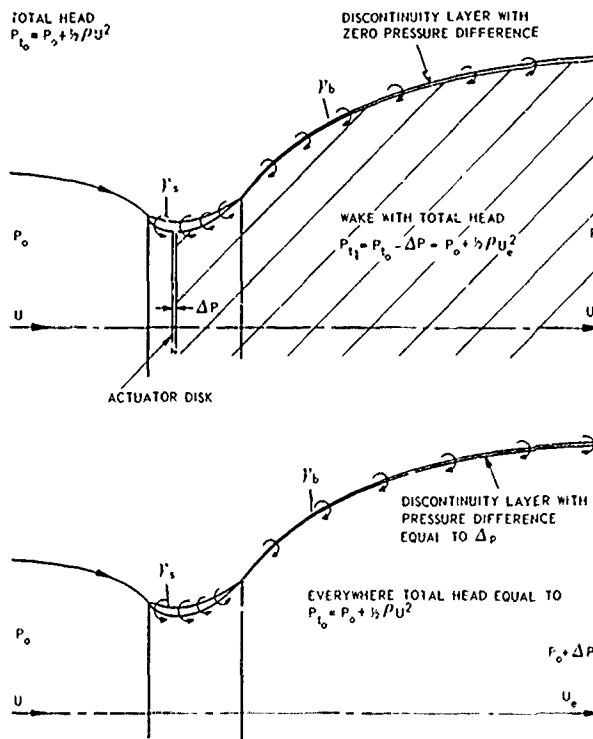


Fig. 3.12 Annular wing with actuator disk, causing a constant pressure drop Δp across the disk, and the potential flow analogon (bottom)

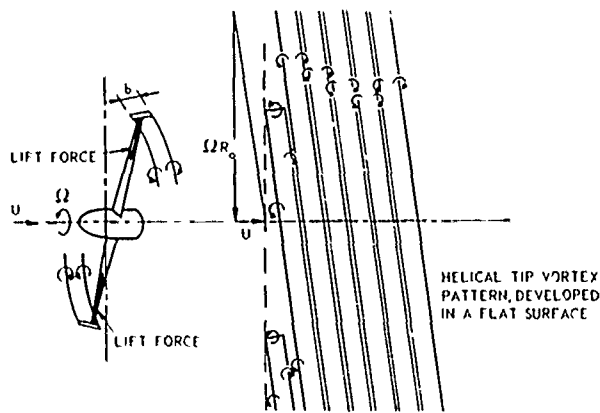


Fig. 3.13 Horizontal-axis wind turbine with tip vortices, tip vortices, traced by the tip vortices during a number of revolutions

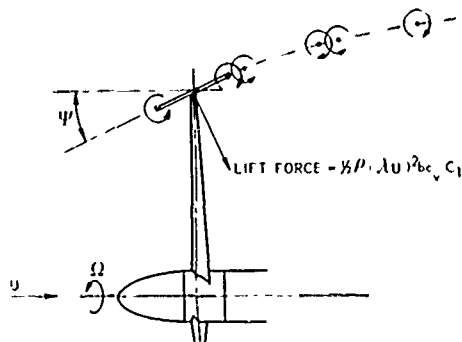


Fig. 3.14 Tilted tip vane, producing an axial component of the lift force

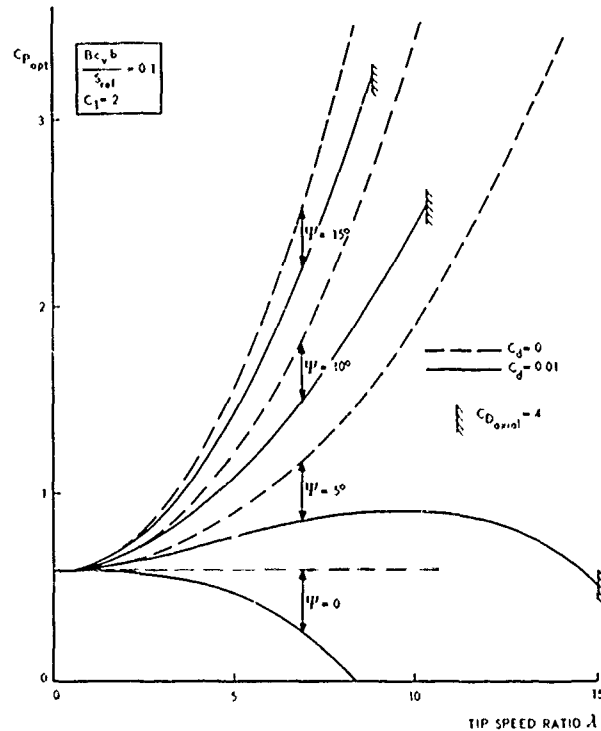


Fig. 3.15 Influence of the tilt angle Ψ and profile drag C_d on the optimum power output of a wind turbine with tip vortices, as a function of the tip-speed ratio λ

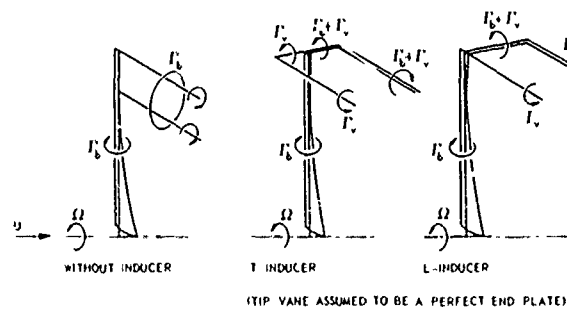


Fig. 3.16 Interference between turbine blade and tip vane

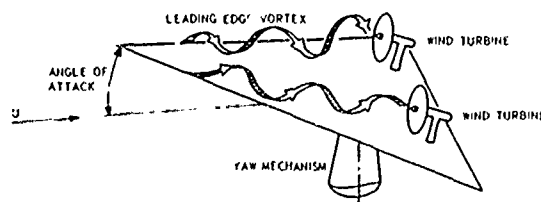


Fig. 3.17 Vortex augmentor concept of Ref. 3.18

4 THEORY OF WIND DRIVEN TURBINES

List of symbols

A	$= \sigma' C_l \cos \theta / (4 \sin^2 \theta) =$ factor in Eq. (4.4.34) and Eq. (4.4.44) (-)
a	amplitude of vertical displacement in Eq. (4.3.2) (m)
a'	axial induction factor (-)
a'	tangential induction factor (-)
B	number of rotor blades (-)
b'	location of axis of rotation in Eq. (4.3.3) (m)
b	wing span in Sect. 4.3.2 (m)
C	$= \cos \theta (\cos \theta - X \sin \theta) =$ factor in Eq. (4.4.47) (-)
c	chord length of rotor blade (m)
C_D	drag coefficient of three-dimensional body, e.g. in Eq. (4.2.2) (-)
C_D	$= D / (\frac{1}{2} \rho U^2 S_{ref}) =$ rotor drag coefficient (-)
C_d	drag coefficient of aerofoil section (-)
$(C_d)_{min}$	minimum profile drag coefficient (-)
C_{do}	profile drag coefficient taken as a constant at the low-angle-of-attack approximation (-)
c_{hub}	blade chord at hub radius (m)
C_L	lift coefficient of flutter machine (-)
C_l	lift coefficient of aerofoil section (-)
$(C_l)_{design}$	section lift coefficient at λ_{opt} (-)
$(C_l)_{max}$	maximum lift coefficient (-)
C_{L_α}	$= \partial C_L / \partial \alpha =$ slope of lift curve (degree ⁻¹ or radian ⁻¹)
C_{l_α}	$= \partial C_l / \partial \alpha =$ slope of lift curve (degree ⁻¹ or radian ⁻¹)
C_{L_δ}	$= \partial C_L / \partial \delta =$ lift increase due to flap deflection in Eq. (4.3.11) (radian ⁻¹)
C_m	$=$ pitching moment / $(\frac{1}{2} \rho U^2 c^2) =$ pitching-moment coefficient of aerofoil section in Eq. (4.3.5) (-)
$C_{\dot{m}}$	$=$ mass flow through rotor / $(\rho U 2R) =$ mass-flow coefficient in Fig. 4.39 (-)
C_{mo}	zero-lift pitching-moment coefficient in Eq. (4.5.24) (-)
C_P	$= P / (\frac{1}{2} \rho U^3 S_{ref}) =$ power coefficient (-)
C_P	$= P / (\frac{1}{2} \rho U^3 B c b) =$ power coefficient of a B-bladed flutter machine (-)
C_P	$= P / (\frac{1}{2} \rho U^3 2RH) =$ power coefficient of a two-dimensional turbine with a vertical axis (-)
$(C_P)_{opt}$	optimum power coefficient (-)
C_Q	$= Q / (\frac{1}{2} \rho U^2 S_{ref} R_O) = C_P / \lambda =$ torque coefficient (-)
c_r	chord length of flap in Eq. (4.3.15) (m)
C_t	tangential force coefficient (-)
$\overline{C_t}$	tangential force coefficient averaged over a complete revolution (-)
c_{tip}	chord length at the tip (m)
D	$= 2R_O =$ rotor diameter (m)
D	drag force or axial force (N)
d	distance between vortex sheets in Fig. 4.13 (m)
d	diameter of shaft in Fig. 4.21 (m)
ds_t	element of vortex sheet in t-direction in Eq. (4.5.63) (m)
ds_θ	element of vortex sheet in θ -direction in Eq. (4.5.63) (m)
F	tip correction factor due to Prandtl (-)
F	real part of the Theodorsen function in Eq. (4.5.29) (-)
f	tip correction factor as a function of ϕ in Eq. (4.4.36) (-)
F^*, F^{**}	higher-order tip correction factors in the Eqs (4.4.40 and 4.4.46) (-)
G	imaginary part of the Theodorsen function in Eq. (4.5.29) (-)
H	height of rotor (m)
H	$= p + \frac{1}{2} \rho U^2 =$ constant of Bernoulli (N/m ²)
i	local blade setting angle (degrees)
i	$= (-1)^{1/2} =$ imaginary unit (-)
J	$= U / nD =$ advance ratio of propeller (-)
J_0, J_1	Bessel function of the first kind in Eq. (4.5.29) (-)
k	$= \omega c / U =$ reduced frequency in Eq. (4.3.6) (-)
k	$= \frac{1}{2} c / R =$ reduced frequency in Eq. (4.5.28) (-)
k	tip correction factor due to Goldstein or Lock and Yeatman (-)
\overline{M}	moment averaged over one revolution of a vertical-axis turbine in Eq. (4.2.4) (Nm)
N	normal force or axial force (N)

n	number of revolutions per second in Fig. 4.30 (s^{-1})
P	power (W)
p	static pressure (N/m^2)
Q	torque of rotor (Nm)
R	radius of two-dimensional vertical-axis turbine (m)
r	$= z_0/c$ = dimensionless amplitude of vertical displacement in Eq. (4.3.6) (-)
r	local radius (m)
Re{ }	real part of { } (-)
Re _c	$= U_{rel}c/\nu$ = Reynolds number referred to chord length (-)
r _{hub}	hub radius (m)
R _o	maximum radius or tip radius (m)
\vec{r}_t	vector in t-direction in Eq. (4.5.58) (m/s)
\vec{r}_θ	vector in θ -direction in Eq. (4.5.58) (m/radian)
s	arc length along troposkien (m)
s	$= x_0/c$ = dimensionless position of the axis of rotation in Eq. (4.3.6) (-)
S _{ref}	reference area of the turbine; area swept by the rotor (m^2)
T	tangential force (N)
t	time (s)
U	wind velocity (m/s)
u	axial induced velocity in Eq. (4.5.14) (m/s)
U _{ax}	resultant axial velocity (m/s)
u _{av}	averaged axial induced velocity in Eq. (4.5.18) (m/s)
U _n	velocity component normal to blade element in Eq. (4.5.49) (m/s)
U _{rel}	total velocity relative to blade element (m/s)
U _{tan}	resultant tangential velocity (m/s)
v	velocity component in y-direction (m/s)
V _g	gust velocity in Sect. 4.5.5 (m/s)
V _R	radial velocity component in Eq. (4.5.19) (m/s)
V _{ϕ}	azimuthal velocity component in Eq. (4.5.20) (m/s)
w _t	total induced velocity at the plane of the rotor in Fig. 4.9 (m/s)
X	$= \Omega r/U = \lambda r/R_0$ = local tip-speed ratio (-)
x	co-ordinate in wind direction (m)
x	distance along blade chord (m)
X _{hub}	$= \Omega r_{hub}/U$ = speed ratio at the hub radius (-)
x _o	location of the axis of rotation in Eq. (4.3.3) (m)
x _o	location of the point of attachment in Eq. (4.5.23) (m)
Δx	displacement of vortex sheet during one revolution (m)
y	horizontal co-ordinate perpendicular to the wind; lateral co-ordinate (m)
y	$= \lambda/(1-a)$ = variable used in Sect. 4.5.2 (-)
z	vertical co-ordinate (m)
z _o	amplitude of vertical displacement in Eq. (4.3.1) (m)
α	angle of attack (degrees or radians)
$\bar{\alpha}$	angle of attack, determining the lift in a curved flow in Eq. (4.5.21) (degrees)
$\alpha'_{00}, \alpha'_{50}$	
α'_{100}	angle of attack at leading edge, mid chord and trailing edge in the Eqs (4.5.21) and (4.5.22) (radians)
α_{max}	angle of attack at maximum lift or maximum angle of attack during one revolution of a vertical-axis turbine (degrees)
Γ	circulation (m^2/s)
γ	strength of vortex sheet (m/s)
γ	slope of a troposkien blade shape (radians or degrees)
Γ_b	circulation of bound vorticity (m^2/s)
γ_b	strength of bound vortex sheet (m/s)
Γ_i	circulation around blade number i in Sect. 4.5.3 (m^2/s)
Γ_{io}	maximum circulation during a revolution of a blade number i in Sect. 4.5.3 (m^2/s)
Γ_o	$= B \Gamma_{io}$ = maximum circulation of B blades during one revolution (m^2/s)
γ_o	$= \Gamma_o/2\pi R = (\alpha/4\pi)C_l (1-a)U$ = maximum strength of bound vortex sheet (m/s)
Γ_r	circulation around B blades at radius r (m^2/s)
Γ'_r	circulation around one blade with $B \rightarrow \infty$ at radius r (m^2/s)
γ_s	strength of shed vortex sheet (m/s)
γ_t	strength of trailing vortex sheet (m/s)
Γ_∞	total circulation at radius r for $B \rightarrow \infty$ (m^2/s)
δ	flap deflection in Eq. (4.3.11) (radians)

δ	angle between U_{rel} and the normal to the radius in Eq. (4.5.44) (degrees)
δ_o	amplitude of harmonic flap deflection (radians)
η	aerodynamic efficiency of turbine in Sect. 4.4.6 (-)
η	$= H/2R_o$ = height-to-diameter ratio of rotor (-)
θ	angle between wind velocity and chord in Eq. (4.3.1) (radians)
θ	angle between U_{rel} and plane of rotation for a horizontal-axis turbine (degrees)
θ	angle in cylindrical or spherical co-ordinates (degrees)
θ_o	amplitude of harmonically varying θ (radians)
θ_p	blade pitch angle in the Figs 4.24 and 4.48 (degrees)
θ_t	value of θ at the tip of the rotor blade (degrees)
λ	$= \Omega R/U$ or $= \Omega R_o/U$ = tip-speed ratio of a two-dimensional vertical-axis turbine or of a three-dimensional vertical-axis and horizontal-axis turbine (-)
ν	kinematic viscosity of air (m^2/s)
ρ	density of air (kg/m^3)
σ	$= Bc/R$ or Bc/R_o = solidity ratio of a two-dimensional or a three-dimensional vertical-axis turbine (-)
σ	$= (B/S_{ref}) \int_{r_{hub}}^{R_o} c \, dr$ = solidity ratio of a horizontal-axis turbine (-)
σ'	$= Bc/2\pi r$ = local solidity ratio of a horizontal-axis turbine (-)
ϕ	phase angle in Eq. (4.3.1) (radians)
ϕ	azimuth angle (degrees)
ϕ_1	$= -\phi$ = negative phase angle in Eq. (4.3.9) (radians)
$\phi(k)$	$= (J_o - iJ_1) (F + iG) + iJ_1$ = Sears function (-)
ψ	phase angle in Eq. (4.3.2) (radians)
Ω	angular velocity of rotor (radians/s)
ω	angular frequency (s^{-1})
ω	$= \nabla \times \vec{U} = \text{curl } \vec{U}$ = rotation (s^{-1})
ω_s	rotation of shed vorticity (s^{-1})
ω_t	t-component of rotation in Sect. 4.5.7.3 (s^{-1})
$\omega_x, \omega_y, \omega_z$	x-, y- and z-component of rotation in the Eqs (4.5.65) through (4.5.67) (s^{-1})
ω_θ	θ -component of rotation in Sect. 4.5.7.3 (s^{-1})

4.1 Introductory remarks

The very purpose of a wind turbine is to extract energy from the air flow and then convert it into mechanical energy. The performance calculations of wind turbines are mostly based upon a steady flow, in which the influence of the turbulence of the atmospheric boundary layer (unsteadiness, gusts) is neglected.

The loss of energy in a steady incompressible flow, is aerodynamically indicated by a decrease of the so-called Bernoulli constant H , i.e. a decrease of

$$H = p + \frac{1}{2}\rho U^2,$$

where p = static pressure (N/m^2),
 ρ = air density (kg/m^3),
 U = velocity of the air (m/s).

The way in which such a decrease could be accomplished is discussed in Appendix B.

Viscous dissipation (transformation of flow energy into heat), e.g. by putting a screen perpendicular to the flow (cf. Sect. 3.3.1, Eq. (3.3.10)), cannot be regarded as a useful form of energy extraction.

In a steady flow, the most powerful aerodynamic force (lift) cannot extract energy from the flow, because the lift is always perpendicular to the flow. It would be possible to drive a turbine with pure drag forces, but a large part of the extracted energy would be dissipated into heat, which results in a low efficiency. It is shown in Appendix B that the utilization of lift forces with the related small viscous drag force is only possible, when the flow through the turbine is unsteady.

In Appendix B it has also been discussed that, although the flow through the turbine is unsteady in an absolute (fixed-to-earth) reference frame, a steady flow could be obtained in the case of a horizontal-axis turbine when the reference frame is fixed to the rotor blades. An energy loss in the flow can be shown to occur in that case after modification of the equations of motion (adding centrifugal and Coriolis forces). This brings about a fundamental difference in describing the flow through horizontal-axis (propeller type) and vertical-axis (or cross-wind type) wind turbines.

A classification of wind turbines into devices utilizing drag or lift forces and into horizontal-axis or vertical-axis turbines can be made from aerodynamic considerations. However, a large number of mechanical devices has been invented, which can be called wind turbines, but cannot be classified according to the above-mentioned scheme. Also, the nomenclature is not unequivocal, e.g. by a horizontal-axis turbine is usually meant a turbine with its rotor-axis parallel to the wind. In case of a turbine with its axis horizontal, but perpendicular to the wind, the name cross-wind turbine is sometimes used, but a vertical-axis turbine can also be considered as a cross-wind turbine.

The discussion of the theory of wind-driven turbines will be limited to some types. The choice of these types will be discussed from examples of turbines, given in the figures 4.1 through 4.4.

Figure 4.1 shows some examples of horizontal-axis turbines with the rotor-axis parallel to the wind direction. The discussion of the theory will be limited to the low-solidity (high-angular-velocity) type, because this type is most promising for large-scale applications. The multi-bladed type with its low angular velocity and correspondingly high torque is mostly used for rural applications. The high mutual interference between the blades of a multi-bladed rotor might be a challenge to the theorist, but an accurate calculation is hardly worth the trouble, because of the kind of application for such a type of turbine.

The Enfield-Andreau turbine and the tip turbines shown at the bottom of figure 4.1 have been invented to by-pass the difficulty to step up the low RPM of a large wind turbine to the high RPM needed for an electric generator. The first one, which has actually been built, uses the hollow rotor blades as a centrifugal pump, sucking air through the hollow tower, which drives a small turbine in the lower part of the tower. The efficiency proved to be low and this type will not be discussed further. The second one uses the high tip speed of a low-solidity wind turbine to drive small turbines. The additional problems of this concept (blade loading, gyroscopic effects on the small turbine) are much larger than the original gearing problem and, thus, this type will also be left out here.

Figure 4.2 shows two types of vertical-axis wind turbines. The Darrieus turbine, with its blades curved to alleviate the bending moments due to centrifugal forces (cf. Fig. 2.6 and Appendix D), is an intensively studied concept nowadays. The main advantage is the cheap blade construction, apart from the more common advantage of insensitivity to wind direction (no yaw control, contrary to the horizontal-axis turbine). The drum-type turbine is theoretically interesting, because the fictitious infinitely high turbine is a two-dimensional analogue of the Darrieus turbine. The drum-type has also the possibility to vary the blade setting angle during a revolution (e.g. RPM control), but this destroys the insensitivity to wind direction. Therefore, the drum-type will be discussed only as a two-dimensional analogue of the Darrieus wind turbine.

The types discussed above are primarily driven by a component of the lift force. Figure 4.3 shows some types that are primarily driven by a drag force. They are listed as vertical-axis turbines, but will operate also as a horizontal-axis turbine with their axes perpendicular to the wind (cross-wind types). In that case, however, the insensitivity to the wind direction is lost. The cup turbine operates due to a drag difference between the concave and convex side of the cup. It is actually used only as a wind velocity meter and will not be discussed further. The example of the simple articulated panemone is given, because it offers an occasion, by means of a rough performance estimate, to show the low tip-speed ratio and low power coefficient inherent to all drag-driven turbines. In order to avoid the flapping blades of an articulated panemone, it is possible to shield one half of a fixed-bladed rotor from the wind stream, but in that case the shield has to be rotated when the wind direction changes. The Savonius turbine is, strictly speaking, not a drag-driven rotor. The rotor can be considered as a wing section with a S-shaped mean line, rotating about its mid chord. At zero angle of attack, the S-shaped mean line causes a torque (zero-lift pitching moment). At small angles of attack, the lift force, acting at the quarter chord point, causes a torque (pitching moment about mid chord), whereas at larger angles of attack the torque is due to the drag difference between the convex and concave side of the rotor. Due to its simple and rugged construction and because of its performance (high torque, not too low power coefficient), the Savonius turbine is often seen in small-scale applications.

Figure 4.4 shows two examples of horizontal-axis cross-wind turbines. Both of them could be operated as vertical-axis turbines. This would be more logical for the drum-type (cf. Fig. 4.2), because a yaw mechanism is avoided, but a flutter machine with a vertical axis has still to be put into the wind direction. The cyclic vertical motion of the flutter machine could be attractive for driving a water pump. Whether this concept is feasible depends on the invention of a elegant solution for the mechanism that has to produce the combined vertical and pitching motions of the wing.

In the next Sections, the performance of the simple articulated panemone and the flutter machine will be discussed briefly. The theory of the horizontal-axis (particularly the low-solidity one) and the vertical-axis (particularly the Darrieus type) wind turbines will be discussed more extensively.

Comparison between theory and experiment is hampered by a lack of reliable experimental data, especially in case of the horizontal-axis turbine. For the vertical-axis Darrieus turbine, rather complete sets of experimental results and comparison with theoretical calculations are available.

4.2 Drag-driven turbine

It is possible to drive a turbine by pure drag forces. The construction of the turbine then has to be such, that elements of the turbine moving in wind direction have a high resistance, and elements moving opposite to the wind have a low resistance. This can be realized by a number of different mechanisms, but the mechanism sketched in Fig. 4.5 offers the possibility of a simple estimation of its performance. The estimation, although rather crude, is useful because it leads to an overestimation of the power coefficients, when certain assumptions are made.

The following assumptions are made in the calculation:

- 1: At the lower half of the turbine, the blades are free from the stops, and the blades (hinged at the nose) direct themselves into the relative wind direction, which is not necessarily parallel to the wind direction U as drawn in Fig. 4.5. When the blades are free from their stops, the drag is neglected and the blades do not contribute to the torque M .
- 2: At the upper half of the turbine, the blades are pressed against the stops, if

$$|U \sin \phi| \geq \Omega R \quad \text{or} \quad |\sin \phi| \geq \Omega R / U = \lambda ; \quad (4.2.1)$$

otherwise the blades are free from the stops and do not contribute to the torque M (see item 1). This leads to the conclusion, that a positive contribution to the torque is only possible if $\lambda < 1$.

- 3: The velocity through the rotor is assumed to be equal to the wind velocity U . Also the mutual interference between the blades (e.g. one blade entering the wake of a preceding blade) is neglected. This means that the solidity of the rotor

$$\sigma = Bc/R \quad (\text{with } B = \text{number of blades}) \quad (4.2.2)$$

is assumed to be low.

- 4: The normal force on the blade (N) depends on the component of the relative velocity normal to the blade chord

$$|U \sin \phi| - \Omega R ,$$

and the normal force can be calculated from the corresponding drag coefficient for a flat plate normal to the flow, thus

$$\begin{aligned} N &= \frac{1}{2} \rho (|U \sin \phi| - \Omega R)^2 C_D c H \\ &= \frac{1}{2} \rho U^2 C_D c H (|\sin \phi| - \lambda)^2 , \end{aligned} \quad (4.2.3)$$

with C_D = drag coefficient ($C_D \approx 2$),
 c = chord of the blade,
 H = height of the rotor.

The average torque of one blade during one revolution of the rotor can be calculated from Eq. (4.2.3), with the condition of Eq. (4.2.1), and with $a = [\arcsin \lambda]$

$$\begin{aligned} \bar{M} &= \frac{2}{2\pi} \int_a^{\pi/2} N R d\phi \\ &= \frac{1}{2\pi} \rho U^2 C_D c H R \left[(1 + \lambda^2) \left(\frac{\pi}{4} - \frac{1}{2} \arcsin \lambda \right) - \frac{3}{2} \lambda \cos (\arcsin \lambda) \right] \\ &= \frac{1}{2\pi} \rho U^2 C_D c H R F(\lambda) . \end{aligned} \quad (4.2.4)$$

The generated power can be calculated for a B -bladed rotor from

$$P = B \bar{M} \Omega ,$$

and the corresponding power coefficient from

$$C_P = P / \frac{1}{2} \rho U^3 2\pi R H = (\sigma / 2\pi) C_D F(\lambda) . \quad (4.2.5)$$

Figure 4.6 shows the power coefficient as a function of the tip-speed ratio, estimated with Eq. (4.2.5), in which $C_D = 2$ and rather high values of the solidity ratio are inserted. Notwithstanding the high solidity ratio chosen, the power coefficients obtained are low, and the optimum C_P occurs at $\lambda \approx 0.27$.

The torque coefficient C_Q (see Eq. (2.3.6)) is obtained from

$$C_Q = C_P / \lambda = (\sigma / 2\pi) C_D F(\lambda) . \quad (4.2.6)$$

The torque is maximum at $\lambda = 0$, viz.:

$$C_Q = \frac{\sigma}{8} C_D ,$$

and tends to zero when $\lambda \rightarrow 1$. The panemone is self-starting.

4.3 Flutter machine, used as a wind turbine

4.3.1 General remarks

It is known, that an elastic structure, e.g. the wing of an aircraft or the rotor-blade of a wind turbine, might vibrate in such a vibration mode that energy is transferred from the airflow to the vibrating structure (flutter). In case of insufficient mechanical damping, the vibration may become so violent, that the structure disintegrates.

The suspending of a rectangular wing in such a way, that a certain combination of vertical displacements and rotations about an axis parallel to the wing span can be realized (cf. Fig. 4.4), might create a possibility to extract energy from the flow and convert it into mechanical energy.

Energy considerations, including unsteady aerodynamic effects, were published for the first time in Ref. 4.1. In the following Sections, estimates will be made of the amount of energy that can be extracted from an airflow by a flutter machine, by applying quasi-steady aerodynamics. Possible mechanical solutions for the translational and rotational motions and for the conversion of the motion of the wing into mechanical energy will not be discussed.

The only purpose of the discussion is to show whether there is a potential feasibility to use the flutter machine as a wind energy converter.

4.3.2 Energy extracted by a plain aerofoil

The aerofoil can rotate about an axis at a distance x_0 behind the nose of the section (Fig. 4.7). The axis can be displaced vertically (z). The displacements and the rotations vary harmonically with a phase shift ϕ :

$$\begin{aligned} \theta &= \theta_0 \sin \omega t, \\ z &= z_0 \sin (\omega t + \phi) . \end{aligned} \quad (4.3.1)$$

If the axis of rotation would be located at a distance b' behind the nose instead of at the distance x_0 , the same motion of the aerofoil can be described by using different values of z_0 and ϕ , viz. a and ψ (assuming small rotations), thus:

$$\begin{aligned} \theta &= \theta_0 \sin \omega t, \\ z &= a \sin (\omega t + \psi), \end{aligned} \quad (4.3.2)$$

with the conditions

$$\begin{aligned} a^2 &= z_0^2 + 2z_0(x_0 - b')\theta_0 \cos \phi + (x_0 - b')^2\theta_0^2 , \\ \operatorname{tg} \psi &= \frac{z_0 \sin \phi}{z_0 \cos \phi + (x_0 - b')\theta_0} . \end{aligned} \quad (4.3.3)$$

At low reduced frequency, i.e.

$$k = \omega c / U \ll 1 ,$$

lift and pitching moment can be calculated in a quasi-steady way, i.e. they can be calculated from the instantaneous values of velocities and angles.

The usual approximation is applied, in which the aerofoil is replaced by a discrete vortex at $\frac{1}{2}c$, and the relative velocity at $\frac{1}{2}c$, normal to the local mean line, has to be zero (see e.g. Ref. 4.2). This leads to

$$C_L = C_{L_\alpha} \left[\theta - \frac{1}{U} \frac{dz}{dt} + \frac{1}{U} (\frac{1}{2}c - x_0) \frac{d\theta}{dt} \right] , \quad (4.3.4)$$

$$C_m = - \frac{\pi c}{8U} \frac{dz}{dt} + C_L \left(\frac{x_0}{c} - \frac{1}{2} \right) . \quad (4.3.5)$$

When Eq. (4.3.1) is substituted into the Eqs (4.3.4) and (4.3.5), and when the abbreviations

$$k = \omega c / U, \quad r = z_0 / c, \quad \text{and} \quad s = x_0 / c$$

are used, the following results are obtained

$$C_L = C_{L_\alpha} [\theta_0 \sin \omega t - kr \cos (\omega t + \phi) + k(\frac{1}{2} - s)\theta_0 \cos \omega t] , \quad (4.3.6)$$

$$C_m = - \frac{\pi}{8} k \theta_0 \cos \omega t + (s - \frac{1}{2}) C_L . \quad (4.3.7)$$

The extracted power P equals the energy during one period, times $\omega/2\pi$. The power is made dimensionless by means of

$$\frac{1}{2}\rho U^3 cb \quad (b = \text{wing span}) ,$$

which leads to

$$\frac{P}{\frac{1}{2}\rho U^3 cb} = \frac{\omega}{2\pi} \int_0^{2\pi/\omega} \left[\frac{c}{U} \frac{d\theta}{dt} + \frac{1}{U} c_L \frac{dz}{dt} \right] dt .$$

The integral is evaluated for $s = \frac{1}{2}$. Other locations of the axis of rotation can be considered, using different values of r and ϕ (see the Eqs (4.3.2) and (4.3.3)). For $s = \frac{1}{2}$, the following result is obtained:

$$\frac{P}{\frac{1}{2}\rho U^3 cb} = [(k\theta_0)^2/16] (\frac{1}{2}C_{L_\alpha} - \pi) - \frac{1}{2}C_{L_\alpha} kr(\theta_0 \sin \phi + kr) . \quad (4.3.8)$$

The maximum value of the lift slope is $C_{L_\alpha} \approx 2\pi$ (two-dimensional); therefore, the first term in Eq. (4.3.8) will be zero or small and negative. The second term can only be positive, when ϕ is negative. When it is assumed that $C_{L_\alpha} = 2\pi$ and $\phi = -\phi_1$, the result is

$$\frac{P}{\frac{1}{2}\rho U^3 cb} = \pi kr(\theta_0 \sin \phi_1 - kr) = X . \quad (4.3.9)$$

The optimum of this function can be obtained from the requirement that the first and second partial derivatives are zero, viz.:

$$\frac{\partial X}{\partial \phi_1} = \pi kr \theta_0 \cos \phi_1 = 0 ,$$

$$\frac{\partial X}{\partial kr} = \pi(\theta_0 \sin \phi_1 - 2kr) = 0 .$$

This gives the stationary points $(\pi/2, \theta_0/2)$ and $(0, 0)$. The values of X in these points are

$$X(\pi/2, \theta_0/2) = (\pi/4)\theta_0^2 \quad \text{or} \quad X(0, 0) = 0 ,$$

the last value being not of physical interest here.

Because both

$$(\partial^2 X / \partial \phi_1^2)_{\phi_1 = \pi/2} > 0 \quad \text{and} \quad (\partial^2 X / \partial kr^2)_{kr = \theta_0/2} > 0$$

it is a proper maximum.

According to the quasi-steady theory (applicable when $k \ll 1$), the maximum extracted power expressed in θ_0 is

$$\frac{P}{\frac{1}{2}\rho U^3 cb} = \frac{\pi}{4} \theta_0^2, \quad \text{with } \theta_0 = 2kr . \quad (4.3.10)$$

4.3.3 Energy extracted by an aerofoil with plain flap

Next, a wing is considered which moves up and down and which is provided with a plain flap deflected with the same frequency but a different phase. It has been assumed that the lift increment due to flap deflection is independent of the angle of attack. It is possible to combine this motion with a variation of θ of the wing itself, but the realization of such a motion requires a complicated mechanism; the calculation has, therefore, not been carried out.

The lift can be calculated from (cf. Eq. (4.3.4)):

$$C_L = -\frac{1}{U} C_{L_\alpha} \frac{dz}{dt} + C_{L_\delta} \delta . \quad (4.3.11)$$

When the displacement and flap deflection are written as

$$\begin{aligned} z &= z_0 \sin \omega t, \\ \delta &= \delta_0 \sin (\omega t + \phi), \end{aligned} \quad (4.3.12)$$

the power P is made dimensionless by $\frac{1}{2}\rho U^3 cb$ and can be written as

$$\frac{P}{\frac{1}{2}\rho U^3 cb} = \frac{1}{2}kr(C_{L_\delta} \delta_0 \sin \phi - krC_{L_\alpha}) , \quad (4.3.13)$$

when the power needed to drive the flap motion (hinge moment) is neglected. The optimum power can be calculated in a way similar to Sect. 4.3.2 and is obtained when $\phi = \frac{\pi}{2}$ and $\delta_0 = 2krC_{L_\alpha}/C_{L_\delta}$. The optimum is

$$\frac{P}{\frac{1}{2}\rho U^3 cb} = \left(\frac{C_{L_\delta}}{C_{L_\alpha}} / 8 \right) \left(\frac{C_{L_\delta}}{C_{L_\alpha}} / C_{L_\alpha} \right)^2 \delta_0^2 . \quad (4.3.14)$$

When the chord of the flap is denoted by c_r , it can be calculated for a hinged flat plate, that

$$C_{L_\delta} / C_{L_\alpha} = (2/\pi) \{ \arcsin (c_r/c)^{\frac{1}{2}} + [(c_r/c)(1 - c_r/c)]^{\frac{1}{2}} \} . \quad (4.3.15)$$

The value of Eq. (4.3.15) depends on the ratio of flap chord and wing chord, but is always smaller than

one. When $C_{L\alpha} = 2\pi$, an expression similar to Eq. (4.3.10) appears viz.:

$$\frac{P}{\frac{1}{2}\rho U^3 cb} = \frac{\pi}{4} \delta_0^2 \left(\frac{C_{L\alpha}}{C_{L\delta}} \right)^2 . \quad (4.3.16)$$

Although δ_0 might be chosen larger than θ_0 , the Eq. (4.3.15) shows that the value of Eq. (4.3.16) is almost always smaller than the corresponding value of Eq. (4.3.10).

4.3.4 Estimation of power output

In order to estimate the maximum possible amount of energy that can be extracted from the wind by a flutter machine, the maximum possible values of the considered parameters have to be estimated. For the plain aerofoil, one of the conditions is that the instantaneous angle of attack may not exceed a specific value (stalling angle of the aerofoil). The instantaneous angle of attack is

$$\alpha = \theta - \frac{1}{U} \frac{dz}{dt} .$$

According to Eq. (4.3.1),

$$\alpha = \theta_0 \sin \omega t - kr \cos (\omega t + \phi) .$$

With the conditions for the optimum found in Sect. 4.3.2 viz.:

$$\phi = -\frac{\pi}{2} \quad \text{and} \quad \theta_0 = 2kr ,$$

the angle of attack varies under optimal conditions as:

$$\alpha = \frac{1}{2} \theta_0 \sin \omega t . \quad (4.3.17)$$

When a maximum angle of attack during a dynamic stall of about $\frac{1}{3}$ radian is assumed, Eq. (4.3.17) gives the following conditions:

$$\theta_0 \leq \frac{2}{3} \quad \text{or} \quad kr \leq \frac{1}{3} . \quad (4.3.18)$$

The maximum power output of a single plain aerofoil is

$$\frac{P}{\frac{1}{2}\rho U^3 cb} = \frac{\pi}{9} \approx 0.35 . \quad (4.3.19)$$

For the same value of the parameter θ_0 as that given in Eq. (4.3.18), it is also possible to compare these results with the results given in Ref. 4.1. Contrary to the above given calculations, Ref. 4.1 uses the complete unsteady aerodynamic equations, which give the following result

$$\frac{P}{\frac{1}{2}\rho U^3 cb} \approx 0.6 \theta_0^2 = 0.27 . \quad (4.3.20)$$

A comparison of the Eqs (4.3.19) and (4.3.20) shows that the quasi-steady calculations overestimate the energy output by 30 percent.

The dimensionless quantities given in the Eqs (4.3.19) and (4.3.20) cannot be compared directly with the power coefficients C_p for a horizontal- or vertical-axis wind turbine. The coefficient for a flutter machine is defined relative to the wing area, whereas the power coefficient C_p is defined by means of the area perpendicular to the wind and swept by the rotor (e.g. $\pi D^2/4$).

A horizontal-axis turbine shows a theoretical optimum power coefficient $C_p = 0.59$. When a low solidity ratio (Eq. (2.3.8)) is applied, e.g. $\sigma \approx 0.1$, the dimensionless power related to the rotor-blade area becomes

$$\frac{P}{\frac{1}{2}\rho U^3 \sigma S_{ref}} = 0.59/0.1 = 5.9 .$$

This clearly shows that a flutter machine produces less power per unit area of the aerodynamic active elements than a low-solidity horizontal-axis turbine.

It is conceivable to construct a flutter machine consisting of a cascade of B aerofoils with a mutual separation equal to the chord c or less. In this case a reference area comparable with the reference area for a conventional wind turbine may be defined, viz.

$$S_{ref} = Bcb ,$$

and the corresponding maximum power coefficient (when unfavourable interference effects are neglected) becomes

$$C_p = \frac{P}{\frac{1}{2}\rho U^3 Bcb} \approx 0.27 .$$

This compares less unfavourable with a conventional wind turbine than the coefficient referred to the total blade area, but the solidity ratio is high, viz.:

$$\sigma = Bcb/S_{ref} = 1 .$$

According to Ref. 4.1, the quasi-steady calculations are valid if

$$k < \frac{1}{4} \quad \text{or} \quad \frac{1}{3} . \quad (4.3.21)$$

It is, thus, advantageous not to exceed this value of k by choosing r not too small (see Eq. (4.3.18)). It follows then from Eq. (4.3.18) that the related optimum value of θ_0 is obtained at $r \approx 1$, i.e. at a displacement $z_0 \approx c$.

A possible advantage of this concept is the lower acceleration of the blade elements of a flutter machine, compared with those of e.g. a horizontal-axis turbine. With $\phi = \pi/2$, $x_0 = c/2$ and $z_0 \approx c$, the maximum acceleration of a blade of the flutter machine is approximately

$$\omega^2 c (\cos \omega t + \frac{1}{2} \sin \omega t)_{\max} \approx \omega^2 c ,$$

which can be written as

$$\omega^2 c = k^2 U^2 / c ;$$

while the maximum centrifugal acceleration of a horizontal-axis turbine at high λ is approximately

$$\Omega^2 R_0 = \lambda^2 (c/R_0) U^2 / c \approx \lambda U^2 / c .$$

The flutter machine, therefore, reveals a potential feasibility to operate as a wind energy converter, when an elegant construction for the rotational and flapping motion can be realized. The flutter machine has to be considered, however, as a device with a high solidity ratio, which implies relatively high manufacturing costs.

4.4 Horizontal-axis turbine

4.4.1 General remarks

At first sight, a strong analogy seems to exist between the aerodynamics of an airplane propeller, a helicopter rotor and a horizontal-axis wind turbine. It could be expected then, that the performance calculation of a horizontal-axis wind turbine can take advantage of the experience from airplane-propeller and helicopter-rotor theory and experiment.

An important difference between a propeller or helicopter rotor and a horizontal-axis wind turbine is, that in the first case the thrust or lift is the most important quantity and the torque somewhat less important, whereas in the second case the torque is much more important than the force in wind direction. Moreover, the torque is more difficult to estimate, because it is composed of a component of the lift force (critically dependent on the angle of attack) and the profile drag of the rotor blade.

A further important difference between an airplane propeller and a horizontal-axis wind turbine is, that a propeller in cruise condition reveals small perturbation velocities with respect to the speed of flight, whereas an optimally operating wind turbine shows perturbation velocities that are not small with respect to the wind velocity. This appreciably affects the possibilities to formulate a mathematical model for the vortex wake behind the rotor. In case of the propeller, a cylindrical wake with a periodic structure can be defined (slipstream contraction can be neglected), whereas in case of a horizontal-axis turbine the vortex wake expands appreciably (cf. Fig. 3.3) and the vortex structure varies downstream, i.e. the structure becomes a function of the induced velocities, which leads to a nonlinear wake structure and thus to a complex iterative calculation procedure.

An airplane propeller in take-off conditions does have more in common with an optimally operating wind turbine (large perturbation velocities, but a large slipstream contraction instead of a large wake expansion). However, no detailed calculation method for this operating condition of an airplane propeller can be found in the literature.

In some flight regimes of a helicopter, the aerodynamics of the rotor is more similar to that of a wind turbine, e.g. in autorotation. In this field new developments in calculation methods (enabled by the development of the digital computer) can be found in the literature.

In the next Sections, the blade-element theory, the vortex theory for small perturbations (essentially the propeller theory), and the possible extension to large perturbation velocities will be discussed, with an emphasis on the underlying assumptions. Some results of the theory will be reviewed and some remarks on optimization procedures will be made. Comparison with experiments is hampered by lack of recent and accurate test results.

The discussions will be limited to the case of a horizontal-axis wind turbine with its axis parallel to the wind and immersed in a steady, homogeneous and non-turbulent wind stream, i.e. the effects of the atmospheric boundary layer will be excluded.

4.4.2 Theory for an infinite number of blades

When the number of blades of a rotor tends to infinity, it is assumed that the circulation around an elemental blade at radius r (Γ_r') tends to zero, while the total circulation of B blades (Γ_r) remains finite, thus

$$\Gamma_r = \lim_{\substack{B \rightarrow \infty \\ \Gamma_r' \rightarrow 0}} B \Gamma_r' = \text{finite} .$$

When $B \rightarrow \infty$, the flow is axisymmetric, i.e. independent of the azimuth angle ϕ . From each elemental-blade trailing edge a vortex sheet springs, whose local strength depends on the local "bound" vorticity. For a discussion of this vortex system see Appendix C.

The discussion in this Section is based on the theory of Glauert (Ref. 4.3). The induced velocities are denoted by so-called "induction" factors. At the rotor, the axial and tangential velocity at a radius r are:

$$U_{ax} = (1-a)U, \quad (4.4.1)$$

$$U_{tan} = (1+a')\Omega r, \quad (4.4.2)$$

with Ω = angular velocity of the rotor.

When a cylindrical wake is assumed (cf. App. C), the induced velocities far behind the rotor are twice the values at the rotor.

$$U_{ax\infty} = (1-2a)U, \quad (4.4.3)$$

$$U_{tan\infty} = (1+2a')\Omega r. \quad (4.4.4)$$

When it is assumed that the momentum equations can be applied to the elemental annular streamtube with radius r and thickness dr (cf. Appendix C), the axial momentum equation gives an expression for the normal force on the annulus

$$dN = 4\pi r \rho U^2 a(1-a)dr, \quad (4.4.5)$$

when the static pressure deficit due to the tangential velocities in the wake far downstream is neglected.

The tangential force on the rotor blade elements in the annulus (dT) gives rise to a torque $dQ = r dT$. When the equation for the angular momentum is applied and the wake expansion is neglected, the total tangential force on the annulus is

$$dT = 4\pi r^2 \rho U \Omega a'(1-a)dr. \quad (4.4.6)$$

When the chord of the rotor blade is small with respect to the span of the blade, the chordwise pressure distribution of a blade element at the annulus is identical to that of a two-dimensional wing section (profile) with a relative velocity and angle of attack equal to those of the blade element. This means that the local lift and drag of the blade element can be calculated from the data on two-dimensional profiles (C_l vs α , C_d vs α) and the local U_{rel} and angle of attack α .

Because C_l is perpendicular to U_{rel} and C_d parallel to U_{rel} , it follows from the velocity triangle in Fig. 4.9 that in case of a B-bladed rotor

$$\begin{aligned} dN &= \frac{B}{2} \rho U_{rel}^2 C_l (C_l \cos \theta + C_d \sin \theta) dr \\ &= \pi r \rho \sigma' C_l \frac{(1-a)^2 U^2 \cos \theta}{\sin^2 \theta} [1 + (C_d/C_l) \tan \theta] dr, \end{aligned} \quad (4.4.7)$$

$$\begin{aligned} dT &= \frac{B}{2} \rho U_{rel}^2 C_d (C_l \sin \theta - C_d \cos \theta) dr \\ &= \pi r \rho \sigma' C_l \frac{(1-a)^2 U^2 \sin \theta}{\sin^2 \theta} [1 - (C_d/C_l) \cot \theta] dr, \end{aligned} \quad (4.4.8)$$

$$\text{with } \sigma' = Bc/2\pi r = \text{local solidity ratio.} \quad (4.4.9)$$

The induction factors a and a' can now be calculated from the Eqs (4.4.5)-(4.4.8). The induced velocities at the blade element are generated, however, by vortices (lift forces) only and not by the profile drag, because, within the small-chord approximation, the profile drag does not induce velocities at the rotor blade itself. Therefore, C_d has to be set equal to zero, when the induction factors are calculated. Thus the equations are

$$a/(1-a) = \sigma' C_l \cos \theta / (4 \sin^2 \theta), \quad (4.4.10)$$

$$a'/(1+a') = \sigma' C_l / (4 \cos \theta). \quad (4.4.11)$$

When the relation, obtained from the velocity triangle (Fig. 4.9)

$$X \tan \theta = \frac{1-a}{1+a'}, \quad (4.4.12)$$

is used, with

$$X = \Omega r / U = (\Omega R_0 / U) r / R_0 = \lambda r / R_0 = \text{local tip-speed ratio.} \quad (4.4.13)$$

Eliminating a and a' from the Eqs (4.4.10)-(4.4.12) gives

$$\sigma' C_l = 4 \sin \theta \frac{\cos \theta - X \sin \theta}{\sin \theta + X \cos \theta}. \quad (4.4.14)$$

Dividing the equations (4.4.10) and (4.4.11) and using Eq (4.4.12) leads to

$$X = \frac{a}{a'} \tan \theta,$$

which can also be written as

$$\frac{a' \Omega r}{a U} = \tan \theta.$$

As Fig. 4.9 shows, this means that the total induced velocity is perpendicular to the relative velocity. This can be understood, because the lift force is perpendicular to the relative velocity and the change in linear momentum has to be in the direction of the applied force, which results in a total induced velocity that is also perpendicular to the relative velocity.

The power generated by the blade elements can be obtained from

$$dP = \Omega r dT,$$

and the power coefficient of the whole turbine from

$$C_P = \frac{P}{\frac{1}{2} \rho U^3 \pi R_O^2} = \frac{1}{\frac{1}{2} \rho U^3 \pi R_O^2} \int_{r_{hub}}^{R_O} dP.$$

Using the Eqs (4.4.8), (4.4.10) and (4.4.14) leads to

$$C_P = (8/\lambda^2) \int_{x_{hub}}^{\lambda} \sin^2 \theta (\cos \theta - X \sin \theta) (\sin \theta + X \cos \theta) [1 - (C_d/C_l) \cotg \theta] X^2 dX. \quad (4.4.15)$$

For actual calculations, the angle of attack has to be obtained from (Fig. 4.9)

$$\alpha = \theta - i, \quad (4.4.16)$$

and with this value of α , C_l and C_d can be obtained from the profile data.

The range of useful values of θ will now be discussed. From the velocity triangle follows, that a wind turbine might operate in a θ -range

$$0 \leq \theta \leq 90^\circ.$$

The lower boundary is the condition $U = 0$, $\Omega \neq 0$, or $a = 1$; the upper boundary is the condition $\Omega = 0$, $r = 0$ or $a' = -1$. When $C_l = 0$, the induced velocities are zero ($a = a' = 0$), and it follows from Eq. (4.4.12) that

$$(\tg \theta)_{C_l=0} = 1/X. \quad (4.4.17)$$

In order to satisfy the continuity equation (mass conservation), the velocity far downstream cannot be smaller than zero (there cannot be any backflow). Such a condition can occur in a real flow (turbulent wake state and vortex ring state; Ref. 4.4), but the equations cease to be valid in that case. It follows from Eq. (4.4.3) that

$$a \leq \frac{1}{2}.$$

With the equations (4.4.10) and (4.4.14), this can also be written as

$$a = \cos \theta (\cos \theta - X \sin \theta) \leq \frac{1}{2}$$

$$\text{or } \{(\tg 2\theta)\}_a \leq \frac{1}{X}. \quad (4.4.18)$$

In reference 4.3, the conditions for optimum power generation in the case that $C_d = 0$ are discussed. Because of the assumed independence of different blade elements along the span, the integrand of Eq. (4.4.15) can be optimized for each radial position (X) separately, for a given value of the tip-speed ratio λ , thus

$$\frac{\partial}{\partial \theta} \sin^2 \theta (\cos \theta - X \sin \theta) (\sin \theta + X \cos \theta) = 0,$$

which results in

$$X = \frac{\sin \theta (2 \cos \theta - 1)}{(1 - \cos \theta) (2 \cos \theta + 1)}, \quad (4.4.19)$$

or, when this is inserted into Eq. (4.4.14),

$$\sigma' C_l = 4(1 - \cos \theta), \quad (4.4.20)$$

or, from the product of both,

$$2\pi X \sigma' C_l = (\lambda B \frac{C}{R_O} C_l)_{\text{optimum}} = 8\pi \sin \theta \frac{2 \cos \theta - 1}{2 \cos \theta + 1}. \quad (4.4.21)$$

The distribution along the span of the optimum of θ and the optimum of C_l are shown in the figures 4.10 and 4.11. When the lift coefficient is chosen constant along the span, Fig. 4.11 reveals the chord distribution along the span.

Also shown in the figures is the possible range of θ and C_l . A negative C_l might be tolerated along a part of the span at certain off-design conditions, but too high values of C_l (or too low values of θ) extend the formulae out of the range of validity. Figure 4.11 shows that, in the present theory, only the turbine performance over a relatively narrow range at the high-lift side of the optimum can be calculated.

Ref. 4.3 also gives the optimum of C_P in case $C_d = 0$ ($C_l/C_d = \infty$), whereas Ref. 4.5 gives the influence of C_l/C_d on the optimum of C_P in case of C_l/C_d is constant along the blade span. The results are shown in Fig. 4.12. This figure shows that, when a low value of λ is chosen (which corresponds to a large chord and many blades, according to Fig. 4.11), the optimum of C_P is appreciably reduced.

Usually, this power reduction at low λ is explained by considering the work done on the air by the torque of the rotor, viz.

$$\Delta P = - \int a' \Omega dQ.$$

It is argued, however, in Appendix C (Sect. C.5), that this power reduction is probably cancelled for the

greater part, when also the effect of the static pressure deficit in the wake is considered.

When we return to Fig. 4.11, it appears that the circulation at the tip is non-zero. This is caused by the assumption of an infinite number of blades. In the next Section, the influence of a finite number of blades will be discussed.

4.4.3 Tip correction theories

4.4.3.1 Linearized correction

With a finite number of blades, the circulation around the blade has to decrease continuously to zero towards the tip, because of the possibility of a cross-flow around the tip, which decreases the pressure difference between upper and lower side of the tip profile. This effect is analogous to that of an air-plane wing of finite span, but the vortex calculations are more complex in case of a wind turbine.

Prandtl (Ref. 4.6) introduced a relatively simple method to estimate this so-called "tip-loss" effect. He considered the helical vortex sheets behind the turbine (cf. Appendix C) to be rigid planes moving with a velocity equal to the axial induced velocity aU with respect to the undisturbed external flow. Because this was still a complex problem to solve, he simplified it further by considering a set of equidistant parallel flat plates, with a mutual distance (Fig. 4.13) of

$$d = (2\pi R_0/B) \sin \theta_t \approx (2\pi r/B) \sin \theta, \quad (4.4.22)$$

with θ_t = helix angle at the tip.

With a conformal transformation, the reduction in potential difference between two plates approaching the tip could be calculated. It was assumed that this reduction in potential difference was equal to the reduction of the circulation around the rotor blade. The reduction factor found by Prandtl was

$$\begin{aligned} F &= (2/\pi) \arccos [\exp - (\pi/d)(R_0 - r)] \\ &= (2/\pi) \arccos [\exp - (B/2)(1 - r/R_0) / \{(r/R_0) \sin \theta\}] . \end{aligned} \quad (4.4.23)$$

When the circulation for a rotor with an infinite number of blades is denoted by Γ_∞ , the circulation for a B-bladed rotor is then

$$\Gamma = F \Gamma_\infty . \quad (4.4.24)$$

Γ_∞ can be calculated from Sect. 4.4.2 (because of the axisymmetry) by considering the induced tangential velocities far downstream, viz.

$$\Gamma_\infty = 2\pi r 2a'\Omega r = 4\pi r a'\Omega r .$$

Because the total induced velocity w_t is perpendicular to U_{rel} (Fig. 4.9), w_t can be expressed in the tangential velocity component

$$w_t = a'\Omega r / \sin \theta ,$$

or with the expression for Γ_∞

$$w_t = \Gamma_\infty / 4\pi r \sin \theta .$$

At a given value of θ (thus a given value of w_t), the circulation is reduced by the factor F (which also depends on θ) according to Eq. (4.4.24), and the equation for w_t becomes

$$w_t = \Gamma / 4\pi r F \sin \theta .$$

Because the total circulation of the B blades is

$$\Gamma \approx \frac{B}{2} C_l C_u U_{rel} ,$$

the formula for w_t can be written as

$$w_t = (\sigma' C_l / 4F \sin \theta) U_{rel} , \quad (4.4.25)$$

which can be regarded as the fundamental equation to calculate the turbine performance.

From the fact that w_t is perpendicular to U_{rel} , it follows that

$$U_{rel} \sin \theta = U - w_t \cos \theta .$$

Together with Eq. (4.4.25), the following relations can be obtained

$$w_t / U = [(4F / \sigma' C_l) \sin^2 \theta + \cos \theta]^{-1} \quad (4.4.26)$$

$$U_{rel} / U = [(\sigma' C_l / 4F) \cotg \theta + \sin \theta]^{-1} . \quad (4.4.27)$$

From the velocity triangle (Fig. 4.9), the relation

$$\operatorname{tg} \theta = \frac{U - w_t \cos \theta}{\Omega r + w_t \sin \theta} = \frac{1 - (w_t / U) \cos \theta}{X + (w_t / U) \sin \theta}$$

follows, or, with Eq. (4.4.26):

$$\sigma' C_l = 4F \sin \theta \frac{\cos \theta - X \sin \theta}{\sin \theta + X \cos \theta} \quad (4.4.28)$$

The power coefficient can be calculated from the tangential force, which leads to

$$C_p = (8/\lambda^2) \int_0^\lambda F \sin^2 \theta (\cos \theta - X \sin \theta) (\sin \theta + X \cos \theta) [1 - (C_d/C_l) \cot \theta] X^2 dX \quad (4.4.29)$$

Apart from the factor F , this formula is identical to Eq. (4.4.15). Figure 4.14 shows the influence of the tip correction on the local power coefficient ($dC_p/d(r/R_0)$), when $C_d = 0$. The influence on the optimum θ is small. This means that most of the conclusions drawn from the theory for $B = \infty$ also apply to a finite number of blades.

It can be revealed from Fig. 4.14 that the tip loss decreases with increasing tip-speed ratio λ (due to the decrease of θ), which is also an argument to design a wind turbine with a high λ .

4.4.3.2 Theory of Wilson and Lissaman

In Ref. 4.7, a theory for the tip correction is given that slightly deviates from the theory of the preceding Section. It uses the momentum equation in the same way as that in Ref. 4.3 and has, therefore, to interpret the correction factor F in terms of velocities.

When Fig. 4.13 and Ref. 4.6 are considered, the potential difference between the plates might also be interpreted as the difference between w_t and the average of the velocity between the plates w_t^* times the distance d . Deep inside the plates ($r \rightarrow 0$), $w_t^* \rightarrow 0$ or $w_t - w_t^* \rightarrow w_t$, i.e. the fluid moves with the vortex sheet, whereas approaching the tip of the plates ($r \rightarrow R_0$), $w_t^* \rightarrow w_t$ or $w_t - w_t^* \rightarrow 0$. This leads to the interpretation that at the vortex sheets, thus also at the blade elements, the full induced velocities are present (aU , $a'\Omega r$), but that between the vortex sheets the induced velocities are reduced and that the average induced velocities could be obtained by the factor F , viz. aFU and $a'F\Omega r$.

To apply this concept to the momentum equations, the additional and more or less logical assumption has to be made that far downstream similar arguments can be used, i.e. the average induced velocities far downstream are $2aFU$ and $2a'F\Omega r$. It must be noticed that, when the total induced velocity at the blade element is perpendicular to the relative velocity at the blade element ($X(a'/a) = \tan \theta$), the total average induced velocity is also perpendicular to the relative velocity at the blade element.

In Ref. 4.7 then the assumption is made that the total circulation around the blade elements at radius r ,

$$\Gamma = \frac{B}{2} C_l c U_{rel} = \frac{B}{2} C_l c (1+a') \Omega r / \cos \theta \quad (4.4.30)$$

is equal to the circulation, calculated along a circle with radius r far downstream

$$\Gamma = 2\pi r 2a'F\Omega r \quad (4.4.31)$$

Such a relation is strictly valid only in axisymmetric flow, because, due to the radial velocities from the cross-flow around the blade tips (Fig. 4.13), the stream surface becomes deformed and a radial transport of vorticity may take place, which invalidates the assumption above.

Eq. (4.4.31) can also be interpreted as $\Gamma = F \Gamma_\infty$, used in the preceding Section. From the Eqs (4.4.30) and (4.4.31) it follows that

$$\frac{a'F}{1+a'} = \frac{\sigma' C_l}{4 \cos \theta} \quad (4.4.32)$$

which can be compared with Eq. (4.4.11) for an infinite number of blades.

In Ref. 4.7 the axial momentum equation (Eq. (4.4.5)) is applied; but " a " is replaced by the average value " aF ", which ultimately leads to the following relation:

$$\frac{(1-aF)aF}{(1-a)^2} = \frac{\sigma' C_l \cos \theta}{4 \sin^2 \theta} \quad (4.4.33)$$

which can be compared with Eq. (4.4.10) for an infinite number of blades.

The linearized approach of the preceding Section should give a somewhat different left hand side of the equation, viz. $aF/(1-a)$. The inclusion of a higher-order term can be questioned (see Sect. 4.4.3.3), but in Ref. 4.8 it is quoted, that it reduces appreciably the computation time for an optimization calculation.

The ratio of the Eqs (4.4.32) and (4.4.33), together with Eq. (4.4.12) gives

$$X \frac{a'}{a} = \tan \theta \frac{1-aF}{1-a} \quad (4.4.34)$$

which shows that neither the local total induced velocity (w_t) nor the average one (Fw_t) is perpendicular to the relative velocity at the blade element. This could also be restored by including higher-order terms in Eq. (4.4.32). This would lead to a left-hand term equal to

$$\frac{a'F(1-aF)}{(1+a')(1-a)}$$

The induction factors can be written explicitly, viz.

$$a = \{2A + F - [F^2 + 4AF(1-F)]^{1/2}\} / 2(A+F)^2, \quad (4.4.34)$$

with

$$A = \sigma' C_1 \cos \theta / (4 \sin^2 \theta),$$

and

$$a' = \sigma' C_1 / (4F \cos \theta - \sigma' C_1). \quad (4.4.35)$$

When $F \rightarrow 1$, i.e. $B \rightarrow \infty$ or $r/R_0 \rightarrow 0$, the result of Sect. 4.4.2 is found again.

When $F \rightarrow 0$, i.e. $r/R_0 \rightarrow 1$, $C_1 \rightarrow 0$ (Eq. (4.4.33)) and the values for a and a' become indeterminate. The values at the tip ($r/R_0 = 1$) are not important, however, and can be omitted.

The formulae obtained are too complicated to permit an elimination of a and a' in order to get an explicit expression for $\sigma' C_1$ (cf. the Eqs (4.4.14) and (4.4.28)), and an iteration procedure is necessary for the calculation.

4.4.3.3 Higher-order correction

In the Refs 4.7 and 4.8, the average values of the induced velocities are applied directly into the momentum equations, which, strictly, is not correct. The variation of the induced velocities with azimuth angle ϕ (Fig. 4.15) has to be taken into account. In Ref. 4.6, however, the variation with ϕ is not explicitly shown, and it is hard to obtain it from the formulae given. Therefore, a sinusoidal variation between the rotor blades (and vortex sheets) is assumed (Fig. 4.15), viz.

$$(aU)f = (aU)F + (aU)(1-F) \cos B\phi, \quad (4.4.36)$$

$$(a'\Omega r)f = (a'\Omega r)F + (a'\Omega r)(1-F) \cos B\phi. \quad (4.4.37)$$

The same distribution has been assumed far downstream, but the maximum interference factors then are $2a$ and $2a'$.

When the axial momentum equation is applied to an elemental streamtube through the rotor (Fig. 4.15), and when the static pressure deficit in the wake far downstream is neglected, the contribution to the normal force is

$$d(dN) = r d\phi dr p 2afU(1-af)U = 2rd\phi dr p U^2 (af - a^2 f^2).$$

Integrating over ϕ leads to

$$dN = 4\pi r p U^2 (aF - a^2 F^*) dr, \quad (4.4.38)$$

with

$$F = \frac{1}{2\pi} \int_0^{2\pi} f d\phi, \quad (4.4.39)$$

and

$$F^* = \frac{1}{2\pi} \int_0^{2\pi} f^2 d\phi = F^2 + \frac{1}{2}(1-F)^2. \quad (4.4.40)$$

In a similar way, it can be found that

$$dT = 4\pi r^2 p \Omega U (a'F - a'^2 F^*) dr. \quad (4.4.41)$$

When $F \rightarrow 1$, i.e. $B \rightarrow \infty$ or $r/R_0 \rightarrow 0$, $F^* \rightarrow 1$ and the formulae of Ref. 4.3 are obtained.

When $F \rightarrow 0$, i.e. $r/R_0 \rightarrow 1$, $F^* \rightarrow \frac{1}{2}$, which expresses the fact that, when the average of the induced velocities is zero, the average of the squares of the induced velocities need not to be zero.

From the above equations, it follows that dN and dT become negative when the tip is approached. This seems physically unrealistic, but, as it is limited to values of r/R_0 very close to one, it could be accepted. It is an indication that, in spite of the apparently more accurate higher-order terms, some other effects have been neglected.

Effects possibly neglected in the calculation are the non-axisymmetrically distributed trailing vorticity and the pressure term in the linear momentum equation (cf. the discussion in Appendix C in case of an axisymmetric flow).

When the blade-element expression is equated to the momentum expressions, the following formulae are obtained

$$\frac{aF - a^2 F^*}{(1-a)^2} = \frac{\sigma' C_1 \cos \theta}{4 \sin^2 \theta}, \quad (4.4.42)$$

$$\frac{a'F - a'^2 F^*}{(1+a')(1-a)} = \frac{\sigma' C_1}{4 \cos \theta}. \quad (4.4.43)$$

The ratio of these two equations, together with Eq. (4.4.12), leads to

$$X = \frac{a}{a'} \tan \theta$$

which shows that the total induced velocity is perpendicular to the relative velocity at the blade element (cf. Sect. 4.4.2).

Solving "a" from Eq. (4.4.42) gives

$$a = (A + \frac{1}{2}F) / (A + F^*) - \frac{1}{2}[F^2 + 4A(F - F^*)]^{\frac{1}{2}} / (A + F^*) \quad (4.4.44)$$

with

$$A = \sigma' C_1 \cos \theta / (4 \sin^2 \theta) \quad .$$

When $F \rightarrow 0$, $F^* \rightarrow \frac{1}{2}$ and "A" has to be zero or negative, otherwise the square root becomes imaginary. This means that C_1 as well as "a" have to be zero or negative.

When the energy equation averaged over an annular streamtube is applied,

$$\int_{\phi=0}^{2\pi} (1 + a'f) \Omega r \, d(\phi) = \int_{\phi=0}^{2\pi} (1 - af) U \, d(\phi)$$

this yields

$$(a'F - a'AF^* + a'^2F^* - a'^2AF^{**})X^2 = aF - 2a^2F^* + a^3F^{**} \quad (4.4.45)$$

with

$$F^{**} = \frac{1}{2\pi} \int_0^{2\pi} f^3 d\phi = F^3 + \frac{3}{2}F(1-F)^2 \quad (4.4.46)$$

When $a' = a \tan \theta / X$ is substituted, this yields

$$a = \frac{F^*}{2F^{**}(1+C)} - \frac{1}{2F^{**}} [F^{*2}(1+C)^2 - 4FF^{**}C]^{\frac{1}{2}} \quad (4.4.47)$$

with

$$C = \cos \theta (\cos \theta - X \sin \theta) \quad .$$

When $F \rightarrow 0$, then $F^* \rightarrow \frac{1}{2}$, $F^{**} \rightarrow 0$ and Eq. (4.4.47) becomes indeterminate 0/0. C can be interpreted as the induction factor "a" for $F = 1$ (i.e. for $B = \infty$). Because the argument of the square root should not become negative, the possible range of F and C is limited. This limitation is not very important, because it is in the range $C > \frac{1}{2}$, which is also outside the range of applicability of the momentum equations (violation of continuity equation).

It seems possible to obtain solutions by putting Eq. (4.4.47) equal to Eq. (4.4.44), but the question remains whether these complicated calculations attain a better agreement with experiment than the linearized correction of Sect. 4.4.3.1.

4.4.4 Linearized vortex wake theory

Consider the wake behind a rotor with a finite number of blades. When the induced velocities are small with respect to the wind velocity, the helical vortex sheets move downstream with a velocity almost equal to the wind velocity. Therefore, the vortex sheets move downstream like a rigid body. Due to the small induced velocities, the wake expansion can also be neglected, which leads to a cylindrical wake.

Prandtl (Ref. 4.6) already made a simplified calculation, but Goldstein (Ref. 4.9) was the first who calculated the induced velocities from the rigid helical vortex sheets. However, these results were limited to the case of an optimum circulation distribution along the span of the blade. The optimum distribution was such, that it revealed a minimum rotational energy in the wake at a given axial force on the rotor (i.e. an optimum efficiency for an airplane propeller). Such an optimum distribution for an airplane at cruise condition need not to be identical with the distribution for a maximum energy output in case of a wind turbine.

In order to apply the calculations of Ref. 4.9 also to non-optimum conditions, the method of Lock and Yeatman (Ref. 4.10) could be used. The underlying assumptions are:

- The total induced velocity at radius r depends solely on the circulation at radius r.
- The total induced velocity is perpendicular to the relative velocity at the blade element.

The total induced velocity could be calculated from

$$w_t = \Gamma / 4\pi r k \sin \theta \quad (4.4.48)$$

with

Γ = total circulation of B blades at radius r;

k = numerical factor, calculated by Goldstein as a function of r/R_0 , $\sin \theta$ and B.

Because of the underlying assumptions and because of the identity of the Eqs (4.4.48) and (4.4.25), the equations of Sect. 4.4.3.1 can be used, when the factor F is replaced by k.

Because the Eqs (4.4.48) and (4.4.25) are identical, it is to be expected that the tip correction theory of Sect. 4.4.3.1 and the linearized vortex wake theory give similar results. Larger deviations would be possible, when the induced velocities would also be calculated for non-optimum circulation distributions.

It must be emphasized that the mutual independence of different blade elements along the span, when the theory of Lock and Yeatman is used, stems only from the (implicit) assumption of a definite shape for the circulation distribution.

When $B = \infty$, the flow is axisymmetric and the mutual independence of the blade elements can be proven (when the wake expansion is neglected). Because the condition $B = \infty$ is better approximated when λ increases, it is to be expected that the error due to the assumption of Lock and Yeatman will be moderate also with a non-optimum circulation distribution at high values of λ .

4.4.5 Extended numerical methods

It is possible to extend the existing calculation methods in various directions, but all these extensions consequently lead to a more complicated computer program than the relatively simple programs discussed so far.

Possible directions to extend the calculation method are:

1: From lifting line to lifting surface.

The above-discussed calculation methods assumed the bound vorticity to be concentrated at the $\frac{1}{2}$ -chord line, whereas the chordwise pressure distribution is assumed to be equal to that of a two-dimensional wing section. This could be extended by several lifting surface approximations, like those of Weissinger (Ref. 4.11) and Multhopp (Ref. 4.12), the acceleration potential method (e.g. Van Holten, Ref. 4.13), or even a modern panel method (e.g. Ref. 4.14).

2: From a cylindrical towards an expanding wake.

The only direct calculation of induced velocities known in the literature is that for a cylindrical rigid vortex wake with a given circulation distribution, belonging to an optimally operating airplane propeller at cruise conditions (Ref. 4.9). In Ref. 4.15 a cylindrical wake is applied, but the circulation is not given beforehand. The induced velocities are not given, therefore, a comparison with the results of Ref. 4.9 is not possible. The influence of the wake expansion is discussed in Appendix C for an axisymmetric wake, but could be investigated for a B-bladed rotor by a so-called "fixed-wake" method. This means, that the shape of the wake is a part of the input data of the computer program and does not follow from the calculations.

The ultimate goal would be the calculation with an expanding wake, the shape of which is determined by the calculation method, using an iteration procedure (cf. the analogous but less complicated problem for the wake of an aircraft wing, see e.g. Ref. 4.16). Such a method is outlined in Ref. 4.15, but the completion of the computer codes including all these features are still a long way ahead.

Because of a number of reasons, the "high- λ " wind turbine seems the most promising (cf. Sect. 2.4). This leads to rather small chord lengths (small solidity ratio σ') at the most effective parts of the rotor blade ($r/R_0 > 0.5$). Therefore, the extension of the calculation method in the direction of a lifting-surface theory does not seem to be urgent.

There are more doubts about the validity of the determination of the induced velocities (tip effects and wake expansion). Because the induced velocities determine the angle of attack α of the blade elements, which in turn very sensitively influences the local lift force on the blade, an extension in the direction of item 2 seems to be the most urgent.

A very readable review of the state-of-the-art of rotor aerodynamics is given in Ref. 4.17. The necessity to use these complicated calculation methods depends on the discrepancies between the results obtained by the more or less "simple" methods and the experimental results, which are, however, very scarce. Wind tunnel tests often are performed at such a low Reynolds number, that the appropriate aerodynamic data of the wing sections are missing, or the data are obtained from "field" or "free-air" measurements, which can hardly be compared with calculations because of wind-shear and atmospheric-turbulence effects which are not accounted for in the calculation methods.

When it is considered that, at the one hand, the computer codes containing an expanding vortex wake, finite chord-effects, etc., are very complex while, at the other hand the inhomogeneous and turbulent-flow effects are neglected, the question can be raised whether such complex computer codes really make sense. The implementation of inhomogeneous and turbulent-flow effects in the aerodynamic performance calculation still is an unsolved problem (cf. Sect. 5.1).

4.4.6 Aerodynamic optimization

In the case of a wind turbine, the aerodynamic optimization of a rotor means that the geometry of the rotor blades is varied in such a way that the power output C_p becomes a maximum.

For a turbine with an infinite number of blades, such an optimization has already been discussed in Sect. 4.4.2. In the case of a turbine with a finite number of blades, the optimum geometry cannot be given explicitly. In Ref. 4.8, the aerodynamic optimization of a wind turbine is briefly discussed, and a special part of that approach will be commented on below.

In Ref. 4.8, an aerodynamic efficiency for a ring element of a wind turbine is defined in analogy with an airplane propeller, viz.

$$\eta = \frac{\Omega dQ}{(1-a)U dN} = \frac{\text{power output of rotor}}{\text{work done by air through axial force } N}$$

It is then stated, that $\eta = \eta_{\max}$ is a necessary condition for an aerodynamically optimized design.

From the energy equation (cf. Appendix C, Sect. C.4)

$$dP = \Omega dQ = (1-a)U dN - a'\Omega dQ,$$

it follows for the above-defined efficiency, η , that

$$\eta = \frac{1}{1+a'}.$$

The highest possible η can be obtained by making a' as small as possible, i.e. by making Q as small as possible. This can be obtained by choosing Ω as high as possible at a fixed power output. This conclusion was also obtained for a rotor with an infinite number of blades (Sect. 4.4.2).

It must be noticed, that this conclusion is drawn from a theory that does not take the static pressure deficit in the wake into account (Appendix C). There are indications that the power loss due to wake rotation might be compensated largely by the influence of the static pressure deficit in the wake. At the other hand, a turbine with a low λ (slow-running turbine) shows a high solidity. It might be that the present tip-correction theories do not properly represent the strong mutual interference of the blades in

the case of a high-solidity rotor.

For a rotor with a given Ω (or λ), a' cannot be chosen independently and the use of η in an optimization procedure does not seem very worthwhile.

The simplest and most direct way to obtain an optimum value of C_p is to require an optimum value of $dC_p/d(r/R_0)$ at each spanwise location. This procedure is admissible when it is assumed that the blade elements are mutually independent.

The optimization has to be carried out for a fixed value of λ and a fixed number of blades B . The optimization results in an optimum value of θ and $(c/R_0)C_1$ at each spanwise station of the rotor blade. The actual shape of the rotor blade is not completely fixed, because C_1 depends on $\alpha = \theta - i$ and because a certain degree of freedom exists in the choice of the chord- and twist-distribution along the span.

In order to simplify the calculations, a fixed value of C_1/C_d is assumed during the optimization procedure.

The formulae for the optimization will be summed-up below for the different calculation methods, discussed in the Sections 4.4.3 and 4.4.4.

The formulae for the linearized tip correction and the linearized vortex wake are identical, using only k instead of F in the latter.

$$C_p = \frac{8}{\lambda^2} \int_{x_{hub}}^{\lambda} F \sin^2 \theta (\cos \theta - X \sin \theta) (\sin \theta + X \cos \theta) [1 - (C_d/C_1) \cot \theta] X^2 dX .$$

The condition for the optimum C_p is

$$(\theta)_{opt} \Rightarrow \text{MAX} \left[F \sin^2 \theta (\cos \theta - X \sin \theta) (\sin \theta + X \cos \theta) [1 - (C_d/C_1) \cot \theta] \right] ,$$

$$\lambda, X, C_d/C_1 = \text{const.}$$

and the corresponding lift-times-chord distribution

$$\left(\frac{c}{R_0} C_1 \right)_{opt} = \left[\frac{8\pi}{B} \frac{r}{R_0} F \sin \theta \frac{\cos \theta - X \sin \theta}{\sin \theta + X \cos \theta} \right]_{\theta=(\theta)_{opt}} .$$

In the theory of Wilson and Lissaman, the formulae are

$$C_p = \frac{8}{\lambda^2} \int_{x_{hub}}^{\lambda} aF(1-aF) [\text{tg} \theta - (C_d/C_1)] X^2 dX .$$

The condition for optimum C_p is

$$(\theta)_{opt} \Rightarrow \text{MAX} \left[aF(1-aF) [\text{tg} \theta - (C_d/C_1)] \right] ,$$

$$\lambda, X, C_d/C_1 = \text{const.}$$

with the additional formulae

$$X = \frac{a}{a-1} \frac{1-aF}{1-a} \text{tg} \theta ,$$

$$a = \{ 2A+F - [F^2 + 4AF(1-F)]^{1/2} \} / 2(A+F)^2 ,$$

$$a' = \sigma' C_1 / (4F \cos \theta - \sigma' C_1) ,$$

$$A = \sigma' C_1 \cos \theta / (4 \sin^2 \theta) .$$

Due to the complexity of the formulae, a double iteration cycle is necessary, which results in finding the values of $(\theta)_{opt}$ and $(\sigma' C_1)_{opt}$. From the latter can be obtained

$$\left(\frac{c}{R_0} C_1 \right)_{opt} = \frac{2\pi}{B} \frac{r}{R_0} (\sigma' C_1)_{opt} .$$

The formulae for the higher-order correction theory are

$$C_p = \frac{8}{\lambda^2} \int_{x_{hub}}^{\lambda} (aF - a^2 F^*) [\text{tg} \theta - (C_d/C_1)] X^2 dX .$$

The condition for optimum C_p is

$$(\theta)_{opt} \Rightarrow \text{MAX} \left[(aF - a^2 F^*) [\text{tg} \theta - (C_d/C_1)] \right] ,$$

$$\lambda, X, C_d/C_1 = \text{const.}$$

with the additional formulae

$$a = \frac{1}{2} \frac{F^*}{F^{**}} (1+C) - \frac{1}{2} \frac{1}{F^{**}} [F^{*2} (1+C)^2 - 4FF^*C]^{1/2} ,$$

$$C = \cos \theta (\cos \theta - X \sin \theta) ,$$

$$F^* = F^2 + \frac{1}{2} (1-F)^2 ,$$

$$F^{**} = F^3 + \frac{3}{2} F (1-F)^2 .$$

Despite its apparent complexity, only a single iteration cycle is necessary, which discloses the values of $(\theta)_{\text{opt}}$ and $(a)_{\text{opt}}$. From these values can be obtained that

$$\left[\frac{c}{R_0} C_l \right]_{\text{opt}} = \left[\frac{8\pi}{B} \frac{r}{R_0} \frac{\sin^2 \theta}{\cos \theta} \frac{aF - a^2 F^*}{(1-a)^2} \right]_{(a, \theta)_{\text{opt}}}$$

Figure 4.16 shows some typical results, obtained by the above optimization procedures. The influence of the different methods on the value of $(\theta)_{\text{opt}}$ is very small. The influence on $(cC_l/R_0)_{\text{opt}}$ is larger. The higher-order tip-correction theory leads to an increased chord and/or increased lift coefficient at the tip. It is, however, highly questionable whether this result is acceptable from an aerodynamic point of view. Especially the assumption of the mutual independence of the blade elements might be violated in the tip region, due to the radial displacement and "rolling-up" effects of the trailing vortex sheet.

The optimum shape is very close to the Glauert solution (Sect. 4.4.2) and leads to a rather impractical blade shape, viz. a strongly non-linear taper and a large blade twist, especially close to the blade root.

A more practical blade shape design requires a direct rather than an inverse method for a given blade geometry. This will be discussed in the next Section for the linearized tip-correction theory.

4.4.7 Calculation method for a given blade geometry

4.4.7.1 Description of the method

In these calculations it is assumed that the blade geometry $(c/R_0, i)$ is given, as well as the number of blades B , the tip-speed ratio λ and the aerodynamic profile data $C_l = f(\alpha)$ and $C_d = f(\alpha)$.

From Eq. (4.4.28) it follows that $C_l = f(\theta)$, viz.:

$$C_l = \frac{8\pi r/R_0}{8c/R_0} F \sin \theta \frac{\cos \theta - \lambda \sin \theta}{\sin \theta + \lambda \cos \theta}, \quad (4.4.49)$$

with

$$F = \frac{2}{\pi} \arccos [\exp - (B/2)(1 - r/R_0)/\{(r/R_0) \sin \theta\}]$$

From the aerodynamic data it follows that

$$C_l = f(\alpha) = f(\theta - i) \quad (4.4.50)$$

The intersection of both curves in the C_l -vs- θ plane gives the operating point of the blade element under consideration (see Fig. 4.17). There are some difficulties, which will be discussed below.

Generally, there is more than one point of intersection between the curves of the Eqs (4.4.49) and (4.4.50).

An intersection with the dashed part of the curves in Fig. 4.17 means that the induction factor $a > \frac{1}{2}$. Consequently this solution has to be omitted (see discussion in Sect. 4.4.2).

The lift curve might intersect the full line part of the curve ($a < \frac{1}{2}$) twice (or even three times), when the curves intersect in the stalling region. Though all the solutions are possible, the unstalled solution will be preferred.

It is also possible that no solution can be found, i.e. the curve of Eq. (4.4.49) remains below the curve of Eq. (4.4.50). This operating region is often designated as the "turbulent-wake" state, and is beyond the scope of the calculation methods discussed above.

Figure 4.17 also shows that this turbulent-wake state is most easily reached with negative values of the setting angle i , whereas large positive setting angles might lead to negative values of C_l , which means a thrust or "propeller" state.

When the operating points (i.e. C_l , θ , and, thus, C_d) have been obtained along the entire blade span, the power coefficient C_p can be obtained from Eq. (4.4.29). The aerodynamic blade loading can also quite easily be obtained.

Some results calculated with the above-described method will be discussed below. These results might differ from results obtained with the other calculation methods, but the general conclusions obtained from one method will also apply to the results of a different method (see also Ref. 4.8 and the reports quoted there).

4.4.7.2 The ideal rotor shape

The optimization procedure (Sect. 4.4.6) results in a θ - and C_l -distribution along the blade span at a given value of λ and C_l/C_d . When a constant C_l (thus constant α) along the span is chosen ($(C_l)_{\text{design}}$), the corresponding c/R_0 and i can be obtained. Figure 4.18 shows a specific result for $B = 2$, $\lambda = 8$, and three values of $(C_l)_{\text{design}}$.

The blade terminates at $r_{\text{hub}}/R_0 = 0.10$ in this case. The blade shows a large non-linear taper and a large blade twist, especially close to the hub.

Figure 4.19 shows the influence of the choice of the design lift coefficient on the C_p -vs- λ curve. A low value of the design lift coefficient leads to a broader operating range of λ , mainly caused by the

larger available α -range from optimum towards stall.

The decrease of $(C_p)_{opt}$ is mainly due to the decrease of C_l/C_d at the chosen value of the design lift coefficient. Also the λ at which the optimum is obtained changes by this effect.

Though the design lift coefficient has to be chosen equal to the C_l value at which C_l/C_d attains its maximum, in order to obtain an optimum C_p , there may be structural, operational and cost considerations for choosing a different value. These considerations are, however, out of the scope of this work.

The value of $r_{hub}/R_0 = 0.10$ is chosen rather arbitrarily. From a structural and costs point of view, it might be favourable to increase r_{hub}/R_0 , because the largest part of the blade area and also the largest part of the blade twist variation is concentrated near the hub (see Fig. 4.18). Figure 4.20 gives an impression of the power loss due to increasing r_{hub}/R_0 , which, of course, has to be balanced against blade-cost reduction.

The shaft between blade hub and rotor axis only produces drag, which means an additional power loss. Figure 4.21 gives an estimation of the power loss. It shows that below $r_{hub}/R_0 \approx 0.30$ the additional power losses are insignificant.

The shape of the C_p -vs- λ curve is also affected by the profile characteristics of the aerofoil section chosen. Figure 4.22 shows the influence of the aerofoil data, characterized by the maximum lift coefficient $((C_l)_{max})$ and the minimum profile drag $((C_d)_{min})$. At a fixed value of the design lift coefficient, the maximum lift coefficient determines mainly the value of λ at which the blade stalls, whereas the minimum drag coefficient mainly affects the optimum value of C_p .

4.4.7.3 More practical blade shapes

The aerodynamically optimized blade shape (Sect. 4.4.7.2) is a very complicated one to produce. Therefore, the complexity of the shape has to be reduced as far as possible, considering the power-loss penalties involved.

In this Section, results of calculations will be given for rotor blades with NACA 23012 aerofoil sections $(C_l)_{max} \approx 1.79$, $(C_d)_{min} \approx 0.0060$, $(C_l/C_d)_{max} \approx 125$. A first simplification is to reduce the non-linear taper to a linear chord distribution along the blade span. The twist distribution is given by a power law (see Fig. 4.23) which approximates the optimum twist distribution rather closely, except near the hub, where the twist is somewhat reduced.

Figure 4.24 gives the C_p -vs- λ curves for a two-bladed rotor with twisted blades and linear taper for a number of different pitch angles θ_p (for the definition of θ_p , see Fig. 4.24). The optimum value of C_p does not differ significantly from the value for the ideal blade shape. It must be remembered, however, that for the ideal blade $(C_l/C_d)_{max} = 100$ instead of 125 in the present case. This means that avoidance of the sudden chord increase near the hub and a slight reduction of the twist results in only a small power loss.

Figure 4.25 shows the angle-of-attack distribution along the blade span as a function of the tip-speed ratio λ . For the sake of comparison, the α -distribution of the "ideal" shape is also given. Due to the twist reduction near the hub, the spanwise α -variation is much stronger along that part of the blade span. The chord reduction amplifies this trend. The power losses at the optimum are mainly caused by deviations from the optimum C_l/C_d -value along a part of the blade span.

A further simplification of the blade shape consists of omitting the twist altogether. The figures 4.26 through 4.28 show the C_p -vs- λ curves for untwisted blades with different taper ratios but a constant total rotor solidity (σ) . It also has to be noticed, that r_{hub}/R_0 is taken equal to 0.20 in this case, to avoid that a part of the blade stalls early and in that way deteriorates the turbine performance.

Compared with the twisted blade design of Fig. 4.24, the optimum C_p is only reduced with 6 %, but the reduction is stronger for the non-optimum values of C_p .

A remarkable fact revealed from these figures is the rather favourable performance of the constant-chord design, which is in itself the ultimate goal of simplicity. The main cause of the power loss can be discerned from Fig. 4.29. The very strong α -variation along the blade span at all values of λ causes at each λ a deviation from the optimum C_l/C_d and a premature blade stall near the hub, even at rather high tip-speed ratios like $\lambda = 8$.

When the main purpose is the design of a cheap wind turbine, an untwisted rotor blade with a constant chord seems to be a good choice, with only limited power losses. This rather favourable behaviour is only obtained at sufficient high Reynolds numbers (about 3×10^6), where α_{max} is sufficiently high. For a small-scale turbine, the untwisted rotor blade might behave badly, due to the premature stall, aggravated by the low Reynolds number (low α_{max}).

4.4.8 Concluding remarks

The calculation methods commonly used for a horizontal-axis wind turbine are based on a blade-element theory (blade chord negligible with respect to blade span), where the induced velocities are determined from momentum considerations combined with a tip correction factor (finite number of blades) or from a linearized vortex-wake calculation, which can be shown to be almost identical with the momentum theory including a tip correction.

A basic assumption underlying all blade-element theories is the mutual independence of different blade elements along the span. This independence exists only in case of a rotor with an infinite number of blades and a non-expanding (cylindrical) wake. It is difficult, however, to estimate the influence of the wake expansion and of the finite number of blades.

It is shown in Appendix C that, in the case of a rotor with an infinite number of blades, when wake expansion and static pressure deficit in the wake (due to wake rotation) are taken into account, the

so-called power loss due to wake rotation is almost compensated. This power loss due to wake rotation was the main improvement by Glauert (Ref. 4.3) of the simple estimation by Betz (Ref. 4.18). The present considerations show, however, that this improvement is at least questionable (see App. C). As far as experiments indicate unfavourable power coefficients for a low- λ high-Q (high-solidity) turbine, this might be caused by mutual blade interference (cascade effect), which becomes significant at a high-solidity turbine and is neglected in the blade-element theories considered.

Apparently the best available estimate of the induced velocities in the case of a finite number of rotor blades is given by a linearized vortex wake calculation (Goldstein, Lock and Yeatman, Refs 4.9 and 4.10). The calculation is based, however, on a specific shape of the spanwise circulation distribution, which corresponds to the optimum distribution for an aircraft propeller in cruise condition (i.e. high thrust, low torque). When the actual circulation distribution for a wind turbine differs from this optimum propeller distribution, differences in the induced velocities can be expected.

Figure 4.30 shows the difference in circulation distribution between an optimally operating propeller and a wind turbine at a comparable tip-speed ratio (or advance ratio in case of a propeller). At three spanwise stations, the implicitly used circulation distributions to calculate the induced velocities have been indicated, by scaling the propeller-distribution up and down. The deviations between the circulation distribution of the wind turbine and the corresponding circulation distributions of Goldstein are large. Moreover, the wake expansion is also neglected.

Estimating the induced velocities from momentum considerations with a tip correction factor lead to almost identical results. "Improvements" of the theory by using "higher-order" tip corrections are highly questionable. The only way to improve the calculation method seems to be the application of vortex-wake calculations, either a fixed-wake or a more complicated deformable-wake calculation (iterative procedure) and inclusion of the influence of a finite blade chord (lifting-surface theory instead of lifting-line theory), especially close to the hub.

Although there are enough theoretical indications that the blade-element theory needs further refinement, lack of reliable experimental data makes it still difficult to decide whether more elaborate vortex wake calculations have to be performed.

With the existing blade-element theories, a rotor blade can be designed which produces an optimum C_p at a given value of the tip-speed ratio λ .

A first condition to reach $(C_p)_{opt}$ is to choose the lift/drag ratio equal to $(C_l/C_d)_{max}$ of the profile considered and to keep it constant along the entire blade span, i.e. the corresponding C_l and, thus, also the corresponding α has to be taken constant along the blade span. $(C_l/C_d)_{max}$ has to be at least equal to or larger than 100 (at $\lambda \approx 8$), but a further increase, by choosing more sophisticated aerofoil sections, results in only a slight further increase of C_p .

A second condition is that both a strongly varying blade chord length along the span and a strongly varying blade twist are accepted, which leads to a very complicated rotor blade.

It is possible to approach the optimum very closely by taking a linearly tapered blade, but with still a strongly varying blade twist.

Introduction of a rotor blade without twist results in a power loss penalty of about 6 to 10 % (at the higher Reynolds numbers, i.e. for relatively large-scale turbines). This might be acceptable for a single production unit (reduction of tooling costs), but loses its attraction in case of mass production.

Choosing an untwisted blade design, the constant-chord (untapered -) blade, seems rather attractive, because the blade area in the hub region is reduced, where the blade stall starts at relatively high values of λ .

The blade-element theory predicts an increased power output when very high values of the tip-speed ratio λ are chosen, i.e. a very low solidity ratio, because:

- The power loss due to the tip-correction factor decreases with increasing λ .
- The power loss due to wake rotation decreases with increasing λ .

This tendency is opposed to the power loss due to the profile drag, which increases with λ . Sophisticated aerofoil sections have to be applied in that case to attain very high values of $(C_l/C_d)_{max}$.

Because the power loss due to wake rotation is questionable, but is anyhow very small at $\lambda > 10$, the predicted preference for a low-solidity high- λ turbine depends strongly on the accuracy of the tip correction factor applied.

More elaborate computer codes, including the effects of relaxed vortex wakes, rolled-up tip vortices (instability of vortex sheets) and lifting-surface theories (finite blade-chord effects) are being developed (Ref. 4.15), but the completion is still a long way ahead.

Considering the possibly large effects of flow inhomogeneity and turbulence (unsteadiness) of the atmospheric boundary layer on the wind-turbine performance, the usefulness of such complicated computer codes may be questioned.

4.5 Vertical-axis turbines

4.5.1 General remarks

An important aerodynamic difference between vertical-axis and horizontal-axis turbines is the appearance of unsteady flow phenomena. During a revolution of the rotor of a vertical-axis turbine in a steady wind stream, the flow direction and velocity relative to an element of the rotor blade vary in a cyclic way, whereas, in the case of a horizontal-axis turbine, the flow relative to a blade element is steady.

Even more drastic for the set-up of a calculation method for a vertical-axis turbine is the impossibility to relate the torque of the rotor to the change in angular momentum of the flow, even in time-averaged sense (see remark Appendix B). Momentum considerations, therefore, only deal with the induced velocity components in the direction of the undisturbed wind velocity.

For the same reasons as given for the horizontal-axis turbines, the theoretical discussion will be limited to low-solidity rotors. A typical high-solidity vertical-axis turbine is the Savonius rotor (for an extensive experimental survey of this type of turbine one is referred to Ref. 4.19.) The optimum values of C_p are restricted to ≈ 0.16 , but its main feature is its high starting torque, almost linearly decreasing with increasing λ . Ref. 4.19 includes an extensive list of references on the subject.

The discussion of a drum-type high-solidity turbine in Ref. 4.20 is interesting because of the attempt to apply angular-momentum considerations. Ref. 4.20 also gives some experimental results.

The principal features of the vertical-axis turbine will be elucidated by considering a two-dimensional rotor, i.e. an infinitely high turbine with a finite diameter.

Next, the three-dimensional vertical-axis turbine will be discussed with special emphasis on the Darrieus type. Especially for the Darrieus type of vertical-axis turbine, experimental data on power and torque coefficients are rather complete, which is in sharp contrast with the situation for horizontal-axis turbines.

4.5.2 Two-dimensional momentum theory

When an element of a rotor blade of a vertical-axis turbine rotates with an angular velocity Ω at a radius R and the wind velocity U is reduced to $(1-a)U$ by the induction factor a (cf. Sect. 4.4.2), which might be a function of the azimuth angle ϕ (when induced cross-flow velocities are neglected), the velocity relative to the blade element is (see Fig. 4.31)

$$U_{rel}^2 = (\Omega R + (1-a)U \sin \phi)^2 + \{(1-a)U \cos \phi\}^2,$$

which can be written as

$$U_{rel}/U = [\{\lambda + (1-a) \sin \phi\}^2 + \{(1-a) \cos \phi\}^2]^{1/2}. \quad (4.5.1)$$

Figure 4.32 shows the influence of the tip-speed ratio λ and a constant induction factor a on the relative velocity. At the higher tip-speed ratios, Eq. (4.5.1) can be approximated by

$$U_{rel}/U \approx \lambda + (1-a) \sin \phi. \quad (4.5.2)$$

When the chord of the blade element is perpendicular to the radius, the angle of attack of the blade element can be calculated from (see Fig. 4.31)

$$\alpha = \arctan \frac{(1-a) \cos \phi}{\lambda + (1-a) \sin \phi}. \quad (4.5.3)$$

At higher tip-speed ratios, this can be approximated by

$$\alpha \approx \frac{(1-a) \cos \phi}{\lambda}. \quad (4.5.4)$$

Figure 4.31 shows the influence of λ and a on the angle of attack. At low λ , there is a strong asymmetry of α with varying ϕ . This asymmetry reduces with increasing λ , but, even at $\lambda = 6$, a certain asymmetry is perceptible.

By analogy with the momentum theory for a horizontal-axis turbine, the force component on the blade element in the direction of the wind can be related to the change in momentum in wind direction. The usual assumption is made that the induced velocity far downstream is twice the induced velocity at the rotor, i.e. $(1-2a)U$.

A difference with the theory for a horizontal-axis turbine is, that " a " might be a function of ϕ . Another difference is the neglect of cross-flow-induced velocities which are analogous to the tangential-induced velocities at a horizontal-axis turbine.

The determination of the induction factor " a " is connected with the assumed functional dependence of " a " with the azimuth angle ϕ . The simplest approach stems from Templin (Ref. 4.21), which will be called the "single-streamtube" theory. In this approach, a is assumed to be independent of ϕ .

From the momentum equation, the force in wind direction D (per unit height) can be derived as

$$D = 2R \rho 2a(1-a)U^2.$$

From the forces on the blade elements of a B -bladed rotor, averaged during one revolution, it follows that

$$D = \frac{B}{2\pi} \int_0^{2\pi} \frac{1}{2} \rho U_{rel}^2 C_{l1} \cos(\phi + \alpha) d\phi,$$

in which $C_{l1} = f(\alpha) \approx C_{l1\alpha}$ at angles of attack below the stall. Here and in the sequel, it will be assumed that in the vertical-axis turbines symmetrical profiles are applied, unless stated otherwise.

The above equations result in

$$a(1-a) = \frac{1}{8} \frac{Bc}{R} \frac{1}{2\pi} \int_0^{2\pi} (U_{rel}/U)^2 C_{l1} \cos(\phi + \alpha) d\phi. \quad (4.5.5)$$

Because a is implicitly contained in U_{rel}/U and α , Eq. (4.5.5) cannot be solved directly, but an iteration procedure has to be applied. Ref. 4.21 shows a way out, by the introduction of the variable

$$y = \lambda/(1-a).$$

Then Eq. (4.5.5) becomes:

$$\frac{1}{1-a} = 1 + \frac{1}{8} \frac{Bc}{R} \frac{1}{2\pi} \int_0^{2\pi} \{ (y + \sin \phi)^2 + \cos^2 \phi \} C_l \cos \left\{ \phi + \arctan \left[\frac{\cos \phi}{y + \sin \phi} \right] \right\} d\phi \quad (4.5.6)$$

For a given geometry of the turbine (Bc/R) and a given value of y , the value of $(1-a)$ can be calculated. From that, the corresponding tip-speed ratio can be calculated, viz.

$$\lambda = y(1-a)$$

The generated power is calculated from the tangential force, T , in which the profile drag is included (cf. Sect. 4.2.2); thus

$$P = \Omega R \frac{B}{2\pi} \int_0^{2\pi} \frac{1}{2} \rho U_{rel}^2 c (C_l \sin \alpha - C_d \cos \alpha) d\phi,$$

or the corresponding power coefficient

$$C_p = P / \frac{1}{2} \rho U^3 2R = (1/4\pi) (Bc/R) \lambda \int_0^{2\pi} (U_{rel}/U)^2 C_l \sin \alpha [1 - (C_d/C_l) \cot \alpha] d\phi \quad (4.5.7)$$

These formulae are still so complicated, that a numerical solution has to be chosen. To get some insight into the behavior, a strongly approximated solution will be given. Assume:

$$\lambda \gg 1,$$

$$C_l \approx C_{l\alpha},$$

$$\alpha \approx \frac{(1-a)}{\lambda} \cos \phi \ll 1,$$

$$\cos(\phi + \alpha) \approx \cos \phi.$$

Applying this to Eq. (4.5.6) gives the following result

$$\frac{1}{1-a} = 1 + \frac{1}{16} \frac{Bc}{R} C_{l\alpha} \left(y + \frac{1}{y} \right) \approx 1 + \frac{1}{16} \frac{Bc}{R} C_{l\alpha} y,$$

which can also be written as

$$a = \frac{1}{16} \frac{Bc}{R} C_{l\alpha} \lambda \quad (3.5.8)$$

An approximate expression for the power coefficient can be obtained from Eq. (4.5.7) with

$$\sin \alpha \approx \alpha,$$

$$\cos \alpha \approx 1,$$

$$C_d \approx C_{d0}.$$

This leads to

$$C_p = \frac{1}{4} \frac{Bc}{R} C_{l\alpha} \frac{(1-a)^4}{\lambda} (y^2 + 1) - \frac{1}{2} \frac{Bc}{R} C_{d0} \lambda (1-a)^2 (y^2 + 1).$$

Because also $y \gg 1$, and with Eq. (4.5.8), this can be approximated by

$$C_p = 4a(1-a)^2 - \frac{1}{2} \frac{Bc}{R} C_{d0} \lambda^3 \quad (4.5.9)$$

When this result is compared with Eq. (3.2.6) and when it is reminded that $U_r/U = 1-a$, the above equation shows that a vertical-axis turbine also approaches the ideal power coefficient derived by Betz, when the profile drag is neglected and a constant induced velocity is assumed across the rotor. Notwithstanding the very crude approximations, which have been used to obtain the Eqs (4.5.8) and (4.5.9), some general insight can be obtained with these formulae.

Figure 4.33 shows the C_p -vs- λ variation with $C_{d0} = 0$ (dashed curves) for three values of the rotor solidity Bc/R . The optimum C_p is always equal to the Betz value $16/27$ ($a = 1/3$), but the value of λ at which this optimum is obtained is inversely proportional to the rotor solidity.

As discussed in Sect. 3.2.2, the simple momentum theory breaks down, when $a \geq 1/2$, which corresponds with $C_p = 0.5$ (if $C_{d0} = 0$). This limit is also indicated in Fig. 4.33.

The profile drag affects the C_p -vs- λ curves appreciably, especially at high λ , as could be expected from Eq. (4.5.9). When the profile drag is taken into account, the optimum C_p decreases with decreasing rotor solidity. The limit $a = 1/2$, which is connected with a certain value of $\lambda Bc/R$, shifts to lower values of C_p or even disappears from the operating range of the turbine at low rotor solidity.

The maximum angle of attack occurring during a revolution is also shown in Fig. 4.33, which can be estimated from

$$|\alpha_{\max}| = (1-a)/\lambda \quad (\text{radians})$$

The approximations used in the Eqs (4.5.8) and (4.5.9) are valid for small angles of attack, certainly smaller than the stalling angle, which is indicated in Fig. 4.33. Therefore, the calculated C_p -vs- λ curves have also a low- λ bound, which is also indicated. This shows that, at a high rotor solidity, the λ -range that can be calculated with this simplified theory is very narrow.

The values given in Fig. 4.33 must not be looked at too closely, because of the approximations applied. The general trends, however, will be similar to those obtained with the complete Eqs (4.5.1), (4.5.3), (4.5.5) and (4.5.7). The main advantage of the complete equations, besides a higher accuracy, is the possibility to extend the calculations into the stalled region, when the full profile data are included. The $a = 1/2$ limit, however, remains.

Another approach, called the "multiple-streamtube" theory and proposed by Strickland (Ref. 4.22), assumes that the induction factor a varies in a direction perpendicular to U , but is constant in the direction of U (see Fig. 4.34).

The force in wind direction on the elemental streamtube (dD) can be related to the change in momentum in that elemental streamtube, thus

$$dD = R \cos \phi \, d\phi \, \rho \, 2a(1-a)U^2$$

Each blade element passes the elemental streamtube twice, viz. once downwind and once upwind. It follows from Eqs (4.5.1) and (4.5.3) that U_{rel} and $|u|$ are equal at ϕ and $(\pi-\phi)$, which means that dD is equal in both cases. The average force can then be calculated from blade element theory, viz.

$$dD = B \frac{2}{2\pi} \int_{\phi}^{\phi+d\phi} \frac{1}{2} \rho U_{rel}^2 C_{l_1} \cos(\phi+\alpha) d\phi$$

Combining both equations leads to

$$a(1-a) = (1/4\pi)(Bc/R)(U_{rel}/U)^2 C_{l_1} \cos(\phi+\alpha)/\cos \phi \quad (4.5.10)$$

The power coefficient C_p can be calculated with the same Eq. (4.5.7), but now the induction factor $a = a(\phi)$. The trick to solve Eq. (4.5.10) directly by substituting $y = \lambda/(1-a)$ and solving $(1-a)$ cannot be done, because y would vary across the rotor diameter. Therefore, Eq. (4.5.10) can only be solved by an iteration procedure.

Also in this case some insight can be obtained by an approximate solution, similar to the method leading to the Eqs (4.5.8) and (4.5.9). The result is

$$a \approx (1/4\pi)(Bc/R)C_{l_1 \alpha} \cos \phi (\lambda + 2 \sin \phi) / \left[1 + (1/4\pi)(Bc/R)C_{l_1 \alpha} \cos \phi 2 \sin \phi \right] = \\ \approx (1/4\pi)(Bc/R)C_{l_1 \alpha} \lambda \cos \phi \quad (4.5.11)$$

which is valid in the range $-\frac{\pi}{2} \leq \phi \leq +\frac{\pi}{2}$.

This approximation shows some resemblance with Eq. (4.5.8). It is also clear from this equation that $a = 0$ at $\phi = +90^\circ$ and -90° . Figure 4.35 shows the dependence of " a " from ϕ according to the multiple-streamtube theory. At low values of the rotor solidity and high values of λ , the variation is almost like $\cos \phi$, but, at higher solidity and lower λ , the variation becomes asymmetric. This asymmetry is also found experimentally (Ref. 4.23) and stems mainly from the asymmetry in U_{rel} (see Fig. 4.32).

Differences in the power coefficients between single- and multiple-streamtube theories can only be discerned by taking higher-order terms into account. This is caused by the smoothing effect of the integration during one revolution. The differences between the theories will, therefore, be more clearly demonstrated by calculating the blade loading, i.e. the product of α and U_{rel}^2 .

The Kaman Aerospace Corp. assumes a "bullet-shaped" velocity distribution across the rotor. The parameters needed to quantify the velocity distribution are determined from an over-all momentum balance. This assumption has a profound influence on the blade loading (Ref. 4.24), but the validity of this assumption has not been demonstrated.

So far, only the variation of the induction factor " a " in a direction perpendicular to the wind velocity has been considered. It is to be expected, however, that the induced velocity also varies in wind direction between the upwind and downwind blade positions, which results in larger angles of attack for the upwind blade position ($\phi = 180^\circ$) and lower angles of attack for the downwind blade position ($\phi = 0^\circ$).

Within the scope of momentum theory, it is not possible to calculate the streamwise variation of the induced velocity. The only possibility is to look for empirical information, which is not yet available. The streamwise velocity variation is connected with a downstream divergence of the streamlines (continuity equation), which implies velocity components perpendicular to the wind velocity.

The only way to overcome the above-mentioned problems in determining the induced velocities, is to calculate them from the shed vorticity in the wake downstream.

4.5.3 Two-dimensional vortex theory

In the case of a steadily rotating two-dimensional vertical-axis wind turbine, the circulation Γ around the blade varies with its azimuthal position. Due to this variation in time, vorticity is shed from the blade. By the combination of the rotational motion and the downstream transport velocity, a cycloidally shaped vortex sheet with varying vortex strength is formed (Fig. 4.36). The induced velocity components from this vortex sheet deforms this cycloidal shape. Therefore, an exact determination of the induced velocities and the corresponding shape of the vortex sheets is a very complex problem.

From Fig. 4.36, some remarks can be made, which prove useful in subsequent discussions of the vortex wake. Each time the rotor blade passes a certain azimuthal position (e.g. ϕ_1), the circulation varies from Γ_1 to $\Gamma_1 + [(d\Gamma/d\phi)\Delta\phi]_1$ and the amount of vorticity shed in the wake is $-[(d\Gamma/d\phi)\Delta\phi]_1$. These "patches" of shed vorticity are located downstream at the points of intersection between the streamline through the azimuthal position ϕ_1 and the corresponding parts of the vortex sheet. This streamline also coincides with the "upwind" azimuthal position ϕ_2 , where an amount of vorticity equal to $-[(d\Gamma/d\phi)\Delta\phi]_2$ is shed into the wake.

The vorticity distribution in the wake can, therefore, also be described as follows. On each streamline in the wake, a row of vortices is located. From each blade stems a double row of vortices, one from the upwind and one from the downwind blade position. In case of an infinite number of blades, the streamline consists of a continuous distribution of vorticity. This aspect has been elaborated by Holme (Ref. 4.25).

Ref. 4.25 describes the method extensively. Therefore, only an outline of the method will be given. When the circulation around one blade at orbital position ϕ is considered to be

$$\Gamma_b(\phi) = \frac{1}{2} C_l \alpha U_{rel} ,$$

the chord length can be expressed as a part of the rotor circumference $2\pi R$, using the solidity ratio $\sigma = Bc/R$, viz.

$$c = \frac{\sigma}{2\pi B} (2\pi R) .$$

Thus

$$\Gamma_b(\phi) = \frac{\sigma}{4\pi} C_l \alpha U_{rel} \left(\frac{2\pi R}{B} \right) .$$

In case of an infinite number of blades, there exists a continuous, but yet unknown distribution of bound vorticity on a circle with radius R , which can be defined by a vortex sheet density

$$\gamma_b(\phi) = \lim_{\substack{B \rightarrow \infty \\ c \rightarrow 0 \\ \sigma = \text{constant}}} \frac{\Gamma_b}{2\pi R/B} = \frac{\sigma}{4\pi} C_l \alpha U_{rel} . \quad (4.5.12a)$$

The streamlines in the wake are considered to be straight (non-expanding wake) and parallel to the undisturbed wind velocity. The strength of the vorticity on the part of the streamline inside the circle is constant and depends on the gradient of the bound vorticity at the upwind intersection between streamline and circle, whereas the strength of vorticity on the downstream part of the streamline outside the circle is also constant, but with a strength which depends on the sum of the gradients at the upwind and downwind intersections of the streamline with the circle.

The strength of vorticity on the streamline depends also on the transport velocity, which is assumed to be constant along the entire streamline, but depends also on the strength of the bound and shed vorticity.

From this bound and shed vorticity, the induced velocities at the bound vorticity (circle) can be calculated. After a linear relation between the local circulation and the local radial velocity has been derived, a set of linear algebraic equations is obtained, when a Fourier series for the bound vorticity distribution is assumed.

The determination of the average transport velocity, which determines the strength of the shed vorticity as well, is still a problem. In Ref. 4.25 two "hypotheses" are given, viz.:

- the transport velocity is equal to the mean velocity of the mass flow through the turbine, and
- the transport velocity is determined by considering the momentum and energy balance.

Application of the two hypotheses leads to a difference in tip-speed ratio λ of less than 0.5 %, and in Ref. 4.25 it is concluded that the first hypothesis, being the simplest to apply, can be adopted for future calculations.

Figure 4.38 shows the power coefficient as calculated by Holme. Comparing this with the power coefficient given in Fig. 4.33 reveals a large similarity, but there are slight differences. The optimum inviscid ($C_{d0} = 0$) power coefficient is slightly less (8 %) than the Betz optimum 16/27, which also has its effect on the values of C_p with $C_{d0} = 0.01$. The stall boundary of Fig. 4.37 also differs slightly, due to the larger angles of attack at the upwind blade positions.

Figure 4.39 shows a comparison of the results obtained with the single-streamtube theory and the multiple-streamtube theory with the results of Ref. 4.25 for inviscid flow ($C_{d0} = 0$). In case of the streamtube theories, the complete equations (not the approximated ones) have been applied.

Besides the power coefficient, also the rotor drag coefficient C_D and the mass flow coefficient C_m have been given. The last two are defined as

$$C_D = \frac{\text{force in wind direction}}{\frac{1}{2} \rho U^2 2R} ,$$

$$C_m = \frac{\text{mass flow through rotor area}}{\rho U 2R}$$

The differences in the average mass flow between the three methods is small. The differences in total rotor drag C_D and power coefficient C_p are larger.

The multiple-streamtube theory is closer to the vortex wake theory than the single-streamtube theory, especially for the power coefficient.

The greatest achievement of the vortex theory of Ref. 4.25 is the prediction of the variation in load between the upwind and the downwind blade positions. For a typical configuration, Ref. 4.25 shows, that the maximum normal force at the upwind position is 1.5 times the maximum at the downwind position. The maximum tangential load is in the upwind position even three times the maximum at the downwind position. The momentum (streamtube) theories predict maxima that have equal magnitudes at upstream and downstream positions.

The induced velocities calculated in Ref. 4.25 will be discussed somewhat further by considering a fixed bound-circulation distribution.

It follows from the simplified momentum considerations (see approximations preceding Eqs (4.5.8) and (4.5.9)), that a first-order approximation of the bound-circulation distribution is (see Eq. (4.5.12a))

$$\gamma_b \approx \frac{\sigma}{4\pi} C_l \frac{(1-a) \cos \phi}{\lambda} \{ 1 + (1-a) \sin \phi \} U$$

$$\approx \frac{\sigma}{4\pi} C_l (1-a) U \cos \phi = \gamma_0 \cos \phi . \quad (4.5.12b)$$

When the blades move from ϕ to $\phi+d\phi$, the shed vorticity is transported in wind direction over a distance

$$(1-a)U \frac{d\phi}{\Omega} = \frac{1-a}{\lambda} R d\phi ,$$

and covers a distance in y-direction of

$$dy = R \cos \phi d\phi .$$

The amount of shed vorticity can be expressed as (see Eq. (4.5.12b))

$$-\frac{d}{d\phi} (\gamma_0 \cos \phi R d\phi) d\phi = \gamma_0 \sin \phi R (d\phi)^2 .$$

The average shed rotation in the parallelogram is

$$\omega_s = \frac{\gamma_0 \sin \phi R (d\phi)^2}{[(1-a)/\lambda] R d\phi R \cos \phi d\phi} = \frac{\lambda}{1-a} \gamma_0 \frac{\sin \phi}{R \cos \phi} .$$

The shed vortex sheet strength can then be expressed as

$$\gamma_s = \omega_s R \cos \phi d\phi = \frac{\lambda}{1-a} \gamma_0 \sin \phi d\phi . \quad (4.5.13)$$

The induced velocities can now be calculated from Ref. 4.25. The bound vorticity induces only radial velocity components on the circle, equal to

$$v_R = \frac{1}{2} \gamma_0 \sin \phi ,$$

which leads to longitudinal and lateral components

$$u = v_R \cos \phi = \frac{1}{2} \gamma_0 \sin \phi \cos \phi , \quad (4.5.14)$$

$$v = v_R \sin \phi = \frac{1}{2} \gamma_0 \sin^2 \phi , \quad (4.5.15)$$

because of the symmetry about the wind direction, only azimuth-angles between 0 and π need to be considered. The shed vorticity induces longitudinal components on the circle equal to

$$\left. \begin{aligned} u &= -\frac{3}{2} \frac{\lambda}{1-a} \gamma_0 \cos \phi , & 0 \leq \phi \leq \frac{\pi}{2} \\ u &= +\frac{1}{2} \frac{\lambda}{1-a} \gamma_0 \cos \phi , & \frac{\pi}{2} \leq \phi \leq \pi \end{aligned} \right\} \quad (4.5.16)$$

and lateral components equal to

$$v = \frac{1}{2} \frac{\lambda}{1-a} \gamma_0 \sin \phi . \quad (4.5.17)$$

Taking the average u between the points ϕ and $\pi-\phi$, i.e.

$$u_{av} = -\frac{\lambda}{1-a} \gamma_0 \cos \phi , \quad 0 \leq \phi \leq \frac{\pi}{2}$$

it follows from Eq. (4.5.12b) that

$$u_{av}/U = -(\lambda/4\pi) C_l (Bc/R) \cos \phi . \quad (4.5.18)$$

This is equivalent to Eq. (4.5.11), obtained from the multiple-streamtube theory, and demonstrates that, in a first-order approximation, the multiple-streamtube theory comes close to the vortex theory of Ref. 4.25, as was also seen in Fig. 4.39.

At the higher values of λ for which the vortex theory of Ref. 4.25 is valid, it is clear from comparing the Eqs (4.5.14) and (4.5.15) with the Eqs (4.5.16) and (4.5.17), that the induced velocities due to the bound vorticity are small with respect to the induced velocities due to the shed vorticity. This vortex theory is valid for only a very large number of blades ($B \rightarrow \infty$) and it seems interesting to look for the influence of a finite number of blades. This is most easily done for the influence of the bound vorticity, when an azimuthal variation like $\cos \phi$ (see Fig. 4.40) is assumed, viz.

$$\Gamma_i = \Gamma_{i0} \cos \left(\phi + i \frac{2\pi}{B} \right) .$$

When

$$\Gamma_0 = B \Gamma_{i0} ,$$

the induced velocities at one blade by the remaining $(B-1)$ blades are

$$v_R = -(\Gamma_0/4\pi RB) \sum_{i=1}^{B-1} \left[\frac{\cos(i2\pi/B) \cotg(i2\pi/B)}{S_I} \cos \phi - \frac{2 \cos^2(i\pi/B)}{S_{II}} \sin \phi \right] ,$$

$$v_\phi = -(\Gamma_0/4\pi RB) \sum_{i=1}^{B-1} \left[\frac{\cos(i2\pi/B)}{S_{III}} \cos \phi - \frac{\sin(i2\pi/B)}{S_{IV}} \sin \phi \right] .$$

It can be shown that $S_I = S_{IV} = 0$, that $S_{III} = -(B-2)$, and that $S_{II} = -1$. The induced velocities are,

when $\gamma_0 = \Gamma_0/2\pi R$ is introduced for reasons of comparison,

$$v_R = \frac{1}{2} \gamma_0 \frac{B-2}{B} \sin \phi, \quad (4.5.19)$$

$$v_\phi = \frac{1}{2} \gamma_0 \frac{1}{B} \cos \phi, \quad (v_R = v_\phi = 0, \text{ if } B = 1) \quad (4.5.20)$$

In the limit $B \rightarrow \infty$, the results $v_R = \frac{1}{2} \gamma_0 \sin \phi$ and $v_\phi = 0$ of Ref. 4.25 are re-obtained.

From the above formulae, it is clear that, in case of a small number of blades, large deviations from the case $B \rightarrow \infty$ can occur. For instance, if $B = 2$, then $v_R = 0$ and $v_\phi = \frac{1}{2} \gamma_0 \cos \phi$, in contradiction with the case $B \rightarrow \infty$.

The influence of a finite number of blades on the induced velocities of the shed vorticity is more complicated and will not be investigated here.

Because the shed vorticity is discretized in the downstream direction by the finite number of blades, it is more or less natural to discretize the continuous vortex sheet also in the azimuthal direction. This leads to a fully numerical approach.

When a computer code is compiled for such a case, a logical extension is to vary the downstream transport velocity $(1-a)U$ with the azimuth angle. The solution of this problem necessitates an iteration procedure, but it is still much simpler than the calculation of a fully relaxed wake (i.e. taking wake expansion and thus flow retardation in the wake into account). Wilson et al. reported on such relaxed-wake calculations at the Third Wind Energy Workshop of September 1977 (Ref. 4.26). In Fig. 4.41 (Ref. 4.26) are compared the angle of attack variation calculated with the relaxed-wake analysis for a one-bladed rotor, the fixed-wake analysis of Holme ($B = \infty$), and the multiple-streamtube theory of Strickland for a common value of the solidity ratio $Bc/R = 0.2$ and for a tip-speed ratio $\lambda = 3.54$.

Though none of the methods leads to identical results, it is clear that both vortex methods indicate a different behaviour between the upstream and the downstream blade position, which could not be obtained from momentum considerations.

From this comparison, it is also clear that the difference in calculated power output will be less than the differences in calculated blade load variation during one revolution, because of the smoothing effect of the integration over one revolution, which is needed to obtain the power output.

Taking the finite number of blades into account has a special effect on the downwind blade positions ($210^\circ < \phi < 300^\circ$, notice the deviating definition of ϕ).

When $B = \infty$, $v_\phi = 0$ and $v_R \neq 0$, whereas with $B = 1$, $v_\phi = v_R = 0$. This large difference possibly is responsible for the differences in α between fixed-wake ($B = \infty$) and relaxed-wake ($B = 1$) results in the range $150^\circ < \phi < 210^\circ$, shown in Fig. 4.11.

Relaxed-wake calculations have also been pursued by Fannucci and Walters (Ref. 4.27) and Brulle et al. (Ref. 4.28).

4.5.4 Stream-curvature effects

Several authors have indicated the influence of the stream curvature due to the rotational motion and the finite blade chord (see e.g. Ref. 4.29).

In the preceding Sections, the lifting-line approximation was implicitly assumed, i.e. the chord length was assumed to be very small with respect to the radius R . When c/R is not very small, the velocity due to rotation (ΩR) is no longer parallel to the blade chord everywhere.

When the thickness distribution of the aerofoil section is neglected, the influence of the angle-of-attack variation along the chord on the lift and pitching moment can be estimated from thin-aerofoil theory (see e.g. Ref. 4.30), viz.:

$$C_l = 2\pi \bar{\alpha}, \text{ with } \bar{\alpha} = \frac{1}{2} (\alpha'_{50} + \alpha'_{100}), \quad (4.5.21)$$

and

$$C_{mo} = \frac{\pi}{16} (\alpha'_{00} + 2\alpha'_{50} - 3\alpha'_{100}), \quad (4.5.22)$$

where the subscripts at the angle of attack indicate the chordwise location at which the α is obtained (see Fig. 4.42).

From Fig. 4.42, it follows that the point of attachment of the profile (x_0) has a direct effect on the lift, but that the pitching moment is not affected by x_0 , viz.:

$$\bar{\alpha} = -(3/4 - x_0/c) c/R, \quad (4.5.23)$$

$$C_{mo} = (\pi/8) c/R. \quad (4.5.24)$$

Figure 4.43 shows that, for normally used values of $x_0/c = \frac{1}{4}$ or $\frac{1}{2}$, a negative effective angle of attack is induced by the stream curvature. This means a lift increase for the upwind blade positions and a lift decrease for the downwind blade positions. The pitching moment induced by the stream curvature is always tail-heavy.

Because the vortex-wake theories (Sect. 4.5.3, Fig. 4.41) also indicate larger (negative) angles of attack upwind and smaller (positive) angles of attack downwind, the stream curvature increases this effect, which is important for the blade loading.

The influence of the stream curvature on the power output, i.e. the influence on the tangential force T parallel to the blade chord c , is more difficult to estimate for an infinitely thin flat aerofoil.

It boils down to the determination of the finite suction force on the infinitely thin leading edge by an infinitely low pressure on the leading edge (see Ref. 4.31).

During a revolution of the rotor, the external angle of attack varies with the azimuth angle approximately as:

$$\alpha \approx \frac{1-a}{\lambda} \cos \phi ,$$

whereas the stream-curvature-induced angle of attack along the chord is constant during one revolution, viz.

$$\alpha' = - (x/c - x_0/c) c/R .$$

The resultant angle of attack can be described as the superposition of an antisymmetric angle of attack distribution α_1 with respect to $x/c = \frac{1}{2}$ (second normalized distribution of Birnbaum) and a constant angle of attack along the chord α_0 (first normalized distribution of Birnbaum). The tangential force coefficient C_t solely depends on α_0 (Refs 4.30, 4.31) and can be calculated from

$$C_t = 2\pi\alpha_0^2 = 2\pi [\alpha + (x_0/c - 1/2)c/R]^2 . \quad (4.5.25)$$

In this case, the total lift force is Eqs ((4.5.21) and (4.5.23)):

$$C_l = 2\pi(\alpha + \bar{\alpha}) = 2\pi [\alpha + (x_0/c - 3/4)c/R] , \quad (4.5.26)$$

and it is shown, that

$$C_t \neq C_l(\alpha + \bar{\alpha}) ,$$

in case of stream curvature. The tangential force coefficient averaged during one revolution is a measure for the power output. Using the approximation for α from Eq. (4.5.4), this average value is

$$\begin{aligned} \overline{C_t} &= \frac{2\pi}{2\pi} \int_{-\pi}^{+\pi} \left[\left[\frac{(1-a)}{\lambda} \right] \cos \phi + (x_0/c - 1/2)c/R \right]^2 d\phi \\ &= 2\pi \left[(1/2) \left\{ \left[\frac{(1-a)}{\lambda} \right]^2 + (x_0/c - 1/2)^2 (c/R)^2 \right\} \right] . \end{aligned}$$

The contribution of the streamline curvature to the average tangential force is always positive. This positive contribution to the power coefficient can be estimated for a B-bladed rotor from

$$\Delta C_p \approx B \Delta \overline{C_t} \frac{1}{2} \rho (\Omega R)^2 c \Omega R / \frac{1}{2} \rho U^3 2R = \frac{1}{2} \Delta \overline{C_t} (Bc/R) \lambda^3 ,$$

with

$$\Delta \overline{C_t} = 2\pi (x_0/c - 1/2)^2 (c/R)^2 .$$

This can also be written as

$$\Delta C_p = (\pi/B^2) (x_0/c - 1/2)^2 (Bc\lambda/R)^3 . \quad (4.5.27)$$

When the induction factor is taken from the approximate equation (4.5.8) (it should be remembered that $a = \frac{1}{2}$ may be regarded as a maximum value in practical operating conditions), the range of $Bc\lambda/R$ is

$$0 \leq Bc\lambda/R < 4/\pi .$$

Figure 4.44 shows the increase of the power coefficient due to stream curvature. For the commonly used values of x_0/c between $\frac{1}{4}$ and $\frac{1}{2}$, the influence is not large, although not negligible.

The increase of the negative angle of attack at the upwind blade positions initiates an early blade stall, but, it is difficult to assess whether these stream curvature effects are adversely affected by viscosity (boundary-layer effects).

Another remark is, that a possible improvement of the calculation methods by using lifting-surface theories (e.g. panel methods) necessitates a careful consideration of the leading-edge flow (i.e. a large number of panels at the leading edge). The above considerations implicitly contain the conclusion that a more accurate determination of the lift (blade loading) not always means a more accurate determination of the tangential force (power output).

4.5.5 Unsteady effects

As remarked in Sect. 4.5.1, the vertical-axis turbine shows a cyclic lift variation during a revolution. In the preceding sections, quasi-steady aerodynamics has been applied throughout. Because the so-called reduced frequency k is low for the commonly applied solidity ratios, viz.

$$k = \omega l_{ref}/U_{ref} \approx \Omega \frac{1}{2} c / \Omega R = \frac{1}{2} c / R , \quad (4.5.28)$$

the neglect of unsteady aerodynamic effects seems warranted. Ashley (Ref. 4.32), however, drew attention to the fact that the influence on the tangential force (suction peak) was larger than the influence on the lift itself.

The unsteady effects can be estimated by considering simplified rotor aerodynamics, viz. (see Sect. 4.5.2)

$$U_{rel} = \Omega R , \quad \alpha = \frac{1-a}{\lambda} \cos \phi \quad \text{and} \quad \phi = \Omega t .$$

This can be regarded as an airplane wing moving through the air with a velocity ΩR and subjected to a periodic gust of magnitude

$$v_g = \Omega R a = (1-a)U \cos \phi .$$

The largest simplification is the assumption that the wake trails downstream as a straight line, whereas in case of an actual turbine, the wake shows a more or less cycloidal shape. Also the mutual interference between the blades ($B \neq 1$) has been neglected. The quasi-steady wake effects are included to a first order

of magnitude in the induction factor "a". Therefore, the simplification is restricted to the unsteady effects of the wake.

Ref. 4.33 calculates the sinusoidal gust effect on the lift. The result is

$$C_l = \operatorname{Re} \left\{ \frac{\pi \rho c \Omega R (1-a) U e^{i\Omega t} \phi(k)}{\frac{1}{2} (\Omega R)^2 c} \right\} = 2\pi \frac{1-a}{\lambda} \operatorname{Re} \left\{ e^{i\Omega t} \phi(k) \right\},$$

with $\phi(k)$ the so-called Sears function:

$$\phi(k) = (J_0 - iJ_1)(F + iG) + iJ_1.$$

This leads to

$$C_l = 2\pi \frac{1-a}{\lambda} \left[(J_0 F + J_1 G) \cos \Omega t - (J_0 G - J_1 F + J_1) \sin \Omega t \right]. \quad (4.5.29)$$

In the quasi-steady case, the lift coefficient is

$$(C_l)_{qs} = 2\pi \frac{1-a}{\lambda} \cos \Omega t. \quad (4.5.30)$$

The tangential force coefficient has to be calculated from the suction force on the leading edge (cf. Sect. 4.5.4), which depends solely on the first normalized Birnbaum lift distribution. A careful analysis leads to (see also Eq. (4.5.25))

$$\alpha_0 = \frac{C_l}{2\pi} = \frac{1-a}{\lambda} \operatorname{Re} \left\{ e^{i\Omega t} \phi(k) \right\}$$

and thus

$$C_t = 2\pi \alpha_0^2 = 2\pi \left(\frac{1-a}{\lambda} \right)^2 \left[(J_0 F + J_1 G) \cos \Omega t - (J_0 G - J_1 F + J_1) \sin \Omega t \right]^2. \quad (4.5.31)$$

In the quasi-steady case, the tangential force coefficient is

$$(C_t)_{qs} = 2\pi \left(\frac{1-a}{\lambda} \right)^2 \cos^2 \Omega t. \quad (4.5.32)$$

The instantaneous angle of attack is

$$\frac{1-a}{\lambda} \cos \Omega t \quad \text{or} \quad \frac{1-a}{\lambda} e^{i\Omega t}.$$

This shows, that the common method to calculate C_t , viz.

$$C_t = C_l^2 \alpha = 2\pi \left(\frac{1-a}{\lambda} \right)^2 \operatorname{Re} \left\{ e^{i\Omega t} \phi(k) \right\} \operatorname{Re} \left\{ e^{i\Omega t} \right\},$$

leads to a result different from Eq. (4.5.31).

Figure 4.45 shows that the unsteadiness of the flow has a significant effect on the tangential force. The influence on the lift is smaller, but cannot be neglected. The power output is proportional to the tangential force coefficient averaged over one revolution, thus

$$\overline{C_t} = \frac{1}{2\pi} \int_{-\pi}^{+\pi} C_t d\phi = 2\pi \left(\frac{1-a}{\lambda} \right)^2 \left[(J_0 F + J_1 G)^2 + (J_0 G - J_1 F + J_1)^2 \right]. \quad (4.5.33)$$

In the quasi-steady case, the average value is

$$(\overline{C_t})_{qs} = 2\pi \left(\frac{1-a}{\lambda} \right)^2. \quad (4.5.34)$$

The ratio of the Eqs (4.5.33) and (4.5.34) is a measure for the decrease of the power output due to unsteady effects. The ratio of the Eqs (4.5.29) and (4.5.30), with $\Omega t = \phi = 0$, is a measure for the decrease of the lift amplitude due to unsteady effects. Both ratios have been given in Fig. 4.46 as a function of c/R .

Though the profile drag has not been taken into account, which might change the power ratio still further, it is clear from this figure that, for a commonly used value $c/R = 0.10$, the power is reduced by 16 % due to unsteady effects.

Ref. 4.32 gives a more complete discussion, which also includes the influence of the variation of the relative velocity U_{rel} during one revolution.

4.5.6 Two-dimensional vertical-axis rotor with variable pitch

An important difference between a vertical-axis and a horizontal-axis turbine is, that the blade element of a horizontal-axis turbine operates under the same (optimal) conditions during one revolution, whereas the blade element of a vertical-axis turbine cannot operate under optimal conditions during the entire revolution.

It is obvious that several investigators looked for means to improve the vertical-axis turbine in this respect by applying variable pitch (see e.g. the Giromill, Ref. 4.28). Apart from the greater structural complexity, the pitch control has to follow the wind direction, i.e. the turbine loses its independence from the wind direction.

The driving force of the turbine is the component of the aerodynamic force perpendicular to the radius. The main part of the aerodynamic force is the lift, which is perpendicular to U_{rel} . Therefore, the driving force component is governed by the angle between U_{rel} and the normal to the radius, which is

mainly determined by the wind velocity (only modified by the induced velocities) and changes sign at $\phi = +\pi/2$ and $-\pi/2$. In order to generate a positive driving force during the entire revolution, the lift force has to change sign in step with the sign of the angle between U_{rel} and the normal to the radius.

An idealized case of such a variable-pitch turbine is represented by a pitch distribution which keeps the lift constant during a revolution, only flipping from positive to negative lift at $\phi = +\pi/2$ and from negative to positive at $\phi = -\pi/2$, which necessitates an almost instantaneous jump in pitch angle at these values of ϕ .

In the case that $B \rightarrow \infty$, the bound vorticity can be represented by

$$\gamma_b = \gamma_0 \frac{\cos \phi}{|\cos \phi|}$$

The shed vorticity only leaves the circumference of the turbine at $\phi = +\pi/2$ and $\phi = -\pi/2$ and, when a constant transport velocity equal to $(1-a)U$ is assumed, it can be represented by

$$\gamma_s = 2 \frac{\lambda}{1-a} \gamma_0$$

Figure 4.47 shows the vortex system of such an idealized turbine.

The velocities on the circumference that are induced by the bound vorticity are symmetrical about $x = 0$ and $y = 0$ and can be calculated (Ref. 4.25) from

$$v_\phi(\phi) = -\frac{\gamma_0}{2\pi} \int_{-\pi}^{+\pi} \frac{\cos \theta}{|\cos \theta|} d\theta = 0, \quad (4.5.35)$$

$$\begin{aligned} v_R(\phi) &= -\frac{\gamma_0}{4\pi} \int_{-\pi}^{+\pi} \frac{\cos \theta}{|\cos \theta|} \cotg \frac{1}{2}(\theta - \phi) d\theta \\ &= -\frac{\gamma_0}{\pi} \ln \left[\frac{\cos \frac{\phi}{2} - \sin \frac{\phi}{2}}{\cos \frac{\phi}{2} + \sin \frac{\phi}{2}} \right]; \quad 0 \leq \phi \leq \frac{\pi} {2}. \end{aligned} \quad (4.5.36)$$

The velocities induced by the shed vorticity are

$$\begin{aligned} u(\phi) &= -\frac{2\lambda}{1-a} \frac{\gamma_0}{2\pi} \int_0^\infty \left[\frac{(1 - \sin \phi) d\frac{x}{R}}{(1 - \sin \phi)^2 + (\frac{x}{R} - \cos \phi)^2} + \frac{(1 + \sin \phi) d\frac{x}{R}}{(1 + \sin \phi)^2 + (\frac{x}{R} - \cos \phi)^2} \right] \\ &= -\frac{\lambda}{1-a} \frac{\gamma_0}{\pi} \left[\pi + \arctg \frac{\cos \phi}{1 - \sin \phi} + \arctg \frac{\cos \phi}{1 + \sin \phi} \right], \end{aligned} \quad (4.5.37)$$

$$\begin{aligned} v(\phi) &= \frac{2\lambda}{1-a} \frac{\gamma_0}{2\pi} \int_0^\infty \left[\frac{(\frac{x}{R} - \cos \phi) d\frac{x}{R}}{(1 - \sin \phi)^2 + (\frac{x}{R} - \cos \phi)^2} - \frac{(\frac{x}{R} - \cos \phi) d\frac{x}{R}}{(1 + \sin \phi)^2 + (\frac{x}{R} - \cos \phi)^2} \right] \\ &= -\frac{\lambda}{1-a} \frac{\gamma_0}{\pi} \ln \left[\frac{1 - \sin \phi}{1 + \sin \phi} \right]. \end{aligned} \quad (4.5.38)$$

The average axial velocity is

$$u_{av} = \frac{1}{2} [u(\phi) + u(\pi - \phi)] = -\frac{\lambda}{1-a} \gamma_0, \quad (4.5.39)$$

which turns out to be constant across the turbine. From Eq. (4.5.37), it can be shown that, when the lower boundary is extended from 0 to $-\infty$, far downstream in the wake

$$(u_{av})_\infty = -\frac{2\lambda}{1-a} \gamma_0, \quad (4.5.40)$$

which is the rather obvious solution for the velocity between two vortex sheets of constant strength and extending towards infinity in both directions.

Because $a = -u_{av}/U$, the value of the induction factor can be obtained from Eq. (4.5.39), viz.

$$a = \frac{1}{2} - \frac{1}{2} (1 - 4\lambda\gamma_0/U)^{\frac{1}{2}}. \quad (4.5.41)$$

Applying the energy equation (see e.g. Sect. 3.2.1) leads to the power coefficient

$$\begin{aligned} C_p &= 4a(1-a)^2 = 4 \left[\frac{1}{2} - \frac{1}{2} (1 - 4\lambda\gamma_0/U)^{\frac{1}{2}} \right] \left[\frac{1}{2} + \frac{1}{2} (1 - 4\lambda\gamma_0/U)^{\frac{1}{2}} \right]^2 \\ &= 2\lambda \frac{\gamma_0}{U} \left[1 + (1 - 4\lambda\gamma_0/U)^{\frac{1}{2}} \right]. \end{aligned} \quad (4.5.42)$$

The total radial velocity due to the wind velocity U and the induced velocities $v_R(\phi)$, $u(\phi)$ and $v(\phi)$ are calculated from

$$v_R = U \cos \phi + v_R(\phi) + u(\phi) \cos \phi + v(\phi) \sin \phi$$

From this, the tangential force can be calculated, viz.

$$dT = \rho \gamma_0 \frac{\cos \phi}{|\cos \phi|} v_R R d\phi,$$

and thus also the power coefficient:

$$C_P = \frac{\Omega R \int dT}{\frac{1}{2} \rho U^3 2R} = \lambda \frac{\gamma_0}{U} \int_{-\pi}^{+\pi} \frac{\cos \phi}{|\cos \phi|} \frac{v_R}{U} d\phi .$$

The result of the evaluation of the above integral is given below term by term

$$\int_{-\pi}^{+\pi} \frac{\cos^2 \phi}{|\cos \phi|} d\phi = 4 , \quad \int_{-\pi}^{+\pi} \frac{\cos \phi}{|\cos \phi|} \ln \left[\frac{\cos \frac{1}{2}\phi - \sin \frac{1}{2}\phi}{\cos \frac{1}{2}\phi + \sin \frac{1}{2}\phi} \right] d\phi = 0 ,$$

$$\int_{-\pi}^{+\pi} \frac{\cos^2 \phi}{|\cos \phi|} \pi d\phi = 4\pi ,$$

$$\int_{-\pi}^{+\pi} \frac{\cos^2 \phi}{|\cos \phi|} \left(\operatorname{arctg} \frac{\cos \phi}{1-\sin \phi} + \operatorname{arctg} \frac{\cos \phi}{1+\sin \phi} \right) d\phi = 0 ,$$

because the sum of the two arc tangents is

$$\frac{\pi \cos \phi}{2 |\cos \phi|} ,$$

and the last integral

$$\int_{-\pi}^{+\pi} \frac{\cos \phi}{|\cos \phi|} \ln \left(\frac{1-\sin \phi}{1+\sin \phi} \right) \sin \phi d\phi = 0 .$$

This leads to the result

$$C_P = \lambda \frac{\gamma_0}{U} \left(4 - 4 \frac{\lambda}{1-a} \frac{\gamma_0}{U} \right) = 4a(1-a)^2 , \quad (4.5.43)$$

because

$$a = \frac{\lambda}{1-a} \frac{\gamma_0}{U} \quad (\text{see Eq. (4.5.39)}),$$

which is identical to Eq. (4.5.42) deduced from the energy equation. When this is compared with the results of Ref. 4.25 at zero profile drag (see Fig. 4.39), which result is derived with comparable approximations, it can be shown that the variable-pitch rotor obtains only 8 % more power than the fixed-pitch rotor.

The main advantage of the variable-pitch turbine lays in the possibility to control the power output at constant angular velocity and varying wind speed. In that respect, the blade pitch variation needed to maintain constant lift during a revolution seems to be interesting and will be considered below.

When the angle between the relative velocity and the normal to the radius is denoted by δ and when it is assumed that $U_{rel} \approx \Omega R$, this angle can be estimated (Figs 4.47 and 4.48) from

$$\delta = \frac{v_R}{\Omega R} = \frac{\cos \phi}{\lambda} + \frac{v_R(\phi)}{\Omega R} + \frac{u(\phi)}{\Omega R} \cos \phi + \frac{v(\phi)}{\Omega R} \sin \phi . \quad (4.5.44)$$

The blade-pitch angle θ_p necessary to maintain a (constant) angle of attack α can be calculated from

$$\theta_p = \delta - \alpha \frac{\cos \phi}{|\cos \phi|} . \quad (4.5.45)$$

When it is assumed, as before, that $C_{l_\alpha} = 2\pi$, there is a relation between γ_0 and α , viz.

$$\gamma_0 = \frac{B\Gamma_b}{2\pi R} = \frac{B\frac{1}{2} 2\pi\alpha c \Omega R}{2\pi R} = \frac{1}{2} \left[\frac{Bc}{R} \right] \alpha \Omega R ,$$

thus

$$\alpha = 2\gamma_0 / [(Bc/R)\Omega R] . \quad (4.5.46)$$

By using also the expression $a = \lambda(\gamma_0/U)/(1-a)$, this leads to the following result

$$\begin{aligned} \theta_p = & \frac{\cos \phi}{\lambda} - \frac{a(1-a)}{\pi \lambda^2} \ln \left[\frac{\cos \frac{1}{2}\phi - \sin \frac{1}{2}\phi}{\cos \frac{1}{2}\phi + \sin \frac{1}{2}\phi} \right] - \frac{a}{\pi \lambda} \left[\left[\pi + \frac{\pi \cos \phi}{2 |\cos \phi|} \right] \cos \phi + \right. \\ & \left. + \sin \phi \ln \left[\frac{1-\sin \phi}{1+\sin \phi} \right] \right] - \frac{2a(1-a)}{(Bc/R)\lambda^2} \frac{\cos \phi}{|\cos \phi|} . \end{aligned} \quad (4.5.47)$$

Notice, that the second term at the right-hand side can only be evaluated in the range $0 \leq \phi \leq \pi/2$ (Eq. (4.5.36)), but that $v_R(\phi)$ is symmetrical about $x = 0$ and $y = 0$.

Figure 4.49 shows some calculated results. Notwithstanding the crude approximations used, the calculations show the possibility of operating the turbine at optimum C_P ($a = 1/3$) at constant angular velocity and variable wind speed (i.e. variable λ). The strong blade-pitch variation in the range $80^\circ < \phi < 110^\circ$ are mainly due to the velocities induced by the shed vorticity.

The above calculations are too crude to permit an actual performance estimation. Such an estimation has to include a more refined method for the calculation of the induced velocities, and has also to include viscous effects (profile drag and blade stall). Ref. 4.28 is referred to for some results of such an elaborate calculation.

Finally, still the question remains whether it is worthwhile to increase the power output at constant angular velocity by installing such an intricate blade pitch device.

4.5.7 Three-dimensional turbines

4.5.7.1 Straight or curved blades

The choice between straight or curved blades (troposkien) is mainly determined by structural considerations. This was already discussed in Sect. 2.4.2 and results of some simplified calculations have been given in Fig. 2.6. The conclusion reached with these considerations was that the straight-bladed turbine can only be applied in the case of lower angular velocities (thus lower λ), contrary to a turbine with curved blades.

The choice of the blade shape has also influence on the calculation method. In case of a straight-bladed turbine, two-dimensional theory (Sect. 4.5.2 and 4.5.3) can be used with only a slight modification, viz. including a finite-wing theory to account for "tip-loss" effects. Though this is a simplified approach, leaving the curvature of the trailing vortex sheets out of consideration, it may be workable in view of other intricate aspects, which are usually omitted, like stream curvature (Sect. 4.5.4) and unsteady aerodynamics (Sect. 4.5.5).

In case of a turbine with curved blades (Darrieus turbine), the deviation from two-dimensional theory will be still larger. Up till now, momentum theories (single- or multiple-streamtube theories) are the only successfully applied performance prediction methods (Refs 4.21 and 4.22). Vortex theories become very complicated in case of curved blades and, because of the magnitude of stream curvature and of unsteady effects, the application of a three-dimensional vortex theory only makes sense when curvature and unsteady effects are included.

Theoretically, the Darrieus turbine has a somewhat smaller power coefficient than the straight-bladed turbine. Moreover, with a given height and diameter, the reference area of a Darrieus turbine is about 0.65 times the reference area of a straight-bladed design (slightly depending on the height/diameter ratio). This means, that a straight-bladed turbine has a 1.5 times larger power output than a Darrieus turbine with the same height and diameter. A straight-bladed design can be applied with a blade-pitch control, which is almost impossible in case of a Darrieus turbine.

In the next Sections, the discussions will be restricted to the Darrieus turbine. The performance prediction models of Templin (Ref. 4.21) and Strickland (Ref. 4.22) are chosen more or less arbitrarily for the next discussion; similar models have been formulated by other investigators, see e.g. the Refs 4.7, 4.34, 4.35 and 4.36.

4.5.7.2 Momentum theories

The basic ideas are similar to those given in Sect. 4.5.2. Because of the blade curvature, different blade elements are oriented differently in space, which affects the magnitude of the relative velocity and angle of attack of the blade elements. The blade curvature also causes the distance from blade element towards the axis to be different from element to element. It is assumed, that only the velocity components normal to the leading edge of the blade element affects the aerodynamic force; the velocity components parallel to the leading edge have no effect. The equations for U_{rel} and α can be derived as follows (see Fig. 4.50).

The local wind velocity at the blade element, $(1-a)U$, can be decomposed into a radial and a tangential component, viz.

$$(1-a)U \cos \phi \quad \text{and} \quad (1-a)U \sin \phi .$$

The tangential component adds to the velocity due to rotation Ωr , which leads to a resultant tangential velocity

$$U_{tan} = \Omega r + (1-a)U \sin \phi . \quad (4.5.48)$$

Of the radial component, only the component normal to the blade element affects the aerodynamic force (Fig. 4.50), thus

$$U_n = (1-a)U \cos \phi \sin \gamma . \quad (4.5.49)$$

This leads to the following equations for U_{rel} and α

$$U_{rel} = [\Omega r + (1-a)U \sin \phi]^2 + [(1-a)U \cos \phi \sin \gamma]^2]^{\frac{1}{2}} ,$$

or

$$U_{rel}/U = [\lambda r/R_0 + (1-a) \sin \phi]^2 + [(1-a) \cos \phi \sin \gamma]^2]^{\frac{1}{2}} , \quad (4.5.50)$$

$$\alpha = \arctg \frac{(1-a) \cos \phi \sin \gamma}{\lambda r/R_0 + (1-a) \sin \phi} , \quad \text{where } \lambda = \Omega R_0/U . \quad (4.5.51)$$

For the case $r/R_0 = 1$ and $\gamma = 90^\circ$ (equatorial plane), the above equations reduce to the Eqs (4.5.1) and (4.5.3).

The troposkien might be approximated by a parabola (Ref. 4.21), thus

$$r/R_0 = 1 - (z/\eta R_0)^2 ,$$

with:

$$\eta = \frac{\text{rotor height}}{\text{diameter}} = \frac{H}{2R_0} ,$$

and with the angle between normal and vertical (γ)

$$\gamma = \frac{\pi}{2} - \arctg [(2/\eta)(z/\eta R_0)] .$$

With the above formulae, the Eqs (4.5.50) and (4.5.51) can be used to gain insight into the influence of the blade curvature on the distribution along the blade span of angle of attack and relative velocity. For $\lambda = 3$ and a constant induction factor $a = 1/3$, these distributions are shown in Fig. 4.51 for some azimuth angles.

The relative velocity is mainly affected by the reduction of the circumferential velocity when r/R_0 decreases (increasing z).

The angle of attack is nearly constant along a large part of the blade span. Blade elements close to the axis, however, show large angles of attack, which leads to blade stall. Due to the small radial distance of these elements, the effect on the power output will be small.

The induction factor "a" has to be calculated from the "drag" force in wind direction D , caused by the lift forces on the blades. Refs 4.21 and 4.22 include also the profile drag forces, but this is not strictly correct (cf. the discussion for the horizontal-axis turbine in Sect. 4.4.2). However, because C_d is always positive, the influence on D is almost cancelled during a revolution.

The drag force calculated from blade element theory is

$$D = \frac{1}{2} \rho U^2 R_0^2 \left(\frac{Bc}{R_0} \right) \int_{-\eta}^{+\eta} \frac{d(z/R_0)}{\sin \gamma} \frac{1}{2\pi} \int_{-\pi}^{+\pi} \left(\frac{U_{rel}}{U} \right)^2 C_l (\cos \alpha \cos \phi \sin \gamma - \sin \alpha \sin \phi) d\phi . \quad (4.5.52)$$

The momentum theory gives

$$D = \frac{1}{2} \rho U^2 R_0^2 \int_{-\eta}^{+\eta} d(z/R_0) \int_{-r/R_0}^{+r/R_0} 4a(1-a) d(y/R_0) , \quad (4.5.53)$$

with y = coordinate perpendicular to U and z .

In case of the single-streamtube theory of Ref. 4.21, Eq. (4.5.53) reduces to

$$D = \frac{1}{2} \rho U^2 S_{ref} 4a(1-a) .$$

When a fixed value of $\lambda/(1-a)$ is assumed, Eq. (4.5.52) can be evaluated directly (see Eqs (4.5.50) and (4.5.51)). Combining the Eqs (4.5.52) and (4.5.53) results in

$$a(1-a) = (1-a)^2 F\left(\frac{\lambda}{1-a}\right) \quad \text{or} \quad \frac{1}{1-a} = 1 + F\left(\frac{\lambda}{1-a}\right) ,$$

from which $(1-a)$ may be calculated. This determines the value of λ (cf. Eq. (4.5.6) for the two-dimensional case).

In case of the multiple-streamtube theory of Ref. 4.22, this direct calculation is no longer possible, because "a" depends on z and y and, thus, an iteration procedure must be followed (see the discussion of the two-dimensional case in Sect. 4.5.2).

In the discussion of the iteration procedure for the performance prediction of a horizontal-axis turbine (Sect. 4.4.7.1), the complication of multiple solutions emerged, which depended on the shape of the lift curve. Such a complication is not present in the performance prediction of a vertical-axis turbine, when the single-streamtube theory is used. This is caused by the averaging process over a complete revolution.

Using the multiple-streamtube theory, the complication of multiple solutions emerges again, because the drag of an elemental streamtube is determined by the lift force on one specific blade element (more precisely two, viz. at ϕ and $(\pi-\phi)$) at one specific angle of attack. The resulting equation is

$$4a(1-a)(r/R_0) \cos \phi = (1/\pi)(Bc/R_0)(1/\sin \gamma)(U_{rel}/U)^2 C_l (\cos \alpha \cos \phi \sin \gamma - \sin \alpha \sin \phi) ,$$

because, from the Eqs (4.5.50) and (4.5.51),

$$(U_{rel}/U)_{\pi-\phi} = (U_{rel}/U)_{\phi} ; (\alpha)_{\pi-\phi} = -(\alpha)_{\phi} ; C_l(-\alpha) = -C_l(\alpha) .$$

The above equation can also be written as

$$C_l = \frac{4\pi a(1-a) \sin \gamma (r/R_0) \cos \phi}{(Bc/R_0)(U_{rel}/U)^2 (\cos \alpha \cos \phi \sin \gamma - \sin \alpha \sin \phi)} . \quad (4.5.54)$$

The lift coefficient is also determined by α (Eq. (4.5.51)) and the profile data. This leads to C_l -vs- α curves from momentum theory (Eq. (4.5.54)) and from the profile data. The point of intersection determines the operating point of the blade element (Fig. 4.52). Because of the application of symmetric profiles for vertical-axis turbines, the multiple solutions are restricted to the stalling area in most cases. At high λ , there is also the possibility, that no solution can be obtained.

When λ and "a" have been calculated (single streamtube) or "a" has been calculated for a given λ (multiple streamtube), the power coefficient can be determined from:

$$C_p = \lambda \left(\frac{B C_0}{R_0} \right) \left(\frac{R_0^2}{S_{ref}} \right) \int_{-\pi}^{+\pi} \frac{(r/R_0) d(z/R_0)}{2\pi \sin \gamma} \int_{-\pi}^{+\pi} \left(\frac{U_{rel}}{U} \right)^2 C_l \sin \alpha \left[1 - \left(\frac{C_d}{C_l} \right) \cot \alpha \right] d\phi \quad (4.5.55)$$

In case of a parabolic blade shape, $R_0^2/S_{ref} = 3/8\eta$.

4.5.7.3 Vortex theories

Section 4.5.3 dealt with a vortex theory for a two-dimensional vertical-axis turbine with an infinite number of blades. When a non-expanding wake and a constant vortex transport velocity in the wake were assumed, a rather simple vortex model appeared.

The extension of the theory to three dimensions for a turbine with straight blades of finite length by applying a simple aspect-ratio correction to the lift and adding a corresponding induced drag term to the profile drag might seem to be obvious.

The trailing vortex system of a vertical-axis turbine differs, however, from that of an airplane wing in level flight, viz.:

- The trailing vortex sheet is not straight, but has a cycloidal shape.
- The strength of the vortex sheet varies downstream due to the orbital lift variation.

The above simple approach can be used as a first step, but a more complete description of the vortex system seems desirable (Giromill, Ref. 4.28; see also Ref. 4.27).

The combination of trailing vorticity (due to spanwise lift variation) and shed vorticity (due to orbital lift variation) is common in helicopter aerodynamics (see e.g. Ormiston, Ref. 4.37). The vortex system for a helicopter in high-speed forward flight is often simplified to a planar wake, which is, however, not possible in case of a three-dimensional Darrieus wind turbine.

Within the assumption of a non-expanding wake and a constant transport velocity, the basic idea of Sect. 4.5.3 (Fig. 4.36) can still be used, i.e. at a fixed spanwise and azimuthal position at the rotor circumference, each passing blade brings the same amount of shed and trailing vorticity in the wake. This vorticity is transported downstream by a constant velocity, which results in a streamline with equidistant patches of vorticity. In case of a rotor with an infinite number of blades, the wake is completely filled with vorticity and the straight streamlines are lines with a constant vorticity.

The main complication of a three-dimensional wake is, that the orientation in space of the vorticity vector differs from streamline to streamline. This will be exemplified by considering the idealized case of a spherical Darrieus turbine (Fig. 4.53). The only purpose is to show the complexity of the problem.

When a high λ and a constant transport velocity $(1-a)U$ are assumed, the relative velocity and angle of attack are approximately:

$$U_{rel} \approx \Omega R_0 \cos \theta,$$

$$v_R = (1-a)U \cos \phi \cos \theta,$$

thus:

$$\alpha \approx v_R/U = [(1-a)/\lambda] \cos \phi.$$

The bound vorticity of one blade is

$$\Gamma_b = \frac{1}{2} C_l c U_{rel} = \frac{1}{2} C_l c (1-a) U \cos \phi \cos \theta. \quad (4.5.55)$$

The shape of the vortex sheet, springing from a blade at position ϕ , can be described by

$$X = R_0 \cos \theta \cos(\phi - \Omega t) + R_0 [(1-a)/\lambda] \Omega t,$$

$$Y = R_0 \cos \theta \sin(\phi - \Omega t),$$

$$Z = R_0 \sin \theta, \quad (4.5.56)$$

and the shape of the vortex sheet of blade number i of a B -bladed rotor

$$X_i = R_0 \cos \theta \cos(\phi + i2\pi/B - \Omega t) + R_0 [(1-a)/\lambda] \Omega t,$$

$$Y_i = R_0 \cos \theta \sin(\phi + i2\pi/B - \Omega t),$$

$$Z_i = R_0 \sin \theta, \quad (4.5.57)$$

with $0 \leq i \leq B-1$.

The shed vorticity is parallel to the local blade span, but the trailing vorticity is tangential to the vortex sheet, which is not tangential to the sphere, as can be seen from Eq. (4.5.56). The vortex-sheet shape, springing from an orbital position ϕ , depends on two parameters θ and t , and can locally be described by two vectors, viz.

$$\vec{r}_\theta = \left(\frac{\partial X}{\partial \theta}, \frac{\partial Y}{\partial \theta}, \frac{\partial Z}{\partial \theta} \right),$$

$$\vec{r}_t = \left(\frac{\partial X}{\partial t}, \frac{\partial Y}{\partial t}, \frac{\partial Z}{\partial t} \right). \quad (4.5.58)$$

The strength of the vortex sheet due to shed and trailing vorticity can be calculated by dividing the shed and the trailing circulation by the corresponding length of the vortex sheet at the time of origin ($t = 0$).

in t and θ -direction, respectively. Thus with

$$ds_\theta = [\vec{r}_\theta \cdot \vec{r}_\theta]^{\frac{1}{2}} d\theta, \quad ds_t = [\vec{r}_t \cdot \vec{r}_t]^{\frac{1}{2}} dt,$$

the vortex sheet strength becomes (with $|d\phi| = \Omega dt$)

$$\gamma_s = -\frac{\partial \Gamma_b}{\partial \phi} \frac{d\phi}{(ds_t)_{t=0}} = \frac{1}{2}(c/R_0) C_{l\alpha} (1-a) U \cos \theta \sin \phi / W,$$

(shed vorticity) with

$$W = [\cos^2 \theta + 2[(1-a)/\lambda] \cos \theta \sin \phi + [(1-a)/\lambda]^2]^{\frac{1}{2}}, \quad (4.5.59)$$

$$\gamma_t = -\frac{\partial \Gamma_b}{\partial \theta} \frac{d\theta}{(ds_\theta)_{t=0}} = \frac{1}{2}(c/R_0) C_{l\alpha} (1-a) U \sin \theta \cos \phi, \quad (4.5.60)$$

(trailing vorticity).

The direction of the shed vorticity is parallel, but opposite to $(\vec{r}_\theta)_{t \rightarrow 0}$ and the direction of the trailing vorticity is also parallel and opposite to $(\vec{r}_t)_{t \rightarrow 0}$. These directions can be given by the "direction cosines" of the vectors \vec{r}_θ and \vec{r}_t , thus at $t \rightarrow 0$

$$\left. \begin{aligned} \cos(\theta, x) &= \frac{\partial X}{\partial \theta} \frac{1}{|\vec{r}_\theta|} = -\sin \theta \cos \phi, \text{ with } |\vec{r}_\theta| = [\vec{r}_\theta \cdot \vec{r}_\theta]^{\frac{1}{2}}, \\ \cos(\theta, y) &= \frac{\partial Y}{\partial \theta} \frac{1}{|\vec{r}_\theta|} = -\sin \theta \sin \phi, \\ \cos(\theta, z) &= \frac{\partial Z}{\partial \theta} \frac{1}{|\vec{r}_\theta|} = +\cos \theta; \end{aligned} \right\} \quad (4.5.61)$$

$$\left. \begin{aligned} \cos(t, x) &= \frac{\partial X}{\partial t} \frac{1}{|\vec{r}_t|} = [\cos \theta \sin \phi + (1-a)/\lambda] / W, \\ \cos(t, y) &= \frac{\partial Y}{\partial t} \frac{1}{|\vec{r}_t|} = -(\cos \theta \cos \phi) / W, \\ \cos(t, z) &= \frac{\partial Z}{\partial t} \frac{1}{|\vec{r}_t|} = 0, \text{ with } |\vec{r}_t| = [\vec{r}_t \cdot \vec{r}_t]^{\frac{1}{2}}. \end{aligned} \right\} \quad (4.5.62)$$

The Eqs (4.5.56) through (4.5.62) describe the vortex sheets for a finite number of blades. With the formula of Biot-Savart, the induced velocities can be calculated, at least in principle.

A possible simplification is to look at the limit $B \rightarrow \infty$, $c \rightarrow 0$ for Bc/R_0 finite, in which case the wake is filled continuously with vorticity. In order to facilitate the application of the formula of Biot-Savart, the shed and trailing vorticity have to be decomposed in components parallel to the x , y and z -axis.

This decomposition of the vorticity in the \vec{r}_θ - and \vec{r}_t -directions into the x , y and z -directions can be visualized by considering a volume of the wake which is spanned by the line elements ds_θ , ds_t and Δx . The first two elements are taken at $t = 0$, and the third element is the distance in x -direction covered by the vortex sheets of all B blades, i.e. during a complete revolution, thus

$$ds_\theta = R_0 d\theta,$$

$$ds_t = \Omega R_0 W dt,$$

$$\text{or because } dt = -d\phi/\Omega,$$

$$ds_t = -R_0 W d\phi,$$

$$\Delta x = 2\pi R_0 (1-a)/\lambda.$$

The amount of rotation contained in this volume in the direction of the shed (θ) and trailing (t) vorticity is

$$\left. \begin{aligned} d\Gamma_\theta &= B\gamma_s ds_t = -\frac{1}{2} \frac{Bc}{R_0} C_{l\alpha} (1-a) U R_0 \cos \theta \sin \phi d\phi, \\ d\Gamma_t &= B\gamma_t ds_\theta = +\frac{1}{2} \frac{Bc}{R_0} C_{l\alpha} (1-a) U R_0 \sin \theta \cos \phi d\theta. \end{aligned} \right\} \quad (4.5.64)$$

When these circulations are divided by the respective areas normal to the direction of $d\Gamma_\theta$ and $d\Gamma_t$, the rotation in \vec{r}_θ and \vec{r}_t direction are obtained (ω_θ , ω_t). When it is remembered that the volume of the parallelepiped is

$$\Delta x ds_\theta ds_t |\cos(t, y)| |\cos(\theta, z)| = \text{Vol},$$

the areas normal to \vec{r}_θ and \vec{r}_t are

$$\frac{\text{Vol}}{|ds_\theta|} \quad \text{and} \quad \frac{\text{Vol}}{|ds_t|}.$$

Thus

$$\omega_\theta = \frac{-d\Gamma_\theta}{\Delta x ds_t |\cos(t, y)| |\cos(\theta, z)|},$$

$$\omega_t = \frac{-d\Gamma_t}{\Delta x \, ds_0 \, |\cos(\theta, y)| \, |\cos(\theta, z)|}$$

These rotations can be decomposed in x, y and z direction, viz.:

$$\begin{aligned} \omega_{\theta_x} &= \omega_\theta \cos(\theta, x); \quad \omega_{\theta_y} = \omega_\theta \cos(\theta, y); \quad \omega_{\theta_z} = \omega_\theta \cos(\theta, z); \\ \omega_{t_x} &= \omega_t \cos(t, x); \quad \omega_{t_y} = \omega_t \cos(t, y); \quad \omega_{t_z} = 0 \end{aligned}$$

After some straightforward calculations it follows that

$$\omega_x = -\frac{\Omega}{4\pi} \frac{Bc}{R_0} C_{l_\alpha} \frac{1-a}{\lambda} \frac{\sin \theta \cos \phi}{|\cos \theta| |\cos \theta| |\cos \phi|}, \quad (4.5.65)$$

$$\omega_y = +\frac{\Omega}{4\pi} \frac{Bc}{R_0} C_{l_\alpha} \frac{\sin \theta \cos \theta}{|\cos \theta| |\cos \theta| |\cos \phi|} \quad (4.5.66)$$

$$\omega_z = -\frac{\Omega}{4\pi} \frac{Bc}{R_0} C_{l_\alpha} \frac{\sin \phi}{|\cos \phi|}. \quad (4.5.67)$$

The rotation in the wake inside the sphere stems from points $\{R_0, \theta, (\pi-\phi)\}$, whereas the rotation in the wake behind the sphere consists of the sum of the rotation from the points $\{R_0, \theta, \phi\}$ and $\{R_0, \theta, (\pi-\phi)\}$. When this is taken into account it may be shown that the rotation components in the y- and z-direction in the wake behind the sphere are twice the values inside the sphere and that the rotation component in the x-direction in the wake behind the sphere is zero.

The vorticity components ω_y and ω_z are independent of x, except the jump at the boundary of the sphere, and can be described in cylindrical coordinates (x, r, θ).

From the Eqs (4.5.66) and (4.5.67) it can be shown that the vortex lines in the wake are concentric circles with a vorticity distribution depending only on the radial coordinate r, viz.

$$\omega_{\text{lateral}} = (\Omega/4\pi)(Bc/R_0)C_{l_\alpha} (r/R_0) [1-(r/R_0)^2]^{-\frac{1}{2}}, \quad (4.5.68)$$

inside the sphere and twice that value in the wake behind the sphere. The rotation becomes infinite at the wake boundary ($r/R_0 = 1$), but the total amount of rotation (circulation) integrated along a radius is finite. Behind the sphere, this value is

$$\gamma_{\text{lateral}} = (\Omega/4\pi)(Bc/R_0)C_{l_\alpha} R_0 \int_0^1 (r/R_0) [1-(r/R_0)^2]^{-\frac{1}{2}} d(r/R_0) = (\Omega R_0/8\pi)(Bc/R_0)C_{l_\alpha}. \quad (4.5.69)$$

When this is taken to be accumulated in the wake boundary, the "lateral" vortex wake behind the sphere consists of a cylinder with a constant vortex sheet strength equal to the value of Eq. (4.5.69). Such a cylindrical vortex sheet induces an axial velocity far behind the sphere equal to γ_{lat} , which can also be expressed by an axial induction factor $2a$. This leads to the following approximate expression for the average axial induction factor at the sphere

$$a = (\lambda/16\pi)(Bc/R_0)C_{l_\alpha}. \quad (4.5.70)$$

It is interesting to compare this value with the approximate values of the two-dimensional theories Eqs (4.5.8), (4.5.11), although the contribution of the bound vorticity is not included in Eq. (4.5.70).

The strength of the bound vorticity can be obtained from Eq. (4.5.55) by substituting for the chord length

$$c = \sigma R_0/B,$$

and by defining the bound vortex sheet strength by

$$\gamma_b = \lim_{\substack{B \rightarrow \infty \\ c \rightarrow 0 \\ \sigma = \text{constant}}} \frac{\Gamma_b}{2\pi R_0 \cos \theta/B} = \frac{\sigma}{4\pi} C_{l_\alpha} (1-a)U \cos \phi = \gamma_0 \cos \phi. \quad (4.5.71)$$

From symmetry conditions it follows that, in the y-z-plane through the axis of the rotor, this bound vorticity distribution induces only velocity components in the y-z-plane and no components in x-direction. It can also be shown, that on the average there is no axial flow through the turbine due to the bound vorticity (i.e. no contribution to "a", Eq. (4.5.70)), but there is an average lateral flow through the turbine.

The direct calculation of the flow due to the bound vorticity of Eq. (4.5.71) is complicated and will not be investigated further.

The structure of the axial rotation (ω_x), which exists only inside the sphere, is rather complicated and induces only velocity components in y- and z-direction, in that way also contributing nothing to the axial induced velocities.

It must be remembered that the above exercise has been done for a given bound vorticity distribution, which was a first-order approximation of the bound vortex distribution of a turbine with $B \rightarrow \infty$. A next step would be to start with an unknown bound vortex distribution in a way similar to Ref. 4.25 for the two-dimensional vertical-axis turbine with $B \rightarrow \infty$. Such a calculation will not be executed here.

4.5.7.4 Experimental results

In contrast with the horizontal-axis turbine, there are rather complete test results for the Darrieus turbine. Most of these results are obtained in a wind tunnel. This has the advantage of constant and predictable test conditions (contrary to the stochastic wind conditions in field tests), but the disadvantage of a small size of the model turbine (low Reynolds number) and sometimes large and therefore uncertain blockage corrections on the test results (rotor height in the order of magnitude of the test-section height).

The detrimental effect of very low Reynolds numbers is clearly demonstrated by the preliminary tests of Ref. 4.38. Due to the small scale of the model, the Reynolds number related to the blade chord was about 2×10^4 and, therefore, the profile drag excessively high. This led to very small and even negative C_p -values in the normal operating range of the model turbine. Only by estimating the power loss due to the extravagant profile drag, the authors were able to show the energy-producing potential of the Darrieus turbine.

Ref. 4.39 describes the tests of a 14 ft diameter Darrieus turbine in the 30 ft x 30 ft NAE wind tunnel. There were, however, some troubles with blade imperfections, therefore, the tests of Ref. 4.40 with a 12 ft diameter turbine in the same wind tunnel have to be regarded as the final results.

Figure 4.54 shows the drag coefficient C_D and the power coefficient C_p as a function of the tip-speed ratio, as obtained from the experiments of Ref. 4.40, together with the calculated results of Ref. 4.21. The large discrepancy in C_D is caused by the drag of the turbine support, which is included in the experimental data but not in the calculated data. Ref. 4.40 quotes a support drag (rotor inoperative) of $\Delta C_D \approx 0.25$. When the rotor is operative, the effective support drag will be lower, and Fig. 4.54 suggests that the calculated results are not unrealistic.

The calculated power coefficients show discrepancies, especially at low λ (stalled blades), but the effect of rotor solidity is strikingly well predicted.

Ref. 4.41 gives a rather extensive set of wind tunnel test results. An interesting aspect of these tests is the influence of the Reynolds number on C_p . This could be accomplished by keeping the angular velocity of the turbine constant during one test run, because the relative velocity (and thus the Reynolds number) depends largely on the angular velocity and only to a minor extent to the wind velocity.

Figure 4.55 shows a rather large influence of the Reynolds number on C_p . Figure 4.56 shows the influence of the solidity ratio on C_p . The influence on the operational λ -range agrees with the results of Ref. 4.40 (Fig. 4.54), but the influence on the maximum obtainable C_p is less pronounced. This might be due to the variation of Re_c during the test runs of Ref. 4.40; the one-bladed rotor was tested at smaller maximum angular velocities than the three-bladed rotor. In this respect, it is interesting to notice that Ref. 4.22 claims a better agreement with experimental results, using multiple-streamtube theory instead of single-streamtube theory. This is only true, however, when the experimental results of Ref. 4.41 are used (see Fig. 4.57).

Ref. 4.23 gives results of wind tunnel tests on a very small Darrieus turbine (diameter 0.250 m) with a solidity $Bc/R_0 = 0.256$. In these tests the power output was obtained from the difference between measurements at a fixed angular velocity "wind on" and "wind off". This means that the power coefficient is corrected for the profile drag, which is excessively high at these low Reynolds numbers. The results obtained will not be very accurate, but the main objective of that investigation was to study the influence of wind shear on the Darrieus turbine.

Ref. 4.42 mentions some field tests on a Darrieus turbine with a diameter of 4.72 m. The Reynolds numbers obtained during these field tests were quoted as $Re_c = 1.1 \times 10^6$. The optimum C_p was about 0.44, which is fairly high. A large problem in field testing of a wind turbine is the determination of the reference wind velocity. For some revealing discussions on this subject, the references 4.43 and 4.44 might be consulted.

4.5.8 Concluding remarks

Performance-prediction theories for the Darrieus wind turbine are based primarily on momentum considerations, while only induced velocities in wind direction are taken into account.

There are two variants, viz. the single- and the multiple-streamtube theory. It is difficult to assess these theories by comparing them with experiments.

The two-dimensional vortex theory (Sect. 4.5.3) indicates a preference for the multiple-streamtube theory, and certain experimental data emphasize this view.

The above-mentioned performance-prediction theories do not take into consideration a number of effects, which relative importance could be estimated in a two-dimensional case, viz.

- The variation of the induced velocities along the circumference of the turbine, which leads to blade load differences at upwind and downwind blade positions.
- Stream-curvature effects, i.e. the effect of the finite blade chord.
- Unsteady effects.

In the setting up of a computer code, including vortex wake effects, the influence of a finite blade chord and unsteady effects seems a formidable problem. The vortex-wake calculations will probably be restricted to a cylindrical wake (no wake expansion) and also vortex sheet roll-up effects will be too complex to deal with in a first attempt. The inclusion of finite-chord effects necessarily implies a careful consideration of the blade leading edge (suction peak, tangential force), whereas unsteady effects can also only be taken into account in unseparated flow conditions, which limits the applicability of the calculation method appreciably, because flow separation is present over a large range of λ .

On the other hand, the geometry of a Darrieus turbine is to a large extent fixed by constructional considerations and, consequently, there are only few parameters left for an aerodynamic optimization procedure. Therefore, the question can be put forward whether such a refined performance prediction method is really needed. The situation is further complicated by the turbulent (unsteady) effects, which are present in the atmospheric boundary layer and are neglected in the above-mentioned calculation methods.

The aerodynamics of a Darrieus turbine is, however, an interesting subject and will attract investigators to study some aspects thoroughly. Such studies can only lead to practical results when the before-mentioned three aspects are included in a balanced manner.

4.6 List of references

- 4.1 Greidanus, J.H.: Work done by Aerodynamic Forces in Unit Time on a Vibrating Wing and the Critical Vibration Modes of a Wing (in Dutch).
NLL Report V.1237 (1940).
- 4.2 Pistolesi, E.: Betrachtungen über die gegenseitige Beeinflussung von Tragflügelsystemen. Gesammelte Vorträge der Hauptversammlung 1937 der Lillenthal-Gesellschaft (1937) pp. 214-219.
- 4.3 Glauert, H.: Windmills and Fans. Aerodynamic Theory (ed. W.F. Durand), Chapter XI, Div. L. (Dover Publ. Inc., N.Y., 1963).
- 4.4 Stoddard, F.S.: Momentum Theory and Flow States for Windmills. Wind Techn. Journ. 1, 1 (Spring 1977).
- 4.5 Griffith, R.T.: The Effect of Aerofoil Characteristics on Windmill Performance. Aeron. Journ. (July 1977) pp. 322-326.
- 4.6 Prandtl, L., Betz, A.: Vier Abhandlungen zur Hydrodynamik und Aerodynamik. (Göttingen, 1927) p. 68.
- 4.7 Wilson, R.E., Lissaman, P.B.S.: Applied Aerodynamics of Wind Power Machines. Oregon State Univ. Report NSF/RA/N-74113 (July 1974).
- 4.8 Wilson, R.E., Walker, S.N.: Performance-Optimized Horizontal-Axis Wind Turbines. Proc. Intern. Symp. on Wind Energy Systems (St. John's College, Cambridge, England; 7-9 Sept. 1976).
- 4.9 Goldstein, S.: On the Vortex Theory of Screw Propellers. Proc. Roy. Soc., 123, A (1929) pp. 440-465.
- 4.10 Lock, C.N.H., Yeatman, D.: Tables for Use in an Improved Method of Airscrew Strip Theory Calculations. ARC R&M No. 1674 (Oct. 1934).
- 4.11 Weissinger, J.: The Lift Distribution of Swept-Back Wings. NACA TM 1120.
- 4.12 Multhopp, H.: Methods for Calculating the Lift Distribution of Wings (Subsonic Lifting-Surface Theory). ARC R&M 2884 (1955).
- 4.13 Van Holten, Th.: The Computation of Aerodynamic Loads on Helicopter Blades in Forward Flight, Using the Method of the Acceleration Potential. Delft Univ. of Techn. Report VTH-189 (1975).
- 4.14 Labrujère, Th.E. et al.: An Approximate Method for the Calculation of the Pressure Distribution on Wing-Body Combination at Subcritical Speeds. AGARD CP No. 71 (1970).
- 4.15 Suciu, E. et al.: Potential Aerodynamic Analysis of Horizontal-Axis Windmills. Proc. AIAA 15th Aerospace Sciences Meeting (Los Angeles, Cal., 24-25 Jan. 1977).
- 4.16 Labrujère, Th., De Vries, O.: Evaluation of a Potential Theoretical Model of the Wake Behind a Wing via Comparison of Measurements and Calculations. NLR TR 74063 U (July 1974).
- 4.17 Foley, W.M.: From DaVinci to the Present - a Review of Airscrew Theory for Helicopters, Propellers, Windmills and Engines. Proc. AIAA 9th Fluid and Plasma Dynamics Conf. (San Diego, Cal., 14-16 July 1976).
- 4.18 Betz, A.: Windenergie und ihre Ausnutzung durch Windmühlen. (Vandenhoeck und Ruprecht, Göttingen, 1926).
- 4.19 Blackwell, B.F., et al.: Wind Tunnel Performance Data for Two- and Three-Bladed Savonius Rotors. Sandia Laboratories Energy Report SAND76-0131 (July 1977).
- 4.20 Holgate, M.J.: A Cross Flow Wind Turbine. Proc. Intern. Symp. on Wind Energy Systems (St. John's College, Cambridge, England; 7-9 Sept. 1976).
- 4.21 Templin, R.J.: Aerodynamic Performance Theory for the NRC Vertical-Axis Wind Turbine. NRC LTR-LA-160 (June 1974).
- 4.22 Strickland, J.H.: The Darrieus Turbine: a Performance Prediction Model Using Multiple Stream-tubes. Sandia Laboratories Energy Report SAND75-0431 (Oct. 1975).
- 4.23 VanDeWijdeven, F.J.: A Study of the Darrieus Rotor in a Turbulent Shear Flow. Univ. of Auckland, Dept. Mech. Eng. Proj. Report No. PME 76-36 (4 Oct. 1976).
- 4.24 Reuter Jr., R.C., Sheldahl, R.E. (eds.): Sandia Vertical-Axis Wind Turbine Project Techn. Quarterly Report (April-June 1976). Sandia Laboratories Energy Report SAND76-0581 (Jan. 1977).
- 4.25 Holme, G.: A Contribution to the Aerodynamic Theory of the Vertical-Axis Wind Turbine. Proc. Intern. Symp. on Wind Energy Systems (St. John's College, Cambridge, England; 7-9 Sept. 1976).
- 4.26 Wilson, R.E.: Darrieus Rotor Aerodynamics. Proc. Third Biennial Conf. and Workshop on Wind Energy Conversion Systems (Washington D.C., 19-21 Sept. 1977). JFB Scient. Corp. CONF 770921 (Sept. 1977).
- 4.27 Fannucci, J.B., Walters, R.E.: Innovative Wind Machines; the Theoretical Performance of a Vertical-Axis Wind Turbine. Proc. Vertical-Axis Wind Turbine Techn. Workshop (Albuquerque, New Mexico, 18-20 May 1976). Sandia Laboratories Report No. SAND76-5586 (May 1976).
- 4.28 Brulle, R.V.: Feasibility Investigation of the Giromill for Generation of Electrical Power. Final Report of the Period April 1975 - April 1976. McDonnell Aircraft Co. (Jan. 1977).

- 4.29 Walters, R.E., Migliore, P.G.: The Circulation Controlled Vertical-Axis wind Turbine. Proc. Third Biennial Conf. and Workshop on Wind Energy Conversion Systems (Washington D.C., 19-21 Sept. 1977). JFB Scient. Corp. CONF 770921 (Sept. 1977).
- 4.30 Schlichting, H., Truckenbrodt, E.: Aerodynamik des Flugzeuges. (Springer Verlag, Berlin, 1959) erster Band, pp. 434-436, 400.
- 4.31 Durand, W.F. (ed.): Aerodynamic Theory. (Dover Publ. Inc., N.Y., 1963) Vol. II, pp. 52, 306.
- 4.32 Ashley, H.: Some Contributions to Aerodynamic Theory for Vertical-Axis Wind Turbines. Journ. of Energy, 2, 2 (April-March 1978) pp. 113-119.
- 4.33 Fung, Y.C.: An Introduction to the Theory of Aeroelasticity. (Dover Publ. Inc., N.Y., 1969) pp. 409-411.
- 4.34 James, E.C.: Unsteady Aerodynamics of Variable-Pitch Vertical-Axis Windmill. Proc. AIAA/AAS Solar Energy for Earth Conf. (Los Angeles, Ca., 21-24 April 1975). AIAA Paper No. 75-649.
- 4.35 Muraca, R.J., et al.: Theoretical Performance of Vertical-Axis Windmills. NASA TM TMX-72662 (May 1975).
- 4.36 Shankar, P.N.: On the Aerodynamic Performance of a Class of Vertical-Axis Windmills. Nat. Aeron. Lab. Bangalore Report No. TM AE-TM-13-75 (July 1975).
- 4.37 Ormiston, R.A.: An Actuator Disk Theory for Rotor Wake Induced Velocities. Proc. FDP Specialists' Meeting on Aerodynamics of Rotary Wings (Marseille, France; 13-15 Sept. 1972). AGARD Conf. Proc. CP-111.
- 4.38 South, P., Rangi, R.S.: Preliminary Tests of a High-Speed Vertical-Axis Windmill. NRC, NAE Report LTR-LA-74 (March 1971).
- 4.39 South, P., Rangi, R.S.: A Wind Tunnel Investigation of a 14 Ft. Diameter Vertical-Axis Windmill. NRC, NAE Report LTR-LA-105 (Sept. 1972).
- 4.40 South, P., Rangi, R.S.: An Experimental Investigation of a 12 Ft. Diameter High-Speed Vertical-Axis Wind Turbine. NRC, NAE Report LTR-LA-166 (April 1975).
- 4.41 Blackwell, B.F., et al.: Wind Tunnel Performance Data for the Darrieus Wind Turbine with NACA 0012 Blades. Sandia Laboratories Energy Report SAND76-0130 (May 1976).
- 4.42 Chasteau, V.A.L.: Operational Experience with a 5 m Darrieus Wind Turbine. Univ. of Auckland, Dept. Mech. Eng. Report No. 77/8 (Aug. 1977).
- 4.43 Weingarten, L.I., Blackwell, B.F.: Sandia Vertical-Axis Wind Turbine Program Techn. Quarterly Report (Jan. - March 1976). Sandia Laboratories Energy Report SAND76-0338 (Aug. 1976).
- 4.44 Sheldahl, R.E., Blackwell, B.F.: Free-Air Performance Tests of a 5-Metre Diameter Darrieus Turbine. Sandia Laboratories Report SAND77-1063 (Dec. 1977).

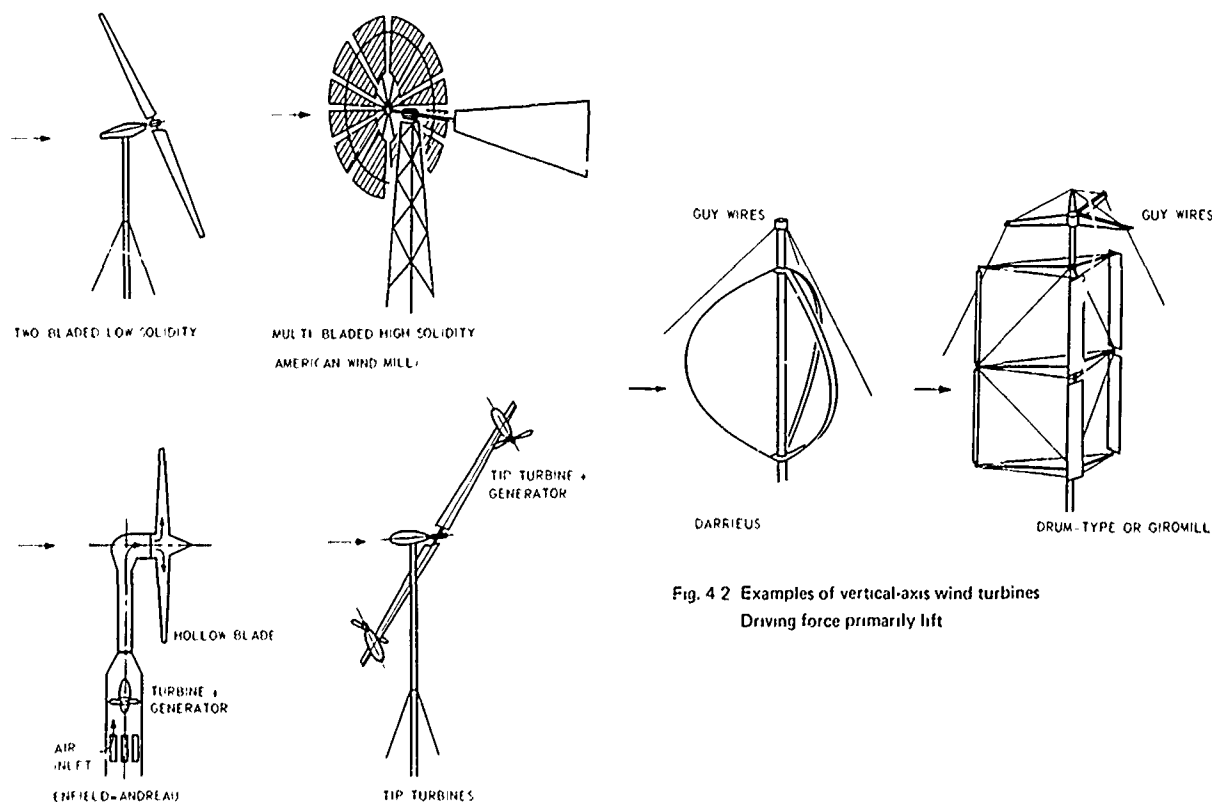


Fig. 4 2 Examples of vertical-axis wind turbines
Driving force primarily lift

Fig. 4 1 Examples of horizontal-axis wind turbines
Driving force primarily lift

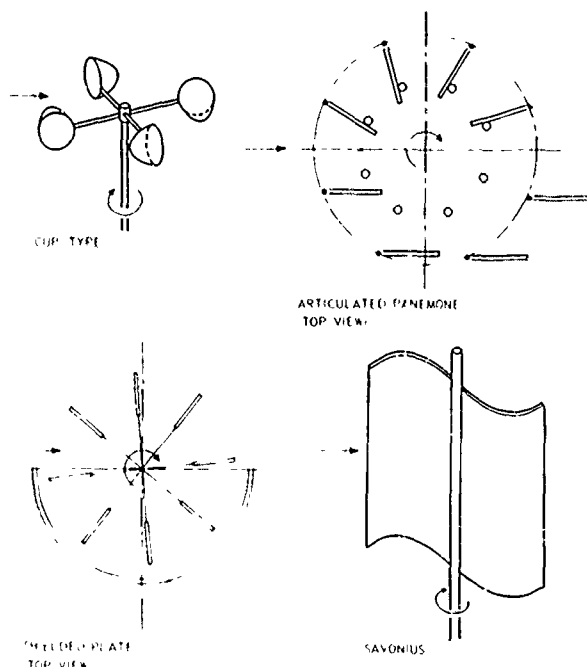


Fig. 4.3 Examples of vertical axis wind turbines
Driving force primarily drag

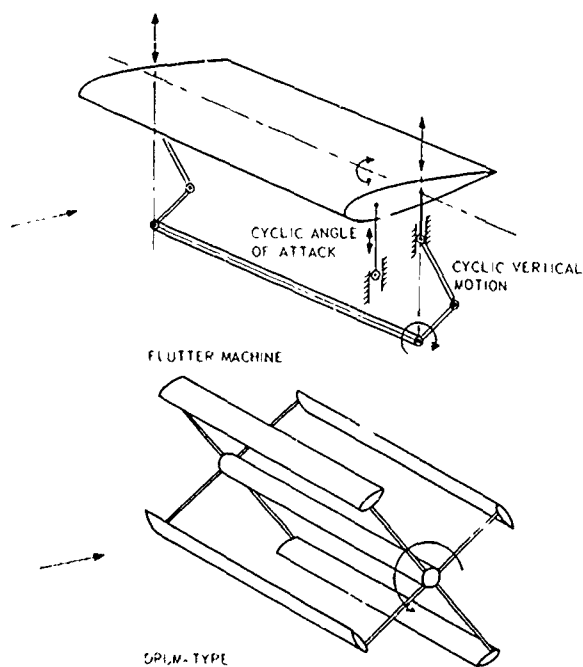


Fig. 4.4 Examples of horizontal-axis cross-wind turbines
Driving force primarily lift

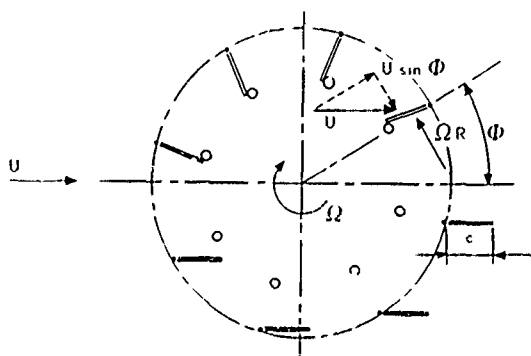


Fig. 4.5 Calculation of the performance of a simply articulated panemone

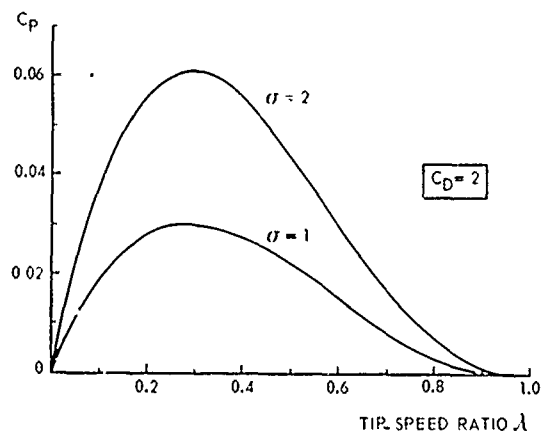


Fig. 4.6 Performance of a simply articulated panemone, estimated with Eq. 4.2.5

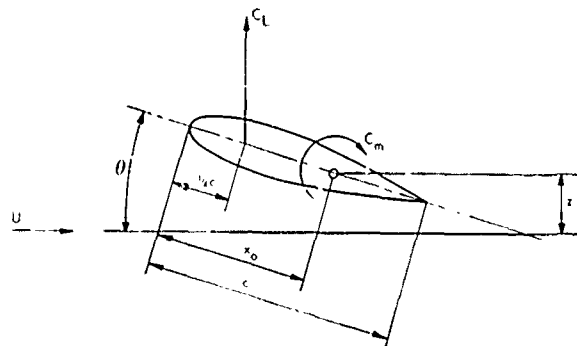


Fig. 4.7 Symbols used for the plain aerofoil calculation of the flutter machine

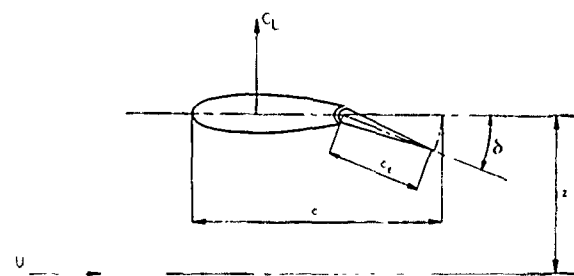


Fig. 4.8 Symbols used for the calculation of the flutter machine with aerofoil and plain flap

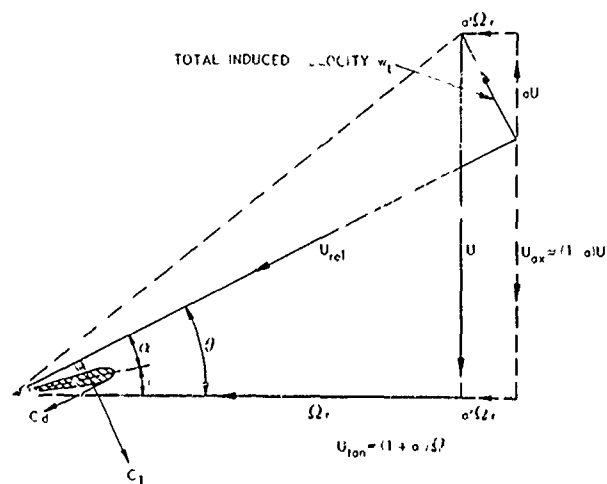


Fig. 4.9 Velocity triangle at blade element

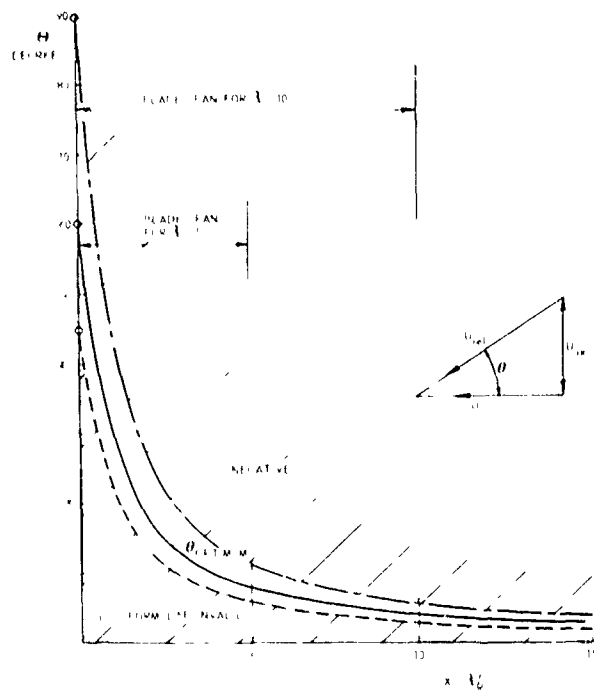


Fig. 4.10 The distribution of the optimum θ and the possible range of variation of θ , according to the theory for infinitely many blades (Ref. 4.3) and $C_d = 0$

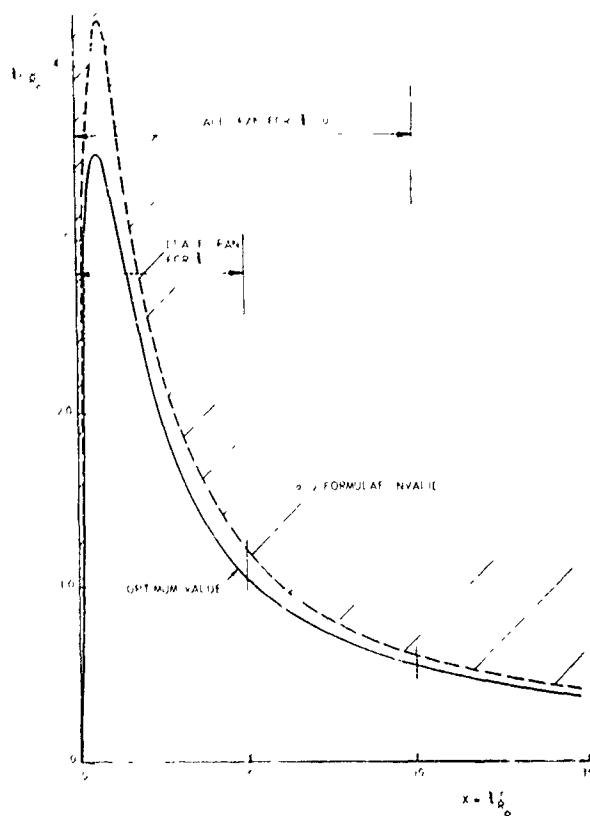


Fig. 4.11 The distribution of the optimum $C_L c$ and the possible range of variation, according to the theory for infinitely many blades (Ref. 4.3) and $C_d = 0$

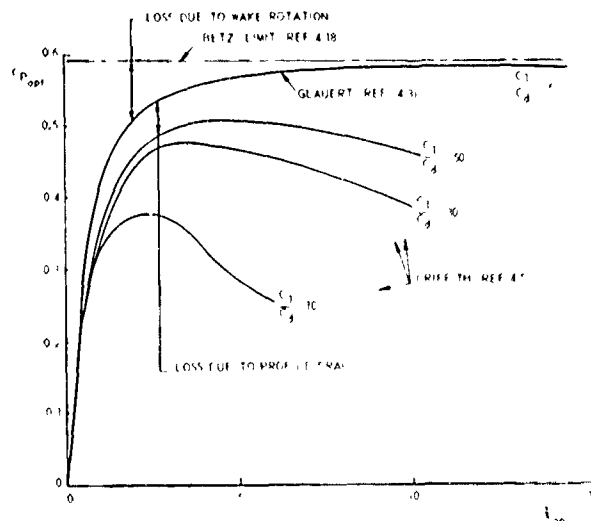


Fig. 4.12 The optimum C_p as a function of the chosen tip speed ratio λ_0 , according to Glauert (Ref. 4.3) Influence of profile drag according to Griffith (Ref. 4.5)

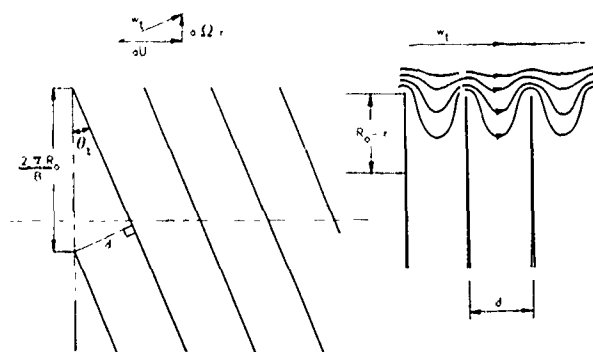


Fig. 4.13 Flow problem solved by Prandtl (Ref. 4.6) to estimate the tip correction factor

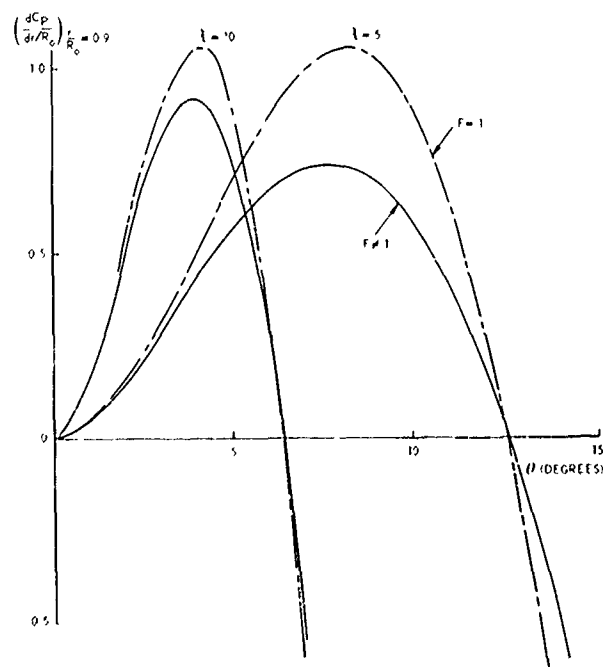


Fig. 4.14 Influence of the tip correction factor F on the local power coefficient. $B=2$, $r/R_0=0.9$, $C_d=0$

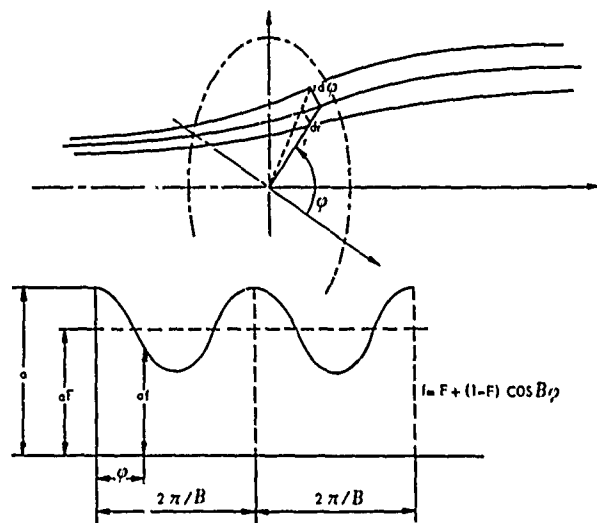


Fig. 4.15 Elemental streamtube through the rotor and the assumed variation of the induced velocity factor with azimuth-angle ϕ

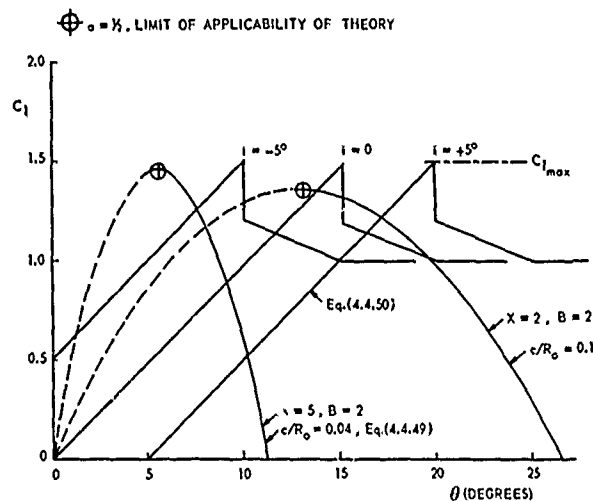


Fig. 4.17 The operating point of a blade element, determined from the intersection of the curve from Eq. 4.4.49 and the lift curve (profile data; simplified)
The dashed part of the curve is inapplicable, because $a > 1/2$

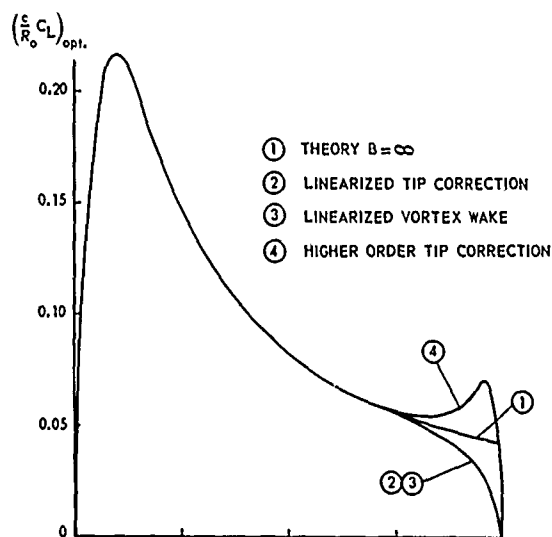


Fig. 4.16 Distribution of the optimum θ and cCl/R_0 along the span, according to different theories
 $B = 2, \lambda = 8, C_d/C_l = 0.01$

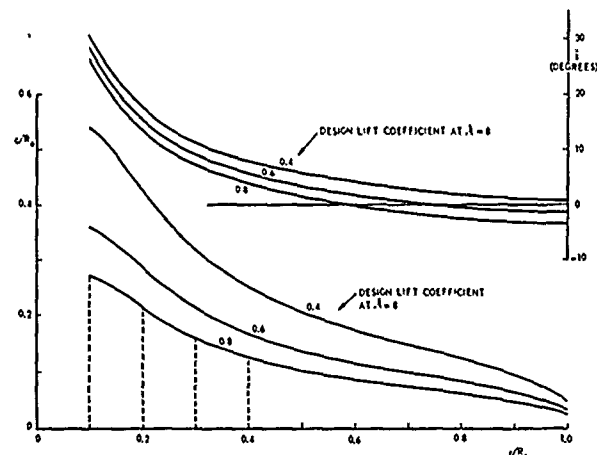


Fig. 4.18 Blade shape (chord and twist distribution) for a two-bladed optimum rotor (ideal shape)
Influence of design lift coefficient

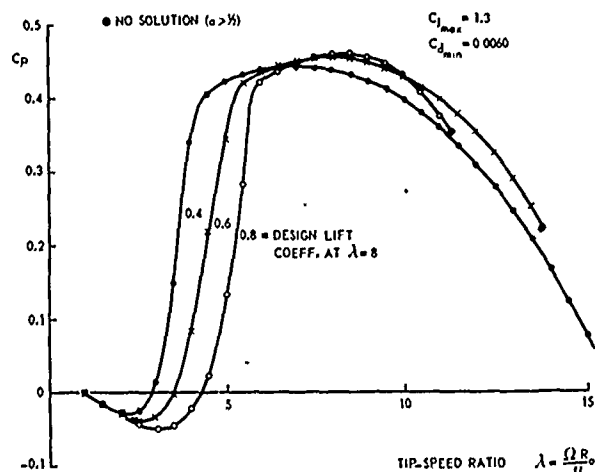
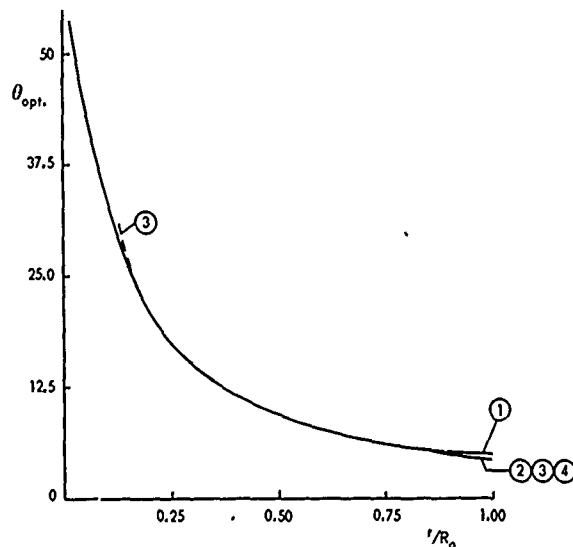


Fig. 4.19 Influence of the chosen design lift coefficient on the power output of an "ideal" rotor shape, cf. Fig. 4.18

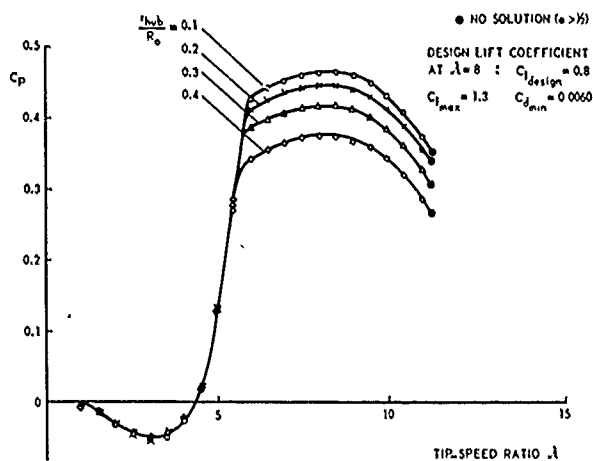


Fig. 4.20 Influence on the power output of omitting a part of the rotor blade at the root
"Ideal" rotor shape

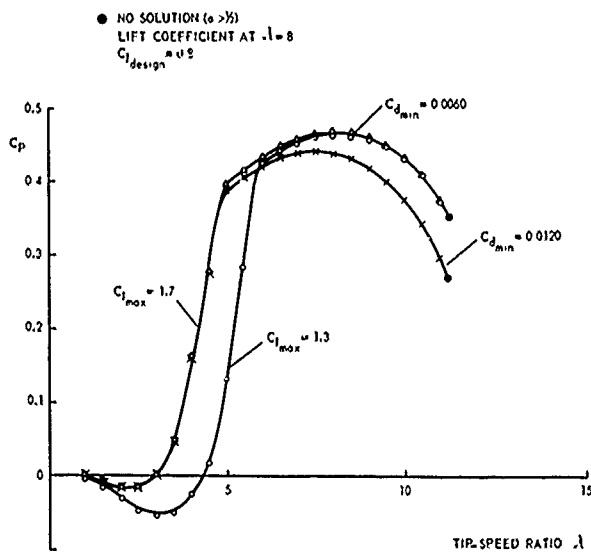


Fig. 4.22 Influence of increasing $C_{p_{max}}$ and increasing $C_{d_{min}}$ on the power output of the "ideal" rotor shape

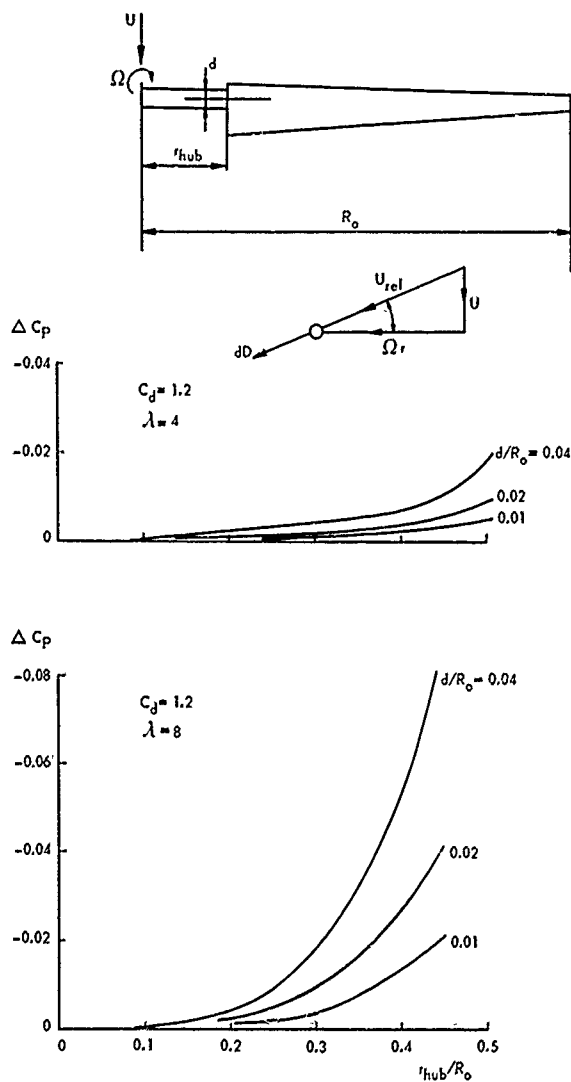


Fig. 4.21 Loss of power output due to a cylindrical shaft between blade root (at r_{hub}) and rotor axis ($r = 0$)

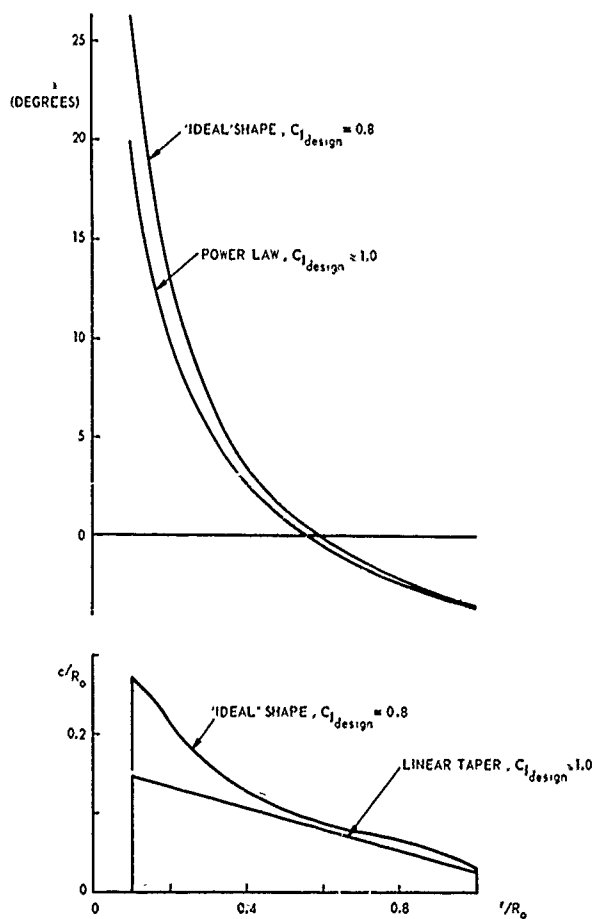


Fig. 4.23 Comparison between the "ideal" blade shape and the twisted blade with linear taper

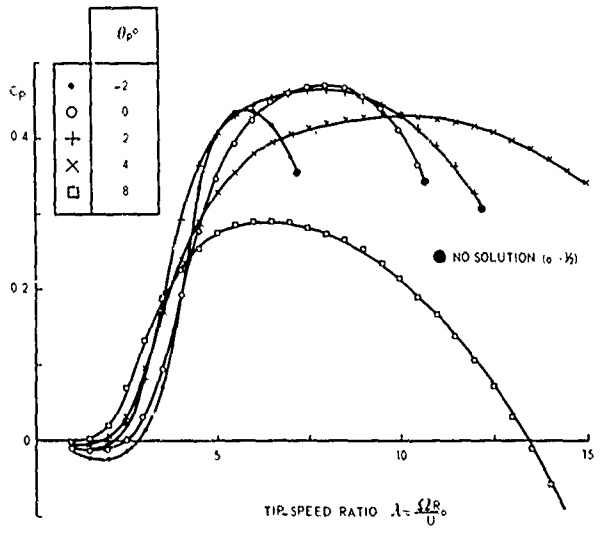


Fig. 4.24 Twisted blade design with linear taper $B=2$, $r_{hub}/R_0=0.10$
 Influence of blade pitch variation
 $c/R_0 = 0.16 - 0.136 r/R_0$
 $i = 11.380 (r/R_0) - 0.487$
 -15.0 (degrees)
 θ_p blade pitch angle positive in the same direction as i .
 The pitch angle is defined as a rigid body rotation with respect to the blade twist distribution $i=f(r/R_0)$

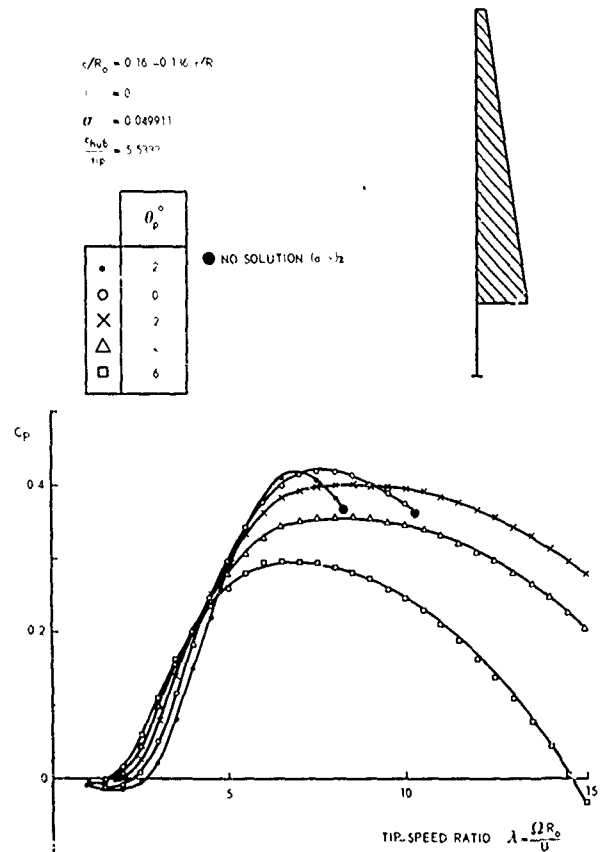


Fig. 4.26 Power output of an untwisted blade. $B=2$, $r_{hub}/R_0=0.2$

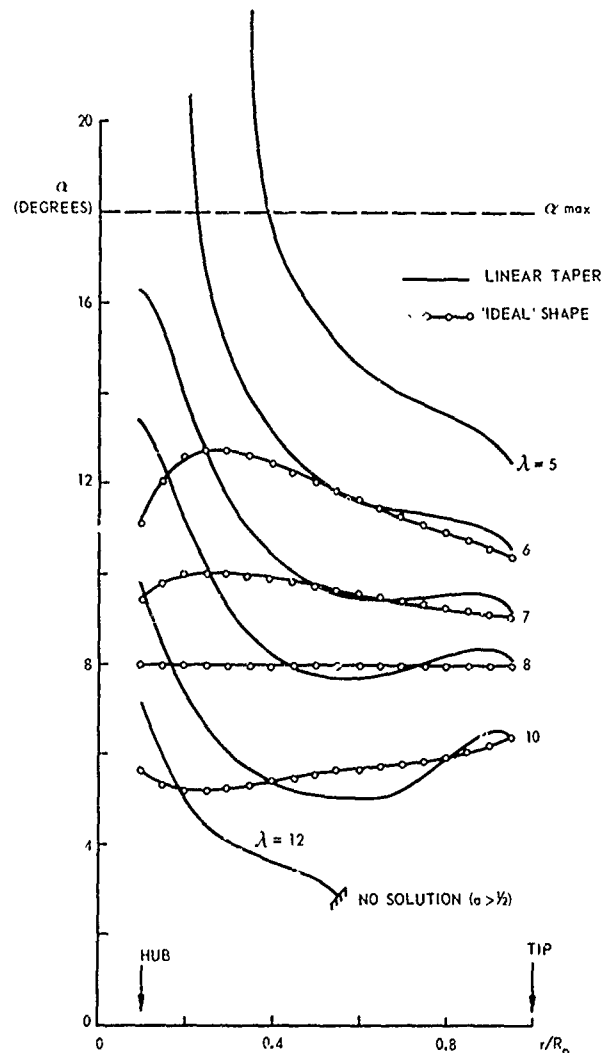


Fig. 4.25 Twisted blade design with linear taper (Fig. 4.24)
 Influence of λ on the spanwise α -distribution at $\theta_p=0$
 Comparison with α -distribution of rotor blade with "ideal" shape

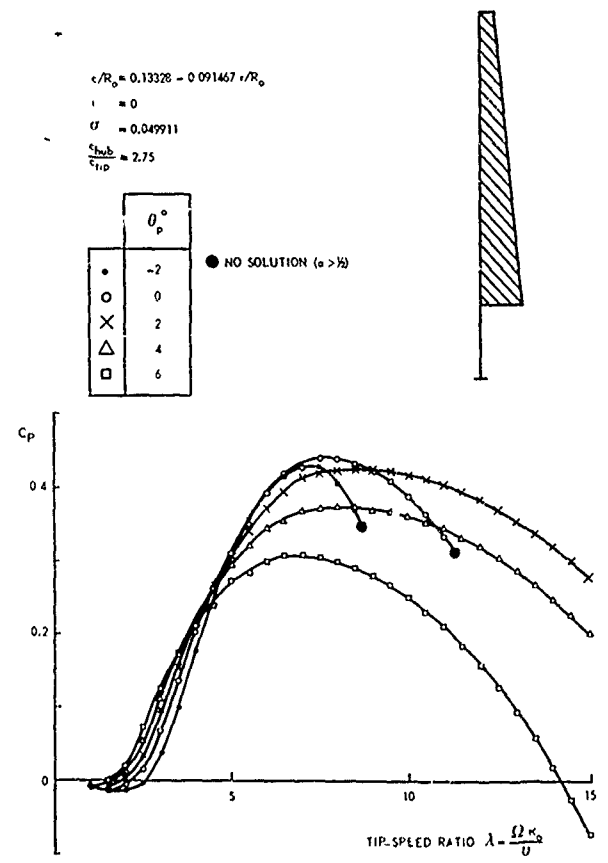


Fig. 4.27 Power output of an untwisted blade. $B=2$, $r_{hub}/R_0=0.2$

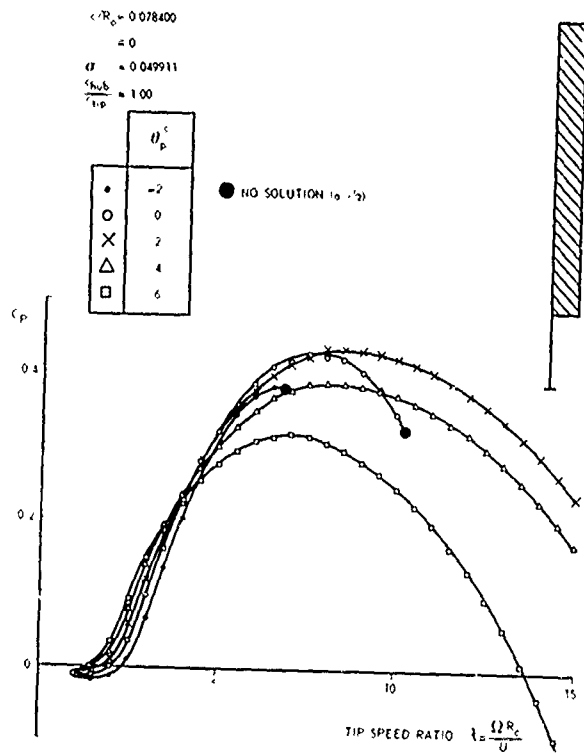


Fig. 4.28 Power output of an untwisted blade. $B=2$, $r_{hub}/R_0=0.2$

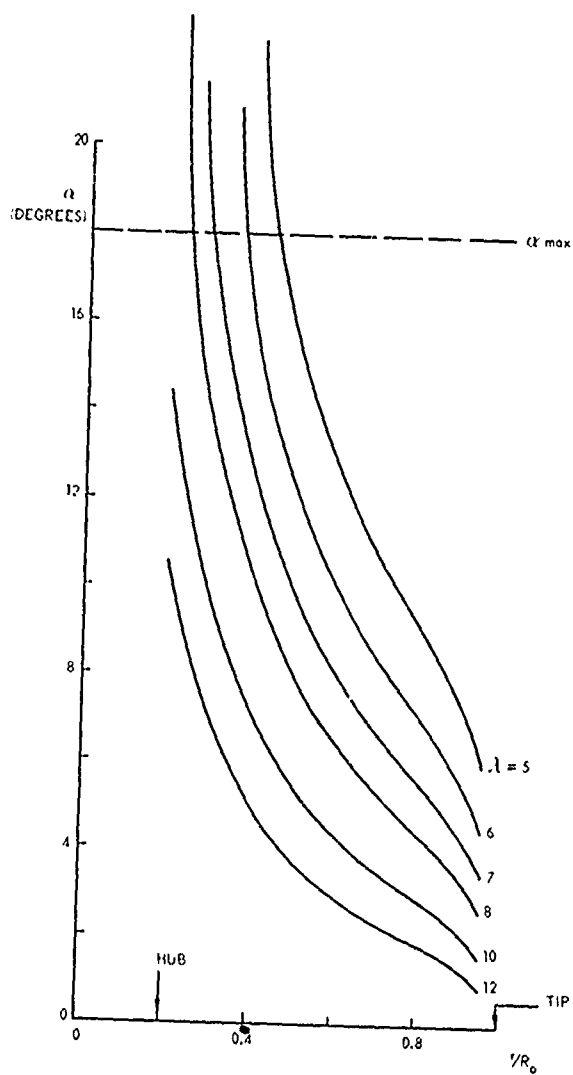


Fig. 4.29 Untwisted blade design without taper (Fig. 4.28)
Influence of λ on the spanwise α -distribution at $\theta_p^c = 0$

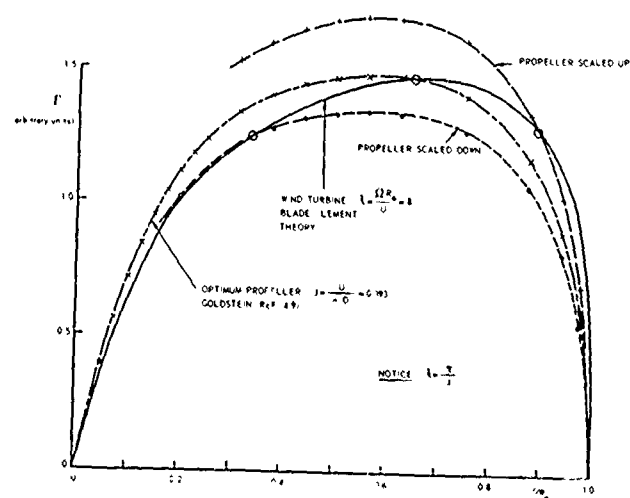


Fig. 4.30 Comparison of the shape of the circulation distribution along the blade span of a typical wind turbine, calculated with a blade-element theory and with the shape of the circulation distribution for an optimum propeller according to Goldstein $B=2$

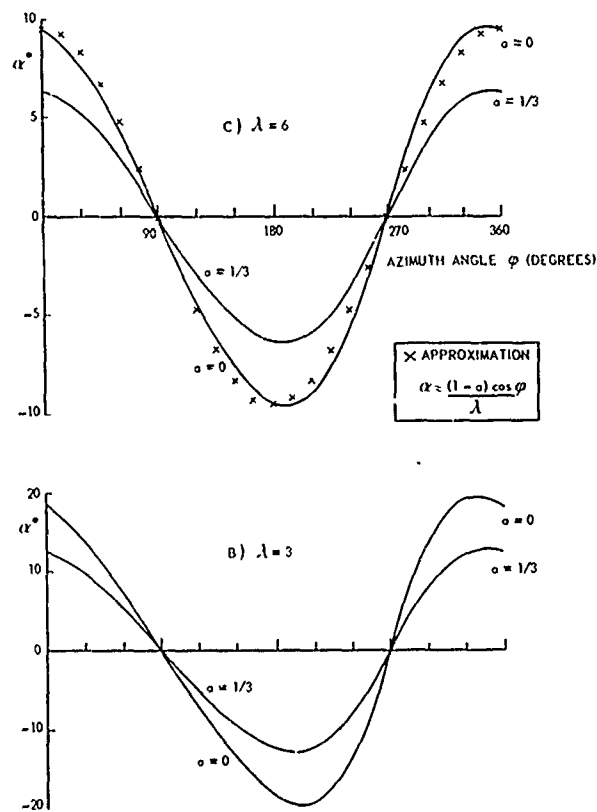
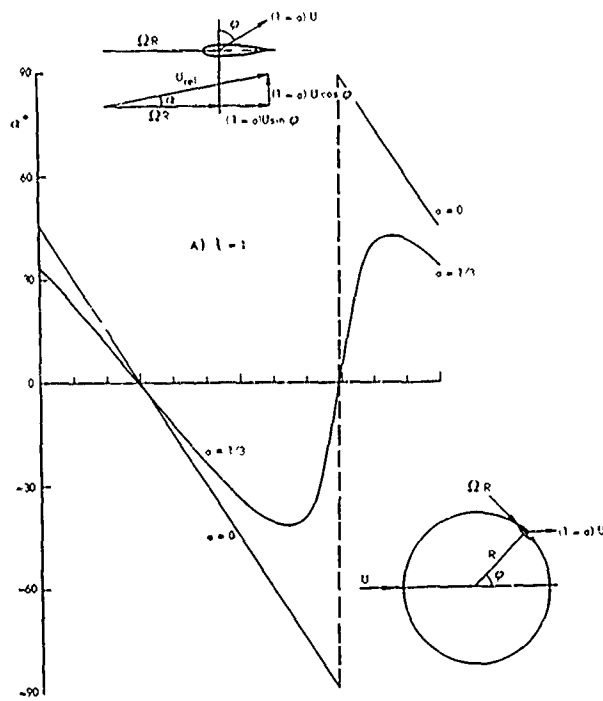


Fig. 4.31 Angle of attack as a function of the azimuth angle ϕ , the tip-speed ratio λ and induction factor a

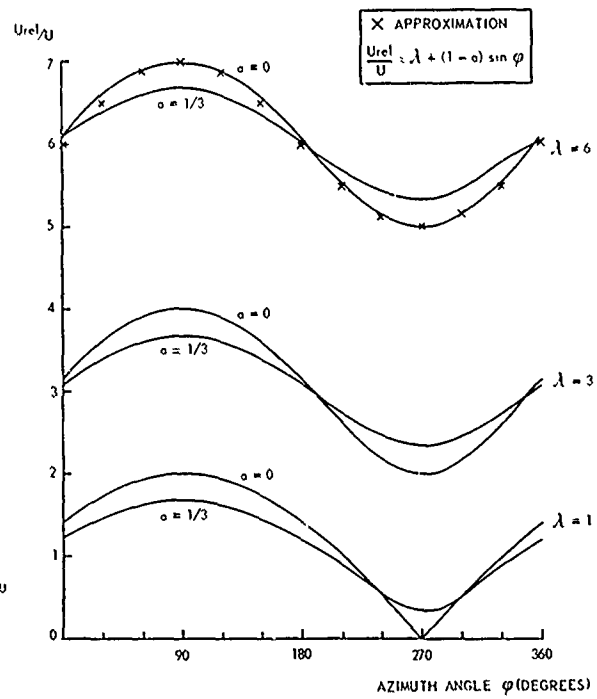


Fig. 4.32 Relative wind velocity as a function of the azimuth angle ϕ , tip-speed ratio λ and induction factor a

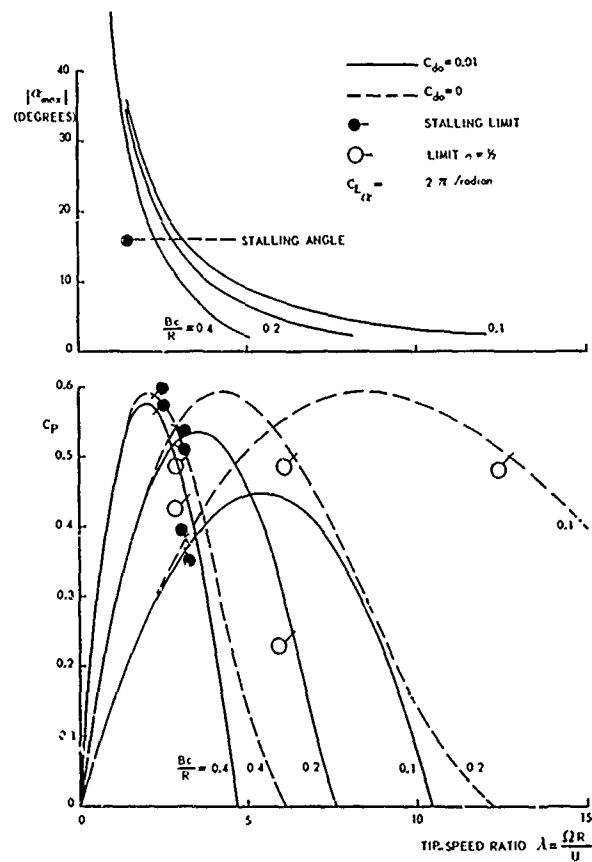


Fig. 4.33 Influence of rotor solidity Bc/R and profile drag C_{d0} on C_p and $|\alpha_{max}|$ of a two-dimensional vertical-axis turbine, according to a simplified theory

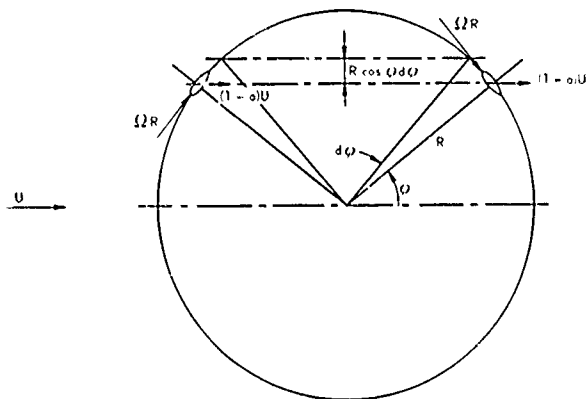


Fig. 4.34 An elemental streamtube, used in the multiple streamtube theory (Ref.4.22)

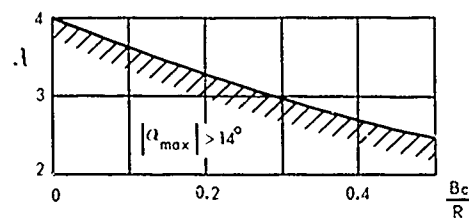


Fig. 4.37 Stall boundary as a function of the tip speed ratio λ and the rotor solidity Bc/R (Ref.4.25)

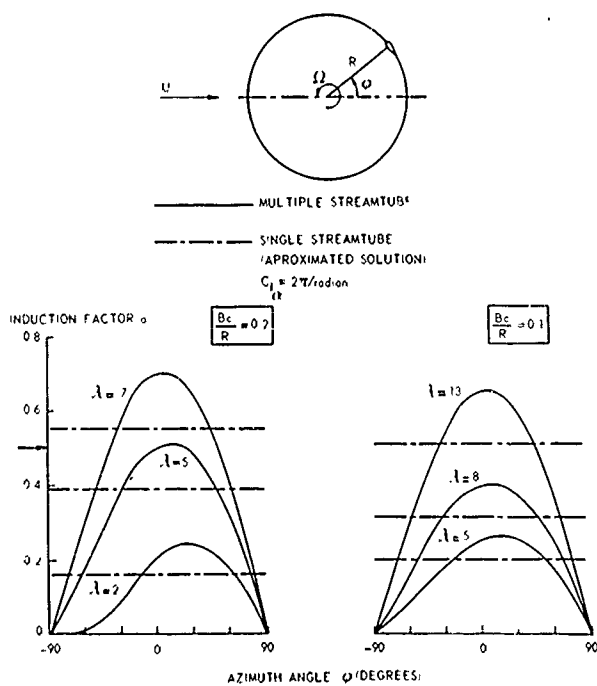


Fig. 4.35 Variation of the induction factor across the rotor diameter, according to the multiple- and the single-streamtube theory

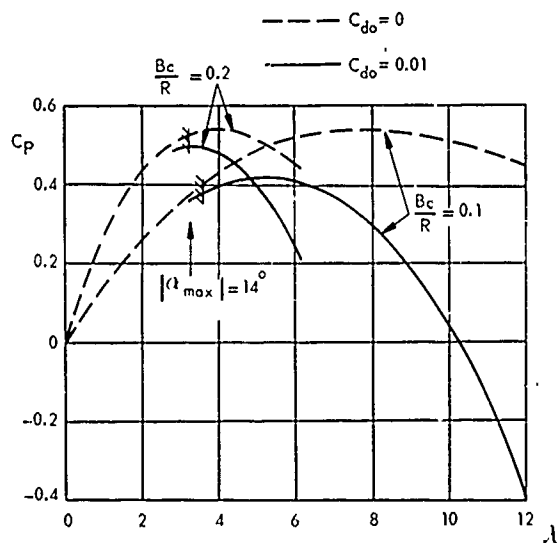


Fig. 4.38 Influence of profile drag, according to the theory of Ref.4.25

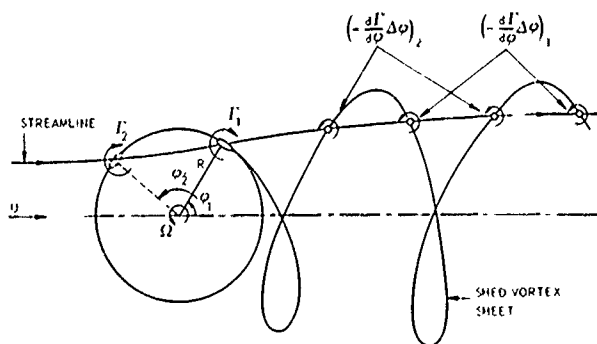


Fig. 4.36 Shed vortex system of a steadily rotating vertical axis turbine in a steady wind stream (two-dimensional)

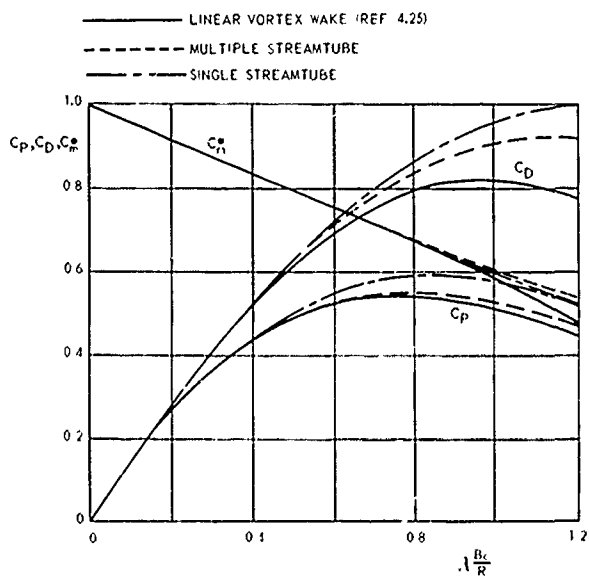


Fig. 4.39 Comparison between three calculation methods for a two dimensional vertical-axis turbine with $C_{d0}=0$

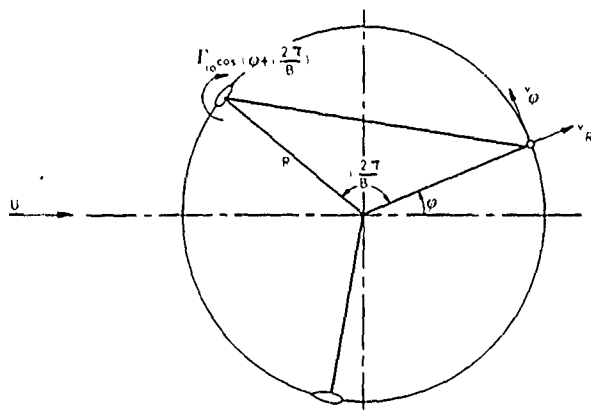


Fig 4 40 Velocities, induced on a blade of a B bladed rotor by the remaining B-1 blades

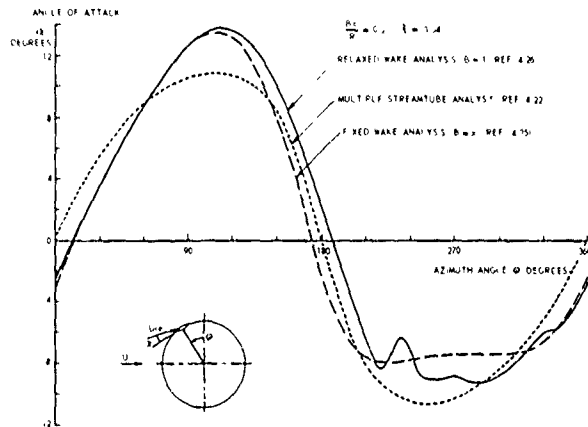


Fig 4 41 Variation of the angle of attack during one revolution, calculated by three different methods (Ref 4.26)
Notice different convention for α and ϕ

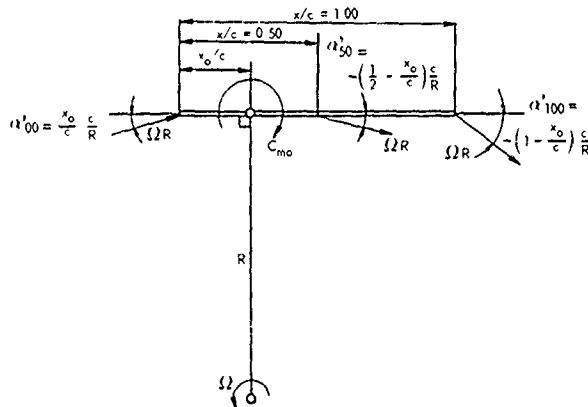


Fig 4 42 Variation of angle of attack along the blade span, depending on the location of the attachment point x

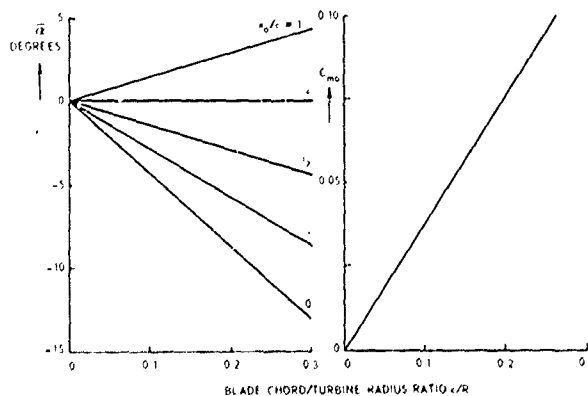


Fig 4 43 The influence of curvature and blade attachment position on effective angle of attack and pitching moment

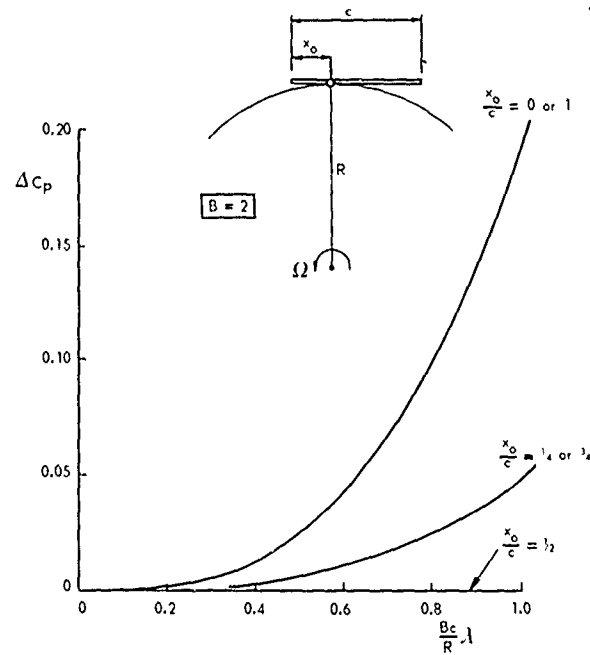


Fig 4 44 Estimated influence of the stream curvature (finite chord length) on the power coefficient

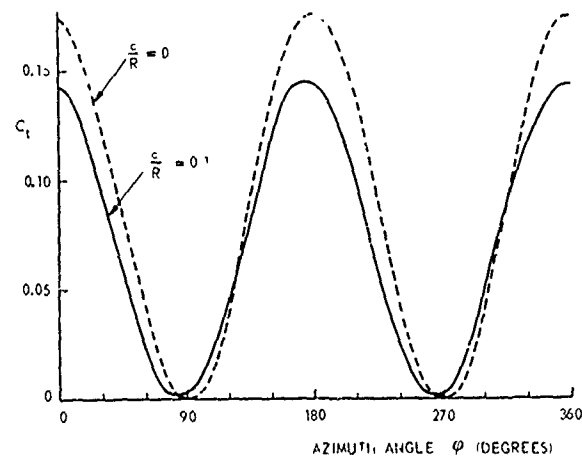
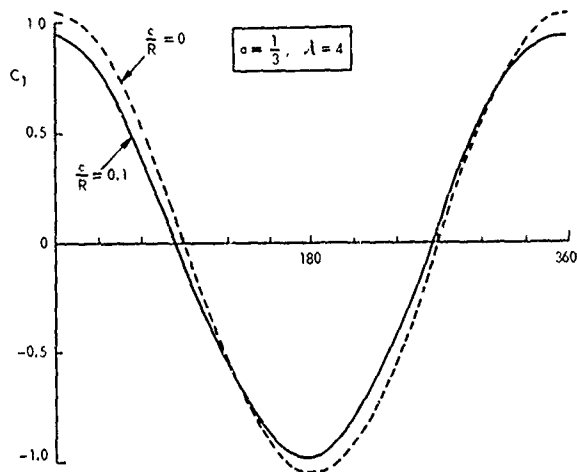


Fig. 4 45 Influence of unsteady aerodynamics on lift and tangential force (profile drag neglected)

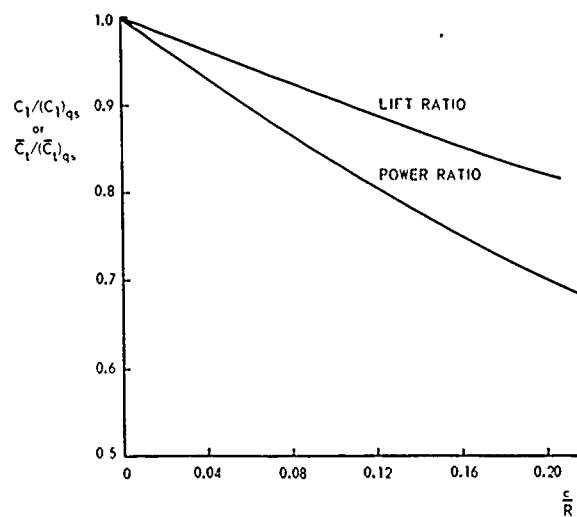


Fig 4.46 The reduction of the lift amplitude and the reduction of the power output as a function of the chord/radius ratio (notice that $k = c/2R$)

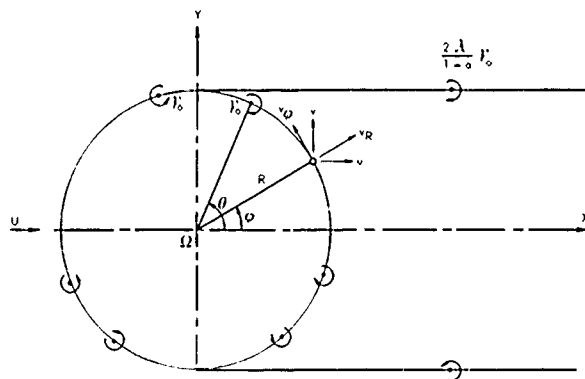


Fig 4.47 Vortex system of an idealized variable pitch turbine

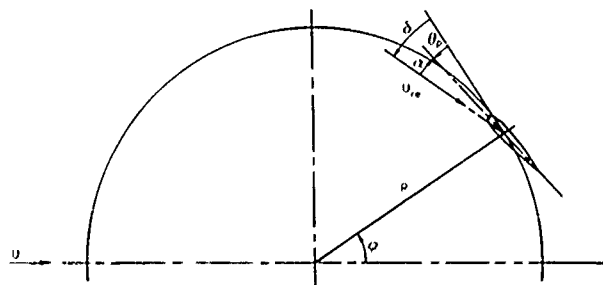


Fig. 4.48 Positive directions of pitch angle, angle of attack and flow angle δ (Eq. (4.5.45))

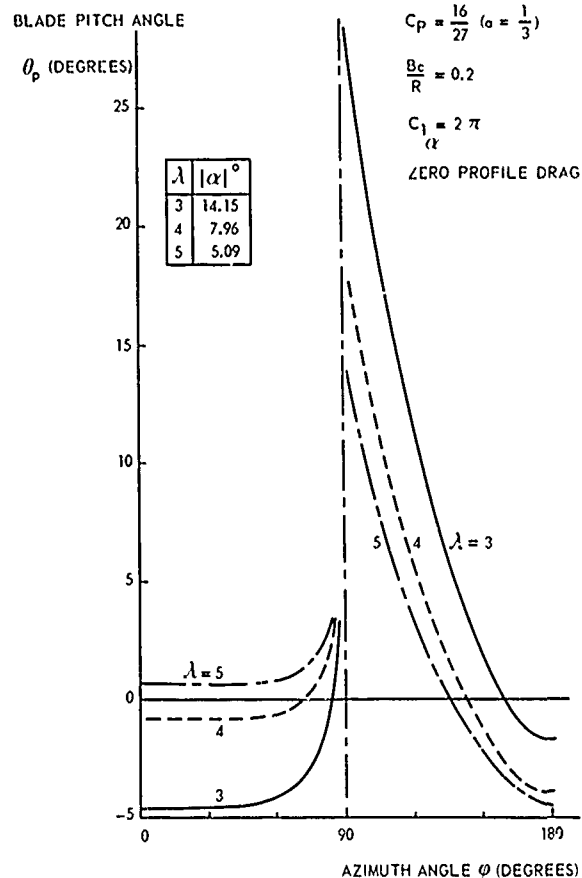


Fig. 4.49 Pitch-angle variation of an idealized variable pitch turbine (Eq. (4.5.47))

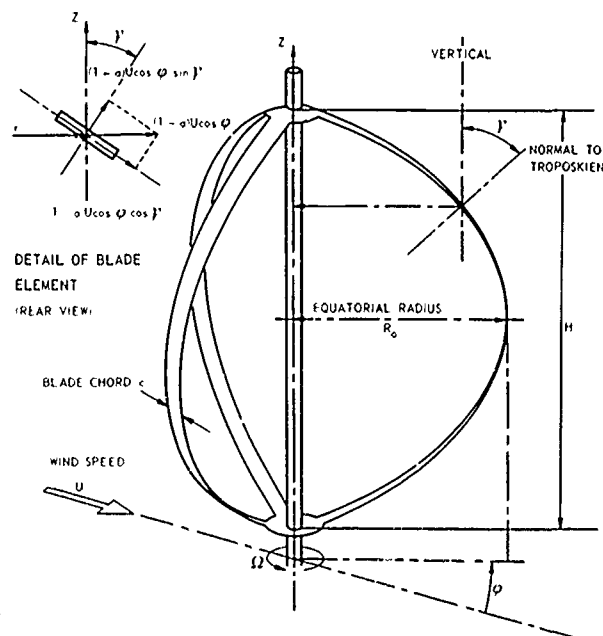


Fig 4.50 The Darrieus turbine; symbols

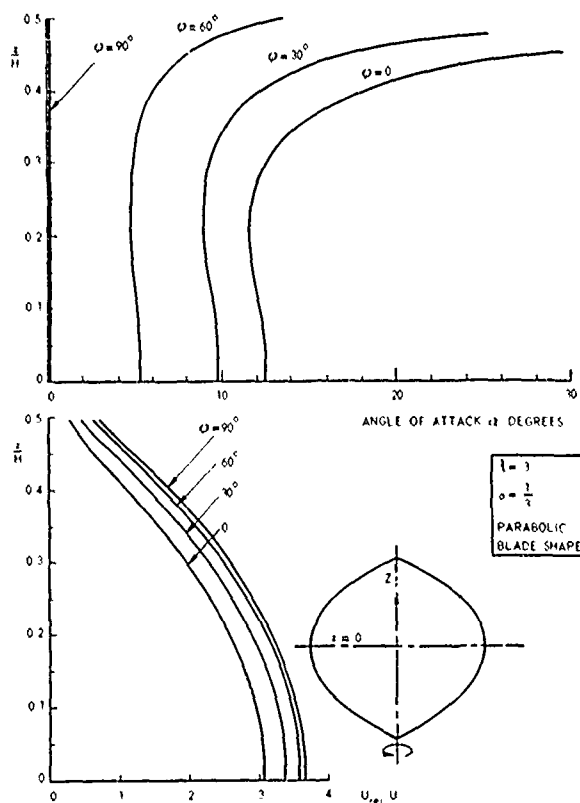


Fig. 4.51 Distribution of angle of attack and relative velocity along the blade span for a parabolic blade shape ($\eta=1$)

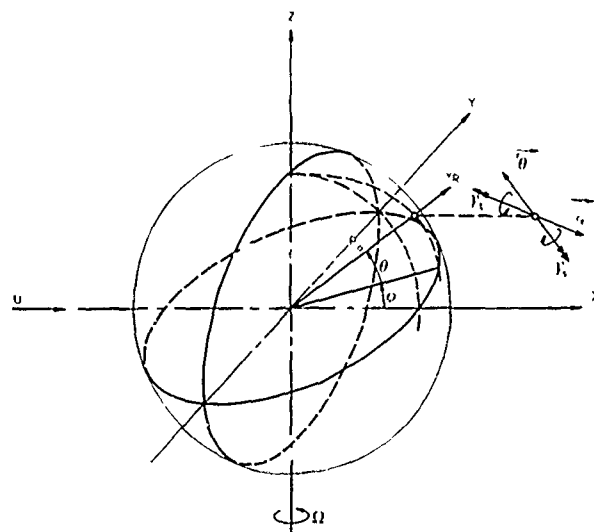


Fig. 4.53 Spherical Darrieus turbine with an infinite number of blades

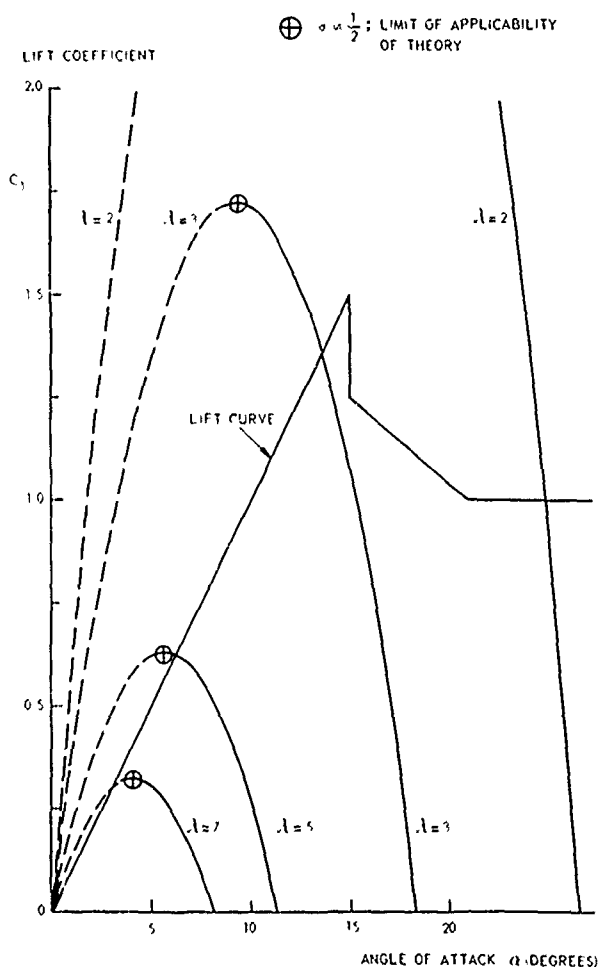


Fig. 4.52 Determination of the operating point of a blade element of a vertical-axis turbine, using multiple-streamtube theory.
 $Bc/R_0 = 0.2$; $r/R_0 = 1$; $\gamma = \pi/2$; $\phi = 0$

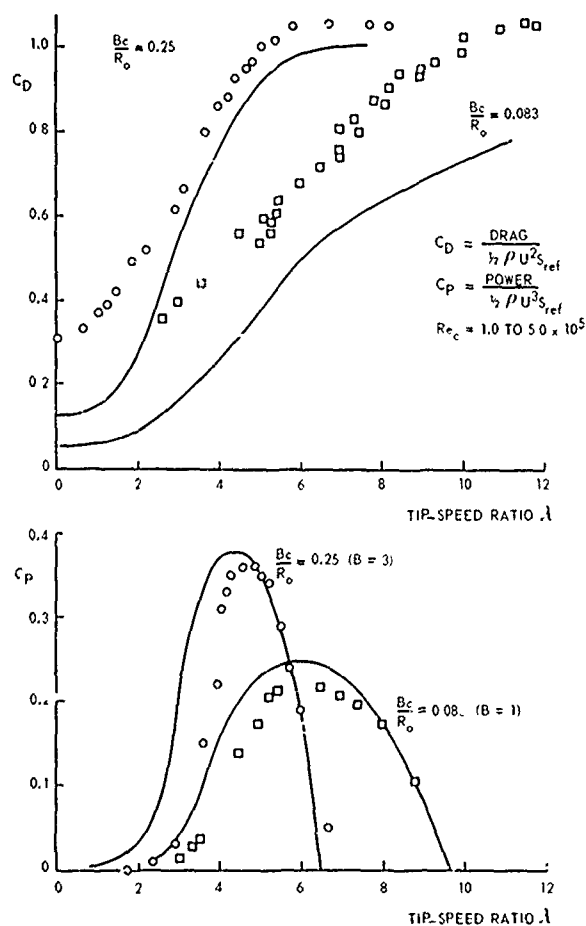


Fig. 4.54 Experimental results of Ref. 4.40, compared with the calculated results of Ref. 4.21 (single-streamtube theory)

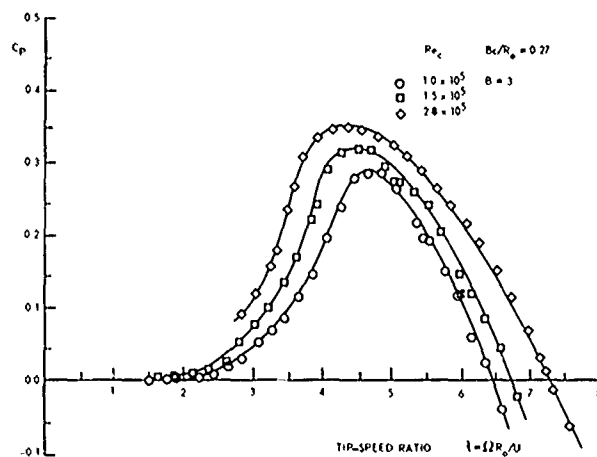


Fig. 4.55 Experimental results of Ref. 4.41; influence of the Reynolds number Re_c on the power output

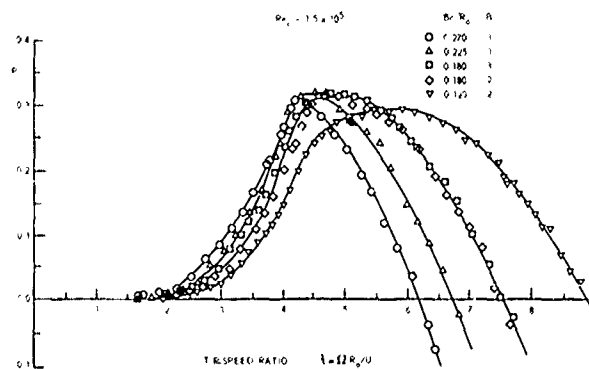


Fig. 4.56 Experimental results of Ref. 4.41; influence of the solidity ratio Bc/R_0 on the power output

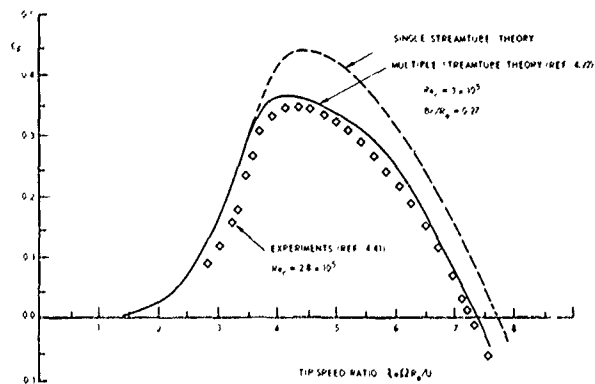


Fig. 4.57 Comparison between calculated results of the single- and the multiple-streamtube theory (Ref. 4.22) with the experimental results of Ref. 4.41

List of symbols

A	$= 0.24/(\alpha B) = \text{factor in Eq. (5.1.28)} (-)$
a	axial induction factor (-)
a	distance between turbine and reference anemometer, measured in wind direction in Fig. 5.21 (m)
a	distance upstream of turbine in Fig. 5.19 (m)
a	$= (U_H - U_{1/2H})/U_{1/2H} = \text{wind shear coefficient} (-)$
B	number of rotor blades (-)
B	constant in logarithmic formula of Eq. (5.3.1) (-)
b	distance between turbine and reference anemometer, measured perpendicular to the wind direction in Fig. 5.21 (m)
b	width of wake (m)
$b_{0.5}$	half-width of the wake (m)
c	chord of rotor blade (m)
C_D	turbine drag coefficient (-)
C_d	drag coefficient of blade section (-)
C_l	lift coefficient of blade section (-)
$C_{l\alpha}$	$= \partial C_l / \partial \alpha = \text{lift curve slope (radian}^{-1}\text{)}$
C_{m_b}	coefficient of bending moment at the blade root in Eq. (5.1.23) (-)
C_{m_y}, C_{m_z}	coefficients of moments about the y- and the z-axis through the rotor (-)
C_N	normal force coefficient (-)
C_Q	torque coefficient (-)
C_t	tangential force coefficient (-)
C_y, C_z	coefficients of forces in y- and z-direction (-)
$\overline{\Delta C_N^2}$	mean-square value of the variations of the normal force coefficient (-)
D	rotor diameter (m)
$E_1(f)$	spectral density of the wind velocity fluctuation (m^2/s)
F	normal force distribution in Eq. (5.1.7) (N/m)
f	dimensionless normal force distribution in Eq. (5.1.8) (-)
f	frequency (Hz)
$f(u)$	probability density of wind fluctuation u (-)
$f_i(\lambda)$	$= (U_i/U_1)^3 = \text{power ratio of turbine } i \text{ in an array, defined by the turbine density } \lambda (-)$
$f_\infty(\lambda)$	power ratio of a turbine in an infinite array (-)
G	tangential force distribution in Eq. (5.1.7) (N/m)
G	$= (U + u_1)/U = \text{gust factor} (-)$
g	dimensionless tangential force distribution in Eq. (5.1.8) (-)
$g(\tau)$	dimensionless lateral covariance (-)
H	height of rotor (m)
h	height of centre of rotor area or hub height (m)
i	local blade setting angle (degrees)
k	$= \omega l_{ref}/U_{ref} = \text{reduced frequency} (-)$
k	Von Karman's constant in Eq. (5.3.1) (-)
k_s	effective height of surface roughness (m)
k_{so}	surface roughness of the terrain without turbines (m)
L	length scale of turbulence in Eq. (5.1.35) (m)
L	separation distance between turbines (m)
L_g	lateral scale of turbulence (m)
l_{ref}	reference length in reduced frequency (m)
m	exponent in power-law wind-velocity distribution (-)
N	normal force or axial force (N)
N	number of turbines in an array (-)
P	power (W)
P_{design}	design power (W)
P_i	power absorbed by turbine number i (W)
P_o	power output of an isolated turbine (W)
P_r	design or "rated" power of a turbine (W)
$P(N)$	power output of turbine number N in an array (W)
$P(U)$	probability of occurrence of a wind velocity U (-)
$P(u_1)$	probability of occurrence of a positive wind fluctuation u_1 (-)
P_1, P_2	power output of turbine number 1 and number 2 (W)
Q	torque of rotor (Nm)
r	local radius or distance between turbine and reference anemometer (m)

$R(N)$	$= [P(N+1) - P(N)]/P_0$ = incremental power ratio of turbine number $N+1$ in an array (-)
R_0	maximum radius or tip radius of a rotor (m)
$R_{11}(\zeta)$	covariance of velocities at two points, separated by a dimensionless distance ζ (m^2/s^2)
S_{land}	land area occupied by one turbine in an array (m^2)
S_{ref}	reference area of a turbine; area swept by the rotor (m^2)
S_s	spoiler area (m^2)
T	tangential force (N)
T	integration time (s)
t	time (s)
U	wind velocity (m/s)
u	wind velocity fluctuation (turbulence) (m/s)
U_d	design wind speed (m/s)
u_f	contribution to velocity fluctuation from frequency f (m/s)
U_H	wind velocity at the highest point of the rotor area (m/s)
$U_{1/2H}$	wind velocity at hub height (m/s)
U_i	wind velocity at turbine number i (m/s)
U_i	cut-in speed (m/s)
u_m	maximum velocity defect in turbine wake (m/s)
U_o	cut-out wind speed (m/s)
U_o	wind velocity outside the atmospheric boundary layer (geostrophic wind speed) (m/s)
U_{rel}	velocity relative to blade element of rotor (m/s)
U_1	wind velocity at the first upwind turbine in an array, i.e. the undisturbed wind velocity (m/s)
u_1	wind velocity increase during a gust (m/s)
U_{10}	wind velocity at a height of 10 m (m/s)
U^*	$= (\tau/\rho)^{1/2}$ = friction velocity (m/s)
U'^*	effective friction velocity with turbines present (m/s)
$U(h)$	wind velocity at hub height for isolated turbine (m/s)
$U'(h)$	wind velocity at hub height for a turbine in an array (m/s)
$U'(k_{so})$	wind velocity at effective roughness height k_{so} , with turbines present (m/s)
ΔU	difference in axial wind velocity due to a small yaw angle β (m/s)
v	velocity component in y -direction (m/s)
ΔV	lateral velocity component due to a small yaw angle β (m/s)
X	$= N$ = force component in x -direction (N)
x	co-ordinate in wind direction (m)
x	$= fL/U_{10}$ = reduced frequency in Eq. (5.1.35a) (-)
x_o	virtual origin of self-preserving wake (m)
X_T	$= -UT/R_0$ = dimensionless integration distance (-)
y	horizontal co-ordinate perpendicular to the wind direction (m)
y	$= fL/U_{10}$ = reduced frequency in Eq. (5.1.35b) (-)
z, Z	vertical co-ordinate (m)
Z_o	lowest point of rotor area (m)
$Z_{1/2H}$	hub height (m)
α	angle of attack (degrees)
α	exponent in power-law wind-velocity distribution (-)
β	wind direction or yaw angle (degrees)
γ	blade slope of trophoslien (degrees)
γ	strength of vortex sheet in Fig. 5.18 (m/s)
δ	thickness of atmospheric boundary layer (m)
δ_1, δ_2	fictitious boundary layer thickness without and with turbines present (m)
ϵ_{gen}	energy dissipation in atmospheric boundary layer due to wind turbines (W/m^2)
ϵ_s	energy dissipation due to surface roughness (W/m^2)
ϵ'_s	energy dissipation due to surface roughness with turbines present (W/m^2)
ζ	$= r/R_0$ = dimensionless radial co-ordinate in Eq. (5.1.29) (-)
ζ	$= (x+x_o)/D$ = dimensionless downstream co-ordinate in Eq. (5.3.14) (-)
η	$= (Z-Z_{1/2H})/H$ = dimensionless vertical co-ordinate in Eq. (5.1.11) (-)
η	$= r/(b/2)$ = dimensionless wake-width co-ordinate in Eq. (5.3.13) (-)
θ	angle between U_{rel} and the plane of rotation of the rotor (degrees or radians)
θ_p	blade-pitch angle (degrees)
λ	$= \Omega R_0/U$ = tip-speed ratio (-)
λ	$= S_{ref}/S_{land}$ = turbine density in an array (-)
λ_{opt}	tip-speed ratio at which the optimum power coefficient is reached (-)
ρ	density of the air (kg/m^3)

σ	solidity ratio of the turbine (-)
τ	wall shear stress (atmospheric boundary layer) (N/m^2)
τ'	wall shear stress with turbines present (N/m^2)
ϕ	azimuth angle or orbital position of blade (degrees)
$\phi(\lambda)$	vertical energy influx for a finite array (W/m^2)
$\phi_{\infty}(\lambda)$	vertical energy influx for an infinite array (W/m^2)
$\phi(u_1)$	error function (-)
Ω	angular velocity of the rotor (radians/s)
ω	$= 2\pi f =$ angular frequency (s^{-1})

5.1 Effects of flow inhomogeneity and turbulence

5.1.1 Introductory remarks

In Section 4 the theory for horizontal- and vertical-axis wind turbines in a non-turbulent homogeneous air flow is discussed. An actual wind turbine is, however, submerged in a turbulent atmospheric boundary layer, i.e. the turbine is subjected to a vertical increase of the average wind velocity (wind shear) and to velocity fluctuations in space and time (turbulence, unsteadiness). Moreover, the local meteorological situation may vary more or less rapidly, e.g. by the passing of a depression or thunderstorm. This makes the description of the velocity field surrounding the turbine even more complicated, because the interaction between the turbulent wind flow and the rotating wind turbine is a non-stationary stochastic process.

This last phrase means that the stochastic process is not simply characterized by an average value and a complete set of moments of fluctuations of wind velocity and direction, but, for instance, that the average wind velocity depends on the integration time considered and does not reach an unequivocal value even by letting the integration time growing to very large values.

When one deals with the influence of the turbulent flow on the wind turbine, it is useful to distinguish between turbulent fluctuations on a scale larger than the rotor diameter and fluctuations on a scale smaller than the rotor diameter. The underlying idea is that fluctuations can only affect the turbine as a whole if the fluctuations act on all blade elements simultaneously, i.e. the fluctuations must have a scale of the order of the rotor diameter or larger. Fluctuations with a smaller scale tend to have opposite effects on different blade elements and the integrated effect might tend to zero. The small-scale fluctuations may also have a deteriorating effect on the rotor performance, e.g. by inducing a local blade stall.

The definition of the integral scale appearing in the theory of homogeneous turbulence may be used for the above-mentioned purpose, but it is not very suitable.

Because there is a kind of inverse relationship between scale and frequency, it might also be possible to define a low-frequency range in which the turbine as a whole is affected, and a high-frequency range of turbulent fluctuations which have only a local effect on the rotor blades. It is clear, however, that a more specific statistical analysis has to be set up to obtain an adequate description of the effect of the turbulent wind flow on the turbine.

Much information about wind fluctuations, peak velocities, etc., can be found in the literature dealing with industrial aerodynamics and a thorough survey of this literature seems profitable for a wind turbine designer. Such a survey has not been made in this report, but the reader is referred to the work of Frost (Ref. 5.1).

Besides the influence of the turbulent wind on the turbine with respect to the power production, the influence on the blade loading is perhaps even more important. Two aspects of the blade loading must be emphasized here, viz.:

- The extreme gust in connection with the specification of an ultimate load case for the rotor blade (Ref. 5.1).
- The contribution to the fatigue loading due to the lasting velocity fluctuations. This is also closely connected to the elasto-mechanic behaviour of the turbine to these load variations.

This Section deals only briefly with the aerodynamic effects related to wind shear and turbulence, because the last item is an underdeveloped area in the literature. The aspects of the turbulence of the wind in relation to turbine control, will be discussed in Section 5.2. The problems connected with field tests have been mentioned in Section 4.5.7.4 (see also the Refs 5.2 and 5.3), and will not be discussed in the subsequent Sections.

5.1.2 Effect of wind shear

Due to the friction with the earth surface, the wind velocity is reduced close to the earth surface, which leads to a kind of "boundary layer", the so-called "atmospheric boundary layer". The vertical variation of the average wind velocity (wind shear) is often represented by a power law (see Sect. 2.2.3) or by a logarithmic law (see e.g. Ref. 5.4), both valid in the lower part of the atmospheric boundary layer (say up to 100 m). There are meteorological conditions where the logarithmic and power laws do not apply, but on relatively flat terrain and wind velocities above say 5 m/s, these cases will be relatively rare.

In practice, the rotor of a wind turbine is placed at some distance above the ground to avoid the extreme low-velocity part of the atmospheric boundary layer (low energy content). This results in a more or less linear velocity increase over the height of the rotor (see Fig. 5.1).

The average wind direction will also vary with height in an atmospheric boundary layer, but this effect will be negligible over the rotor height in most cases.

The influence of a vertical wind shear on a vertical-axis (Darrieus) wind turbine is rather easily estimated by means of the multiple-streamtube theory (Ref. 5.5), by assigning to each streamtube its corresponding wind velocity. It is also possible to divide the rotor area in horizontal slices, each with its own value of the wind velocity, and to apply the single-streamtube theory to each slice separately. Which of the two methods gives the best estimate is difficult to assess, but there is an indication that, in homogeneous flow the multiple-streamtube theory gives better results (see Sect. 4.5.3) and it is to be expected, therefore, that this will also be the case in a shear flow.

In case of a wind shear, there is some arbitrariness in the choice of the reference wind velocity to calculate C_p . There is a growing acceptance of taking the wind velocity at half the rotor height ($Z_{1/2}$, Fig. 5.1).

The influence of a wind shear on a Darrieus turbine can easily be demonstrated by comparing the

output of the same turbine in a uniform flow by making use of the symmetry properties of the rotor about $Z_{1/2H}$.

Defining a dimensionless vertical coordinate

$$\eta = (Z - Z_{1/2H})/H, \quad (5.1.1)$$

the contributions of the horizontal slices of the rotor to the power coefficient C_p in a uniform flow can be represented by

$$dC_p/d\eta,$$

which has to satisfy the following conditions:

$$(dC_p/d\eta)_{+\eta} = (dC_p/d\eta)_{-\eta}, \quad C_p = \int_{-\frac{1}{2}}^{+\frac{1}{2}} (dC_p/d\eta) d\eta, \quad \text{and} \quad (dC_p/d\eta)_{\eta=\pm\frac{1}{2}} = 0.$$

To satisfy the above conditions (representing the power output about λ_{opt}) the simplest interpolation formula is

$$dC_p/d\eta = \frac{3}{2} C_p (1 - 4\eta^2), \quad (5.1.2)$$

which formula will be used to give a first estimation of the wind-shear effect.

In case of a linear wind shear, the velocity distribution can be written as (Fig. 5.1):

$$U/U_{1/2H} = 1 + 2a\eta, \quad \text{with } a = (U_H - U_{1/2H})/U_{1/2H}. \quad (5.1.3)$$

The power output of each slice depends on $(U/U_{1/2H})^3$, and when it is assumed that small variations of the local λ do not affect the $dC_p/d\eta$ around λ_{opt} , the power coefficient in a wind shear $(C_p)_{ws}$ is

$$(C_p)_{ws} = \frac{3}{2} C_p \int_{-\frac{1}{2}}^{+\frac{1}{2}} (1 - 4\eta^2) (1 + 2a\eta)^3 d\eta = C_p (1 + \frac{3}{5} a^2). \quad (5.1.4)$$

This shows that the power output in a linear wind shear is only slightly larger than the power output in a uniform flow with a velocity equal to $U_{1/2H}$.

In Ref. 5.5, the influence of the wind shear is calculated for a 1/7th-power-law velocity profile with $Z_0 = 0$ (or $Z_{1/2H} = H/2$, see Fig. 5.1), which reveals a slightly smaller power output than in a uniform flow.

When a power law velocity profile

$$U/U_{1/2H} = (2\eta + 1)^m \quad (5.1.5)$$

is taken, the power coefficient in a wind shear can be estimated from

$$(C_p)_{ws} = \frac{3}{2} C_p \int_{-\frac{1}{2}}^{+\frac{1}{2}} (1 - 4\eta^2) (2\eta + 1)^{3m} d\eta = \frac{3}{2} C_p \frac{(2)^{3m+2}}{(3m+3)(3m+2)}. \quad (5.1.6)$$

In a uniform flow, $m = 0$ and $(C_p)_{ws} = C_p$. In the case $m = 1/7$, $(C_p)_{ws} = 0.9699 C_p$, which shows a slight decrease of the power output due to the wind shear, in agreement with Ref. 5.5.

The above estimates are only representative for the situation at λ_{opt} . For tip-speed ratios differing strongly from λ_{opt} , Eq. (5.1.2) does not give an adequate representation of the distribution of C_p across the rotor area and the influence of $\partial C_p / \partial \lambda$ has also to be taken into account. It is obvious, however, that the effect of a wind shear on the power output is small. It is also shown, that the assumption of a linear wind shear may lead to power changes with a different sign. The differences will be less when $Z_0 \neq 0$.

Instead of the limited discussion above, it would be possible to set up a more complete analysis by taking $dC_p/d\eta = f(\lambda)$, but a direct calculation as that given in Ref. 5.5 seems preferable.

The influence of the wind shear on the blade loading of a Darrieus turbine could be estimated in a similar way, but the influence will certainly be small, because of the small effect on C_p shown above.

The influence of a wind shear on the power output and the blade loading of a horizontal-axis wind turbine is more complicated, because each blade element is subjected to a varying wind velocity during a revolution of the rotor. Therefore, apart from a possible effect on the power output, a stationary wind shear causes a varying blade load during a revolution (blade fatigue). It is possible to estimate the effect a wind shear by a method developed originally by Glauert (Ref. 5.3). This method resembles the above-given estimates for the Darrieus turbine in so far that it makes use of the known distribution of normal and tangential blade loads in a uniform flow, but the analysis is more complicated.

Ref. 5.6 uses the blade-element theory more directly, but the linearized results agree with those obtained from Ref. 5.7. An almost similar analysis is given by Ref. 5.8, but no explicit formulae are given. Below, the effect of a wind shear will be estimated by the method of Ref. 5.7.

In homogeneous flow, the total normal force and the total torque for a B-bladed rotor can be obtained from dN and dT on the blade elements, thus (see Fig. 5.2)

$$N = X = B \int F dr; \quad Q = -M_x = B \int G dr; \quad (5.1.7)$$

or in dimensionless form,

$$C_N = \frac{N}{\frac{1}{2} \rho U_{1/2H}^2 \pi R_0^2} = B \int f d\left(\frac{r}{R_0}\right); \quad C_Q = \frac{Q}{\frac{1}{2} \rho U_{1/2H}^2 \pi R_0^3} = B \int g \frac{r}{R_0} d\left(\frac{r}{R_0}\right), \quad (5.1.8)$$

where f and g are functions of λ and r/R_0 , which can be calculated from the theory of Section 4.4.

A rotor at constant Ω in a wind shear might exhibit different forces and moments (Fig. 5.2), which, in general, can be calculated from

$$\begin{aligned} C_N + \Delta C_N &= \sum_{i=1}^B \int (f + \Delta f)_i d\left(\frac{r}{R_0}\right), \\ C_Y + \Delta C_Y &= \sum_{i=1}^B \int (g + \Delta g)_i \sin \phi_i d\left(\frac{r}{R_0}\right), \\ C_Z + \Delta C_Z &= \sum_{i=1}^B \int (g + \Delta g)_i \cos \phi_i d\left(\frac{r}{R_0}\right), \\ C_Q + \Delta C_Q &= \sum_{i=1}^B \int (g + \Delta g)_i \frac{r}{R_0} d\left(\frac{r}{R_0}\right), \\ C_{m_Y} + \Delta C_{m_Y} &= \sum_{i=1}^B \int (f + \Delta f)_i \frac{r}{R_0} \sin \phi_i d\left(\frac{r}{R_0}\right), \\ C_{m_Z} + \Delta C_{m_Z} &= \sum_{i=1}^B \int (f + \Delta f)_i \frac{r}{R_0} \cos \phi_i d\left(\frac{r}{R_0}\right), \end{aligned} \quad (5.1.9)$$

with Δf and Δg the increments in f and g due to the increment of the wind velocity ΔU with respect to $U_{\frac{1}{2}H}$. It must be noticed that $C_Y = C_Z = C_{m_Y} = C_{m_Z} = 0$.

The increment of the wind velocity leads to a variation of λ , viz.

$$\lambda + \Delta\lambda = \Omega R_0 / (U_{\frac{1}{2}H} + \Delta U) = (\Omega R_0 / U_{\frac{1}{2}H}) [1 + (U / U_{\frac{1}{2}H})]^{-1} \approx \lambda [1 - (U / U_{\frac{1}{2}H})] \quad (5.1.10)$$

The increment in F can be calculated quite generally from

$$\Delta F = \frac{\partial F}{\partial U} \Delta U + \frac{\partial F}{\partial \lambda} \Delta \lambda,$$

or with Eq. (5.1.10) and because $\partial(U^2)/\partial U = 2U \approx 2U_{\frac{1}{2}H}$,

$$\Delta F = 2F \frac{\Delta U}{U_{\frac{1}{2}H}} - \lambda \frac{\partial F}{\partial \lambda} \frac{\Delta U}{U_{\frac{1}{2}H}} = \frac{\Delta U}{U_{\frac{1}{2}H}} (2 - \lambda \frac{\partial}{\partial \lambda}) F,$$

or in dimensionless form

$$\Delta f = \frac{\Delta U}{U_{\frac{1}{2}H}} (2 - \lambda \frac{\partial}{\partial \lambda}) f. \quad (5.1.11)$$

In a similar way, it can be obtained that

$$\Delta g = \frac{\Delta U}{U_{\frac{1}{2}H}} (2 - \lambda \frac{\partial}{\partial \lambda}) g. \quad (5.1.12)$$

In the case of a linear wind shear, $\Delta U / U_{\frac{1}{2}H}$ can be written as

$$\Delta U / U_{\frac{1}{2}H} = a(r/R_0) \sin \phi, \text{ with } a = (U_H - U_{\frac{1}{2}H}) / U_{\frac{1}{2}H}. \quad (5.1.13)$$

With the Eqs (5.1.11) through (5.1.13), the forces and moments on the complete rotor or on a single rotor blade can be calculated from the Eqs (5.1.9). The main difficulty, however, is to obtain expressions for f and g . Figure 5.3 gives an example of an f - and g -distribution, calculated for a two-bladed rotor with the theory of Sect. 4.4.3.1. Tip effects and partial blade stall make it very complicated to find analytical expressions; therefore, a numerical approach seems inevitable. In order to indicate some general trends of the wind-shear effect, calculations will be shown with strongly simplified expressions for f and g , viz.

$$f = (0.24/B) \lambda r / R_0 \text{ and } g = (0.30 - 0.02\lambda) / B. \quad (5.1.14)$$

Figure 5.4 shows these simplified distributions for a two-bladed rotor (compare these simplified distributions with the distributions of Fig. 5.3).

In order to get an impression about the λ -range in which the simplified expression may apply, the C_N , C_Q and C_p are calculated from f and g , which leads to the following expressions (see Fig. 5.5)

$$\begin{aligned} C_N &= 0.12\lambda, \\ C_Q &= 0.15 - 0.01\lambda, \\ C_p &= \lambda(0.15 - 0.01\lambda). \end{aligned} \quad (5.1.15)$$

The increments in forces and moments due to the wind shear can now be calculated from the Eqs (5.1.9) and (5.1.11) through (5.1.14).

$$\Delta C_N = 0.08\lambda a \frac{1}{B} \sum_{i=1}^B \sin \phi_i, \quad (5.1.16)$$

$$\Delta C_Y = 0.01(30 - \lambda)a \frac{1}{B} \sum_{i=1}^B \sin^2 \phi_i, \quad (5.1.17)$$

$$\Delta C_z = 0.01(30-\lambda)a \frac{1}{B} \sum_{i=1}^B \sin \phi_i \cos \phi_i, \quad (5.1.18)$$

$$\Delta C_Q = 0.00666(30-\lambda)a \frac{1}{B} \sum_{i=1}^B \sin \phi_i, \quad (5.1.19)$$

$$\Delta C_{m_y} = 0.06\lambda a \frac{1}{B} \sum_{i=1}^B \sin^2 \phi_i, \quad (5.1.20)$$

$$\Delta C_{m_z} = 0.06\lambda a \frac{1}{B} \sum_{i=1}^B \sin \phi_i \cos \phi_i. \quad (5.1.21)$$

It must be remembered, that

$$\begin{aligned} \frac{1}{B} \sum_{i=1}^B \sin \phi_i &= \begin{cases} \sin \phi & \text{if } B = 1 \\ 0 & \text{if } B \geq 2 \end{cases}, \\ \frac{1}{B} \sum_{i=1}^B \sin^2 \phi_i &= \begin{cases} \sin^2 \phi & \text{if } B \leq 2 \\ \frac{1}{2} & \text{if } B \geq 3 \end{cases}, \\ \frac{1}{B} \sum_{i=1}^B \sin \phi_i \cos \phi_i &= \begin{cases} \sin \phi \cos \phi & \text{if } B \leq 2 \\ 0 & \text{if } B \geq 3 \end{cases}. \end{aligned} \quad (5.1.22)$$

The following general conclusions can be drawn from the above formulae:

- The normal force (or drag C_N) and the torque (C_Q) are not affected by a linear wind shear, except in case of a one-bladed rotor.
- The side force (C_y) and the "pitching" moment (C_{m_y}) vary as $\sin^2 \phi$ in case of a one- or two-bladed rotor, and show a constant non-zero value in case of a three- or more-bladed rotor. It must be noticed, that C_y and C_{m_y} do not change sign during a revolution.
- The vertical force (C_z) and the "yawing" moment (C_{m_z}) vary as $\sin \phi \cos \phi$ in case of a one- or two-bladed rotor and are zero for a three- or more-bladed rotor.
- The force and moment variations of one blade of a B-bladed rotor can be obtained from the above formulae by restricting the sum to $B = 1$, maintaining the factor $1/B$.

To get some insight into the order of magnitude of the variations due to the wind shear, Fig. 5.5 shows C_N , C_Q and C_p versus λ in a uniform flow, and Fig. 5.6 shows the force and moment increments due to a linear wind shear with $a = 0.10$ (an increase of the wind velocity of 20 % over the rotor height is large).

From the figures, it appears that the maximum force increments during one revolution are small with respect to C_N in uniform flow, which can be regarded as a representative force in connection with the support of the rotor axis. The moment increments, however, especially the pitching moment C_{m_y} , may give a significant contribution compared with the torque of the rotor C_Q (notice that the maximum of $\sin^2 \phi = 1$ and of $|\sin \phi \cos \phi| = \frac{1}{2}$).

The load variation on one blade of a B-bladed rotor can be obtained from Fig. 5.6 by dividing the variation with λ by B and taking the multiplication factor for $B = 1$. These load variations have to be compared with C_N/B and C_Q/B of Fig. 5.5. The percentual load variations are not large, but might be significant for determining fatigue load levels.

Another important blade load fluctuation has to be considered, viz. the blade bending moment at the blade root. This could be estimated from

$$C_{m_b} = M_{\text{blade root}} / \frac{1}{2} \rho U^2 \pi R_0^3 = \int f(r/R_0) d(r/R_0) = (0.08/B)\lambda \quad (5.1.23)$$

$$\Delta C_{m_b} = \int \Delta f(r/R_0) d(r/R_0) = (0.06/B)\lambda a \sin \phi \quad (5.1.24)$$

This shows, that the maximum amplitude of the bending moment fluctuation is about 8 % of the bending moment in uniform flow, at a wind-shear factor $a = 0.10$.

The above-mentioned simplified calculations can be extended by improving the representation of f and g and by including a non-linear wind shear. The actual calculations, however, become so complicated, that a numerical approach has to be chosen instead of the analytical one. In such a case, a more direct calculation with a blade element method seems to be preferable.

This could be envisaged by taking the radial wind velocity distribution for a specific blade position ϕ and apply the blade element theory as if this velocity distribution was present at each blade position (axisymmetric wind velocity distribution). This procedure can be repeated for different blade positions ϕ .

When the blade loads for a proper set of azimuth angles ϕ_i ($i = 1, \dots, B$) are combined, the total rotor load in a wind shear can be obtained. Of course, a lot of aspects have been ignored in this approach (e.g. unsteady effects), but the results might be more useful than the results obtained with the method of Ref. 5.7 or 5.6.

Somewhat related to the effect of wind shear is the influence of a small misalignment of the rotor axis with respect to the wind direction, i.e. of a small yaw angle β . This results in a small decrease of the axial velocity

$$\Delta U = -U(1 - \cos \beta) \approx -\frac{1}{2}U\beta^2,$$

and a small lateral velocity component

$$\Delta V = U \sin \beta \approx U\beta,$$

which are independent of height above the ground or lateral distance. ΔU is small because of its dependence on β^2 . ΔV may not be small with respect to U , but has to be considered with respect to $\Omega r = \lambda U(r/R_0)$, which is much larger than U over a large part of the blade span. The influence of yaw can be calculated according to the method given in Ref. 5.7, but the remarks above already indicate that the influence is small at yaw angles up to 10 degrees.

5.1.3 Effect of turbulence and unsteadiness of the wind

A turbulent boundary layer is often described as a steady flow with a velocity $U = U(z, x)$, on which turbulent velocity fluctuations u, v, w are superimposed. The instantaneous values of the fluctuations cannot be given in a deterministic way; it is only possible to describe them in a statistic manner by RMS-values, cross-correlations and spectra.

In an atmospheric boundary layer, the average wind velocity U and also the average wind direction β are not steady, which makes it difficult to distinguish between U and u, v, w , i.e. between the average velocity and the fluctuating components.

It is thought that the higher-frequency velocity fluctuations are determined by the local characteristics of the atmospheric boundary layer (surface roughness, wind shear, temperature gradient) and that the velocity fluctuations connected with variations in average wind speed and wind direction are determined by the large-scale weather system (barometric pressure distribution) and by large-scale geographic characteristics (ocean or main land, latitude, day or night), thus leading to much lower frequencies.

Figure 5.7 shows a power spectrum of the wind velocity, recorded during several months. This example shows that there indeed is an appreciable frequency gap between the high-frequency "turbulent" fluctuations (peak at 40 cycles/h ≈ 0.01 Hz) and the low-frequency "macro-meteorological" fluctuations (peaks at 0.01 and 0.08 cycles/h). The tentative conclusion can be drawn that the average wind velocity and direction can be defined by using an integration time of 10 to 15 minutes. The deviations of the instantaneous velocity and direction from this 10 minutes average is then called "turbulence".

There are many cases in which this separation between average and turbulence is not so clear, because of a sudden jump of the velocity to a higher (or lower) value, e.g. during a local thunderstorm. Also connected with turbulence as it is usually visualized (e.g. the idealization of local isotropy) is the "gust". Though a gust can be considered as an exceptional strong and large-scale turbulent fluctuation, it is often mentioned separately because of its influence on the turbine loading (strength). In Ref. 5.1, some information about gusts is given. The time history of a gust (slope of the velocity increase, duration of increased velocity level, slope of velocity decrease) is defined by a mathematical expression. Probability distributions for the parameters included in this mathematical expression are given.

The influence of turbulence on a wind turbine is a very complex problem. Ref. 5.9 reports on a first attempt to calculate the aerodynamic response of a wind turbine to turbulence. To that end, a "pseudo" turbulence is generated by a computer code and its influence on the rotor is calculated by a blade-element method. The calculations are still in a preliminary stage.

In order to indicate some of the problems involved, a crude and sketchy discussion will be given of the influence of isotropic turbulence on the normal force of a separate rotor blade of a horizontal-axis turbine.

According to blade-element theory, the normal force distribution along the blade span can be calculated from

$$dC_N/d(r/R_0) = \frac{1}{\pi} C_{l\alpha} (\theta - i) (c/R_0) (U_{rel}/U)^2 \cos \theta, \quad (5.1.25)$$

when the profile drag is neglected. The turbulent fluctuations u, v, w affect U_{rel} and θ . When a high-speed turbine ($\lambda \gg 1$) is considered, it can be shown that the influence on U_{rel} can be neglected with respect to the influence on θ . Furthermore, it can be shown that the influence of v and w on θ can be neglected with respect to the influence of u on θ , which results in the following variation in θ

$$\Delta \theta \approx \frac{u/U}{\lambda r/R_0}. \quad (5.1.26)$$

Because θ is relative small when $\lambda \gg 1$, $\cos(\theta + \Delta \theta) \approx \cos \theta$, and from Eq. (5.1.25) it follows that

$$\Delta \frac{dC_N}{d(r/R_0)} \approx \frac{\Delta \theta}{\theta - i} \frac{dC_N}{d(r/R_0)} = \frac{u/U}{(\lambda r/R_0)(\theta - i)} \frac{dC_N}{d(r/R_0)}. \quad (5.1.27)$$

In case of a high- λ design operating near λ_{opt} , the angle of attack $\alpha = \theta - i$ is almost constant along the span. When the approximation for $dC_N/d(r/R_0)$ given in the Eqs (5.1.8) and (5.1.14) for one blade is taken, Eq. (5.1.27) can be written as

$$\Delta dC_N/d(r/R_0) \approx 0.24/(\alpha B) (u/U) = Au/U. \quad (5.1.28)$$

It must be noted, that A is independent of r/R_0 , which means that the local normal-force fluctuation is proportional to the local wind fluctuation.

At a definite instant t , the normal-force variation due to a turbulent velocity difference $u = u(x, y, z, t)$ can be calculated from

$$\Delta C_N(t) = A \int_0^1 \frac{1}{U} u[(r/R_0), t] d(r/R_0).$$

This is also a stochastic quantity with a time average zero, because $\bar{u} = 0$. In order to obtain a statistical measure of the normal-force fluctuation, the time average of $(\Delta C_N)^2$ has to be considered. When the equation

$$\left[\int_a^b f(x) dx \right]^2 = \int_a^b dx \int_{-x}^{b-x} f(x) f(x+\zeta) d\zeta$$

is used, the square of ΔC_N can be calculated from

$$\Delta C_N^2(t) = A^2 \int_0^1 d(r/R_0) \int_{-r/R_0}^{1-r/R_0} \left(\frac{1}{U}\right)^2 u[(r/R_0), t] u[(r/R_0)+\zeta, t] d\zeta.$$

The time average of this value, indicated by an overbar, could be calculated from the following equation, with T the integration time needed to obtain a meaningful average, thus

$$\overline{\Delta C_N^2} = A^2 \int_0^1 d(r/R_0) \int_{-r/R_0}^{1-r/R_0} d\zeta T^{-1} \int_0^T \left(\frac{1}{U}\right)^2 u[(r/R_0), t] u[(r/R_0)+\zeta, t] dt. \quad (5.1.29)$$

The evaluation of the time integral is very complex, even when isotropic turbulence is assumed that is transported downstream with the main stream velocity U and that is not affected by the turbine.

In the theory of isotropic turbulence, space averages are assumed to be equal to the so-called "ensemble" averages, using the ergodic hypothesis. A time average in a main stream with a velocity U at a fixed point in space can be related to the space average by the Taylor hypothesis. The ensemble average is a theoretical concept of averaging values obtained from a number of independent realizations of a certain configuration at a given instant (e.g. the product of velocity components u at two points fixed in space at a given time t).

When the turbulent fluctuations $u(x, y, z, t)$ are described in a coordinate system moving with the main flow (velocity U), the dimensionless coordinates of an element of a rotor blade rotating with an angular velocity Ω appear to be time dependent in that coordinate system, viz.

$$x = -Ut/R_0, y = -(r/R_0) \cos \Omega t, z = (r/R_0) \sin \Omega t. \quad (5.1.30)$$

This shows, that neither the ergodic nor the Taylor hypothesis can be applied to transform Eq. (5.1.29) into an ensemble average. In order to get some insight into the behaviour of Eq. (5.1.29), a special case will be considered, viz. $\Omega = 0$. When $\Omega = 0$, the time can be expressed in x by $t = -xR_0/U$, and the y - and z -coordinates are independent of t and only depend on the orbital position of the rotor blade ϕ , viz.

$$y = -(r/R_0) \cos \phi \text{ and } z = (r/R_0) \sin \phi.$$

Because of the isotropy of the turbulence, the time average of Eq. (5.1.29) is independent of the blade position ϕ , when $\Omega = 0$. Using Taylor's hypothesis, the time integral can then be transformed into a space average with $X_T = -UT/R_0$, thus

$$T^{-1} \int_0^T \left(\frac{1}{U}\right)^2 u[(r/R_0), t] u[(r/R_0)+\zeta, t] dt = X_T^{-1} \int_0^{X_T} \left(\frac{1}{U}\right)^2 u[(r/R_0), x] u[(r/R_0)+\zeta, x] dx$$

According to the ergodic hypothesis, this space average can be set equal to an ensemble average and is called the lateral covariance, which is independent of r/R_0 in isotropic turbulence. This covariance depends only on the separation distance ζ perpendicular to the main stream and is denoted by

$$R_{11}(\zeta)/U^2 = \overline{u[r/R_0] u[(r/R_0)+\zeta]} / U^2 = (\overline{u^2}/U^2) g(\zeta). \quad (5.1.31)$$

When an often used approximation for g is applied, viz.

$$g = \exp[-|R_0/L_g|],$$

with L_g the so-called "lateral scale" of the turbulence, Eq. (5.1.29) can be integrated, which results in

$$\overline{\Delta C_N^2} = 2A^2 (\overline{u^2}/U^2) \left[L_g/R_0 - (L_g/R_0)^2 [1 - \exp(-R_0/L_g)] \right]. \quad (5.1.32)$$

From Eq. (5.1.15), it follows that C_N for one blade in a uniform flow can be calculated from $C_N = 0.12\lambda/B$ and the factor A can be expressed in C_N (see Eq. (5.1.28)), viz.

$$A = 2C_N/(\alpha\lambda).$$

When this is substituted, into Eq. (5.1.32), the MS-value of ΔC_N divided by C_N^2 can be obtained.

$$\overline{\Delta C_N^2}/C_N^2 = \{8/(\alpha\lambda)^2\} \{\overline{u^2}/U^2\} \left\{ L_g/R_0 - (L_g/R_0)^2 [1 - \exp(-R_0/L_g)] \right\}. \quad (5.1.33)$$

Due to the neglect of the rotation of the turbine blade, the correlation of the velocity at two different blade elements is possibly overestimated, but it is hoped that Eq. (5.1.33) still exhibits some realistic trends:

When the scale L_g becomes very small with respect to R_0 , the expression between the large brackets tends to zero. When L_g becomes very large with respect to R_0 , it can be shown that the expression between the large brackets tends to unity by expanding $\exp(-R_0/L_g)$ into a series.

Figure 5.8 shows the influence of the lateral scale of the turbulence on the RMS-value of the blade-load fluctuations for a specific example. With a turbulence intensity of 15 %, the RMS-value of the load fluctuations is about 20 % of the steady-state load if $L_g \geq R_0$, but, even if $L_g = R_0/10$, the RMS-value is still 10 % of the steady-state load.

The lateral scale of the u -fluctuations in an atmospheric boundary layer depends on a number of factors as surface roughness, height above the ground, wind velocity, etc., and it is not known with great accuracy. Nevertheless, a scale of 50 m at a height of 40 m above the ground seems acceptable (a comparable longitudinal scale is 100 to 200 m). This shows that, even for a 100 m diameter turbine, L_g/R_0 is not

smaller than 1 and the possibility that the load fluctuation level will fall much below 15 to 20 % by lack of correlation along the blade span seems to be small.

The lateral scale will be smaller at a smaller height above the ground, but, in such a case, the rotor diameter will be smaller also and the conclusion above probably remains valid.

Besides the neglect of Ω , which might cause a decrease of correlation along the blade span, the neglect of the influence of the operating turbine on the turbulence, has also to be considered. The dynamics of turbulence, however, is a too complex problem to solve here. One effect can still be visualized by considering the flow retardation in front of the turbine from U to $(1-a)U$ and by using some simple estimations, first proposed by Prandtl (Ref. 5.10).

Consider the turbulence as a vorticity with its axis normal to the main stream, inside a closed loop of fluid elements. In the retarding flow, the closed loop is compressed axially in the ratio $1-a$ and stretched laterally in the ratio $(1-a)^{-1/2}$, which leads to a decrease of the area inside the loop with a factor of $(1-a)^{1/2}$. The rotation inside the loop is thus increased by a factor $(1-a)^{1/2}$. When the axial velocity fluctuation before the retardation was calculated from

$$u = \omega r,$$

it becomes, after the retardation

$$u' = \omega' r' = (1-a)^{-1/2} \omega (1-a)^{-1/2} r = (1-a)^{-1} u,$$

i.e. the retardation increases the u -fluctuation by the factor $1/(1-a)$. This factor has to be included in Eq. (5.1.33). Although such an estimate has to be considered with all reserve, it shows that an influence may be present and may result in an increase of the load fluctuations. See Ref. 5.11 for a more extended discussion of the effect of distortion of a turbulent stream on the fluctuating components.

The conclusion that the u -fluctuations are well correlated along the blade span, even for large-scale wind turbines, depends on the accepted size of the lateral scale L_g of the atmospheric boundary layer. This integral scale, defined by

$$L_g = 1/(\overline{u^2}) \int_0^\infty R_{11}(r) dr, \text{ (separation } r \text{ perpendicular to } U), \quad (5.1.34)$$

is affected by eddies of different sizes, thus a more detailed discussion seems relevant.

An accepted model for a turbulent flow consists of a steady main flow carrying with it a large number of eddies of different sizes and randomly distributed in space. The large eddies, containing most of the turbulent flow energy, correspond to low-frequency fluctuations, whereas the smaller eddies, containing less turbulent flow energy, correspond to higher-frequency fluctuations. The distribution of turbulent energy over a certain frequency range is given in a turbulence "power spectrum" with spectral density $E_1(f)$.

There is some discussion among the experts about the validity of several interpolation formulae given in the literature. By definition, the spectral density has to satisfy the relation

$$\int_0^\infty E_1(f) df = \overline{u^2}.$$

An often used interpolation formula for such a spectrum is given by Davenport (see e.g. Ref. 5.12)

$$f E_1(f) = \frac{2}{3} \overline{u^2} x^2 (1+x^2)^{-3/4}, \quad (5.1.35a)$$

with

$$x = f L / U_{10}, \text{ the reduced frequency, } f: \text{ frequency (Hz), } L: \text{ reference length} = 1200 \text{ m, and } U_{10}: \text{ reference wind velocity at 10 m height (m/s).}$$

Reference 5.4 shows a preference for the expression

$$f E_1(f) = \frac{2}{3} \overline{u^2} y (1+y)^{-5/3}, \quad (5.1.35b)$$

with

$$y = f L / U_{10}, \text{ and } L = 900 \text{ m,}$$

because of the behaviour of the spectral density at $f \rightarrow 0$. In the case of one-dimensional spectrum, $E_1(0)$ has to tend to a finite non-zero value. Eq. (5.1.35b) does behave that way and Eq. (5.1.35a) does not. However, commonly used anemometers measure the total horizontal wind vector instead of the component in the average wind direction. This means that wind spectra obtained with a simple anemometer are not strictly speaking one-dimensional spectra and that a pure one-dimensional spectrum can only be obtained with a special type of anemometer.

Actually, reference 5.4 gives the expression

$$f E_1(f) = A \overline{u^2} y (1+y^{5/3})^{-1}, \quad (5.1.35c)$$

with $A = 2/3$. The author supposes Eq. (5.1.35c) to be a printing error, because A has to show the value

$$A = (5/3\pi) \sin(3\pi/5) \approx 1.793$$

to satisfy the integral condition for the spectrum.

Figure 5.9 shows the Eqs (5.1.35a) and (5.1.35b) for a particular case. The frequency of the peak of the spectra is almost the same, but the spectrum of Eq. (5.1.35b) shows higher spectral densities at low frequencies than the spectrum of Eq. (5.1.35a).

The "peak" frequency can be calculated from the above expressions and appears to be proportional to U_{10} as is shown in the table below.

Equation	f_{peak}
5.1.35a	$(U_{10}/L) \sqrt{3} = 0.00144 U_{10}$
5.1.35b	$(U_{10}/L) \frac{3}{2} = 0.00167 U_{10}$
5.1.35c	$(U_{10}/L) (\frac{3}{2})^{3/5} = 0.00142 U_{10}$

This means that the frequency of the velocity fluctuations that possess much of the turbulence energy increases with increasing wind velocity.

The graphical representation of $E_1(f)$ is often put in the form of an $f E_1(f)$ versus $\log f$ diagram, so that the area below the curve remains a measure of the turbulence energy content, viz.

$$f E_1(f) d(\log f) = E_1(f) df.$$

Besides the energy content within a certain frequency band Δf , (viz. $E_1(f) \Delta f$), a measure of the correlation of fluctuations within a certain frequency band and separated over a certain spatial distance seems useful for a further discussion. This measure is called the "coherence".

In order to avoid too much detail, the definition of coherence will be given in a strongly simplified form by denoting the contribution to u within a small frequency band around f by u_f , thus

$$\text{Coh} = \frac{|\overline{u_f(r) u_f(r+\Delta r)}|^2}{[\overline{u_f(r)^2} \overline{u_f(r+\Delta r)^2}]}.$$

In many cases, the square root of the coherence is used instead of the coherence itself. Ref. 5.12 gives an interpolation formula for the coherence in an atmospheric boundary layer, viz.

$$(\text{Coh})^{1/2} = \exp[-|C f \Delta r / U_{10}|] \quad (5.1.36)$$

The constant C depends on the height above the ground z . Some typical values are (for a suburban region, Ref. 5.8)

$$\begin{aligned} C &= 4.5 \text{ at } z = 40 \text{ m for the lateral coherence } (\Delta r \text{ in } Y\text{-direction}), \\ C &= 6 \text{ at } z = 40 \text{ m for the vertical coherence } (\Delta r \text{ in } Z\text{-direction}). \end{aligned}$$

One can take the separation Δr at which $(\text{Coh})^{1/2} \leq \frac{1}{2}$ as a distance at which the correlation at frequency f becomes insignificant. Figure 5.9 shows an example by using the Eqs (5.1.35a), (5.1.35b), and (5.1.36) (see also Fig. 5.7). There is some debate on the use of consistent values for L and C (corresponding to the same meteorological situation and a more or less unobstructed area), but the general conclusions drawn from this curve will be applicable to wind turbines in many cases.

It is clear from this figure, that in the frequency range containing most of the turbulence energy ($7 \times 10^{-3} < f < 10^{-1} \text{ Hz}$), the correlation length (Δr) at which $(\text{Coh})^{1/2} \leq \frac{1}{2}$ is of the order of magnitude of the rotor radius or larger.

Frequencies above 1 Hz have a correlation length of less than 1 m, which for most wind turbines means that these fluctuations are uncorrelated and do not contribute to a normal-force fluctuation.

The energy spectrum and the coherence are functions of a "reduced" frequency, which means that the frequency increases with the wind speed. A generalized conclusion from Fig. 5.9 might be that fluctuations with a frequency above $f = U/10$ (Hz) are uncorrelated at a separation length above 1 m. For other separation lengths, similar results can be obtained.

When the angular frequency of the rotor is $(\Omega/2\pi)$, comparison with the frequency of the turbulent fluctuations (f) may indicate whether the turbulent fluctuation changes during a revolution of the rotor, i.e. whether the turbulence can be assumed "frozen" during a revolution. The angular frequency can be obtained from

$$\Omega/2\pi = \lambda U / (2\pi R_0).$$

When $\lambda = 8$ and $U = 10$ m/s, the angular frequency is a function of R_0 , as is seen in the table below

R_0 (m)	1	10	25	50
$\Omega/2\pi$ (Hz.)	12.7	1.27	0.50	0.25

Figure 5.9 shows that the frequency of the energy-containing eddies is one order of magnitude lower than the angular frequency of the rotor; thus the concept of frozen turbulence can be applied. The evaluation of Eq. (5.1.29), however, remains still a difficult problem.

When the turbine rotates with a constant angular velocity Ω in a turbulent wind stream, the question can be raised whether the lift variation on a blade element due to a wind velocity fluctuation can be calculated by quasi-steady aerodynamics, or whether it has to be calculated by unsteady aerodynamics, which leads to a time-lag of the lift in response to a wind velocity fluctuation.

This behaviour is indicated by the value of the reduced frequency k of the wind velocity fluctuation with respect to a blade element at a spanwise station r/R_0 and a chord length c/R_0 (cf. Sect. 4.5.5)

$$k = \frac{\omega_{\text{ref}}}{U_{\text{ref}}} \approx \frac{2\pi f(c/2)}{\Omega r} = \frac{f}{\Omega/2\pi} \frac{(c/2)/R_0}{r/R_0},$$

which depends on the ratio of the frequency of the wind-velocity fluctuation and the angular frequency of the rotor, and also on a geometric factor. A typical value for this geometric factor, with $c/R_0 = 0.075$ and $r/R_0 = 0.75$, is 0.05. A typical value for the high-frequency boundary of the energy containing eddies is $f = 0.2$ Hz (Fig. 5.9). Because the angular frequency of the previous example was a function of R_0 , the reduced frequency of the high-frequency boundary of the energy containing eddies also becomes a function of the rotor size R_0 , which is shown in the table below.

R_o (m)	1	10	25	50
$\Omega/2\pi$ (-)	12.7	1.27	0.50	0.25
k (-)	0.001	0.008	0.02	0.04

This shows that the response of a turbine to the energy containing eddies in a wind stream can be calculated with quasi-steady aerodynamics, even in the case of a large turbine.

When the turbine is not operating at $\Omega = \text{constant}$ but at $\lambda = \lambda_{\text{opt}} = \text{constant}$, the inertia of the rotor-gearbox-generator combination has to be considered together with the torque variation of the generator due to the Ω -variation and the output of the $\lambda = \text{constant}$ control mechanism.

Ref. 5.13 discusses the dynamic response of the wind turbine for the case that the generator torque is a function of Ω only and without an effective $\lambda = \text{constant}$ control mechanism. The case considered was essentially a fixed-pitch rotor connected to a generator with a gearbox with a fixed gear-ratio. The generator fed a 12 volt storage battery via a voltage controller. The more general case with a $\lambda = \text{constant}$ control becomes increasingly complex.

A problem related to turbulence is the "gust", i.e. a sudden increase of the wind velocity above the average wind velocity with a certain duration (often 3 to 6 seconds). Such a gust must be discerned from the expectation of a very high average wind velocity (Fig. 2.2). Knowledge of extreme wind velocities (gales, tornadoes) are important for the strength requirements of an inoperative wind turbine, but will not be discussed here.

The wind turbine operates in a velocity range well below these extreme wind velocities (cf. Sect. 2.3.1). The wind velocity is, however, not steady and fluctuations about the average can lead to instantaneous velocities appreciably higher than the average. It is impractical to stop the wind turbine for the relatively short time that the instantaneous wind velocity exceeds the so-called "cut-out" wind velocity whereas the average wind velocity is well below that cut-out speed (turbine control, Sect. 5.2). Therefore, the study of gusts at wind velocities within the operating range of a wind turbine is important in connection with the load on an operative wind turbine.

A rather simple first guess could be made by assuming, that the fluctuations about the average have a normal (Gaussian) distribution with a probability density

$$f(u) = [2\pi \overline{u^2}]^{-\frac{1}{2}} \exp\{-\frac{1}{2} u^2 / \overline{u^2}\}.$$

The probability that a positive fluctuation $u > u_1$ occurs can be calculated from

$$P(u_1) = (2\pi)^{-\frac{1}{2}} \int_a^{\infty} \exp(-\frac{1}{2} y^2) dy = \frac{1}{2} [1 - \phi(u_1)] ,$$

with

$$\phi(u_1) = 2(2\pi)^{-\frac{1}{2}} \int_0^a \exp(-\frac{1}{2} y^2) dy , \quad (\text{the error function}),$$

and

$$a = u_1 / (\overline{u^2})^{\frac{1}{2}} ; \quad y = u / (\overline{u^2})^{\frac{1}{2}} .$$

The magnitude of a gust is often given in the literature by a so-called "gust factor", which can be written in the above approximation as

$$G = (U + u_1) / U = 1 + [u_1 / (\overline{u^2})^{\frac{1}{2}}] [(\overline{u^2})^{\frac{1}{2}} / U] . \quad (5.1.37)$$

Figure 5.10 shows the gust factor G as a function of the probability of occurrence $P(u_1)$ and the turbulence intensity of the wind flow. It must be noticed, that $P(u_1)$ gives the probability at a certain wind velocity U , i.e. it has to be considered as a conditional probability. The total probability can be obtained by multiplying $P(u_1)$ by $P(U)$, the probability of occurrence of a wind velocity U .

For example, when it is assumed that $P(U=17 \text{ m/s}) = 0.02$ (or, more correctly, $P(16.5 \leq U \leq 17.5 \text{ m/s}) = 0.02$), the probability of occurrence of one 10 second gust in a year (or two gusts of 5 seconds; in this simple approach, there is no possibility to discriminate) at that wind velocity is

$$P(u_1) = \frac{10}{365 \times 24 \times 3600} \times \frac{1}{0.02} = 1.6 \times 10^{-5} .$$

The gust factor can then be obtained from Fig. 5.10, viz. $G \approx 1.8$ (20 % turbulence intensity) or $G \approx 1.4$ (10 % turbulence intensity), which leads to a gust velocity of 30.6 and 23.8 m/s, respectively. Still higher gust velocities are possible, but their probability of occurrence will be still smaller, e.g. once in 50 years. This example shows the influence of the turbulence intensity on the maximum possible gust velocity. The turbulence intensity is related to the surface roughness but also to the height above the ground; therefore, a more detailed knowledge of the actual atmospheric boundary layer is necessary.

Although the above discussion brings about some important aspects about gusts, it gives not a reliable basis for estimating gust loads on operating wind turbines, because:

- The "tail" of the Gaussian distribution is not a suitable model for the estimate of rare events like strong gusts.
- The model does not include the "duration" and the "shape" of the gusts.

For a more detailed review of gust data, one is referred to the forthcoming handbook announced in Ref. 5.1.

5.2 Turbine control

5.2.1 Introductory remarks

A discussion of turbine control is intimately connected with the energy conversion system chosen for a specific design and the type of wind turbine used, viz. a horizontal- or a vertical-axis turbine.

In most cases, the mechanical energy of the rotor is converted into electric energy by a generator-gear-box combination (Sect. 2.3.2). When the turbine is operative, the torque of the generator has to be matched to the torque of the rotor. The torque matching is done by a control system, the extent of which is also affected by the scale of the turbine (a small-scale turbine has a mechanical regulator and a voltage controller, whereas a large-scale turbine may have a control system with a mini-computer) and by the mode of operation ($\lambda = \text{constant}$ or $\Omega = \text{constant}$, cf. Sect. 2.3.2).

The type of turbine affects the control system, because a horizontal-axis turbine needs a yaw control to turn the rotor into the wind direction, which is not necessary in case of a Darrieus turbine. Moreover, a horizontal-axis turbine is sometimes provided with a blade-pitch control, which is not possible in case of a Darrieus turbine (a very complex blade-pitch control is applied to the Giromill, however, see Ref. 5.14). Furthermore, the control system has to start the turbine when the wind velocity comes above the cut-in speed and it has to stop the turbine when the wind velocity comes above the cut-out speed or below the cut-in speed (cf. Sect. 2.3.2); moreover the control system has to provide a number of safety measures, such as the emergency stop during malfunctioning of sub-systems or during a runaway (overspeeding).

It takes a complete control-system analysis to deal with the above series of control functions in a proper way, which is outside the scope of this section. Also the various ingenious mechanical control systems that have been invented for small-scale turbines will not be discussed. Only those aspects which are related to aerodynamics and apply to large-scale WECS will be dealt with in the following Sections.

5.2.2 Starting and stopping

As discussed in Sect. 2.3.1, wind velocities below the cut-in speed are not important with respect to the annual energy production and the wind turbine only has to be started-up when the wind velocity raises above this cut-in speed. The wind velocity has to be measured with an independent wind sensor (anemometer). Problems related to the position of the wind sensor and the fluctuating character of the wind will be discussed in the next Section.

To start the turbine, the rotor has to be unlocked (the locking is necessary to prevent occasional movements of the rotor during a standstill) and, in the case of a horizontal-axis turbine, the rotor has to be turned into the wind direction. What happens next depends on the self-starting ability of the turbine, which is discussed below.

The existing performance theories for horizontal- and vertical-axis turbines give the possibility to calculate the torque coefficient $C_Q = C_p/\lambda$ also at low λ . The rotor blades are stalled, however, at low λ and the calculated results become inaccurate. Moreover, the theory itself fails at $\lambda = 0$, because the model with which the induced velocities are determined becomes inadequate.

Calculations for a low-solidity Darrieus turbine reveals at low λ a small λ -range with negative C_p , thus also negative C_Q -values. At $\Omega = 0$, the wind velocity is not reduced by the operating turbine ($a = 0$) and the angle of attack of a blade element and the relative velocity are (see Eqs (4.5.50) and (4.5.51))

$$\alpha = \arctg(\cotg\phi \sin \gamma) ,$$

$$U_{rel} = U [\sin^2 \phi + \cos^2 \phi \sin^2 \gamma]^{\frac{1}{2}} ,$$

or, in case $\gamma = \pi/2$ (blade element at equator plane),

$$\alpha = \frac{\pi}{2} - \phi \quad \text{and} \quad U_{rel} = U .$$

The lift distribution on the rotor blade located at a certain azimuth angle ϕ in the wind stream gives rise to a trailing vortex sheet, which induces a downwash along the blade span by which the actual angle of attack along the blade is reduced in a way similar to an airplane wing in rectilinear flight. A slight difference with the usual wing theory is the non-planar trailing vortex sheet due to the curved blade geometry of a Darrieus turbine, but that is not a fundamental difficulty.

An indication of the azimuthal variation of the torque at $\Omega = 0$ can be obtained by considering a blade element at the equator plane ($\gamma = \pi/2$). The torque coefficient is proportional to the tangential force coefficient of the blade element, which can be calculated from

$$C_t = C_l \sin \alpha - C_d \cos \alpha = C_l \cos \phi - C_d \sin \phi ,$$

with

$$\alpha = \frac{\pi}{2} - \phi .$$

Except for relatively small α -ranges (and thus ϕ -ranges) where the flow around the blade element is attached and where the profile characteristics (C_l, C_d) depend on the profile geometry and Reynolds number, the profile characteristics over a large part of all possible α -values are relatively insensitive to the profile geometry. Important in this respect is the "flat plate" lift beyond the stall, with a maximum at $\alpha \approx 45^\circ$.

Figure 5.11 shows C_l vs α and C_d vs α , together with C_t vs ϕ , calculated from the above formula. The data are sketchy and only intended to reveal the general trend.

The lift in the attached flow region around $\alpha = 180^\circ$ is lower than in the attached flow region around $\alpha = 0$, because the sharp-edged trailing edge becomes a leading edge in that case. This has a marked effect

on the C_t ($\alpha = 180^\circ$, $\phi = 270^\circ$).

When a one-bladed rotor is unlocked, the blade probably moves towards $\phi = 180^\circ$, where it is in a stable position. A two-bladed rotor shows a neutral or slightly unstable stability at $\phi = 0$ and 180° , but when the rotor starts to move at a certain azimuth angle different from these neutral positions, the inertia of the rotor may overcome these neutral positions and, thus, it may continue to rotate. For a three-bladed rotor the probability of a continuous rotation from standstill is smaller. Although there is a possibility that the Darrieus turbine starts to rotate from a standstill, the velocity due to rotation modifies the flow around the blades in such a way, that at relatively low λ the torque may become negative again, in which case the rotor will not speed up any further. Usually, it is necessary to apply an external torque to drive the turbine through the "negative torque dip" into the λ -range with positive $dC_Q/d\lambda$.

It is possible to use the generator as a drive motor to speed up the turbine, thereby consuming power from the grid instead of supplying it. Figure 2 of Ref. 5.15 shows, however, that there is also an aerodynamic means to speed up the turbine to its operational range, viz. by combining the Darrieus turbine with a Savonius rotor, which is self-starting.

Figure 5.12 gives an estimation of the torque at a velocity of $U = 7$ m/s for a Darrieus turbine, combined with two Savonius rotors, through application of the experimental data of the Refs 5.16 and 5.17. The interference between the Darrieus turbine and the Savonius rotors has been neglected. An essential aspect is the difference in rotor diameter between the Savonius rotor and the Darrieus turbine in order to match the positive C_Q -vs- λ range of both turbines.

A low-solidity horizontal-axis turbine with a blade-pitch angle for optimum C_p also shows a negative C_p and C_Q at low λ , which means that also such a turbine is not self-starting (cf. e.g. Fig. 4.24).

At $\Omega = 0$, there may be a positive torque on the rotor, notwithstanding the blade is completely stalled. The angle of attack can be calculated from

$$\alpha = \frac{\pi}{2} - i.$$

Because the lift C_l is perpendicular to U and U is parallel to the axis of rotation in the case of $\Omega = 0$, the lift is equal to the tangential force driving the turbine and the drag is equal to the normal force, which is perpendicular to the plane of rotation.

Figure 5.11 shows that C_l is always positive as long as i is positive; therefore, a positive torque at $\Omega = 0$ seems very probable. The negative torque dip at low λ can be overcome by using the generator as a drive motor, but also by using a variable-pitch rotor. The purpose of the variable pitch is to decrease the angle of attack during the "speed up" of the rotor; in that way flow separation on the blades is avoided. Such a variable-pitch rotor means a complication, but it is often desirable from other points of view (feathering during storms e.g.).

In order to stop a rotating turbine, a mechanical brake can be applied, but in order to reduce the necessary braking capacity, several aerodynamic means have been proposed to reduce the power output of the rotor voluntarily. In the case of a horizontal-axis turbine with a variable-pitch rotor, aerodynamic braking is easily provided by increasing the pitch angle. For both the horizontal-axis and the vertical-axis turbine, aerodynamic braking can be provided by using spoilers, i.e. a relatively small flat surface protruding from the aerofoil contour, which causes flow separation and, in that way, a lift decrease and a drag increase. Also the drag on the flat plate itself is important. The decrease of the power coefficient due to a spoiler, located at a radius r/R_0 and with a total spoiler surface S_s , which operates on a turbine with a tip-speed ratio λ can be calculated (assuming $U_{rel} = \Omega r$) from the formula

$$\Delta C_p = - (\lambda r/R_0)^3 (S_s/S_{ref}) C_d,$$

where C_d is the drag coefficient of the spoiler with area S_s . The drag coefficient of a flat plate normal to the flow is

$$C_d \approx 1.0 \text{ if height} \approx \text{width (square plate),}$$

$$C_d \approx 2.0 \text{ if height} \gg \text{width (two-dimensional strip).}$$

Figure 5.13 shows the power loss due to a spoiler, estimated from the above formula. This reveals that rather small spoiler areas are sufficient, especially at high λ , but the diagram also reveals that the influence decreases rapidly at low λ . In order to relate the spoiler area to the blade area instead of to the rotor reference area, it must be remembered that, for a Darrieus turbine with a height equal to the diameter, the following formula applies

$$S_{blades}/S_{ref} = 1.13 Bc/R_0,$$

whereas for a horizontal-axis turbine with $\lambda_{opt} \approx 8$, the solidity is about

$$\sigma = S_{blades}/S_{ref} \approx 0.050.$$

Roughly speaking, a spoiler area of the order of magnitude of 2 percent of the rotor blade area seems sufficient to decelerate the turbine down to low angular velocities. Ref. 5.18 shows some experimental results obtained with a Darrieus turbine (notice, that in Ref. 5.18 the power coefficient contains the factor 27/16). The experimental points in Fig. 5.13 show that the simple calculation suffices for an order-of-magnitude estimate of the required spoiler area. An accurate calculation is difficult due to interference effects (induced blade stall etc.) and due to the inaccurate estimate of U_{rel} (U_{rel} varies during a revolution). An accurate calculation does not seem worthwhile, however, when the purpose of such a spoiler system is regarded.

When the turbine has been brought to a standstill and has been locked in its parking position, still important aerodynamic loads may occur, e.g. during a severe storm. This will be discussed in Sect. 5.2.4.

5.2.3 Control during normal operation

As discussed earlier (see also the Figs 2.2 and 2.3), the wind statistics for a specific landscape or for a specific turbine site reveal a "cut-in" speed, below which the turbine does not need to operate, due to the low annual energy content; they also reveal a "design" speed, above which the contribution to the annual energy production is outweighed by the cost increase due to the increase of the installed power. Above this design speed, the turbine is not always stopped, but the output of the rotor is limited to the so-called "design" power by artificial means and only stopped at a still higher velocity, the so-called "cut-out" speed.

An idealized performance diagram of a wind turbine is sketched in Fig. 5.14 for a 50 m diameter turbine, with a $(C_p)_{opt} = 0.4$, a cut-in speed $U_i = 5$ m/s, a design speed $U_d = 17$ m/s, and a cut-out speed of $U_o = 24$ m/s. The idealization in this diagram is the assumption of $C_p = (C_p)_{opt}$ (i.e. $\lambda = \lambda_{opt} = \text{constant}$) in the wind velocity range from U_i to U_d , and the assumption of a constant power output $[C_p = (C_p)_{opt}(U_d/U)^3]$ in the wind velocity trajectory from U_d to U_o .

It takes a control-system analysis and a cost-benefit analysis to decide which control system has to be preferred to approach the ideal performance diagram as close as possible.

As mentioned in Sect. 2.3.2, an interesting case to consider is the $\Omega = \text{constant}$ mode of operation, which was extensively studied in connection with a Darrieus turbine (Ref. 5.19). The main idea is that a synchronous generator connected to a utility grid is forced by the grid to rotate with a fixed number of revolutions, irrespective of the torque applied to the generator. The generator is connected to the rotor by a gear-box with a fixed gear-ratio; the rotor is, therefore, also forced to rotate at a constant angular velocity.

With a given geometry of the Darrieus turbine, the idealized performance diagram of Fig. 5.14 can only be approached by changing the number of revolutions of the rotor. With the C_p -vs- λ curve of Fig. 4.57, the performance curves at $\Omega = \text{constant}$ have been calculated and given in Fig. 5.15.

This figure shows that Ω determines U_i and U_d ; U_i corresponds with $\lambda = 7.27$ (see Fig. 4.57) and U_d corresponds with $\lambda \approx 3.7$. In order to approximate the ideal performance diagram more closely at low wind velocity, it seems necessary to apply a gear-box with at least two gear-ratios. As mentioned already in Sect. 2.3.2, an attractive property of this system is that there is an automatic safeguard to overspeeding at high wind velocities due to the stall of the rotor blades, as long as the generator is not pulled out of its frequency by sudden torque fluctuations. For a more detailed discussion, see Ref. 5.19 and the Technical Quarterly Reports of the SANDIA LABORATORIES.

A similar discussion can also be given for a horizontal-axis turbine with a fixed blade-pitch angle. The calculated example of Fig. 4.24 will be used with $\theta_p = 0$ and extrapolated in the high- λ region. The calculated $\Omega = \text{constant}$ performance curves are shown in Fig. 5.16.

The $\Omega = \text{constant}$ operation seems also possible with a horizontal-axis turbine. The necessity to choose at least two values of Ω can be avoided, when the horizontal-axis turbine is provided with a variable-pitch rotor. In that case, the ideal performance diagram can be approximated closely at one value of Ω .

In the discussions so far, the wind velocity U is mentioned only superficially. In Sect. 5.1.3, it was discussed that the wind velocity is not constant but fluctuates irregularly about an average value. Moreover, the frequency of the energy-containing fluctuations was shown to be such, that the aerodynamic torque of the rotor follows these velocity fluctuations closely. This has no consequence for the $\Omega = \text{constant}$ mode of operation with a fixed blade-pitch angle, where the maximum power output is determined by blade stall. However, when blade-pitch control is used to limit the power output at high wind velocities, there is a possibility of exceeding the design power, when the pitch control is slower than the wind velocity variation.

This behaviour is elucidated in Fig. 5.17, which shows the importance of choosing the proper value of Ω , when the overshoot has to be minimized, which may depend on the magnitude of the gust. Large gusts may occur even at wind velocities within the normal operating range of the turbine, as was shown in Sect. 5.1.3.

The $\lambda = \lambda_{opt} = \text{constant}$ mode of operation (variable Ω) improves the power production at low wind velocities, but the problems of maintaining the design power at high wind velocities and the corresponding possibility of an overshoot remain.

Important input signals for a wind turbine control system are the wind velocity and the wind direction, which can be measured by suitable sensors (e.g. anemometer and wind vane). It is here that some problems arise for large-scale WECS. Upstream of the turbine a stagnation area exists and downstream the wake is found; both regions where the undisturbed wind velocity and wind direction cannot be measured. Moreover, putting the sensors too far from the turbine makes the determination of the instantaneous wind velocity and wind direction very uncertain because of the stochastic character of the wind.

Figure 5.18 shows some simple models that may be used to estimate the stagnation of the wind velocity in front of an optimally operating wind turbine ($a = 1/3$). The semi-infinite row of ring vortices seems a good model for a horizontal-axis turbine. The actual stagnation effect will be some mixture of the three types given. Figure 5.19 shows the numerical result of the estimations. It seems warranted to conclude that a distance of at least twice the rotor diameter is necessary to avoid a detectable stagnation on the reference anemometer in front of the turbine. The stagnation will vary with λ (variation of a), but the estimate is too crude to justify any further detail. The wake behind the turbine decays less rapidly than the stagnation in front of the turbine and a location of the anemometer in the wake should be avoided altogether (cf. Sect. 5.3).

When the reference anemometer is installed on a mast at some distance from the wind turbine, at least two masts are necessary to avoid the wake, because of the variations in the wind direction.

In the case of a vertical-axis wind turbine, the reference anemometer is often situated on top of the turbine, whereas, in the case of a horizontal-axis turbine with its rotor placed downwind of the tower, the reference anemometer is often situated on the nacelle. In both cases, a careful calibration of the position error has to be made at different values of λ . In the case of a horizontal-axis turbine with an upwind rotor, the only possibility is to install two anemometers, placed diametrically at some distance from the turbine while the upstream one is used.

The problem with a distant reference mast (carrying an anemometer and a wind vane) is to predict the wind velocity and direction at the location of the turbine (with the turbine inoperative). A measure of the correlation between the instantaneous velocity at the reference mast U_1 and the instantaneous velocity at the turbine site U_2 is the covariance $COV(U_1, U_2)$. The dependence of this covariance on the separation distance r and the time delay τ is sketched in Fig. 5.20 for the case that the mast is placed exactly upstream of the turbine. The covariance at $\tau = 0$ decreases rapidly with increasing r ($r_2 > r_1 > 0$). It is possible to improve the correlation by applying a time delay to the signal obtained from the reference mast, which is equal to the transport time r/D_1 . For other wind directions the situation is worse, however, see Fig. 5.21. The data of Fig. 5.20 actually represent $COV(U_1, U_3)$ with $a = r \cos \beta_1$ instead of r ; therefore, $COV(U_2, U_3)$ has to be introduced also, which leads to a further decrease of $COV(U_1, U_2)$. In turbulence theory, $COV(U_2, U_3)$ is the so-called lateral correlation, which decreases more rapidly with increasing b than the longitudinal correlation $COV(U_1, U_3)$ decreases with increasing a . Moreover, the lateral correlation cannot be improved by time delay.

The correlation between the wind directions, $COV(\beta_1, \beta_2)$, is smaller than that between the wind velocities, because the wind direction fluctuations are mainly caused by lateral velocity fluctuations, which are correlated less than the longitudinal velocity fluctuations, which mainly determine the wind velocity U_1 and U_2 .

Statistical considerations (Ref. 5.20) indicate that the retarded instantaneous wind velocity at the reference mast is not the best prediction of the instantaneous wind velocity at the turbine. The best prediction is, according to Ref. 5.20, a weighted sum of the average wind velocity and the retarded instantaneous wind velocity at the reference mast, on the understanding that the best prediction is equal to the retarded instantaneous velocity when the normalized covariance approaches 1, and is equal to the average wind velocity when the normalized covariance approaches zero.

In practical case, the above discussion means that an accurate prediction of the instantaneous value of the wind velocity at the turbine is highly improbable. The prediction of the instantaneous value of the wind direction even seems impossible. A possible way out is to use a filtering technique, to get rid of the high-frequency fluctuations and to try to predict the low-frequency fluctuations at the turbine from the low-frequency fluctuations measured at the reference mast. A further analysis is needed to choose a suitable "integration time" for the filters, in order to predict those frequencies which are required for the control system with a sufficient accuracy.

In this respect one has to think of those velocity fluctuations that have to be followed by the blade pitch control in order to maintain the design power. Fluctuations in wind direction are only important, when the frequency of the fluctuation can be followed by the yaw control; the rate of change of yaw is limited by precession forces and power requirements.

5.2.4 Safety aspects

It is a specialized branch to investigate which measures the control system has to take in order to handle malfunctioning of one or more of the sub-systems. This aspect will, therefore, be discussed neither here nor in the following Sections.

The possibility of aerodynamic braking by spoilers in case of a runaway (e.g. when the link between rotor and generator is disconnected unintentionally or is broken) has been discussed in Sect. 5.2.2. The spoilers could be activated by a centrifugal switch.

There is one aerodynamic aspect, however, that is to be discussed under this heading, viz. whether a wind turbine can withstand a severe storm. When a turbine is locked in its parking position, the aerodynamic force on the blades are lower than those in the case of a rotating turbine at the same wind speed, as a consequence of the increased relative velocity. The aerodynamic force on a parked turbine may even be lower in a severe storm than during normal operation at the design wind speed. Take, e.g., an extreme wind velocity of 40 m/s blowing normal to a blade element; then the normal force is determined by the drag coefficient $C_d = 2.0$ and is proportional to

$$C_d U^2 = 2 \times 40^2 = 3200 \text{ m}^2/\text{s}^2.$$

A turbine operating at $\lambda = 5$ at a wind velocity $U = 15 \text{ m/s}$ may have a lift coefficient $C_l \approx 1.0$; the corresponding normal force on the blade element is then proportional to

$$C_l (\lambda U)^2 = 1.0 \times (5 \times 15)^2 = 5625 \text{ m}^2/\text{s}^2,$$

which shows that the aerodynamic force on the blade element is higher during normal operation than during a standstill in a severe storm.

Due to the absence of the centrifugal forces during a standstill, the bending moments in the rotor blade may be higher in a severe storm than during normal operation, notwithstanding the higher aerodynamic load.

For the Darrieus turbine, the aerodynamic "buckling" has been discussed in Ref. 5.21. This effect is also possible with a horizontal-axis turbine (cf. Fig. 2.8). This is the reason why it is sometimes advised to keep the turbine operative at a constant Ω during a severe storm (it is also mentioned as an advantage of the $\Omega = \text{constant}$ operating mode, see Sect. 2.3.2).

Although the blade bending stresses might be alleviated during a severe storm by maintaining a constant angular velocity, the total forces on the tower may become high, due to the higher aerodynamic load on the blades which is transferred to the tower, whereas the blade bending stress alleviating centrifugal forces are not transferred to the tower.

In the case of a horizontal-axis turbine with a variable-pitch rotor, the aerodynamic loads during a severe storm, with the rotor locked in the parking position may be strongly decreased by "feathering", i.e. choosing such a value θ_p , that the average lift on the blade is zero and the drag low

(i.e. $C_d \ll 2.0$). This is only effective when the rotor is aligned in the wind direction. Because of the "gustiness" of the wind, such an alignment cannot be perfect all the time. A two-bladed horizontal-axis turbine with its blades locked horizontally in the "feathered"-pitch position is insensitive to wind direction fluctuations (horizontal gusts) but not to vertical gusts. A three- or more-bladed turbine is always sensitive to wind direction fluctuations (horizontal and vertical gusts).

5.3 Wind turbine "farms"

5.3.1 Introductory remarks

In the preceding Sections, the discussions were centred on the isolated wind turbine in homogeneous (Sect. 4) or in inhomogeneous (Sect. 5.1) flow. Such a situation is found in rural applications of wind energy, e.g. when each remote farm has its own wind turbine (and solar heat system).

Consideration of wind energy as a means to deliver a substantial amount of electric energy to the utility grid, however, means a large number of turbines on a certain land area. Such an array of wind turbines is sometimes called a wind-turbine "farm", which word emphasizes the dependence of the output on the weather system ("harvesting" of the wind energy and the existence of "good" and "bad" wind-energy years).

In the case of a wind-turbine farm, the question arises how closely the wind turbines can be packed on a given land area. There are two reasons to pose this question viz.:

- to minimize the use of land in cases where land is scarce (e.g. in The Netherlands),
- to reduce the costs by minimizing the length of access-roads, cables, etc., and by centralizing control systems.

The separation distance between wind turbines will be determined by their (mutual) interaction. There are two possible ways of interaction, viz.:

- the mutual interaction of turbines placed in a row perpendicular to the wind direction. Such an interaction is mainly caused by "blockage" effects, i.e. local velocity and direction deviations aside of the turbine (connected with the stagnation upstream of the turbine).
- the interaction of turbines placed in a row downstream. Such an interaction is caused by the wake (reduced velocity) of the upstream turbine, acting on the downstream turbine. The influence of the downstream turbine on the upstream one is negligible in practical cases (cf. Fig. 5.19).

It is the second item; the wake interaction, which mainly determines the necessary separation distance between the turbines in a wind-turbine farm. Therefore, only the wake-interaction effects will be discussed in the following Sections.

The study of the wake interaction is limited in most cases to the prediction of the reduction of the wind velocity at the location of a certain wind turbine due to the presence of the other (upstream) turbines (power reduction). The possible increase of the turbulence level of the flow (fatigue loading) is rarely considered.

An early estimate of the velocity reduction due to an unlimited array of wind turbines was made by Templin (Ref. 5.22). His basic idea was to calculate the velocity reduction by considering the wind turbines as extra surface roughness elements added to an already rough terrain.

In practical cases, a wind-turbine farm consists of a limited array; the above estimation of the velocity reduction will, thus, only be valid for a downwind part of the array, because the turbines at the upwind edge of the array do not suffer any reduction in the wind velocity.

Crafoord (Ref. 5.23) extended the theory of Templin by using a vertical energy balance, to estimate the downwind wind-shear variation. Both theories assume, however, that the separation between the wind turbines is so large that single wakes are no longer discernable, i.e. direct wake effects are neglected. Lissaman (Ref. 5.24) tries to include these direct wake effects by considering first the wake decay of a single turbine. Then, by adding the velocity reductions of wakes at different stages of decay (wind turbines at different distances), he estimates the velocity reduction due to the upwind part of a turbine array.

The above-mentioned theories contain some uncertainties; therefore, experimental data are badly needed. An early wind tunnel measurement exists of the interaction between two horizontal-axis wind turbines (Ref. 5.25). More recently, wind tunnel measurements have been performed on a limited array of turbines (represented by circular wire grids; Ref. 5.26).

5.3.2 Wake-interaction theories

5.3.2.1 Surface roughness theory

The discussion of Ref. 5.22 is based on the idea that wind turbines can be considered as extra roughness elements on an already rough terrain. The difference in velocity profile of the turbulent boundary layer due to this extra roughness can then be determined. In order to be able to use the formulae for a turbulent boundary layer on a rough surface, it is necessary to consider an infinite array of homogeneously distributed wind turbines and to assume that the separate "wakes" of the extra roughness elements are completely smeared out and are no longer individually discernible in the total wind profile.

Ref. 5.22 starts from the logarithmic velocity profile for a turbulent boundary layer over a rough

surface, viz.

$$U/U^* = (1/k) \ln(z/k_s) + B, \quad (5.3.1)$$

with

U : horizontal velocity
 $U^* = \sqrt{\tau/\rho}$ = so-called friction velocity
 τ : surface shear stress
 ρ : air density
 k : Von Karman's constant (≈ 0.40)
 z : height above the surface, where U is measured
 k_s : effective "roughness height"
 B : number, which is constant at a sufficient high Reynolds number, which is always true for an atmospheric boundary layer over rough terrain ($B \approx 8.5$).

When the above-mentioned numerical values of the constants are used, Eq. (5.3.1) becomes

$$U/U^* = 2.5 \ln(z/k_s) + 8.5. \quad (5.3.2)$$

In Ref. 5.22, then the effect of the presence of the wind turbines on an effective wall shear stress is estimated. It seems obvious to translate the "drag" on the wind turbines into an additional shear stress by dividing this drag force by the land (surface) area corresponding to one turbine, which introduces the notion of turbine "density" λ .

It is also obvious, however, that the average wind-velocity reduction due to the turbines might affect the original wall shear stress too.

With the assumption that the wall shear stress is determined solely by the roughness height and the velocity at that height, the effective roughness height for the terrain with turbines can be defined.

For a determination of the power loss caused by the turbine-induced velocity reduction, the logarithmic velocity profile for a terrain with and without turbines at the same wind velocity outside the atmospheric boundary layer (the so-called geostrophic wind U_0) has to be calculated. A difficulty is, however, that the logarithmic velocity profile is scaled with the friction velocity, which is different for the cases with and without turbines and which drops out at the determination of the effective roughness height.

Returning to the determination of the wall shear stress with turbines, in Ref. 5.22 the drag of the turbine is calculated from

$$D = C_D \frac{1}{2} \rho [U'(h)]^2 S_{ref},$$

with

C_D : turbine drag coefficient, which is taken equal to 1. An optimally operating turbine has a $C_D \approx 8/9$, but when the tower drag is included, $C_D = 1$ seems a good average value.
 $U'(h)$: wind velocity at the centre of the rotor area, in case of a horizontal-axis turbine this is the velocity at the hub height.
 S_{ref} : area swept by the rotor.

When the land area occupied by one turbine is denoted by S_{land} , the turbine density λ can be defined by

$$\lambda = S_{ref}/S_{land},$$

and the additional surface stress is

$$\Delta \tau = D/S_{land} = (\lambda/2) \rho [U'(h)]^2. \quad (5.3.3)$$

When the original roughness height is denoted by $k_s = k_{s0}$ and when it is assumed that the velocity at $z = k_{s0}$ determines solely the wall stress due to the original surface roughness (see Eq. (5.3.2)), the total wall stress with turbines present is

$$\tau' = \rho [U'(k_{s0})/8.5]^2 + (\lambda/2) \rho [U'(h)]^2,$$

or, by definition:

$$[U'^*]^2 = [U'(k_{s0})/8.5]^2 + (\lambda/2) [U'(h)]^2. \quad (5.3.4)$$

When Eq. (5.3.2) is used with k_s as the effective roughness height for the combination of original surface roughness and turbines, the values of $U'(k_{s0})$ and $U'(h)$ can be expressed in the average friction velocity U'^* . When these values are substituted in Eq. (5.3.4), the friction velocity drops out and the following relation appears

$$1 = (1/8.5)^2 [2.5 \ln(k_{s0}/k_s) + 8.5]^2 + (\lambda/2) [2.5 \ln(h/k_s) + 8.5]^2.$$

Because $h/k_s = (h/k_{s0})(k_{s0}/k_s)$, the above formula can be written as

$$h/k_{s0} = \exp \left[0.4 \left\{ \left[\frac{2}{\lambda} \right] \left[1 - (Y/8.5)^2 \right]^{1/2} - Y \right\} \right], \quad (5.3.5)$$

with

$$Y = 8.5 - 2.5 \ln(k_s/k_{s0}).$$

This relation is also shown in Fig. 5.22. In Ref. 5.22 the uncertainties in the determination of k_s by the assumptions made are emphasized and estimated values of k_s for roughness elements on a smooth surface are compared with experimental values. There are large discrepancies at values of $\lambda < 5 \times 10^{-3}$. It is possible, however, that a comparison of the effect of extra roughness elements on an already rough surface might lead to a better agreement.

In the above discussion, the friction velocity U'^* has not been determined; this velocity is a kind

of "scale" factor for the velocity in the log law. Such a remark also applies to U^* for the terrain without turbines (k_{so}). The velocity profiles with and without turbines can only be compared at equal wind velocity outside the boundary layer ($z > \delta$), where $U(z > \delta) = U_0$ and where δ is the so-called boundary-layer thickness.

In civil-engineering structural design, the power-law wind velocity profile is widely accepted and reads

$$U(z)/U_0 = (z/\delta)^\alpha \quad (5.3.6)$$

The log law (Eq. (5.3.2)) applies only to the lower part of the wind profile, but when a fictitious value of the boundary-layer height δ_1 in the log law is taken to obtain $U(\delta_1) = U_0$, the following modified expression can be found

$$\frac{U(z)}{U_0} = \frac{2.5 \ln(z/k_{so}) + 8.5}{2.5 \ln(\delta_1/k_{so}) + 8.5} \quad (5.3.7)$$

Matching the Eqs (5.3.6) and (5.3.7) in the lower part of the wind velocity profile for two types of terrain leads to the results summarized in the following table.

Type of terrain	Type of velocity distribution			
	power law		log law	
	δ (m)	α	δ_1 (m)	k_{so} (m)
Open country	275	0.16	380	1.5
Rough wooded terrain	400	0.28	3000	12

Eq. (5.3.7), with k_s instead of k_{so} , could be used to describe the velocity profile with turbines present. The problem of estimating U^* is now exchanged for the problem of estimating δ_2 . In Ref. 5.22, two possibilities are considered, viz. $\delta_1 = \delta_2 = \text{constant}$ and $\delta_1/k_{so} = \delta_2/k_s = \text{constant}$.

With these two assumptions and Eq. (5.3.5), the power ratio at hub-height can be calculated from

$$\left[\frac{U^*(h)}{U(h)} \right]^3 = \frac{[2.5 \ln(h/k_{so}) - 2.5 \ln(k_s/k_{so}) + 8.5][2.5 \ln(\delta_1/k_{so}) + 8.5]}{[2.5 \ln(h/k_{so}) + 8.5][2.5 \ln(\delta_2/k_{so}) - 2.5 \ln(k_s/k_{so}) + 8.5]} \quad (5.3.8)$$

This power ratio is shown in Fig. 5.23 for a height $h = 30$ m, for two types of terrain ($k_{so} = 1.5$ and 12 m) and for two assumptions about δ . The supposition $\delta/k_s = \text{constant}$ shows the largest decrease with increasing λ . From the table above, which gives the influence of k_{so} on δ_1 , it appears that the assumption $\delta/k_s = \text{constant}$ is rather well confirmed by the two examples given, viz. $\delta_1/k_{so} = 253$ for open country and $\delta_1/k_{so} = 250$ for rough wooded terrain (but δ_1 is a rather fictitious value).

Moreover, the assumption $\delta/k_s = \text{constant}$ gives the expected result, namely that the decrease of the power ratio is less in the case of rough wooded terrain, contrary to the assumption $\delta = \text{constant}$ (see Fig. 5.23). The theory of Ref. 5.22 gives a maximum acceptable value of λ of about 2×10^{-3} . Beyond that value, the power ratio decreases rapidly. When the separation distance between two turbines is denoted by L , this value of λ means

$$(\pi/4) D^2 / L^2 < 2 \times 10^{-3} \quad \text{or} \quad L/D > [(\pi/8) \times 10^3]^{\frac{1}{2}} \approx 20$$

In Ref. 5.23, the power ratio of a turbine in a finite array is estimated by means of a method that closely follows the theory of Ref. 5.22.

In Ref. 5.23, the description of the power ratio for an infinite array is given. The energy dissipation due to the surface roughness ϵ_s and due to the wind turbines ϵ_{gen} are assumed to be replenished by a vertical energy influx by turbulent mixing processes $\phi_\infty(\lambda)$. When other energy sources are disregarded, the energy balance for an infinite array reads

$$\phi_\infty(\lambda) = \epsilon_s + \epsilon_{gen} \quad (5.3.9)$$

The energy dissipation flux due to surface roughness depends on a number of factors, which are not of interest for the discussion below. The energy flux due to the wind turbines depend on the design (or "rated") power P_r and the power ratio in an infinite array $f_\infty(\lambda)$ (\equiv Eq. (5.3.8)), thus

$$\epsilon_{gen} = P_r f_\infty(\lambda) / L^2 \quad (5.3.10)$$

with L = mesh width of the square array.

In Ref. 5.23 then a finite array is considered. Take a volume of air with the height equal to the turbine diameter D , the width equal to L and also the length equal to L , starting at turbine number i and ending at turbine number $i+1$. The energy balance for this volume reads

$$\frac{1}{2} \rho U_i^3 L D + \phi(\lambda) L^2 - \epsilon_s^i L^2 - P_i = \frac{1}{2} \rho U_{i+1}^3 L D$$

with

- U_i : wind velocity at turbine i
- U_{i+1} : wind velocity at turbine $i+1$
- $\phi(\lambda)$: energy influx for a finite array
- ϵ_s^i : energy dissipation due to surface roughness for a finite array
- P_i : power absorbed by turbine i .

When the power ratios are defined by

$$f_i(\lambda) = (U_i/U_1)^3 ; f_{i+1}(\lambda) = (U_{i+1}/U_1)^3 ; \text{etc. ;}$$

the "rated" or "design" power is defined by (U_1 = wind velocity at first turbine)

$$P_r = C_p \frac{1}{2} \rho U_1^3 \frac{\pi D^2}{4}$$

and the vertical energy influx for a finite array $\phi(\lambda)$ is assumed to be equal to the influx for an infinite array $\phi_\infty(\lambda)$, according to Eq. (5.3.9). The energy balance can then be written as

$$f_{i+1}(\lambda) = f_i(\lambda) - (\pi/4)(D/L) \left[f_i(\lambda) - f_\infty(\lambda) - (c_s - c_s^1) L^2 / P_r \right] . \quad (5.3.11)$$

In Ref. 5.23 the last term between parentheses is neglected, i.e. the decrease of the energy dissipation due to surface roughness between two adjacent turbines, and a rather simple recurrent expression for the power ratio of a turbine in a finite array appears. The value of $f_\infty(\lambda)$ could be obtained from Eq. (5.3.8) or a similar kind of estimate. The recursion formula reads

$$f_{i+1}(\lambda) = f_i(\lambda) - c_p \left(\frac{\pi}{4} \lambda \right)^{1/2} \left[f_i(\lambda) - f_\infty(\lambda) \right] , \quad (5.3.12)$$

with $f_1(\lambda) = 1$ as a starting value.

The estimates of Ref. 5.22 (Fig. 5.23) can be used to calculate the downstream variation of $f_i(\lambda)$ with the above formula. An example of such a calculation is given in Fig. 5.24. This diagram shows how much energy is available on a land area of a given length in wind direction. The length expressed in turbine diameters D is directly related with the turbine density λ and the number of turbines covering this length, e.g. on a stretch of 100 times the turbine diameter, with a $\lambda = 0.005$, 8 turbines can be placed, with $\lambda = 0.01$, 11 turbines and with $\lambda = 0.02$, 16 turbines can be placed on that stretch. The total amount of energy obtained from a fixed land area increases by increasing the number of turbines (increasing λ), but the added turbines become increasingly inefficient from the point of view of power production.

It is difficult to assess, however, whether these crude assumptions used in the energy balance considerations lead to acceptable results. In Ref. 5.23 are some additional considerations about the energy balance and a large number of diagrams illustrating the influence of several parameters have been given.

In Ref. 5.27 the equations for the atmospheric boundary layer are considered in a somewhat simplified form in order to estimate the influence of atmospheric stability on the power ratio for an infinite array of turbines.

It would also be possible to refine the original calculations of Templin (Ref. 5.22) by applying the boundary layer equations for rough flat plates and by applying measurements of the boundary layer, passing from smooth to rough (see e.g. Ref. 5.28). The measurements of Ref. 5.28 are interesting, because they show that the wall shear stress adjusts itself immediately to the value for the rough wall, while the velocity profile more gradually changes from smooth to fully rough. However, all these boundary layer discussions are unable to describe the direct wake effects, because the individual wakes are assumed to be smeared out at the distances behind the turbines considered. This assumption is possibly justified at small values of λ , but the larger values of λ (smaller separation distances) are especially interesting for finite arrays; thus, a different approach seems worthwhile.

5.3.2.2 Wake-decay theory

An approach that differs strongly from the preceding Section is considering the decay of a wake behind a single turbine and superimposing the wakes of the upstream turbines in order to find the velocity profile at the location of a turbine inside a certain array.

The main problem in this approach is to describe the variation of the wake properties downstream of the turbine, the so-called wake "decay".

A classical way to describe the decay of a turbulent wake in a homogeneous non-turbulent flow, is to assume self-preservation (Fig. 5.25). The notion of self-preservation can be clarified as follows. The wake structure is characterized by its width b , the maximum velocity defect in the centre of the wake u_m and a shape function $f(\frac{r}{b/2}) = f(\eta)$, thus

$$(U_1 - u)/U_1 = 1 - (u_m/U_1) f(\eta) , \quad (5.3.13)$$

with b and u_m functions of $(x + x_0)/D = \zeta$, thus

$$b = b(\zeta) \text{ and } u_m = u_m(\zeta) . \quad (5.3.14)$$

Self-preservation means that $f(\eta)$ is a function independent of ζ and may only differ from object to object (e.g. solid sphere, wind turbine, body of revolution). The functions $b(\zeta)$ and $u_m(\zeta)$ have to be found from the equations of fluid dynamics. The quantity x_0 is the so-called "virtual origin" of the self-preserving flow, which does not need to coincide with the actual origin of the wake ($x = 0$).

When $u_m/U_1 \ll 1$, which means at a large distance behind the turbine, the momentum loss in the wake can be linearized and appears to be proportional to

$$(u_m/U_1) (b/D)^2 .$$

Because pressure differences are zero far behind the turbine, this momentum loss has to be equal to the drag of the turbine and is, therefore, independent of ζ . From mixing-length theory or similar kinds of reasoning, it can be shown that the wake width is proportional to

$$b/D \propto (\zeta)^{1/3} , \quad (5.3.15)$$

and from the momentum loss it follows that the maximum velocity defect is proportional to

$$(u_m/U_1) \propto (\zeta)^{-2/3} . \quad (5.3.16)$$

This simple result is difficult to apply to a wind turbine, because:

- the virtual origin x_0 depends on the wake-generating body;
- it is not a priori known at what distance the wake actually becomes self-preserving; experiments

- Indicate that the Eqs (5.3.15) and (5.3.16) only apply at very large distances during the final decay;
- the effect of wind shear and turbulence of the outer flow is not included although it appears from experiments that this effect cannot be neglected.

Though it seems possible, with the present-day knowledge of turbulent flows, to set up a computer code for the calculation of the wake decay by using an "eddy viscosity" or another turbulent shear stress model, the calculations become very complicated and the results have to be checked with experimental results in any case. It seems more adequate to resort directly to experimental data. This has been done in Ref. 5.24 by taking the extensive test results of Abramovich (Ref. 5.29) about decaying jets. At first sight, this seems contradictory, but it can be assumed that the velocity defect curves in the case of a wake behave similar to the velocity excess curves of a jet in a co-flowing stream, except close to the origin.

In Ref. 5.24, a thorough discussion is given of the wake model used in their computer code. For the sake of completeness, some main points will be repeated here.

The model for a single wake is given in Fig. 5.26 and rests on the following assumptions:

- At a short distance behind the actual turbine, a rectangular velocity defect curve is assumed, with a velocity defect $2aU_1$ and a wake width $2r_0 = [(1-a)/(1-2a)]^{1/2} D$, according to the simple actuator disk theory.
- The wake is divided into a number of regions. With each region, the wake width increases linearly with the downstream distance, but the rate of growth differs from region to region and depends on the "effective" turbulence of the flow. It must be noticed that, for the far wake, in Ref. 5.24 it is assumed that $b \propto \zeta$, whereas Eq. (5.3.15) gives $b \propto (\zeta)^{1/3}$. This "final" decay is possibly too far behind a turbine to be of interest for the wake-decay calculations. In addition, ambient turbulence was neglected.
- The effective turbulence is composed of the ambient turbulence of the atmospheric boundary layer and the "mechanical" turbulence generated by the turbine. The mechanical turbulence has its main effect in the near-wake region, whereas the far wake is affected solely by the ambient turbulence.
- The length of the near wake is determined by the degrading of the potential core, caused by the shear layer. The rate of growth of the wake diameter is determined by the effective turbulence, in which the mechanical turbulence plays a vital role.
- In the transition region, the velocity profile develops from a double shear layer to a self-preserving near-wake profile. It is assumed that the rate of growth of the wake diameter is equal to the rate of growth of the near wake.
- Within a fixed length of $10 r_0$, the mechanical turbulence decays and, behind that distance, the rate of growth of the wake diameter is solely determined by the ambient turbulence.

With the above assumptions, the magnitude of the maximum or "centre-line" velocity defect in the wake can be determined from momentum-loss considerations, the magnitude of which is assumed to be constant throughout the entire wake length and equal to the turbine drag. The influence of ground proximity is calculated by using a mirror image of the wake and superimposing the results.

Ref. 5.24 then discusses the wake-interaction effects within an array of wind turbines. This consists partly of a simple superposition of the computed velocity defects of the separate wakes, but this is complicated by the reduction of the velocity at a certain turbine due to turbines inside the upstream zone of influence. For a more thorough discussion and for computed results, reference has to be made to the original report.

5.3.3 Experimental results

5.3.3.1 Wake behind a single turbine

In Ref. 5.25 some early wind tunnel tests are described on two identical model turbines with a diameter $D = 150$ mm and two blades of constant chord $c = 15$ mm. By measuring directly the power output of the two turbines at different downwind and lateral separations, the wake-turbine interaction could be determined. The power ratio for two turbines placed directly in line with the wind is shown in Fig. 5.27. The lateral separation necessary to obtain just full wind power ($P_2/P_1 = 1.0$) is shown in Fig. 5.28. This figure shows the remarkable result that zero power loss is reached when the rotor areas still overlap each other geometrically, i.e. $y/D < 1.0$.

Very interesting and complete material appeared recently in Ref. 5.30, where wind tunnel tests were carried out on a two-bladed model with a diameter $D = 360$ mm and a constant chord $c = 20$ mm. The tests were carried out with different values of the ambient turbulence intensity. Some of the test results are reproduced in the Figs 5.29 through 5.32.

Fig. 5.29 shows the velocity defect in the wake centre for three different tip-speed ratios of the turbine. $\lambda = 6.6$ corresponds with the optimum C_p of the model turbine. The decrease of the velocity defect behind the turbine approaches a power law at values of x/D between 5 and 8, depending on λ . The power law resembles $(x/D)^{-5/4}$ instead of $(x/D)^{-2/3}$, as is shown in the figure.

The tests shown in this figure were carried out with an ambient turbulence intensity of 1 %. Very interesting is the "mechanical" turbulence intensity along the wake centre, shown in Fig. 5.29. The rapid increase of the turbulence intensity at x/D between 4 and 8 probably corresponds with the termination of the so-called "potential" core, as it was named in Ref. 5.24. This shows, that there are turbulence intensities of more than 10 % in the shear layer of the near wake.

Fig. 5.30 shows the increase of the wake width with downwind separation. The so-called "half width" is that width at which the wake velocity defect is one half of the value at the centre line. The half width decreases initially due to the "potential core" effect.

Fig. 5.31 shows the influence of the ambient turbulence intensity on the wake decay, which is

appreciable. The difference between tests with a horizontal-axis turbine and a Darrieus (vertical-axis) turbine is not significant. Though the ambient turbulence appreciably affects the magnitude of the velocity defect at a given x/D , the rate of decrease is not affected. Ref. 5.30 obtains the following power-laws for the velocity defect and the wake half width, viz.

$$u_m/U_1 \propto (x/D)^{-1.25}, \quad (5.3.17)$$

$$b_{0.5}/D \propto (x/D)^{0.63}. \quad (5.3.18)$$

Figure 5.32 shows the power ratio of a turbine, located just downwind from another turbine. It must be noticed that these results are obtained for a low ambient turbulence level, viz. 1 %. The extrapolated results have been obtained from an interpolation formula given in Ref. 5.30. For a more complete discussion of the test results, reference has to be made to the original report.

5.3.3.2 Wake interaction in a finite array

Due to the limited dimensions of a wind tunnel, test results for a finite array of wind turbines in a wind tunnel are only obtainable by simulating the energy-absorbing effect of a turbine by a small circular wire screen. Such tests have been described in Ref. 5.26.

A more or less realistic simulation of the turbine wake seemed possibly by a wire screen surrounded by a small annular "ring" or diffuser. The applicability of the simulation was judged by comparing measurements on the isolated screen with rotating model tests, such as described in Ref. 5.30.

In the tests described in Ref. 5.26, the turbines were placed on a circular turntable in the test-section floor. The turbines were distributed on this circular area in a rectangular pattern in such a way, that the separation between two turbines (x/D) was maximum at a wind direction $\beta = 0$ and minimum at $\beta = 45^\circ$. The table below gives the x/D , for different numbers of turbines (N) placed on the turntable, together with the corresponding λ -values.

β°	N	37	49	97
	λ	1.5×10^{-2}	2.4×10^{-2}	4.5×10^{-2}
0	x/D	10	8	6
45	x/D	7.1	5.7	4.25

It has to be noticed that in this table the strict definition of $\lambda = S_{\text{ref}}/S_{\text{land}}$ has been used. In an array with different spacings in two directions (which applies in this case), the λ -values cannot be compared with the λ -values for an infinite array, because in that case an equal spacing in two directions was implicitly assumed.

Figure 5.33 shows the power output of three rectangular patterns on a circular area at different wind directions. The wind velocity is the same at all wind directions (isotropic wind). Increasing the number of turbines on a given land area increases the total output, but the total output divided by the number of turbines decreases, however.

At $\beta = 10^\circ$ and 30° , the wake interactions are smallest, whereas at $\beta = 45^\circ$ the interaction is largest, as was to be expected, because x/D is small.

Figure 5.34 shows the power output of a circular array averaged over several wind directions in isotropic wind. It also gives an impression of the variation of the power ratio across the array, by showing the total average, the average of the turbines along the circumference of the circular array and the average of the turbine in the centre of the array. This diagram clearly shows that the central turbine in a rectangular grid of turbines on a circular land area is the least "economic".

It is difficult to compare Fig. 5.34 with the predictions of Crafoord (Fig. 5.24), but the neglect of direct wake interactions seems to lead to an underestimation of the power losses in a finite array (notice that the diameter of the circular array is $\approx 46 D$).

5.3.3.3 Practical applications

The experimental results of the preceding Sections in combination with the preceding theoretical calculations can be applied in two different way, viz.

- 1: to estimate a maximum possible amount of wind energy, which can be obtained from an extensive land area (e.g. an entire country), in order to get a first impression of the feasibility of wind energy conversion for such a country.
- 2: to find the optimum pattern for a finite array of wind turbines on a specific land area, taking the number of turbines as well as the spacing in different directions into account.

The first question is answered by several authors using the surface-roughness theory or some modified form of it, which is especially suited for such a question. Also the result for a large but finite array may be included. The answer is often given as a power output per land area (W/m^2), but this depends critically on the wind statistics used and, therefore, the measure of rotor area per land area (m^2/km^2 or λ) is preferred. The table below gives some estimates of this quantity.

Athor	Ref.	m^2/km^2	λ	type of array
Templin	5.22	1000	1.0×10^{-3}	infinite
Railly	5.27	1500	1.5×10^{-3}	
Ljungström	5.25	14000	1.4×10^{-2}	finite
Bultjes	5.26	20000	2.0×10^{-2}	

This clearly indicates the influence of considering direct wake effects and finite clusters of turbines instead of infinite arrays. However, these high-density finite arrays can only be sparsely distributed across the country and, for a first estimate of the total amount of wind energy for an entire country, the infinite array estimates seem still useful.

Nevertheless, the second question has more practical significance. The authors of Ref. 5.31 applied in their study the computer code of Ref. 5.24, adjusting some numerical constants in order to get a better agreement with the experimental results of the Refs 5.26 and 5.30. The use of the computer code enables a quick survey of different turbine arrays. In Ref. 5.31 two different kinds of array patterns are considered, viz. the row and the rectangular array covering an almost circular land area.

Figure 5.35 shows the calculated output of a single row of turbines, averaged over the wind rose for an isotropic wind distribution. This diagram shows that the economic limit is not reached even for a very large number of turbines placed in a single row, provided that the value of the turbine spacing x/D has to be taken not too small. For an isotropic wind distribution (same wind velocity from all directions), $x/D \approx 3$ seems an acceptable value. By repeating the calculations for a real wind rose, and by putting the row perpendicular to the prevailing wind direction, Ref. 5.21 quotes a value of $x/D \approx 2$ as economically feasible in that case, because of the reduced wind energy content of the wind directions parallel to the row.

The energy output of the circular array is considered for an isotropic wind, but also some cases with a real wind-rose distribution have been considered. The ratio

$$R(N) = [P(N+1) - P(N)]/P_0, \quad (5.3.19)$$

with $P(N+1)$: power output of an array of $N+1$ turbines,
 $P(N)$: power output of an array of N turbines,
 P_0 : power output of an isolated turbine,

could be envisaged as a measure for the economy of adding one turbine to an existing array. Ref. 5.31 quotes a limiting value of $R(N) = 0.75$ below which a further enlargement of the array is not economically feasible.

Figure 5.36 shows results for a cluster-like turbine array. The rectangular pattern shows a separation distance $x/D = 7$ in the direction $\beta = 45^\circ$. Arrays with different numbers of turbines were calculated. The smallest array consisted of a square with 25 turbines, whereas larger arrays formed equilateral polygons. The numbering system of the turbines in the array followed a spiral order of sequence, as sketched in Fig. 5.36.

The relative power output decreases steadily with the increasing number of turbines, but the total energy output $P(N)$ increases, as is shown in the table below.

N	$\frac{P(N)}{N P_0}$	$\frac{P(N)}{P_0}$
25	0.88	22.00
29	0.87	25.23
37	0.85	31.45
45	0.84	37.80
61	0.82	50.02

Also shown in Fig. 5.36 is the relative power increment due to adding one turbine (Eq. (5.3.19)), which shows that, with $x/D = 7$, arrays with $N < 60$ seem economically feasible.

The influence of the wind rose on these cluster-like arrays appeared to be negligible within the accuracy of the calculations, when $x/D > 5$.

Ref. 5.31 gives as a tentative recommendation for acceptable separation distances in case of an isotropic wind distribution

type of array	number of turbines	separation
single row	unlimited	$x/D \geq 3$
rectangular pattern (cluster-like)	$N \leq 20$	$x/D \geq 5$
	$20 < N \leq 60$	$x/D \geq 7$
	$N > 60$	$x/D \geq 9$

which is a far more shaded answer than the λ -values given by the surface roughness theories at the beginning of this Section.

5.4 Short note on literature and bibliographies

Each of the Chapters 1 through 5 and the Appendices contain lists with references cited in the text, but these lists are by no means an exhaustive survey of the literature on wind energy. Readers interested in bibliographies on wind energy are referred to the following volumes:

- 1 Burke, B.L., Merony, R.N.: Energy from the Wind; Annotated Bibliography. Colorado State Univ., Basic Volume (Co., USA; July 1975), First Supplement (Co., USA; April 1977).
- 2 Van Steyn, R.: Wind Energy; a Bibliography with Abstracts and Keywords, Part 1 and 2. Eindhoven Univ. of Techn. (Eindhoven, The Netherlands, July 1975).
- 3 Van Meel, J., Hengeveld, D.: Wind Energy; a Bibliography with Abstracts and Keywords, Part 3 and 4. Eindhoven Univ. of Techn. (Eindhoven, The Netherlands, March 1977).

A partial bibliography, which contains a listing of recent reports generated by the Federal Wind Energy Program of the USA, is distributed recently (July 1978) by the Wind Systems Branch, Energy Technology - Solar Energy Division, U.S. Department of Energy (DOE).

Much information is contained in the proceedings of Symposia and Workshops, a number of which will be listed below:

- 1 Proc. Workshop on Wind Energy Conversion Systems (Washington D.C., 11-13 June 1973)
NSF/RA/W-73-006 (Dec. 1973).
- 2 Proc. Second Workshop on Wind Energy Conversion Systems (Washington D.C., 5-11 June 1975).
The Mitre Corp. MTR-6970 (Sept. 1975).
- 3 Proc. Third Biennial Conf. and Workshop on Wind Energy Conversion Systems (Washington D.C., 19-21 Sept. 1977).
JFB Scient. Corp. CONF-770921 (Sept. 1977).
- 4 Proc. Workshop on Advanced Wind Energy Systems (Stockholm, Sweden; 29-30 Aug. 1974).
Swedish State Power Board.
- 5 Proc. Vertical-Axis Wind Turbine Techn. Workshop (Albuquerque, New Mexico, 18-20 May 1976).
Sandia Laboratories Report SAND76-5586 (July 1976).
- 6 Proc. Intern. Symp. on Wind Energy Systems (St. John's College, Cambridge, England; 7-9 Sept. 1976).
- 7 Proc. Second Intern. Symp. on Wind Energy Systems (Amsterdam, The Netherlands; 3-6 Oct. 1978).
- 8 Proc. Workshop on Wind Turbine Structural Dynamics (Lewis Res. Center, Cleveland, Ohio, 15-17 Nov. 1977).
NASA Conf. Publ. 2034/DOE Publ. CONF-771148 (1978).

In conclusion, the articles appearing in the journal "Wind Engineering" (UK, first volume in 1977) and in the "Journal of Energy" (USA) have to be mentioned.

Just before submitting the present document for publication, the following report was brought to the author's attention:

Miller, R.H., et al.: Wind Energy Conversion, Volume II:
Aerodynamics of Horizontal-Axis Wind Turbines.
M.I.T. Report ASRL TR-184-8 (1978).

This report was not taken into account when preparing the present review.

5.5 List of references

- 5.1 Frost, W.: Engineering Handbook on the Atmospheric Environmental Guidelines for Use in Wind Turbine Generator Development.
Proc. Third Biennial Conf. and Workshop on Wind Energy Conversion Systems (Washington D.C., 19-21 Sept. 1977).
JFB Scient. Corp. CONF-770921 (Sept. 1977).
- 5.2 Weingarten, L.I., Blackwell, B.F.: Sandia Vertical-Axis Wind Turbine Program Techn. Quarterly Report (Jan. - March 1976).
Sandia Laboratories Energy Report SAND76-0338 (Aug. 1976).
- 5.3 Sheldahl, R.E., Blackwell, B.F.: Free-Air Performance Tests of a 5-Metre Diameter Darrieus Turbine.
Sandia Laboratories Report SAND77-1063 (Dec. 1977).
- 5.4 Lumley, J.L., Panofsky, H.A.: The Structure of Atmospheric Turbulence.
(John Wiley & Sons Inc., 1964).
- 5.5 Strickland, J.H.: The Darrieus Turbine: a Performance Prediction Model Using Multiple Stream-tubes.
Sandia Laboratories Energy Report SAND75-0431 (Oct. 1975).
- 5.6 Wilson, R.E., Lissaman, P.B.S.: Applied Aerodynamics of Wind Power Machines.
Oregon State Univ. Report NSF/RA/N-74113 (July 1974).
- 5.7 Glauert, H.: Miscellaneous Airscrew Problems.
Aerodynamic Theory (ed. W.F. Durand) Chapter XII, Div. L
(Dover Publ. Inc., N.Y., 1934).
- 5.8 Spera, D.A.: Structural Analysis of Wind Turbine Rotors for NSF-NASA MOD-0 Wind Power System.
NASA TM X-3198 (March 1975).
- 5.9 Base, T.E., Russell, L.J.: Computer Aided Aerogenerator Analysis and Performance.
Proc. Intern. Symp. on Wind Energy Systems (St. John's College, Cambridge, England; 7-9 Sept. 1976).
- 5.10 Prandtl, L.: Herstellung eindwandfreier Luftströme (Windkanäle).
Handbuch der Experimentalphysik, Band 4, Teil 2.
(Akad. Verl. GmbH, Leipzig, 1932).
- 5.11 Batchelor, G.K.: The Theory of Homogeneous Turbulence.
(Cambridge Univ. Press, London, 1956) pp. 68-75.
- 5.12 Duchène-Marullaz, P.: Full-Scale Measurement of Atmospheric Turbulence in a Suburban Area.
Proc. Fourth Intern. Conf. on Wind Effects on Buildings and Structures (Heathrow, England; 8-12 Sept. 1975).
(Cambridge Univ. Press, London, 1977).
- 5.13 Der Kinderen, W.J.G.J., et al.: Effects of Wind Fluctuations on Windmill Behaviour.
Wind Engineering, 1, 2 (1977) pp. 126-140.
- 5.14 Brulle, R.V.: Feasibility Investigation of the Giromill for Generation of Electrical Power.
Final Report of the Period April 1975 - April 1976.
McDonnell Aircr. Co. (Jan. 1977).
- 5.15 Blackwell, B.F., Feltz, L.V.: Wind Energy - A Revitalized Pursuit.
Sandia Laboratories Report SAND75-0166 (March 1975).
- 5.16 Blackwell, B.F., et al.: Wind Tunnel Performance Data for Two- and Three-Bucket Savonius Rotors.
Sandia Laboratories Energy Report SAND76-0131 (July 1977).
- 5.17 South, P., Rangi, R.S.: Preliminary Tests of a High-Speed Vertical-Axis Windmill.
NRC, NAE Report LTR-LA-74 (March 1971).
- 5.18 South, P., Rangi, R.S.: An Experimental Investigation of a 12 Ft. Diameter High-Speed Vertical-Axis Wind Turbine.
NRC, NAE Report LTR-LA-166 (April 1975).

- 5.19 Banas, J.F., et al.: Application of the Darrieus Vertical-Axis Wind Turbine to Synchronous Electrical Power Generation. Sandia Laboratories Report SAND75-0165 (March 1975).
- 5.20 Dragt, J.B.: On the Use of "Wind Measurements on the Site", a Statistical Consideration (in Dutch). Netherlands Energy Research Foundation ECN, Memo No. FYS-WINDMETINGEN-77-03 (Nov. 1977).
- 5.21 Templin, R.J., South, P.: Some Design Aspects of High-Speed Vertical-Axis Wind Turbines. Proc. Intern. Symp. on Wind Energy Systems (St. John's College, Cambridge, England; 7-9 Sept. 1976).
- 5.22 Templin, R.J.: An Estimate of the Interaction of Windmills in Widespread Arrays. NRC, NAE Report LTR-LA-171 (Dec. 1974).
- 5.23 Crafoord, C.: An Estimate of the Interaction of a Limited Array of Windmills. Univ. of Stockholm, Dept. of Met.; Intern. Met. Inst. in Stockholm, Report DM-16 (Nov. 1975).
- 5.24 Lissaman, P.B.S., Base Jr., E.R.: Energy Effectiveness of Arrays of Wind Energy Conversion Systems. Aero Vironment Inc. Report AV FR 7058 (Pa., USA; May 1977).
- 5.25 Ljungström, O.: Large Scale Wind Energy Conversion Systems (WECS) Design and Installation as Affected by Site Wind Energy Characteristics, Grouping Arrangement and Social Acceptance. Wind Engineering, 1, 1 (1977) pp. 36-56.
- 5.26 Builtjes, P.J.H.: The Interaction of Windmill Wakes. Proc. Second Intern. Symp. on Wind Energy Systems (Amsterdam, The Netherlands; 3-6 Oct. 1978).
- 5.27 Raily, J.W.: A Possible Saturation Criterion for Wind Energy Extraction. Wind Engineering, 1, 1 (1977) pp. 23-35.
- 5.28 Jacobs, W.: Umformung eines turbulenten Geschwindigkeitsprofils. ZAMM, 19 (1939) pp. 87-100.
- 5.29 Abramovich, G.N.: The Theory of Turbulent Jets. (M.I.T. Press, 1963).
- 5.30 Vermeulen, P.: A Wind Tunnel Study of the Wake of a Horizontal-Axis Wind Turbine. Netherlands Organization for Appl. Scient. Res. TNO, Report No. 78-09674 (Sept. 1978).
- 5.31 Builtjes, P.J.H., Smit, J.: Calculation of Wake Effects in Wind Turbine Parks. Wind Engineering, 2, 3 (1978) pp. 135-145.

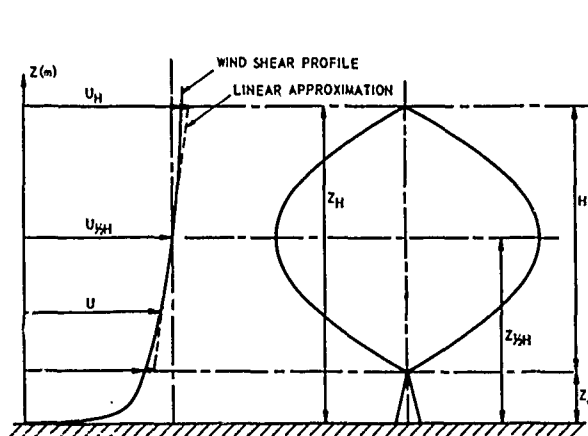


Fig. 5.1 Wind turbine in a wind stream with a vertical velocity gradient (wind shear)

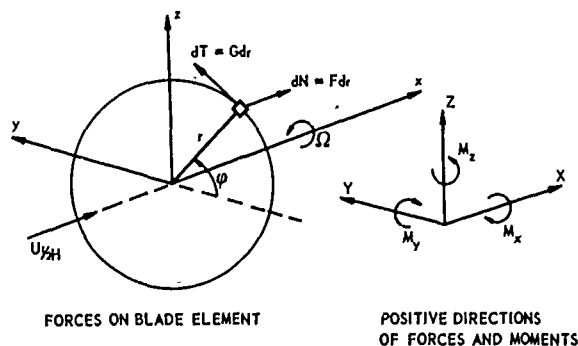


Fig. 5.2 Forces on a blade element of a horizontal-axis wind turbine. Positive directions of total forces and moments on the rotor

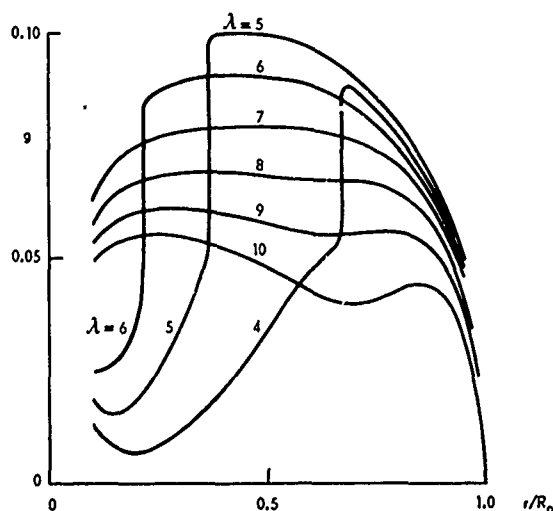
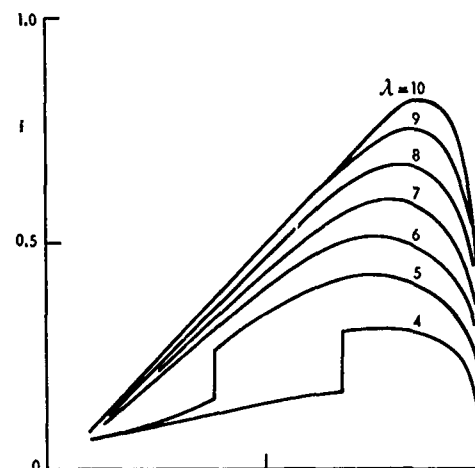


Fig. 5.3 Example of the f- and g-distribution for a two-bladed rotor with $\lambda_{opt} \approx 8$

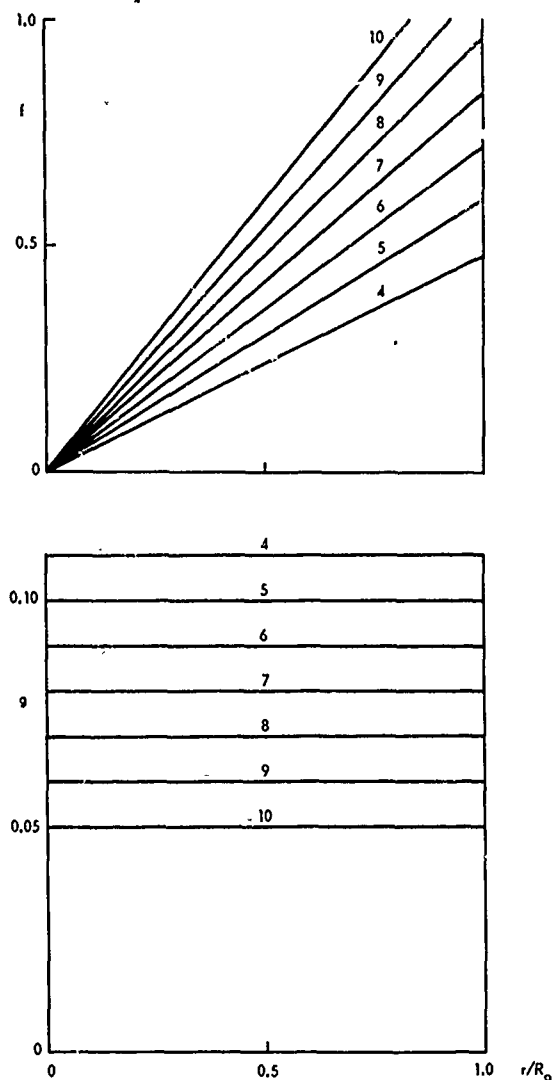


Fig. 5.4 Simplified f - and g -distributions for a two-bladed rotor, according to Eq.(5.1.14)

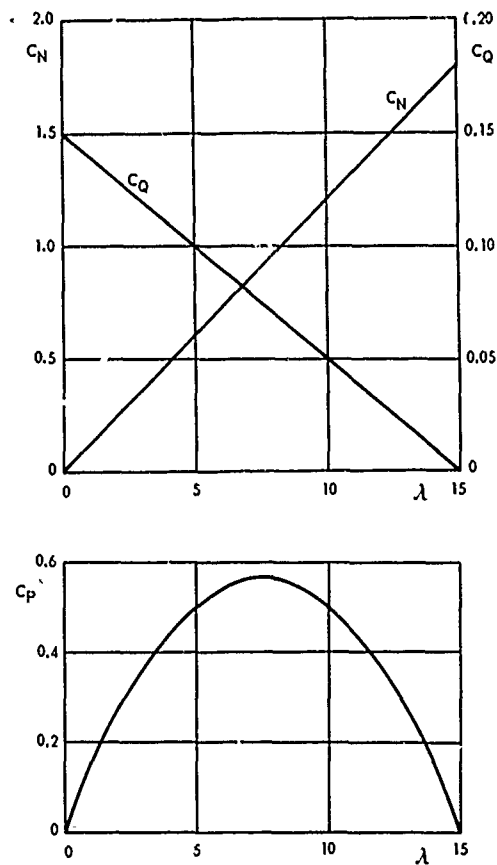
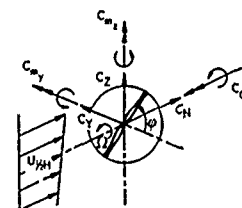


Fig. 5.5 The variation of C_N , C_Q and C_P with λ , in a uniform flow according to the simplified expressions for f and g (see the Eqs. (5.1.14) and (5.1.15))



INCREMENT DUE TO WIND SHEAR	VARIATION WITH λ FOR $a = 0.10$	MULTIPLICATION FACTOR		
		$B = 1$	$B = 2$	$B = 3$
ΔC_H		$\sin \varphi$	0	0
ΔC_V		$\sin^2 \varphi$	$\frac{1}{2}$	
ΔC_{M_y}		$\sin \varphi \cos \varphi$	0	
ΔC_Q		$\frac{2}{3} \sin \varphi$	0	0
ΔC_{M_x}		$\sin^2 \varphi$	$\frac{1}{2}$	
ΔC_{M_z}		$\sin \varphi \cos \varphi$	0	

Fig. 5.6 Variations in forces and moments due to wind shear, according to the simplified equations (5.1.16) through (5.1.21)

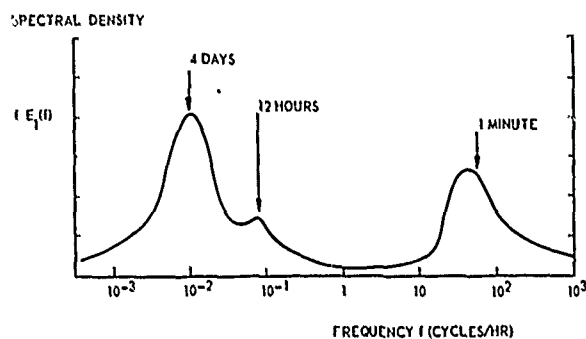


Fig. 5.7 Spectrum of wind velocity, according to Van der Haven and obtained from Ref. 5.4 (spectral density in arbitrary units)

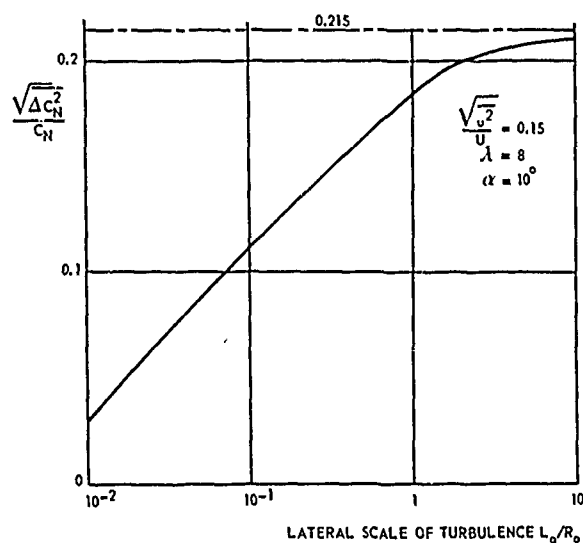


Fig. 5.8 Crude estimation of the influence of the lateral scale of isotropic turbulence on the RMS-value of the normal force fluctuation on one blade of a horizontal-axis wind turbine (Eq.(5.1.33))

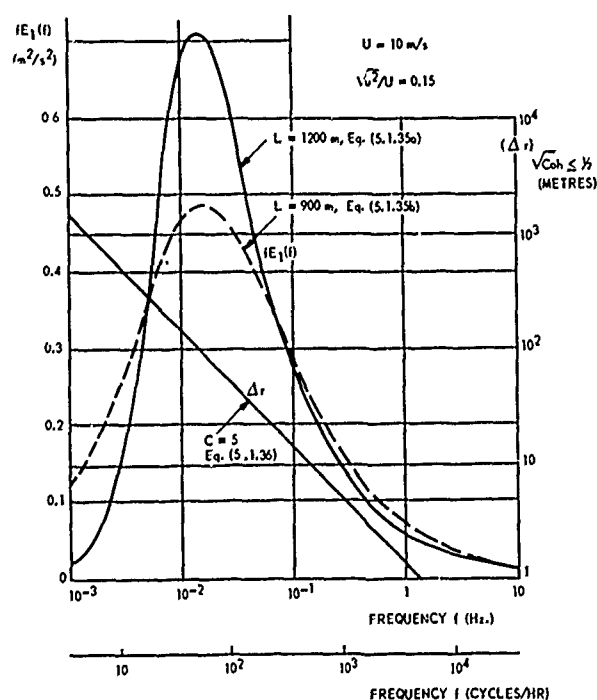


Fig. 5.9 Typical example of the power spectral density $E_1(f)$ and the separation Δr at which the square root of the coherence is decreased to $1/2$, as a function of the frequency of the "turbulent" part of the wind velocity fluctuations

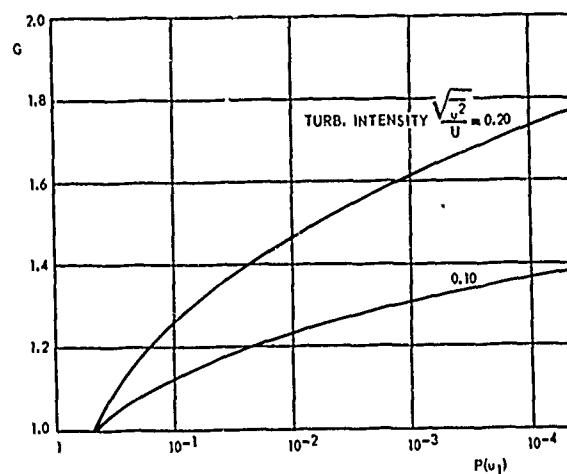


Fig. 5.10 The probability of occurrence of a gust with gust factor G , estimated from a Gaussian distribution of the velocity fluctuations u about the average U . $P(u_1)$ is the probability of occurrence of a fluctuation u_1 and G is equal to $(U + u_1)/U$

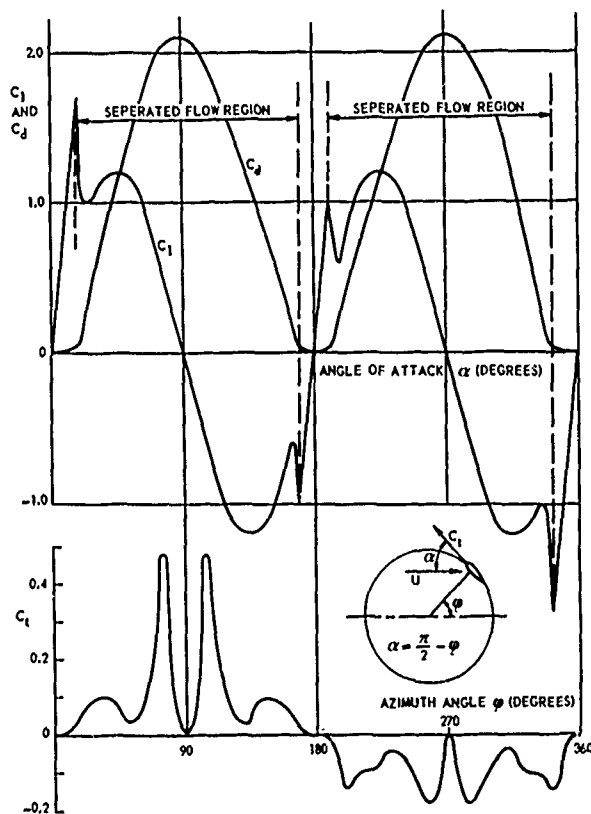


Fig. 5.11 Lift and drag as a function of the angle of attack and the tangential force of one blade as a function of the azimuth angle

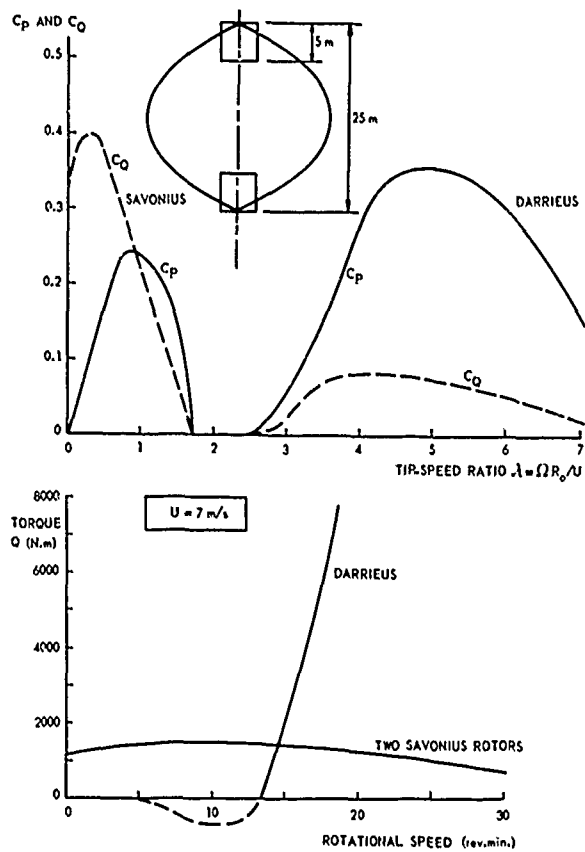


Fig. 5.12 The driving torque of a Darrieus turbine combined with two Savonius rotors

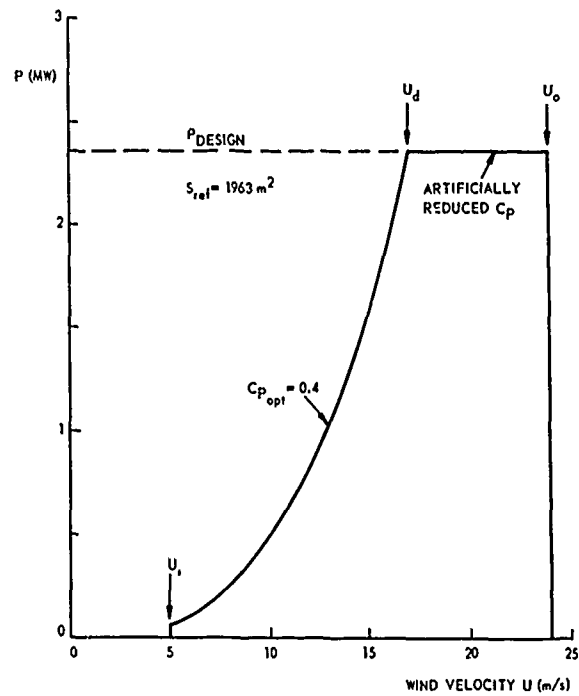


Fig. 5.14 Idealized performance diagram of a wind turbine. P is the aerodynamic power (no conversion and transmission losses)

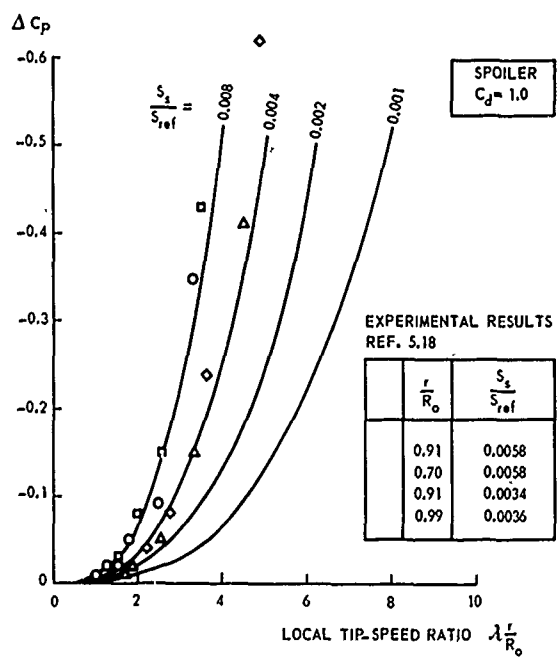


Fig. 5.13 Estimation of the decrease of the power coefficient ΔC_p due to a spoiler with an area S_s , drag coefficient $C_d = 1.0$, and located at a radius r (S_{ref} is the swept area of the rotor) The experimental results are obtained with a Darrieus turbine (Ref. 5.18)

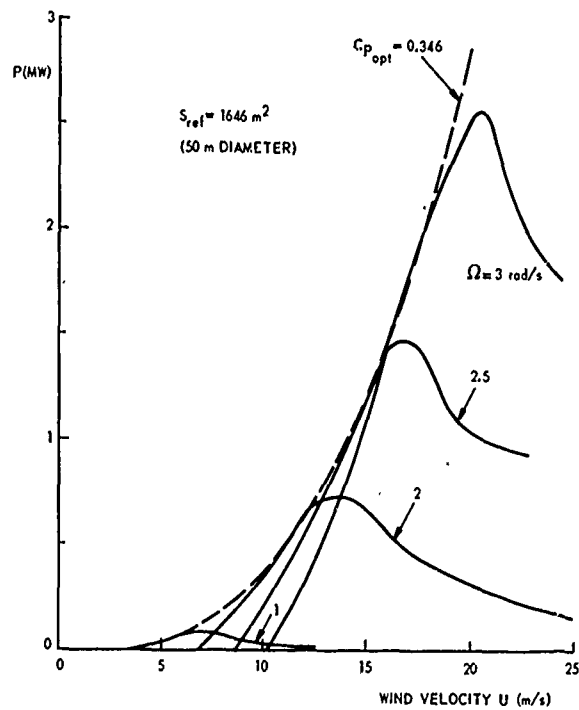


Fig. 5.15 Performance diagrams for a Darrieus turbine, operating at a constant angular velocity, using the C_p - vs - λ curve of Fig. 4.57. P is the aerodynamic power

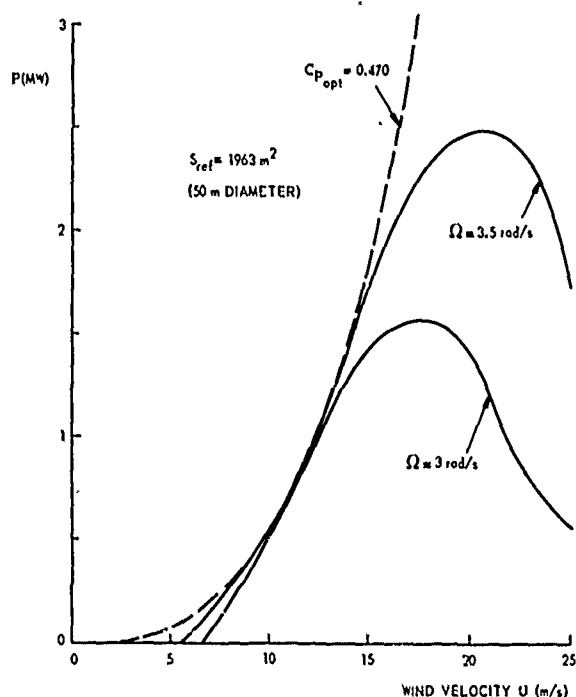
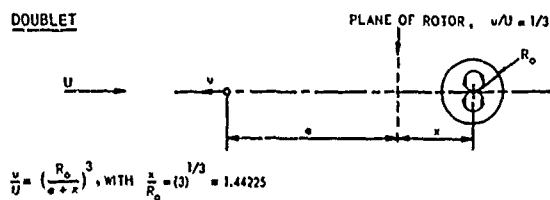


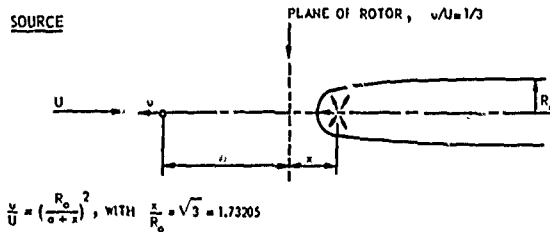
Fig. 5.16 Performance diagrams for a horizontal-axis turbine, operating at a constant angular velocity, using the C_p - vs - λ curve of Fig. 4.24 for $\theta_p = 0$. P is the aerodynamic power

DOUBLET



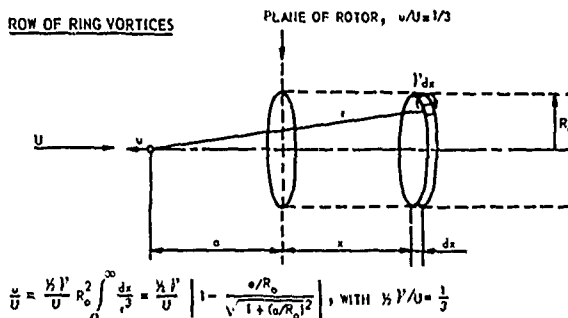
$$\frac{v}{U} = \left(\frac{R_0}{a+x} \right)^3, \text{ WITH } \frac{x}{R_0} = \left(\frac{1}{3} \right)^{1/3} = 1.44225$$

SOURCE



$$\frac{v}{U} = \left(\frac{R_0}{a+x} \right)^2, \text{ WITH } \frac{x}{R_0} = \sqrt{3} = 1.73205$$

ROW OF RING VORTICES



$$\frac{v}{U} = \frac{1}{2} \frac{1}{U} R_0^2 \int_0^\infty \frac{dx}{x^3} = \frac{1}{2} \frac{1}{U} \left[1 - \frac{a/R_0}{1 + (a/R_0)^2} \right], \text{ WITH } \frac{1}{2} \frac{1}{U} = \frac{1}{3}$$

Fig. 5.18 Possible simple models to estimate the stagnation in front of an optimally operating wind turbine

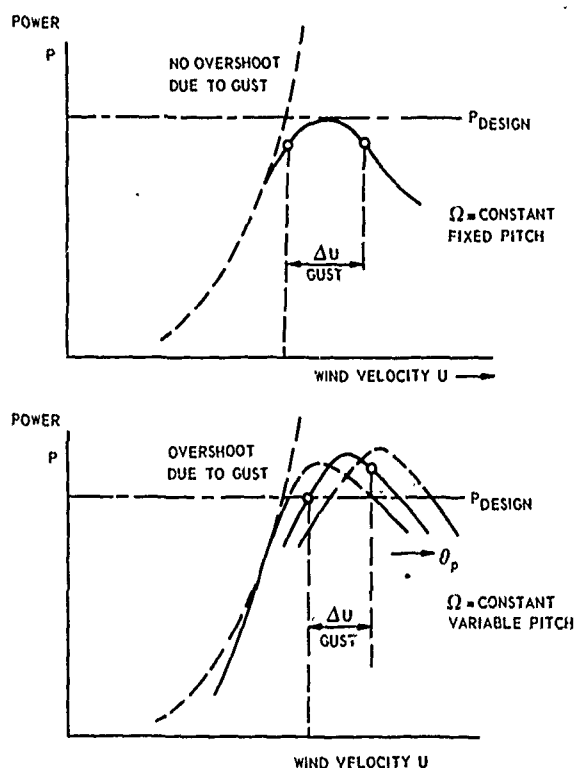


Fig. 5.17 Power overshoot due to a gust ΔU , when the power output is limited by a blade-pitch control, which is slower than the wind-velocity variation

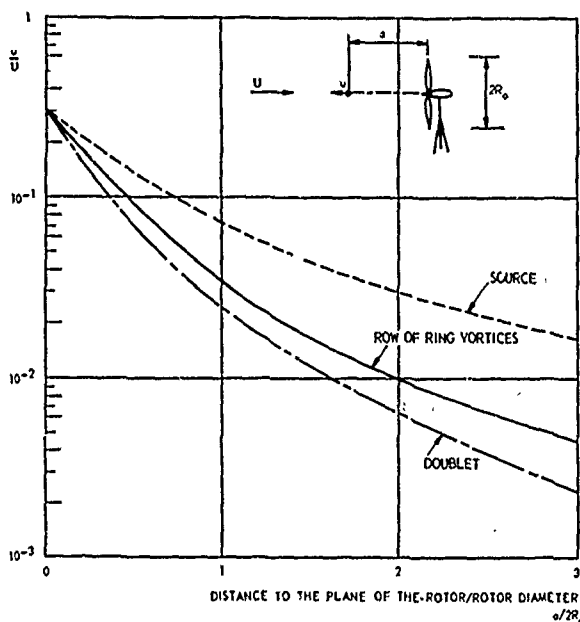


Fig. 5.19 Several estimates of stagnation in front of an operating wind turbine

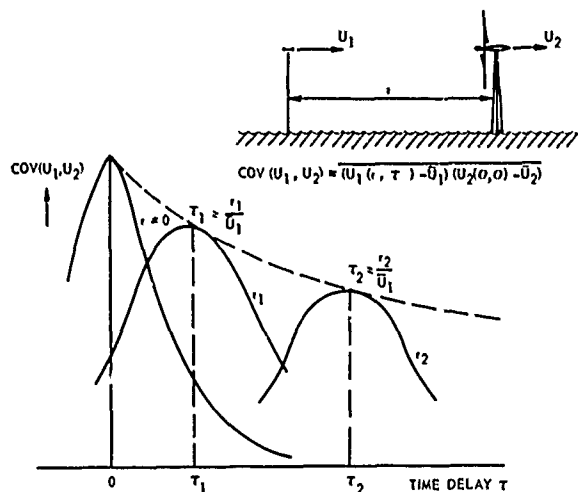


Fig. 5.20 The variation of $COV(U_1, U_2)$ with separation distance r and time delay τ

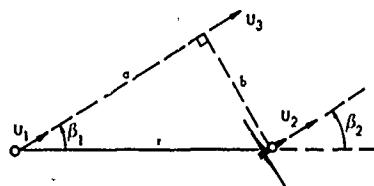


Fig. 5.21 Influence of the average wind direction on $COV(U_1, U_2)$

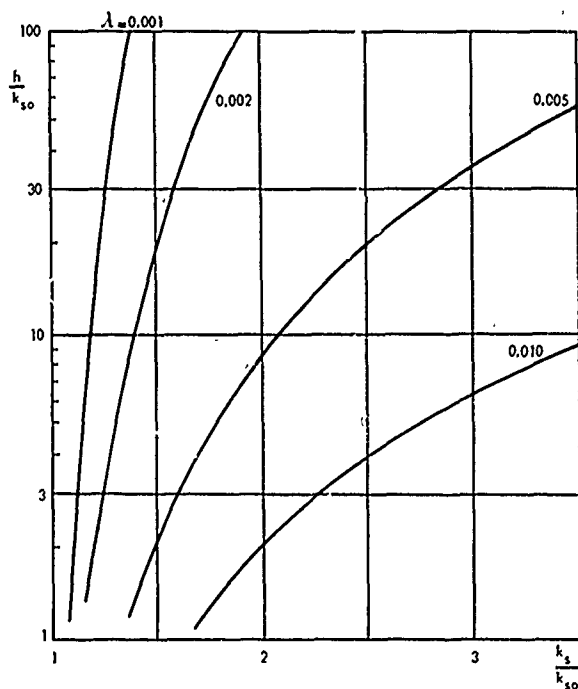


Fig. 5.22 The increase of the effective surface roughness height with turbines (k_s) as a function of the turbine hub-height (h), the turbine density (λ) and the original terrain surface roughness height (k_{s0}), according to Ref. 5.22

POWER RATIO

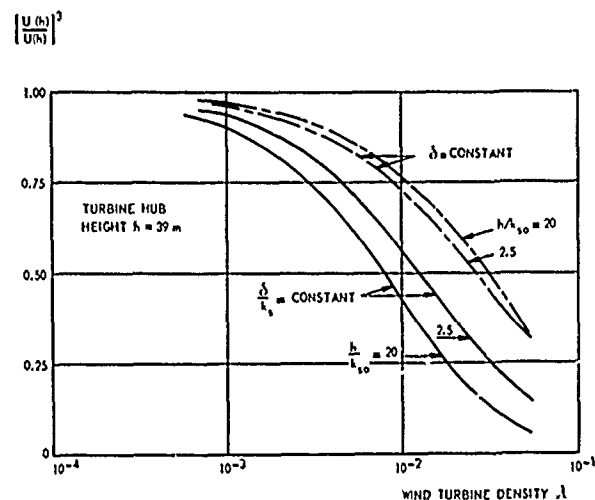


Fig. 5.23 Wind power in an infinite array, compared with the power of an isolated turbine. Influence of the wind turbine density and terrain condition according to Ref. 5.22
 $h/k_{s0} = 20$: open country
 $h/k_{s0} = 2.5$: rough wooded terrain

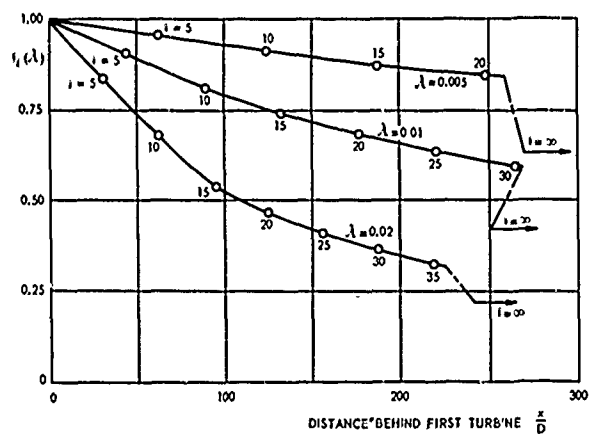


Fig. 5.24 Influence of a finite array on the power ratio $f_i(\lambda)$ according to the theory of Ref. 5.23, using the data for an infinite array of Ref. 5.22
 $C_D = 0.45$
open country $h/k_{s0} = 20$ (see Fig. 5.23)

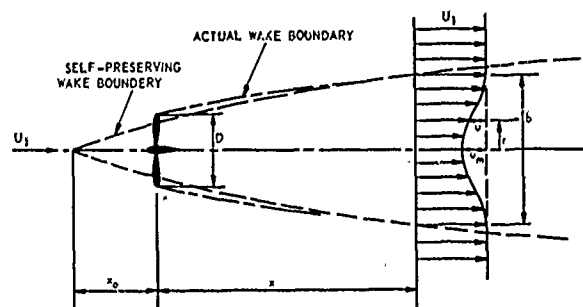


Fig. 5.25 Symbols used to describe self-preserving wake flow

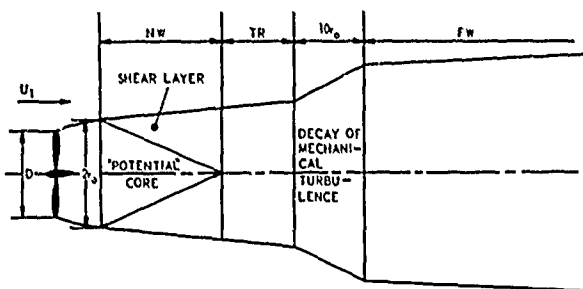


Fig. 5.26 Wake decay regions, defined in Ref. 5.24

NW = near wake

TR = transition region

FW = far wake

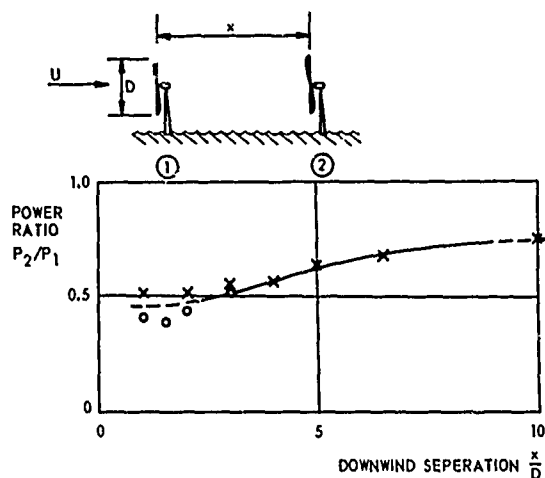
 $2r_0 = D \sqrt{(1-a)/(1-2a)}$; a = axial induction factor

Fig. 5.27 Power loss of a turbine placed exactly behind an upwind turbine (Ref. 5.25)

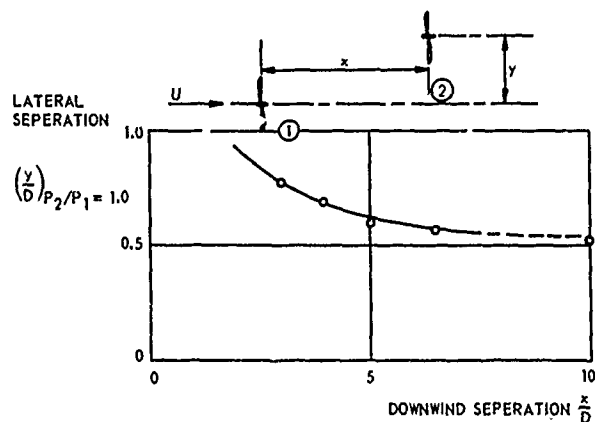


Fig. 5.28 Lateral separation necessary to avoid wake interaction (Ref. 5.25)

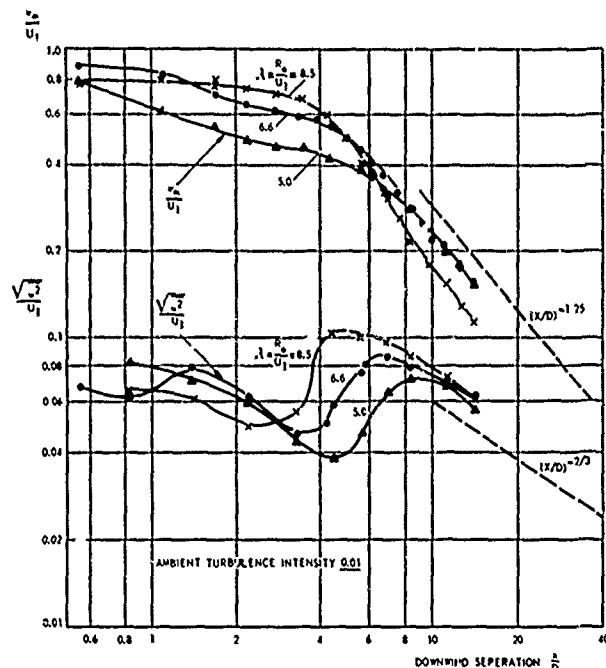


Fig. 5.29 Downstream variation of the maximum velocity defect and the centre-line "mechanical" turbulence intensity for three tip-speed ratios of the turbine (Ref. 5.30)

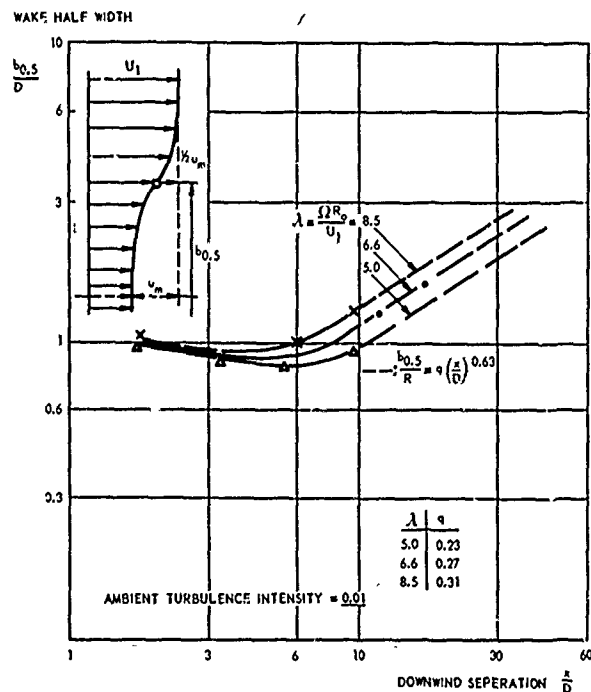


Fig. 5.30 Increase of wake half width with separation distance, as a function of the tip-speed ratio (Ref. 5.30)

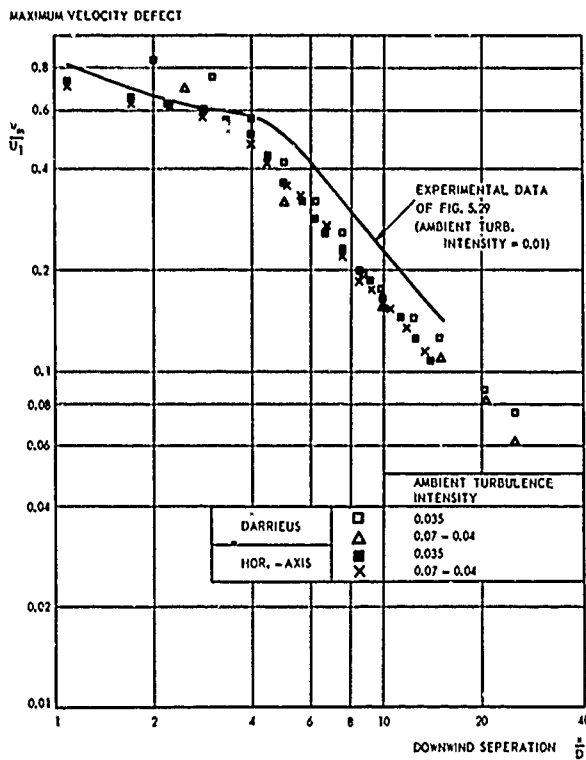


Fig. 5.31 Velocity defect at the wake centre-line as a function of separation distance. Effect of ambient turbulence intensity and type of turbine (Ref. 5.30)

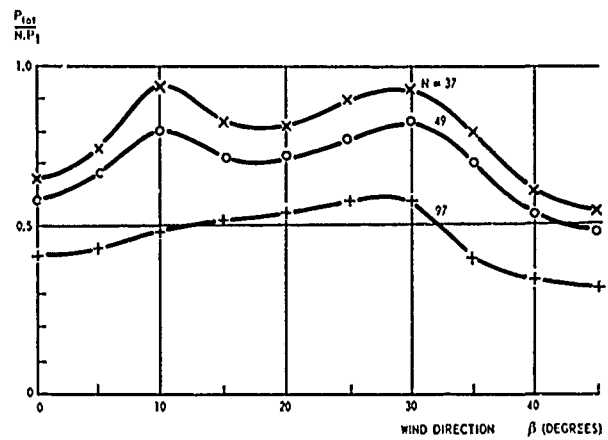


Fig. 5.33 Influence of the number of turbines on a fixed ground area and the influence of the wind direction on the average energy output, according to Ref. 5.26

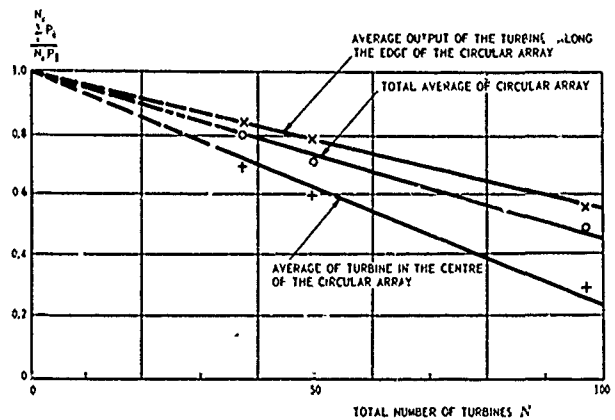


Fig. 5.34 Output averaged over the several wind directions in isotropic wind, according to Ref. 5.26

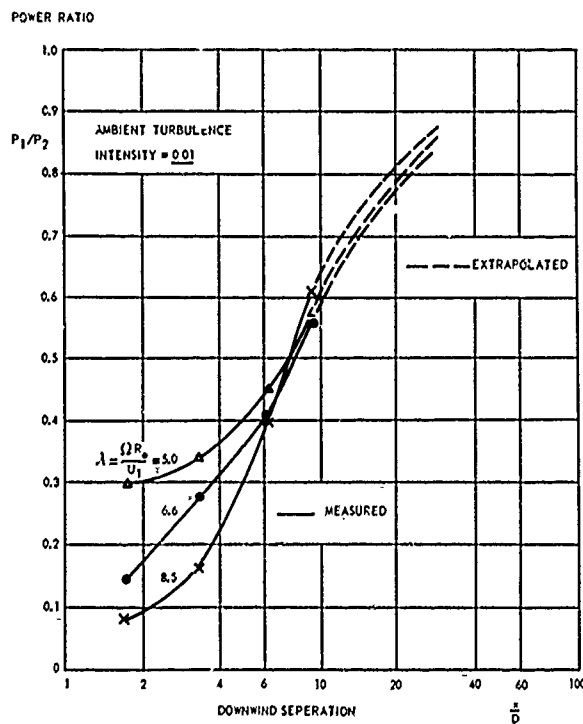


Fig. 5.32 Downwind variation of the power ratio for a turbine located exactly behind an upwind turbine (Ref. 5.30)

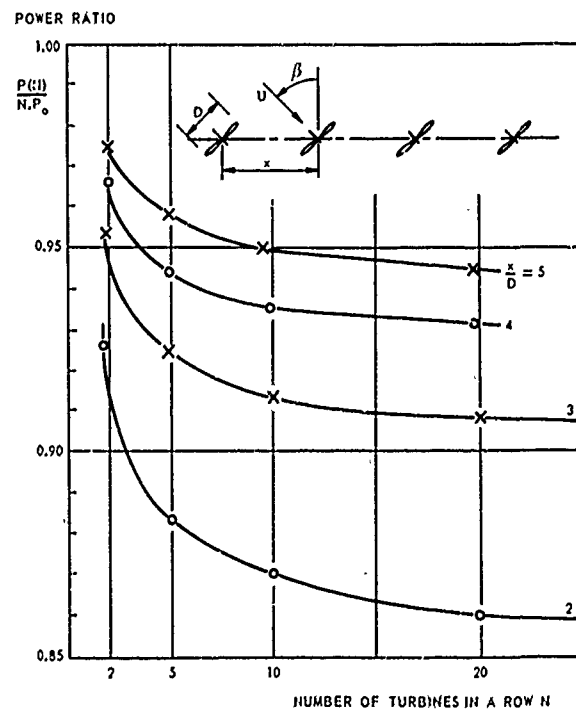


Fig. 5.35 Relative energy output of a single row of N turbines, averaged over several wind directions β for an isotropic wind distribution, according to Ref. 5.31
Influence of turbine spacing

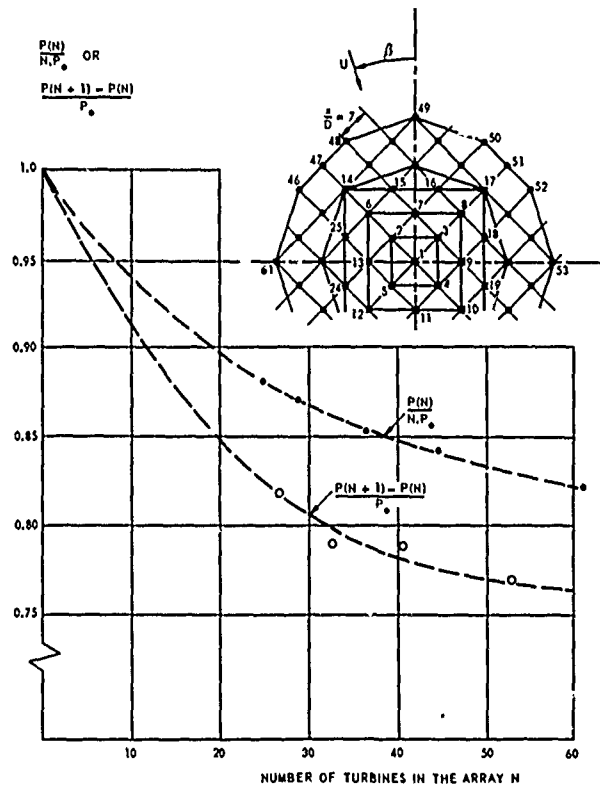


Fig. 5.36 Power ratio and relative increment of the power output due to adding one turbine to the array, averaged for isotropic wind distribution, according to Ref. 5.31

APPENDIX A
STREAM FUNCTION AND VELOCITY DISTRIBUTION DUE TO AN ANNULAR WING WITH A
TRIANGULAR CHORDWISE VORTICITY DISTRIBUTION IN AXISYMMETRIC FLOW

A.1 Introduction

There is an extensive literature on annular wing theory, but those theories are mainly concerned with induced velocities at the chord of the annular wing and not with the velocity field inside the annular wing, which is the prime question in case of a wind concentrator.

In order to get some insight into the induced mass flow through the annular wing, calculations have been carried out on an infinitely thin cylindrical annular wing with a triangular chordwise vorticity distribution, without bothering about the question whether such a chordwise load distribution is compatible with a flat plate aerofoil section. It is hoped that a triangular loading is not too far away from the actual incompressible flow load distribution and the camber of the corresponding aerofoil section is not too large so that the computations are invalidated (this certainly depends on the chord-radius ratio of the annular wing).

The maximum induced mass flow through the annular wing depends on the maximum attainable circulation around the aerofoil section. It is very difficult to set up such a calculation, but some insight into possible bounds can be obtained by calculating the corresponding section lift coefficients. In case of an annular wing, this lift coefficient cannot be simply obtained from the circulation and the velocity at infinity (wind velocity), because of the self-induced axial velocity at the aerofoil chord. These self-induced velocities have been obtained from Ref. A.1.

A.2 Induced axial velocities

Ref. A.2 gives the so-called "Stokes stream function" for an elementary vortex ring of strength γdx (see Fig. A.1)

$$\psi(0, r) = \frac{\gamma dx R r}{4\pi} \int_0^{2\pi} \cos \theta (x^2 + R^2 + r^2 - 2rR \cos \theta)^{-\frac{1}{2}} d\theta \quad (A.1)$$

A triangular vortex distribution with total circulation Γ ,

$$\gamma = 2\Gamma x/c^2, \quad (A.2)$$

leads to a stream function in point $P(0, r)$

$$\psi(0, r) = \Gamma r R / (2\pi c^2) \int_0^{2\pi} \cos \theta d\theta \int_0^c x (x^2 + R^2 + r^2 - 2rR \cos \theta)^{-\frac{1}{2}} dx \quad (A.3)$$

Integration and transformation leads to a stream function expressed in complete elliptic integrals of first and second kind, viz.:

$$\psi(0, r) = \frac{4\Gamma(rR)^{3/2}}{\pi c^2} \left[\frac{2}{3} \left\{ \frac{1-k_1^2}{k_1^3} K(k_1) - \frac{1-k_2^2}{k_2^3} K(k_2) \right\} - \left\{ \frac{2-k_1^2}{3k_1^3} E(k_1) - \frac{2-k_2^2}{3k_2^3} E(k_2) \right\} \right], \quad (A.4)$$

with

$$k_1^2 = 4rR / [(R+r)^2 + c^2]$$

and

$$k_2^2 = 4rR / (R+r)^2$$

When $c \rightarrow 0$ and $k_1 \rightarrow k_2 = k = 4rR / (R+r)^2$, Eq. (A.4) reduces to the stream function of a discrete vortex ring, viz.:

$$\psi_1(0, r) = \frac{\Gamma(rR)^{1/2}}{2\pi} \left\{ \left(\frac{2}{k} - k \right) K(k) - \frac{2}{k} E(k) \right\}, \quad (A.5)$$

which agrees with the formula given in Ref. A.2.

The stream function $\psi(0, r)$ times 2π gives the volume flow through a circle with radius r . The volume flow through the annular wing can be found by taking the limit $r \rightarrow R$. When $r = R$, $k_2 = 1$ and $E(k_2) = 1$. Furthermore

$$\lim_{k_2 \rightarrow 1} (K - k_2^2 K) / k_2^3 = 0$$

It follows from Eq. (A.4) that, if

$$k_1^2 = k^2 = 4 / [4 + (c/R)^2],$$

the following relation holds:

$$2\pi\psi(0, R) = \frac{\Gamma 8R}{(c/R)^2} \left[\frac{2}{3} \frac{1-k^2}{k^3} K + \frac{1}{3} - \frac{2-k^2}{3k^3} E \right] \quad (A.6)$$

Divided by πR^2 , Eq. (A.6) gives the average induced axial velocity (\bar{u}). For non-zero values of c/R ,

$2\pi\psi(0,R)$ is finite. The volume flow through a discrete vortex ring ($c = 0$) is infinite, however, as can be seen from Eq. (A.5) with $r = R$ and $k = 1$.

The distribution of the axial velocity along the radius could be obtained from Eq. (A.4), but it becomes a very intricate expression. In case of the discrete vortex ring (Eq. (A.5)), the expression becomes simpler, viz.:

$$u_1(0,r) = \frac{1}{r} \frac{\partial}{\partial r} \psi_1 = \frac{\Gamma}{2\pi R(1+r/R)} \left[K(k) + \frac{1+r/R}{1-r/R} E(k) \right] \quad (A.7)$$

The induced axial velocity on the axis ($r = 0$) is

$$u_1(0,0) = \Gamma/2R \quad (A.8)$$

which result could have been obtained much simpler from the application of the law of Biot-Savart to a vortex ring of strength Γ .

The induced velocity becomes infinite at the vortex ring ($r \rightarrow R$) (see Fig. A.2). This explains the infinite volume flow in case of a discrete vortex ring¹⁾. When the vorticity is distributed along a finite chord, the induced velocities remain finite and also the volume flow through the annular wing remains finite (cf. Ref. A.1).

In case of a finite chord, the axial induced velocity at the axis can be calculated directly, viz.

$$u(0,0) = \frac{\Gamma}{2R} \frac{2[1+(c/R)^2]^{\frac{1}{2}} - 1}{(c/R)^2[1+(c/R)^2]^{\frac{1}{2}}} \quad (A.9)$$

Figure A.3 shows the average velocity \bar{u} (Eq. (A.6)) and the velocity on the axis (Eq. (A.9)) as a function of the c/R -ratio.

At a fixed value of R and for a given total circulation Γ , the average induced velocity increases with decreasing c/R . The velocity at the axis $u(0,0)$ also increases with decreasing c/R , but it approaches $u(0,0)/(\Gamma/2R) = 1$ when $c/R \rightarrow 0$, which agrees with the results for a discrete ring vortex (Eq. (A.8)). This means that the velocity distribution across the exit plane of the annular wing is almost constant when $c/R > 1$ and approaches the distribution of Fig. A.2 when $c/R \ll 1$.

When $c/R > 1$, $u(0,0) > \bar{u}$. This can be made plausible by remembering that when a certain vorticity distribution at a given sectional geometry is assumed, the condition of zero normal velocity at the aerofoil section has not been fulfilled. This may lead to an outflow through the annular wing, which reduces the axial velocities at $r \rightarrow R$ and leads to an underestimation of \bar{u} .

For a rough estimation of the average induced velocity through an annular wing, apparently Eq. (A.9) can be used if $c/R > 1$, whereas Eq. (A.6) should be applied if $c/R < 0.5$.

A.3 Estimation of section lift coefficient

The self-induced axial velocity component at the aerofoil section of an annular wing (see Fig. A.4) can be calculated from (see Ref. A.1):

$$du(x,R) = (\gamma/\pi) dx' 2R^2 [4R^2 + (x' - x)^2]^{-3/2} [K(k) - E(k)]/k^2 \quad (A.10)$$

with

$$k^2 = 4R^2 [4R^2 + (x' - x)^2]^{-1} = \left[1 + \frac{1}{4} \left(\frac{c}{R} \right)^2 \left(\frac{x'}{c} - \frac{x}{c} \right)^2 \right]^{-1} \quad (A.11)$$

For a triangular vorticity distribution (Eq. (A.2)), Eq. (A.10) becomes

$$du(x,R) = \frac{\Gamma}{2\pi R} k [K(k) - E(k)] \frac{x'}{c} d\left(\frac{x'}{c}\right) \quad (A.12)$$

The integrand becomes singular at $k = 1$, i.e. if $x'/c = x/c$. When the expansion for K and E

$$K = \ln \frac{4}{k'} + \frac{1}{2} \left(\ln \frac{4}{k'} - 1 \right) k'^2 \quad (A.13)$$

$$E = 1 + \frac{1}{2} \left(\ln \frac{4}{k'} - \frac{1}{2} \right) k'^2 \quad (A.14)$$

is used, with

$$k' = (1 - k^2)^{\frac{1}{2}},$$

which is valid for values $1 \leq k < 0.75$ with an error $< 4\%$, Eq. (A.12) can be written as

$$du(x,R) = \frac{\Gamma}{2\pi R} k \left[\left(\ln \frac{4}{k'} \right) \left(1 - \frac{k'^2}{4} \right) - 1 \right] \frac{x'}{c} d\left(\frac{x'}{c}\right) \quad (A.15)$$

A further approximation, with

$$k \approx 1,$$

$$k' \approx \frac{1}{2} \left| \frac{c}{R} \left(\frac{x'}{c} - \frac{x}{c} \right) \right|,$$

$$(K - E) \approx \ln \frac{4}{k'} - 1 \quad (A.16)$$

¹⁾ A discrete vortex ring in an axial external flow also implies that a certain volume is pumped around (back flow outside the ring) and that it does not contribute effectively to the volume flow through the ring.

leads to a solution of Eq. (A.15) that is valid for very small values of k' , i.e. very small values of c/R , viz.:

$$u(x, R) = \frac{\Gamma}{2\pi R} \left[\frac{1}{2} \ln \frac{8}{c/R} - \frac{1}{4} + \frac{1}{2} \frac{x}{c} - \frac{1}{2} \left\{ 1 - \left(\frac{x}{c} \right)^2 \right\} \ln \left(1 - \frac{x}{c} \right) - \frac{1}{2} \left(\frac{x}{c} \right)^2 \ln \frac{x}{c} \right]. \quad (A.17)$$

In order to give an impression of the error due to the approximation of Eq. (A.16), compared with the original approximation of Eq. (A.13) and Eq. (A.14), the ratio of the two integrands can be given, viz.:

$$du_1(x, R)/du_2(x, R) = [\ln(4/a) - 1] k^{-1} [\ln(4/k') (1 - k'^2/4) - 1]^{-1}, \quad (A.18)$$

$$\text{with } a = \frac{1}{2} \frac{c}{R} \left(\frac{x'}{c} - \frac{x}{c} \right), \quad k = (1 + a^2)^{-\frac{1}{2}}, \quad \text{and } k' = (1 - k^2)^{\frac{1}{2}}.$$

The distribution of the error along the integration interval $0 \leq x'/c \leq 1$ for one value of x/c and two values of c/R is given in Fig. A.5. This figure shows that Eq. (A.17) always overestimates the velocity, but, even with $c/R = 2$, the error in the integrated value of $u(x, R)$ will not exceed 8 percent. Therefore, Eq. (A.17) can be used for an order-of-magnitude estimation of the self-induced velocity at the chord of the annular wing. Figure A.6 shows the self-induced velocity distribution along the chord for some values of c/R .

Till now, only the value of Γ has been used. The maximum attainable circulation is difficult to assess, but a maximum section lift coefficient (related to the local velocity) is easier to apprehend.

In order to define a local lift coefficient C_l , an average velocity \bar{U} can be defined from the total section lift on the annular wing, viz.:

$$C_l \frac{1}{2} \rho \bar{U}^2 c = \rho \bar{U} \Gamma = \rho \int_0^c \gamma [U + u(x, R)] dx. \quad (A.19)$$

When Eq. (A.2) is used for γ , the average velocity along the chord can be calculated from

$$\bar{U} = U + 2 \int_0^1 u(x, R) \frac{x}{c} d\left(\frac{x}{c}\right). \quad (A.20)$$

With Eq. (A.17), the average velocity becomes

$$\bar{U} = U + \left[\frac{1}{2} \ln \left(\frac{8}{c/R} \right) + \frac{3}{8} \right] \frac{\Gamma}{2\pi R}. \quad (A.21)$$

From Eq. (A.19), the section lift coefficient can be obtained

$$C_l = \left[\frac{Uc}{2\Gamma} + \frac{c/R}{8\pi} \left[\ln \left(\frac{8}{c/R} \right) + \frac{3}{8} \right] \right]^{-1}. \quad (A.22)$$

The lift coefficient obtained with a given circulation Γ in a wind velocity U on a two-dimensional wing is

$$C_{l0} = 2\Gamma/Uc, \quad (A.23)$$

which shows that $C_l < C_{l0}$, due to the self-induced velocity, when compared with Eq. (A.22). From Eq. (A.22), it appears also that

$$C_l \rightarrow C_{l0}, \text{ when } c/R \rightarrow 0,$$

in other words, when the chord becomes small with respect to the radius of the annular wing, the flow around the profile becomes two-dimensional (see also Ref. A.1).

From the Eqs (A.22) and (A.6), the relation between \bar{U} , c/R and C_l can be obtained, viz.:

$$\frac{\bar{U}}{U} = \frac{4}{\pi c/R} \left[\frac{1}{3} + \frac{2(1-k^2)}{3k^3} k - \frac{2-k^2}{3k^3} \epsilon \right] \left[\frac{1}{C_l} - \frac{c/R}{8\pi} \left[\ln \left(\frac{8}{c/R} \right) + \frac{3}{8} \right] \right]^{-1}, \quad (A.24)$$

$$\text{with } k = [1 + \frac{1}{4}(c/R)^2]^{-\frac{1}{2}}.$$

Eq. (A.24) becomes singular when the denominator tends to zero. The origin of this singularity is most easily resolved by returning to the expression for the circulation, viz.

$$\Gamma = \frac{1}{2} C_l c \bar{U} = \frac{1}{2} C_l c U + \frac{1}{2} C_l c \frac{\Gamma}{2\pi R} \left[\frac{1}{2} \ln \left(\frac{8}{c/R} \right) + \frac{3}{8} \right],$$

or

$$\Gamma = \frac{C_l c U}{2} \left[1 - \frac{C_l c}{4\pi R} \left[\frac{1}{2} \ln \left(\frac{8}{c/R} \right) + \frac{3}{8} \right] \right]^{-1}.$$

It is easily shown that there is a limiting value for C_l , at which $\Gamma \rightarrow \infty$ (which is physically impossible), viz.

$$C_l = \frac{4}{c/R} \left[\frac{1}{2} \ln \left(\frac{8}{c/R} \right) + \frac{3}{8} \right]^{-1}. \quad (A.25)$$

The singularity of Eq. (A.24) is most easily reached when

$$\frac{c/R}{8\pi} \left[\ln \left(\frac{8}{c/R} \right) + \frac{3}{8} \right]$$

becomes a maximum, which is reached at

$$(c/R) = 8e^{-\frac{1}{2}} \approx 6.23.$$

When this value is substituted in Eq. (A.25), it gives a limiting value of the local lift coefficient

$$C_l \approx 4.03$$

Figure 3.11 also shows the singular behaviour of the mass flow amplification at $C_l \approx 4$.

A.4 List of references

- A.1 Dickmann, H.E.: Grundlagen zur Theorie ringförmiger Tragflügel (frei umströmte Düsen). Ing. Archiv, 11 (1940) pp. 36-52.
 A.2 Batchelor, G.K.: An Introduction to Fluid Dynamics. (Cambridge Univ. Press, London, 1970) p. 521.

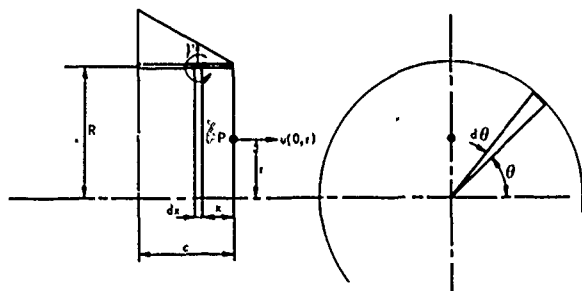


Fig. A.1 Calculation of the induced axial velocities in the exit plane of an annular wing with a triangular vorticity distribution along the chord

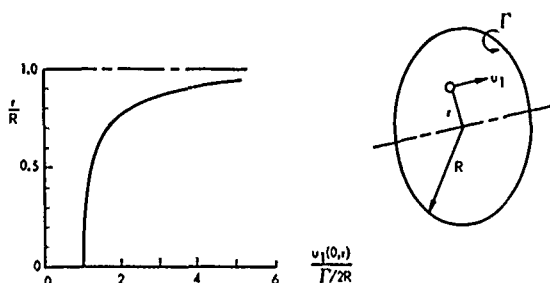


Fig. A.2 Axial velocity induced by a discrete vortex ring

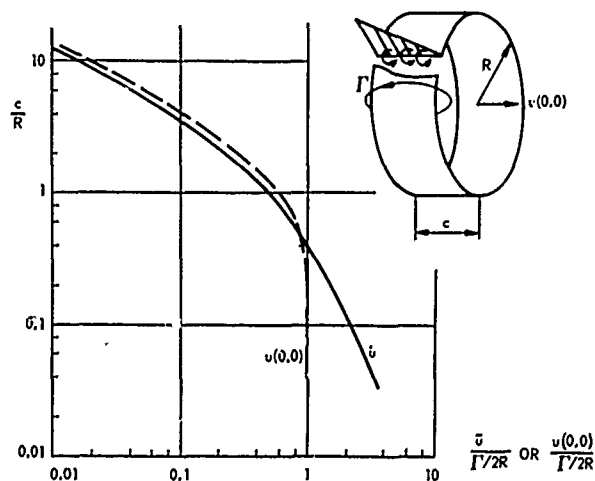


Fig. A.3 Average velocity \bar{u} and velocity on the axis $u(0, 0)$ at the exit of an annular wing with a triangular chordwise vorticity distribution, as a function of the c/R -ratio

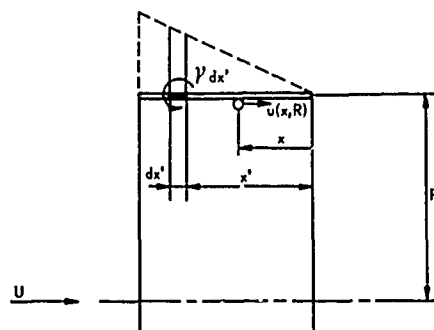


Fig. A.4 Calculation of the induced axial velocity at the wing section of an annular wing

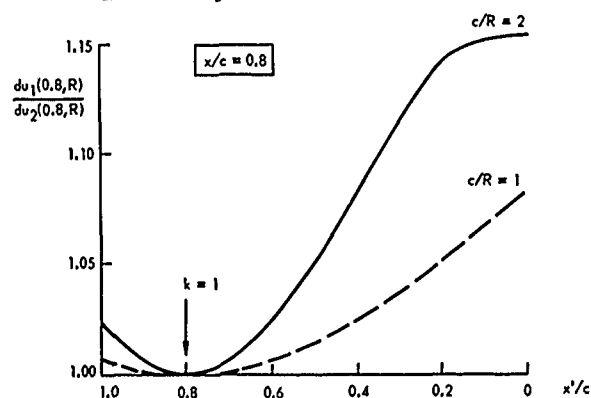


Fig. A.5 Error in Eq. (A.12), when the approximation according to Eq. (A.16) is applied, as a function of x'/c and c/R ; error estimated with Eq. (A.18)

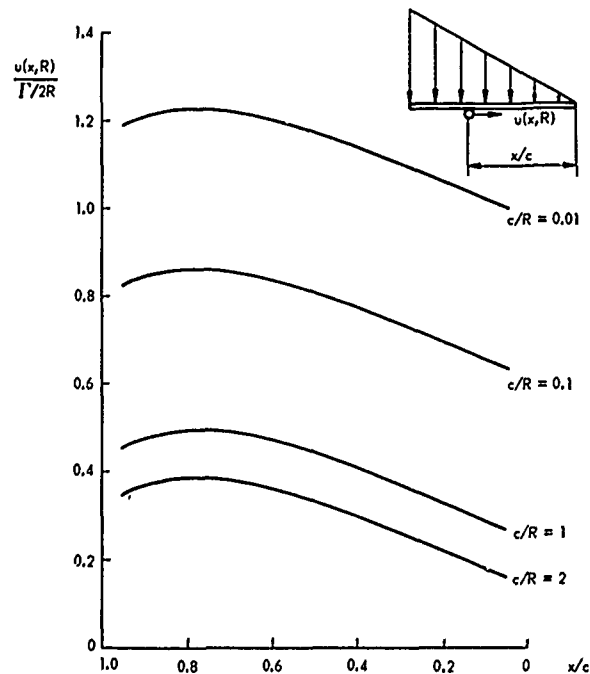


Fig. A.6 Self-induced velocity along the chord of an annular wing with a triangular vorticity distribution

APPENDIX B
ENERGY EXTRACTION FROM AN INCOMPRESSIBLE STEADY FLOW

B.1 The Bernoulli constant H

Energy extraction from an incompressible steady flow is indicated aerodynamically by a decrease of the so-called Bernoulli constant H, when a fluid particle moves along a streamline.

If no energy is lost,

$$H = p + \frac{1}{2}\rho U^2$$

is constant along a streamline.

The conditions for a variation of H in flow direction can more easily be discussed when the incompressible momentum equation is used:

$$\frac{\partial \vec{U}}{\partial t} = \vec{F} + \vec{U} \times \vec{\omega} - \frac{1}{\rho} \nabla H - \nu \nabla \times \vec{\omega} \quad , \quad (B.1)$$

with \vec{F} : external force per unit mass (N/kg)

$\vec{\omega} = \nabla \times \vec{U}$: rotation of fluid element; twice the instantaneous angular velocity (1/s)

ν : kinematic viscosity (m²/s).

In case of a steady ($\partial/\partial t = 0$), inviscid ($\nu = 0$) and irrotational ($\vec{\omega} = 0$) flow, Eq. (B.1) becomes

$$\vec{F} = \frac{1}{\rho} \nabla H \quad . \quad (B.2)$$

The only possibility for the existence of a non-zero gradient of H in flow direction is an external force \vec{F} in flow direction. This is the fictitious situation of an actuator disk perpendicular to the flow, with a drop in total head across the disk (cf. Sect. 3.2.1).

In steady inviscid flow with rotation, Eq. (B.1) becomes

$$\frac{1}{\rho} \nabla H = \vec{F} + \vec{U} \times \vec{\omega} \quad . \quad (B.3)$$

The possibility for a gradient in flow direction can be traced by forming the dot product with \vec{U} from Eq. (B.3), viz.:

$$\frac{1}{\rho} \vec{U} \cdot \nabla H = \vec{U} \cdot \vec{F} + \vec{U} \cdot \vec{U} \times \vec{\omega} \quad . \quad (B.4)$$

The second term on the right-hand side is identically zero; therefore, Eq. (B.4) leads to the same conclusion as Eq. (B.2).

In a steady viscous flow, forming the dot product between \vec{U} and Eq. (B.1) and reminding that $\vec{U} \cdot \vec{U} \times \vec{\omega} = 0$ leads to

$$\frac{1}{\rho} \vec{U} \cdot \nabla H = \vec{U} \cdot \vec{F} - \nu \vec{U} \cdot \nabla \times \vec{\omega} \quad . \quad (B.5)$$

The second term on the right-hand side expresses the dissipation of flow energy into heat due to viscosity and cannot be regarded as a useful form of energy extraction.

The first term on the right-hand side can contribute to ∇H in viscous flow (frictional force), but these forces are usually small. The much more powerful lift force, however, is always perpendicular to \vec{U} and, thus, cannot contribute to ∇H .

The ultimate conclusion is that extraction of a significant amount of energy from a flow has to be connected with unsteady-flow phenomena. A fluid particle flowing through a rotating turbine is subject to such an unsteady flow. However, when the flow is considered in a reference frame moving with the turbine blade, the flow is steady again (when the angular velocity $\vec{\Omega}$ of the turbine is constant). This apparent contradiction will be discussed below. Because viscous forces are not important in this respect (apart from the effect of viscosity in generating rotation in the flow and in that way generating lift), the influence of viscosity will be neglected.

Transformation of Eq. (B.1) into an energy equation by forming a dot product with \vec{U} leads to the following equation

$$\frac{DH}{Dt} = \frac{\partial p}{\partial t} + \rho \vec{U} \cdot \vec{F} \quad , \quad (B.6)$$

with $\frac{D}{Dt} = \frac{\partial}{\partial t} + \vec{U} \cdot \nabla \quad ,$

which is the substantial or material derivative, i.e. a differentiation following the motion of the fluid particle. Eq. (B.6) shows that H may vary due to fluctuating static pressures and due to the work done by external forces. In unsteady flow, the lift force need not be perpendicular to \vec{U} and $\rho \vec{U} \cdot \vec{F}$ might contribute to DH/Dt .

B.2 Choice of the reference frame

The flow through a steadily rotating horizontal-axis turbine in a reference frame attached to "earth" is unsteady (Eq. (B.6)), even when the oncoming flow is steady. When the turbine is considered in a reference frame attached to the turbine blade, the flow is steady, but it rotates as a whole around an axis coinciding with the axis of the turbine.

For a steady flow, Eq. (B.6) becomes

$$\frac{DH}{Dt} = \rho \vec{U} \cdot \vec{F}.$$

In a rotating system, however, the fictitious external forces (Coriolis and centrifugal) have to be added, thus

$$\frac{DH}{Dt} = \rho \vec{U} \cdot \vec{F} - \rho \vec{U} \cdot 2\vec{\Omega} \times \vec{U} - \rho \vec{U} \cdot \vec{\Omega} \times (\vec{\Omega} \times \vec{r}).$$

The second term on the right-hand side is identically zero. The first term on the right-hand side is zero because, in inviscid flow, the only possible force is a lift force that is perpendicular to \vec{U} .

The triple cross product can be written as a gradient, viz.

$$-\vec{\Omega} \times (\vec{\Omega} \times \vec{r}) = \nabla \frac{1}{2} (\vec{\Omega} \times \vec{r})^2,$$

and the energy equation for the relative flow becomes

$$\frac{DH}{Dt} = \rho \vec{U} \cdot \nabla \frac{1}{2} (\vec{\Omega} \times \vec{r})^2 = \frac{D}{Dt} \frac{1}{2} \rho (\vec{\Omega} \times \vec{r})^2.$$

This means that in the relative flow

$$p + \frac{1}{2} \rho U^2 - \frac{1}{2} \rho (\vec{\Omega} \times \vec{r})^2 = \text{constant}. \quad (B.7)$$

In an inviscid relative flow of a rotating system, the Bernoulli equation in the form $p + \frac{1}{2} \rho U^2 = \text{constant}$ can be applied along a streamline at a constant distance from the axis ($r = \text{constant}$). Such streamlines do not exist actually, however, in case of a wind turbine, because of its large wake expansion (cf. Fig. 3.3).

Eq. (B.7) can be interpreted in another way, by considering the velocity in the "earth-bound" or "absolute" reference frame

$$\vec{U}_r = \vec{U}_a + \vec{\Omega} \times \vec{r},$$

with U_r = velocity in a frame fixed to the turbine blade,

U_a = velocity in a frame fixed to earth.

The square of the relative velocity can be calculated from

$$U_r^2 = \vec{U}_r \cdot \vec{U}_r = \vec{U}_a \cdot \vec{U}_a + (\vec{\Omega} \times \vec{r}) \cdot (\vec{\Omega} \times \vec{r}) + 2\vec{U}_a \cdot (\vec{\Omega} \times \vec{r}),$$

and substituted in Eq. (B.7) gives

$$p = \frac{1}{2} \rho U_a^2 + \rho \vec{U}_a \cdot (\vec{\Omega} \times \vec{r}) = \text{constant}. \quad (B.8)$$

Far in front of the turbine, \vec{U}_a is parallel to $\vec{\Omega}$ and the dot product in Eq. (B.8) is zero. Far behind the turbine, the static pressure has to be equal to the pressure far in front of the turbine; thus an energy loss in the flow is only possible when \vec{U}_a is deflected during its passage through the turbine in the direction of $\vec{\Omega} \times \vec{r}$.

The dot product term can be interpreted as the change of angular momentum per unit volume in the flow times Ω , and equals the torque of the turbine times Ω , which is just the generated power of the turbine. It is interesting to notice that the generation of power with a horizontal-axis turbine has to be connected with tangential velocity components in the flow behind the turbine.

It is also interesting to note that, for a vertical-axis turbine, no reference frame fixed to the turbine blade exists which leads to a steady flow in that reference frame. This inherent unsteadiness is a serious drawback in setting up general equations for the vertical-axis turbine. Especially inconvenient is the impossibility to use the equation of the angular momentum (calculation of the torque) in case of a vertical-axis turbine.

APPENDIX C DETERMINATION OF THE INDUCED VELOCITIES IN AXISYMMETRIC FLOW

C.1 Introduction

The bound vorticity on the rotor blades and the trailing vorticity behind the rotor induce velocities that change the wind velocity in front of, at, and behind the rotor. Due to the complexity of the vortex system, these induced velocities can only be determined in some special cases.

The discussion in this Appendix will be restricted to axisymmetric flow, i.e. to a flow where all quantities are independent of the azimuth angle ϕ . It can be shown that this represents a turbine with an infinite number of blades.

The vortex system and the governing equations will be discussed, which will reveal the complexity even in the case of axisymmetric flow. The vortex formulation is applied to a cylindrical (non-expanding) wake with a simple Γ -distribution (constant and linear) only, in order to avoid the difficulty to solve a nonlinear problem.

Then, momentum considerations are used, to get some insight into the effect of wake expansion on the induced velocities at the rotor. The equations arising from this approach are, however, also nonlinear and could be solved only for a special case. Nevertheless, the influence of the wake expansion can be indicated. It then turns out, that also the static pressure deficit in the wake due to the rotation in the wake (connected with the torque), plays an important role.

C.2 The vortex structure; general formulation

Figure C.1 shows a rotor blade, represented by a bound vortex along the span and the trailing vortex sheet behind the blade. Due to the combined action of the axial wind velocity and the rotation of the blade, the vortex sheet gets a helical form. Due to the induced velocities, the rather simple helical shape (determined by U and Ωr) will be modified. When the induced velocities are not small with respect to U , the modification of the shape will be large and the problem becomes nonlinear. This would lead to a complex iterative calculation procedure, which will not be discussed here. For more details, see the Refs C.1, C.2 and C.3.

When the number of blades increases while the total strength of the bound vorticity is kept constant, the rotor disk becomes a vortex sheet with an axisymmetric strength distribution. Behind the rotor, the wake is filled with trailing vorticity, which is also axisymmetrically distributed.

Figure C.2 shows the notation to describe this situation. γ_r is the strength of the bound vorticity at radius r , which is related to the total bound circulation at radius r by

$$\Gamma(r) = 2\pi r \gamma_r. \quad (C.1)$$

In cylindrical coordinates, the continuity equation (mass conservation) for axisymmetric flow can be written as

$$\frac{\partial}{\partial r}(v r) + \frac{\partial}{\partial x}(u r) = 0, \quad (C.2)$$

which is identically satisfied by a stream function $\psi(x, r)$ with $\psi(x, 0) = 0$, when

$$v = -\frac{1}{r} \frac{\partial \psi}{\partial x}; \quad u = \frac{1}{r} \frac{\partial \psi}{\partial r}. \quad (C.3)$$

It must be noticed that, in axisymmetric flow, the tangential velocity component w is not affected by mass conservation. In this Section, u , v and w are the components of the total velocity.

The vorticity components in the wake flow are

$$\omega_x = \frac{1}{r} \frac{\partial}{\partial r}(w r); \quad \omega_r = -\frac{\partial w}{\partial x}; \quad (C.4)$$

$$\omega_\phi = \frac{\partial v}{\partial x} - \frac{\partial u}{\partial r} = -\frac{1}{r} \left[\frac{\partial^2 \psi}{\partial x^2} + \frac{\partial^2 \psi}{\partial r^2} - \frac{1}{r} \frac{\partial \psi}{\partial r} \right]. \quad (C.5)$$

In front of the rotor and outside the wake, the flow is irrotational ($\vec{\omega} = 0$), and it follows from the Eqs (C.4) and (C.5) that it has to satisfy the equations:

$$\frac{\partial^2 \psi}{\partial x^2} + \frac{\partial^2 \psi}{\partial r^2} - \frac{1}{r} \frac{\partial \psi}{\partial r} = 0, \quad \text{and: } w = 0. \quad (C.6)$$

In incompressible and inviscid steady flow within the wake (i.e. in absence of external forces), there is a relation between the velocity \vec{U} , the rotation $\vec{\omega}$ and the Bernoulli constant H (see e.g. Appendix B, Sect. B.1), viz.:

$$\frac{1}{\rho} \nabla H = \vec{U} \times \vec{\omega} \quad (C.7)$$

or, in cylindrical coordinates,

$$\frac{1}{\rho} \frac{\partial H}{\partial x} = v \omega_\phi - w \omega_r, \quad (C.8)$$

$$\frac{1}{\rho} \frac{\partial H}{\partial r} = w \omega_x - u \omega_\phi, \quad (C.9)$$

$$\frac{1}{\rho} \frac{1}{r} \frac{\partial H}{\partial \phi} = u \omega_r - v \omega_x \quad (C.10)$$

The variation of H in a meridional plane on the surface $\psi = \text{constant}$ in the wake can be calculated from (using axisymmetry $\partial/\partial\phi = 0$)

$$\frac{1}{\rho} \frac{\partial H}{\partial s} = \frac{1}{\rho} \frac{\partial H}{\partial x} \frac{\partial x}{\partial s} + \frac{1}{\rho} \frac{\partial H}{\partial r} \frac{\partial r}{\partial s}, \quad (C.11)$$

where ds is a line element on the intersection of the stream surface and the meridional plane, and

$$\frac{\partial x}{\partial s} = \frac{u}{u_s} \quad \text{and} \quad \frac{\partial r}{\partial s} = \frac{v}{u_s}, \quad \text{with} \quad u_s = \sqrt{u^2 + v^2}.$$

Eq. (C.11) can then be written (when the Eqs (C.4), (C.5), (C.8) and (C.9) are used) as

$$\frac{\partial H}{\partial s} = \rho(v \omega_\phi - w \omega_r) \frac{u}{u_s} + \rho(w \omega_x - u \omega_\phi) \frac{v}{u_s} = \rho \frac{w}{u_s} (v \omega_x - u \omega_r).$$

In axisymmetric flow, Eq. (C.10) has to be identically zero and, therefore, the right-hand side of this equation is zero, thus:

$$\frac{\partial H}{\partial s} = 0, \quad \text{and} \quad H = H(\psi). \quad (C.12)$$

Because H varies only normal to $\psi = \text{constant}$, Eq. (C.7) shows that the vortex lines coincide with the stream surfaces. When the circulation $\Gamma(r)$ is defined as

$$\Gamma(r) = 2\pi r w,$$

this circulation is constant in a stream surface $\psi = \text{constant}$, viz.:

$$\begin{aligned} \frac{\partial(w r)}{\partial s} &= \frac{\partial(w r)}{\partial x} \frac{\partial x}{\partial s} + \frac{\partial(w r)}{\partial r} \frac{\partial r}{\partial s} \\ &= -\omega_r r \frac{\partial x}{\partial s} + \omega_x r \frac{\partial r}{\partial s} \\ &= \frac{r}{u_s} (-u \omega_r + v \omega_x) = 0, \end{aligned}$$

thus

$$\frac{\partial \Gamma(r)}{\partial s} = 0, \quad \text{and} \quad \Gamma(r) = \begin{cases} \Gamma(\psi) & \text{in the wake,} \\ 0 & \text{elsewhere.} \end{cases} \quad (C.13)$$

When Eq. (C.7) is used, the gradient of H normal to $\psi = \text{constant}$ can be calculated from

$$\frac{1}{\rho} \frac{\partial H}{\partial \psi} \frac{\partial \psi}{\partial n} = w \omega_s - u_s \omega_\phi = \frac{w}{r} \frac{\partial(w r)}{\partial n} - u_s \omega_\phi,$$

with

$$\omega_s = [\omega_r^2 + \omega_x^2]^{\frac{1}{2}},$$

and

$$n = \text{the normal on } \psi = \text{constant}.$$

The gradient of the stream function is

$$\frac{\partial \psi}{\partial n} = \frac{\partial \psi}{\partial x} \frac{\partial x}{\partial n} + \frac{\partial \psi}{\partial r} \frac{\partial r}{\partial n} = (-v r) \left(-\frac{v}{u_s}\right) + u r \frac{u}{u_s} = u_s r,$$

and the gradient of H can be written as

$$\frac{1}{\rho} \frac{\partial H}{\partial \psi} \frac{\partial \psi}{\partial n} = (w r) r^{-2} \frac{\partial(w r)}{\partial \psi} \frac{\partial \psi}{\partial n} - u_s \omega_\phi,$$

or

$$\frac{1}{\rho} \frac{dH}{d\psi} = \Gamma(2\pi r)^{-2} \frac{d\Gamma}{d\psi} - \omega_\phi r^{-1}. \quad (C.14)$$

There has to be found another relation between H and Γ , which is connected with the role of external forces of the actuator disk, representing the turbine.

The jump in the Bernoulli constant ΔH can be calculated from the static pressures and velocities in front of and behind the actuator disk. In front of the actuator disk, the pressure is p_1 and the velocity components in a "fixed-to-earth" coordinate system are u_1 , v_1 and w_1 . Behind the actuator disk the pressure is p_2 , and the velocity components are u_2 , v_2 and w_2 .

From Eq. (B.8), it follows that (App. B)

$$p_1 + \frac{1}{2} \rho (u_1^2 + v_1^2 + w_1^2) + \rho w_1 \Omega r = p_2 + \frac{1}{2} \rho (u_2^2 + v_2^2 + w_2^2) + \rho w_2 \Omega r,$$

which can also be written as

$$H_1 + \rho w_1 \Omega r = H_2 + \rho w_2 \Omega r,$$

or

$$\Delta H = H_2 - H_1 = \rho (w_1 - w_2) \Omega r. \quad (C.15)$$

From the vortex sheet density of the actuator disk, it follows that:

$$\gamma_r = w_2 - w_1 ,$$

thus

$$\Delta H = -\rho \gamma_r \Omega r = -\rho \frac{\Omega}{2\pi} \Gamma . \quad (C.16)$$

Because $H = \text{constant}$ in irrotational flow and because H is also constant on a stream surface (except for the drop at the actuator disk), from Eq. (C.16), it follows that

$$\left(\frac{\partial H}{\partial r}\right)_{x=0} = -\rho \frac{\Omega}{2\pi} \left(\frac{\partial \Gamma}{\partial r}\right)_{x=0} , \text{ and } \frac{dH}{d\psi} = -\rho \frac{\Omega}{2\pi} \frac{d\Gamma}{d\psi} . \quad (C.17)$$

When Eqs (C.5) and (C.17) are substituted into Eq. (C.14), the equation for the wake flow is

$$\left[\frac{\Omega}{2\pi} + \frac{\Gamma}{(2\pi r)^2}\right] \frac{d\Gamma}{d\psi} + \frac{1}{r^2} \left[\frac{\partial^2 \psi}{\partial x^2} + \frac{\partial^2 \psi}{\partial r^2} - \frac{1}{r} \frac{\partial \psi}{\partial r}\right] = 0 . \quad (C.18)$$

With a given Ω , a given Γ -distribution, and the appropriate boundary conditions, the axisymmetric flow through a wind turbine with an infinite number of blades and an expanding wake could be calculated with the Eqs (C.6) and (C.18). The general solution is still too complicated, because the problem is nonlinear. Therefore, a simplified solution will be discussed next.

C.3 The cylindrical wake

The cylindrical wake is an idealization, which is valid for induced velocities $(U-u)$, $v \ll U$. It is, therefore, successfully applied to the problem of an airplane propeller in cruise condition, but in the case of a wind turbine it is only of limited applicability. However, in the wake far downstream it can be applied without any restriction.

A cylindrical wake means $v = 0$ and $(\partial/\partial x)() = 0$. When this is applied to Eq. (C.18), it gives

$$\left[\frac{\Omega}{2\pi} + \frac{\Gamma}{(2\pi r)^2}\right] \frac{d\Gamma}{dr} \frac{dr}{d\psi} + \frac{1}{r} \left[\frac{d}{dr} \left(\frac{1}{r} \frac{d\psi}{dr}\right)\right] = 0 ,$$

or changing to $w = \Gamma/(2\pi r)$ and $u = (1/r)(d\psi/dr)$

$$\Omega \frac{d(wr)}{dr} + \frac{w^2}{r} + w \frac{dw}{dr} + u \frac{du}{dr} = 0 ,$$

which can be integrated, viz.:

$$\rho \Omega w r + \frac{1}{2} \rho (u^2 + w^2) + \int_0^r \rho \frac{w^2}{r} dr = \rho \Omega w r + \frac{1}{2} \rho (u^2 + w^2) + P(r) = \text{constant} . \quad (C.19)$$

From Eq. (C.16), the first term on the left-hand side can be interpreted as the total pressure jump across the actuator disk: $-\Delta H$. When the total pressure of the undisturbed wind velocity is denoted by H_0 and the undisturbed static pressure by p_0 , the equation of Bernoulli inside the wake is

$$H(r) = H_0 + \Delta H = p_0 + \frac{1}{2} \rho U^2 + \Delta H = p + \frac{1}{2} \rho (u^2 + w^2) ,$$

or

$$-\Delta H + \frac{1}{2} \rho (u^2 + w^2) + p = H_0 . \quad (C.20)$$

When the Eqs (C.19) and (C.20) are compared with each other, it follows that, apart from a constant, $P(r)$ is equal to the static pressure in the wake, viz.:

$$p = P(r) + C ,$$

which constant can be determined by the boundary condition that at $r = R_0$ the pressure $p = p_0$, thus:

$$p - p_0 = P(r) - P(R_0) ,$$

or substituted in Eq. (C.20),

$$-\Delta H + \frac{1}{2} \rho (u^2 + w^2) + P(r) - P(R_0) + p_0 = H_0 . \quad (C.21)$$

Because ΔH and $P(r) - P(R_0)$ depend on w , Eq. (C.21) shows that there is a relation between w and u , i.e. the Γ -distribution along the blade span determines the axial velocity in the wake far downstream.

Two simple examples will now be given.

First example: The circulation is constant along the blade span. This has the following consequences:

$$w = \frac{\Gamma}{2\pi r} = \frac{k}{r} ,$$

$$\Delta H = -\rho \Omega w r = -\rho \Omega k = \text{constant} ,$$

$$P(r) - P(R_0) = \frac{1}{2} \rho (w_0^2 - w^2) ; \quad w_0 = \frac{k}{R_0} ;$$

$$\frac{1}{2} \rho u^2 = \frac{1}{2} \rho U^2 - \rho \Omega k - \frac{1}{2} \rho w_0^2 = \text{constant} .$$

In connection with a future discussion, it is useful to draw attention to the fact that the rotation in the wake causes a variation of the static pressure across the wake equal to $P(r) - P(R_0)$.

Second example: The circulation varies linearly from zero at the axis to a maximum at $r = R_0$. The consequences are:

$$w = \text{constant} = w_0 ,$$

$$\Delta H = -\rho \Omega w_0 r ,$$

$$P(r) - P(R_0) = \frac{1}{2} \rho w_0^2 \ln(r/R_0)^2 ,$$

$$\frac{1}{2} \rho u^2 = \frac{1}{2} \rho U^2 - \rho \Omega w_0 r - \frac{1}{2} \rho w_0^2 [1 + \ln(r/R_0)^2] .$$

The condition $(\partial/\partial x)() = 0$ is strictly speaking only valid in a two-dimensional flow, i.e. in the wake far behind the rotor, where the wake is double-infinite. The wake starts at the actuator disk and it is obvious that $(\partial/\partial x)() = 0$ cannot be valid throughout.

By the equation of Stokes, it can be shown that w is independent of x , also close behind the actuator disk. The w caused by the bound vorticity decreases downstream, but the w caused by the trailing vorticity increases downstream, which results in a tangential velocity independent of x . The axial velocity induced by the trailing vorticity increases downstream, but the bound vorticity does not induce any axial velocity. Therefore, the axial velocity u depends on x . When the vortex lines are restricted to cylindrical surfaces, it can be shown that the axial induced velocities at the actuator disk are one half of the axial induced velocities far behind the actuator disk. The total axial velocity at the rotor is, therefore, the arithmetic mean of the velocity far in front of the rotor (U) and far behind (u_3). From the continuity equation, it follows that this decrease of the total axial velocity in the wake is not compatible with a cylindrical wake. Apart from the region far downstream, it can only be approximately cylindrical in case of small induced velocities.

When the first example is taken, the absorbed power can rather easily be calculated, because ΔH and u_3 are constant across the wake. The absorbed power is

$$P = (\Delta H) \times (\text{volume flow through rotor})$$

$$= \frac{1}{2} \rho (U^2 - u_3^2 - w_0^2) \frac{1}{2} (U + u_3) \pi R_0^2 .$$

or written as a power coefficient,

$$C_p = \frac{1}{2} (1 - u_3/U) (1 + u_3/U)^2 - \frac{1}{2} (1 + u_3/U) (w_0/U)^2 = \frac{1}{2} (1 + u_3/U) [1 - (u_3/U)^2 - (w_0/U)^2] . \quad (C.22a)$$

For later reference, it can also be expressed in the induction factor "a", by $u_3/U = 1 - 2a$, viz.:

$$C_p = 4a(1-a)^2 - (1-a)(w_0/U)^2 . \quad (C.22b)$$

The first term corresponds to the ideal power coefficient derived by Betz (cf. Eq. (3.2.6)). The second term is the power loss due to the wake rotation. Because $\Delta H = \rho \Omega w_0 R_0$, this loss can be minimized for a given value of ΔH by choosing a high value of Ω . It can be shown that this argument is valid for other circulation distributions too.

The calculation of the influence of the wake expansion is complicated, even in case of a constant circulation along the blade span.

C.4 Momentum considerations

Because an exact calculation of the influence of wake expansion with the Eqs (C.18) and (C.6) is very complicated, momentum considerations, as given in Ref. C.4, will be used. The derivation is analogous to the one given in Sect. 3.2.1, but now the radial and tangential components are included and also a variation of flow quantities across the streamtube is admitted.

Figure C.3 shows the control volume around the turbine, represented by an actuator disk. The control surfaces have been put at such a distance from the turbine, that the radial velocity components are negligible and the pressure is equal to the undisturbed pressure p_0 (except in the wake cross-section).

Divide the flow regime into two parts, viz.:

- the streamtube through the rotor,
- the outer flow.

Apply the axial momentum equation to the control volume of the outer flow (upper part Fig. C.3). This gives

$$p_0(S_3 - S_0) - \iint_{\text{stream surface}} (p - p_0) dS_x = \rho U \iint_{\text{control surface}} u_n dS_c ,$$

with

S_x : projection of stream surface normal to X ,

S_c : control surface,

u_n : velocity component normal to control surface.

Because the outer flow is source-free,

$$\iint u_n dS_c = 0 ,$$

and the axial momentum equation results in:

$$I_p = \iint_{\text{stream surface}} (p-p_0) dS_x = p_0(S_3-S_0) \quad (C.23)$$

This means that the axial component of the pressure integral over the outer surface of the streamtube through the rotor (I_p) solely depends on the expansion rate of the streamtube (S_3-S_0).

When the axial force on the rotor is denoted by D , the axial momentum equation, applied to the streamtube through the rotor gives

$$D = \iint_{S_{\text{ref}}} (p_1-p_2) dS = I_p + p_0 S_0 - \iint_{S_3} p_3 dS + \rho \iint_{S_{\text{ref}}} u(u-u_3) dS,$$

or, in view of Eq. (C.23),

$$D = \rho \iint_{S_{\text{ref}}} u(u-u_3) dS - \iint_{S_3} (p_3-p_0) dS \quad (C.24)$$

When the torque of the rotor is denoted by Q , the equation of angular momentum applied to the streamtube leads to

$$Q = \rho \iint_{S_3} u_3 w_3 r_3 dS \quad (C.25)$$

In order to use the equations (C.24) and (C.25), the pressures and velocities just behind the rotor have to be related with those in the wake far downstream.

The continuity equation along an elemental streamtube in the wake gives the following relation

$$u dS_{\text{ref}} = u_3 dS_3 \quad (C.26)$$

Moreover, in Sect. C.3 it was deduced that the circulation is constant along a stream surface, thus

$$wr = w_3 r_3 \quad (C.27)$$

When it is assumed that energy is extracted from the flow only at the rotor, the equation of Bernoulli can be applied separately in front of and behind the rotor, which leads to

$$H_0 = H_1 = p_0 + \frac{1}{2} \rho U^2 = p_1 + \frac{1}{2} \rho (u^2 + v^2),$$

$$H_2 = H_3 = p_3 + \frac{1}{2} \rho (u_3^2 + w_3^2) = p_2 + \frac{1}{2} \rho (u^2 + v^2 + w^2),$$

$$\text{or} \quad p_3 - p_0 = -(p_1 - p_2) + \frac{1}{2} \rho (U^2 - u_3^2) + \frac{1}{2} \rho (w^2 - w_3^2) \quad (C.28)$$

because u and v are continuous through the actuator disk.

The pressure drop over the actuator disk can be calculated from the equation of Bernoulli for the flow relative to the rotating rotor blades (cf. Appendix B, Eq. (B.8)):

$$p_1 + \frac{1}{2} \rho (u^2 + v^2) = p_2 + \frac{1}{2} \rho (u^2 + v^2 + w^2) + \rho w \Omega r,$$

or

$$p_1 - p_2 = \frac{1}{2} \rho w^2 + \rho w \Omega r \quad (C.29)$$

When this is substituted into Eq. (C.28), it yields

$$p_3 - p_0 = \frac{1}{2} \rho (U^2 - u_3^2) - \rho w \Omega r - \frac{1}{2} \rho w_3^2 \quad (C.30)$$

In the wake far downstream, the flow is parallel again ($v = 0$). From the discussion of the cylindrical wake (Eqs (C.19) through (C.21)), it followed that the pressure difference in the wake is determined by the centrifugal forces, due to the tangential velocities, viz.:

$$p_3 - p_0 = P(r_3) - P(R_{03}) = -\rho \int_{r_3}^{R_{03}} (w_3^2/r_3) dr_3 \quad (C.31)$$

From the above formulae it can also be deduced that the loss of total head in the flow is

$$H_0 - H_2 = (p_1 - p_2) - \frac{1}{2} \rho w^2 = \rho w \Omega r \quad (C.32)$$

When Eq. (C.30) is substituted into Eq. (C.24) and when also the relations Eq. (C.26) and (C.27) are used, this leads to

$$\frac{1}{2} \rho \iint_{S_3} (U - u_3)^2 dS = \rho \Omega \iint_{S_3} u_3 w_3 r_3 \left[\frac{1 + \frac{1}{2} w_3 / \Omega r_3}{u_3} - \frac{1 + \frac{1}{2} w / \Omega r}{u} \right] dS, \quad (C.33)$$

for $r_3 = R_{03}$, Eq. (C.30) gives:

$$\frac{1}{2} \rho (U^2 - u_{03}^2) = \rho \Omega w_{03} R_{03} + \frac{1}{2} \rho w_{03}^2 \quad (C.34)$$

The above equations suffice (at least in principle) to calculate the flow behind the turbine and the torque of the turbine, when a distribution of the tangential velocities in the wake far downstream is assumed. It is still a difficult job, however, and, therefore, a special example will be taken.

In the case that $r = \text{constant}$, $wr = \text{constant}$ or $w = k/r$. Applying this to the Eqs (C.30) and (C.31) gives

$$\frac{1}{2}\rho(U^2 - u_3^2) = \rho\Omega k + \frac{1}{2}\rho w_{o3}^2,$$

which shows that also $u_3 = \text{constant}$ in the wake. This equation can also be written as

$$\Omega k = \frac{1}{2}(U^2 - u_3^2) - \frac{1}{2}w_{o3}^2. \quad (\text{C.35})$$

Because $d\Gamma/d\psi = 0$ and $dH/d\psi = 0$ in this special case, from Eq. (C.14), it follows that $\omega_3 = 0$ in the wake and thus in the entire flow field, except on the wake boundary. Eq. (C.5) shows that this is equivalent to

$$\frac{\partial v}{\partial x} = \frac{\partial u}{\partial r}.$$

Because it has been assumed, that u and v are constant through the actuator disk, it follows that $\partial v/\partial x = 0$ at the actuator disk and from the above equation it can be derived that $\partial u/\partial r = 0$ and $u = \text{constant}$ across the actuator disk. Eq. (C.26) can now be written as

$$ur dr = u_3 r_3 dr_3 \text{ and } ur^2 = u_3 r_3^2, \quad (\text{C.26a})$$

and, from Eq. (C.33), it follows then that

$$(U - u_3)^2 = 2\Omega k(1 - u_3/U). \quad (\text{C.36})$$

Eliminating Ωk gives

$$u = \frac{1}{2}(U + u_3) \frac{1 - w_{o3}^2 / (U^2 - u_3^2)}{1 - \frac{1}{2}w_{o3}^2 / \{u_3(U - u_3)\}} = \frac{1}{2}(U + u_3)(1 + A). \quad (\text{C.37})$$

This formula shows that, due to the rotation and the corresponding pressure deficit in the wake,

$$u \geq \frac{1}{2}(U + u_3),$$

with the equal sign for the case $w_{o3} = 0$ (cf. Sect. 3.2.1).

The torque can be calculated from Eq. (C.25):

$$Q = \rho \iint u_3 w_3 r_3 dS_3 = \rho \iint uk dS_{\text{ref}} = \rho uk S_{\text{ref}}.$$

The power coefficient of the wind turbine in this case is

$$C_p = Q\Omega / \frac{1}{2}\rho U^3 S_{\text{ref}} = 2(\Omega k/U^2)(u/U). \quad (\text{C.38})$$

Substitution of the Eqs (C.35) and (C.37) into (C.38) gives

$$C_p = \frac{1}{2}(1 + u_3/U)(1 + A) \left[1 - (u_3/U)^2 - (w_{o3}/U)^2 \right]. \quad (\text{C.22c})$$

Comparison with Eq. (C.22a) shows that the decrease of C_p due to wake rotation is reduced because $w_{o3} < w_o$ and because $A > 0$, when the static pressure deficit and the wake expansion are taken into account.

When the following parameters are defined

$$\lambda = \Omega R_o / U; \quad q = k / U R_o; \quad \mu = u / u_3 = (R_{o3} / R_o)^2; \quad \text{and } u_3 / U = t;$$

the Eqs (C.35), (C.36) and (C.38) can be written as:

$$2\lambda q = (1 - t^2) - (\mu)^{-1} q^2, \quad (\text{C.35a})$$

$$(1 - t)^2 = 2\lambda q [1 - (\mu)^{-1}], \quad (\text{C.36a})$$

$$C_p = 2\lambda q \mu t = \mu^2 (\mu - 1)^{-1} t (1 - t)^2. \quad (\text{C.38a})$$

When q is eliminated and μ is solved from the Eqs (C.35a) and (C.36a), this gives

$$\mu = \frac{1}{4t} \left[1 + 3t + \frac{(1-t)^3}{4\lambda^2} + \left\{ \left[1 + 3t + \frac{(1-t)^3}{4\lambda^2} \right]^2 - 8t(1+t) \right\}^{\frac{1}{2}} \right]. \quad (\text{C.39})$$

When $\lambda \rightarrow \infty$, $\mu \rightarrow (1+t)/2t$. Substituting this into Eq. (C.38a), leads to

$$(C_p)_{\lambda \rightarrow \infty} = \frac{1}{2}(1-t)(1+t)^2 = 4(1-u/U)(u/U)^2 = 4a(1-a)^2,$$

which corresponds to the ideal power coefficient derived by Betz (cf. Eq. (3.2.6)) with $u/U = (1+t)/2 = 1-a$ (see also Eq. (C.22b)).

When $\lambda \rightarrow 0$, $\mu \rightarrow \infty$ (see Eq. (C.39)) and, according to Eq. (C.36a), $2\lambda q \rightarrow (1-t)^2$ or $q \rightarrow \infty$. This means an infinite circulation, which is physically impossible.

The condition that q remains finite when $\lambda \rightarrow 0$ can be obtained from the Eq. (C.36a), viz.

$$(1-t)^2 = 0(\lambda), \quad \text{thus } t \rightarrow (1-\sqrt{\lambda}),$$

and, because $\mu \rightarrow 2+1/8\sqrt{\lambda}$ (Eq. (C.39)) and $q \rightarrow \frac{1}{2}$ (Eq. (C.36a)),

it can be shown that:

$$(C_p)_\lambda \rightarrow 0, \text{ when } \lambda \rightarrow (1-\sqrt{\lambda})$$

The physical restrictions imposed on the formulae (C.38a) and (C.39) can only be obtained by considering a blade-element theory that introduces the lift coefficient of the blade element.

In the commonly used theories, the following assumptions are applied:

- $(p_3 - p_0) = 0$;
- $u = \frac{1}{2}(u + u_3)$, thus $u_3 = 2u - u$;
- $u \, dS_{ref} = u_3 \, dS_3$;
- With respect to w , there is no wake expansion, thus $w_2 r = w_3 r = w r$. It must be noticed, that at the rotor itself $w_{rotor} = \frac{1}{2}w$ and in front of the rotor $w = 0$ (cf. Eq. (C.15) and further).
- The momentum equations are used in the differential form.

With the above assumptions, the equations (C.24) and (C.25) become (Eq. (C.29) is also used):

$$2u(u-u) = \Omega w r + \frac{1}{2}w^2 ,$$

$$dQ = 2\pi \rho u w r^2 dr$$

From the first equation, it follows that it is impossible to keep both u and $w r$ constant along the rotor blade. In order to calculate the influence of the above assumptions by comparing them with the results of the Eqs (C.38a) and (C.39), the case $u = \text{constant}$ (thus $u_3 = \text{constant}$) has been chosen.

When the following parameter is defined:

$$X = \Omega r / U = \lambda r / R_0 ,$$

the equations can be written as

$$2(u/U)(1-u/U) = \lambda q + \frac{1}{2}(\lambda/X)^2 q^2 ,$$

$$dQ = \frac{2\pi \rho U^2 R_0^3}{\lambda^2} (u/U) q X \, dX$$

When q is extracted and when the rotor drag coefficient is defined by

$$C_D = D / \frac{1}{2} \rho U^2 \pi R_0^2 = 4(u/U)(1-u/U) ,$$

the power coefficient (because $dP = \Omega dQ$) becomes:

$$C_p = (4/\lambda^2) u/U \int_0^\lambda X^3 \left[(1 + C_D/X^2)^{\frac{1}{2}} - 1 \right] dX \quad (C.40)$$

For large values of λ and X , the form between brackets becomes

$$(1 + C_D/X^2)^{\frac{1}{2}} - 1 \approx 1 + \frac{1}{2}C_D/X^2 - 1 = \frac{1}{2}C_D/X^2 ,$$

and, thus,

$$C_p = (2/\lambda^2) C_D (u/U) \int_0^\lambda X \, dX = (u/U) C_D = 4(u/U)^2 (1-u/U) ,$$

which is the well-known Betz' expression.

Integrating Eq. (C.40) gives

$$C_p = (\lambda)^{-1} (u/U) (\lambda^2 + \frac{1}{2}C_D) (\lambda^2 + C_D)^{\frac{1}{2}} - \lambda^3 - (C_D^2/\lambda) \ln \left\{ \left[\lambda + (\lambda^2 + C_D)^{\frac{1}{2}} \right] (C_D)^{-\frac{1}{2}} \right\} \quad (C.41)$$

By consideration of the Eqs (C.38a), (C.39) and (C.41), it is possible to investigate the influence of neglecting the wake expansion and the pressure reduction in the wake far downstream, although the cases are not fully comparable, because in case of the wake expansion, both r and u are constant along the blade span, whereas, in the case of cylindrical wake, only u is constant along the span.

The lower part of Fig. C.4 shows the axial velocity through the rotor (u) in the case of an expanded wake, divided by the axial velocity in case of a cylindrical wake [$\frac{1}{2}(u+u_3)$]. Up to common values of λ the influence is small.

The upper part of the figure shows the far more dramatic effect of the wake expansion on C_p . The large loss of energy output due to wake rotation in the case of a cylindrical wake is caused by applying the tangential velocity at the wake boundary equal to $w_0 = k/R_0$, whereas in the case of the expanded wake the tangential velocity at the wake boundary is $w_{03} = k/R_{03}$, which is smaller by a factor $1/\sqrt{u}$. Combined with the small increase of the axial velocity, the power loss due to wake rotation in this latter case is negligible. At low tip-speed ratios, the power output might be even larger than the Betz' limit expression, but it might be questioned whether a real rotor blade can sustain such high lift loads.

At each value of λ , there is a certain value of u_3/U (or u/U) at which C_p is maximum. These optimum values of C_p at each value of λ have been compiled in Fig. C.5. This clearly shows that, when the wake expansion and the static pressure deficit in the wake are taken into account, the optimum power output is equal to the Betz limit up to very low values of λ , where the simple theory for $r = \text{constant}$ along the radius of the rotor blade breaks down.

Also shown in Fig. C.5 is the result of Glauert (Ref. C.4), which shows an optimum, when r as well as u/U are allowed to vary along the span of the rotor blade.

That the effect of wake rotation on the over-all power coefficient can be neglected, due to the balancing effects of wake expansion and static pressure deficit in the wake; can be made plausible by considering the energy equation, viz.

$$dP = \Omega \, dQ = u \, dD - \frac{1}{2} \frac{w}{r} \, dQ$$

This equation states that the power delivered by the turbine (ΩdQ) has to be equal to the work done by

the air on the rotor, through the axial force ($u dD$) and the torque ($\frac{1}{2}(w/r)dQ$); it has to be remembered that the direction of u is in the direction of dD and that the direction of the angular velocity $\frac{1}{2}w/r$ is opposite to the direction of dQ . In Eq. (C.24), the drag force consists of a momentum term and a pressure term, due to the pressure deficit in the wake, thus

$$dD = \rho u(U-u_3) dS_{ref} + \Delta p_3 dS_3,$$

and, from Eq. (C.25),

$$dQ = \rho u_3 w_3 r_3 dS_3 = \rho u w r dS_{ref}.$$

Hence

$$-\frac{1}{2} \frac{w}{r} dQ = -u \frac{1}{2} \rho w^2 dS_{ref}.$$

Because

$$\Delta p_3 dS_3 \approx \frac{1}{2} \rho w_3^2 dS_3 \approx \frac{1}{2} \rho w^2 dS_{ref},$$

the influence of the static pressure deficit in the wake and the influence of the wake rotation almost cancel. The remaining equation for the generated power:

$$dP = \rho u^2 (U-u_3) dS_{ref}$$

is identical to Betz' expression, when the wake rotation is neglected.

C.5 Concluding remarks

The calculation of induced velocities is very complicated, even in axisymmetric flow. By simplification of the problem and by using the momentum equations, it is possible to get insight into the behaviour of the induced velocities.

The assumption that the axial velocity at the rotor is the arithmetic mean of the velocity far in front of and far behind the rotor can be applied for a large range of tip-speed ratios. Only at low values of λ , this assumption might underestimate the axial velocity when, as is usually done, also the static pressure deficit in the wake is neglected.

The tangential velocity w behind the rotor is connected with the bound vorticity at the rotor (circulation Γ) on a common streamline. In the wake far behind the rotor, the radial velocities have to be zero, and the centrifugal forces due to the tangential velocities have to be balanced by the static pressure deficit in the wake. This provides a relation between the allowed combination of axial and tangential velocities.

It is possible to translate the conditions far behind the rotor to conditions just behind the rotor, because the total head and the circulation have to be constant along a streamline in the wake. It can be shown that the tangential velocity at the rotor is one half of the tangential velocity just behind the rotor. (This is important in connection with blade-element theory.)

The determination of the streamline pattern in the wake is complicated; therefore, often a cylindrical wake is assumed. This means that the tangential velocities in the wake far downstream are overestimated. This causes also an overestimation of the power loss due to wake rotation, especially at low λ .

There is a strong indication that the combined effect of wake expansion and static pressure deficit in the wake almost cancels the so-called "power loss due to wake rotation", which appears in the theory of Glauert (Ref. C.4) and in most of the other theories described in this report. This power loss due to wake rotation is only significant at low λ and/or low values of r/R_0 (close to the hub), which means at rather high values of the local solidity ratio σ' . The lifting-line approximation ($c \ll R_0$) used in the above theories becomes less accurate when the solidity becomes large, which means another possible error source in the performance prediction. This also explains the fact that the compensating effect of wake expansion and static pressure deficit has not been recognized in the past when the results of calculations and experiments were compared with each other.

The momentum equations, valid for the entire streamtube through the rotor, are often assumed to be valid also for an elemental streamtube. It is difficult to assess the validity of this assumption, but, regarding the small influence of the static pressure deficit in the wake on the axial velocity at not too small values of λ , the error due to this assumption possibly is small.

C.6 List of references

- C.1 Greenberg, M.D., Powers, S.R.: Nonlinear Actuator Disk Theory and Flow Field Calculations, Including Nonuniform Loading. NASA CR-1672 (Sept. 1970).
- C.2 Greenberg, M.D.: Nonlinear Actuator Disk Theory. Z. Flugwiss., 20, 3 (1972).
- C.3 Wu, T. Y-t.: Flow Through a Heavily Loaded Actuator Disk. Schiffstechnik, 9, 47 (1962).
- C.4 Glauert, H.: Windmills and Fans. Aerodynamic Theory (ed. W.F. Durand), Chapter XI, Div. L (Dover Publ. Inc., N.Y., 1963).

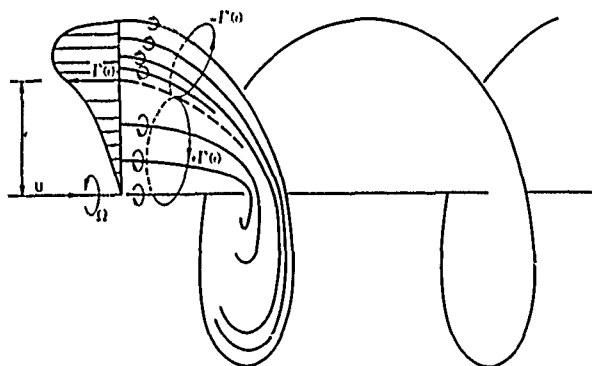


Fig. C.1 The trailing vortex sheet of a rotor blade with a variable circulation along the span of the blade

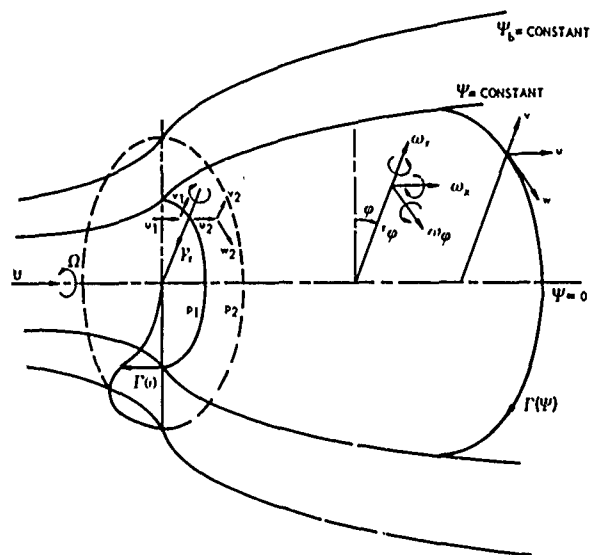


Fig. C.2 Expanding streamlines $\Psi = \text{constant}$ through the plane of the rotor with an infinite number of rotor blades in axisymmetric flow

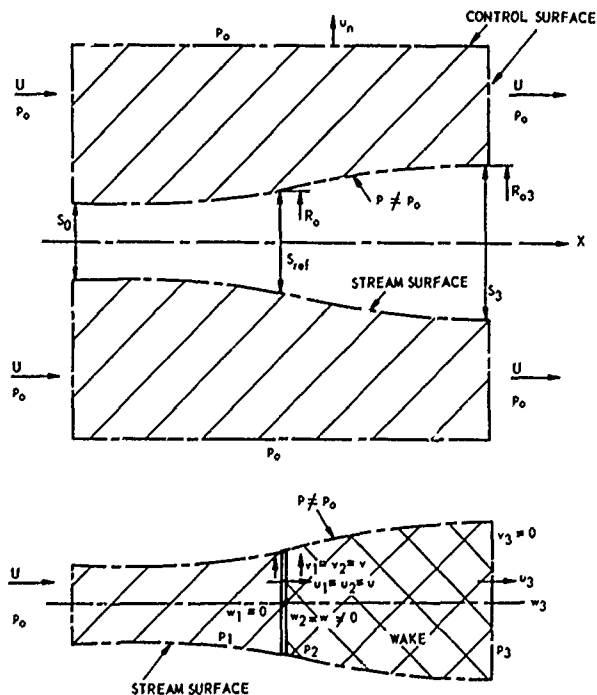


Fig. C.3 Control volumes for momentum considerations

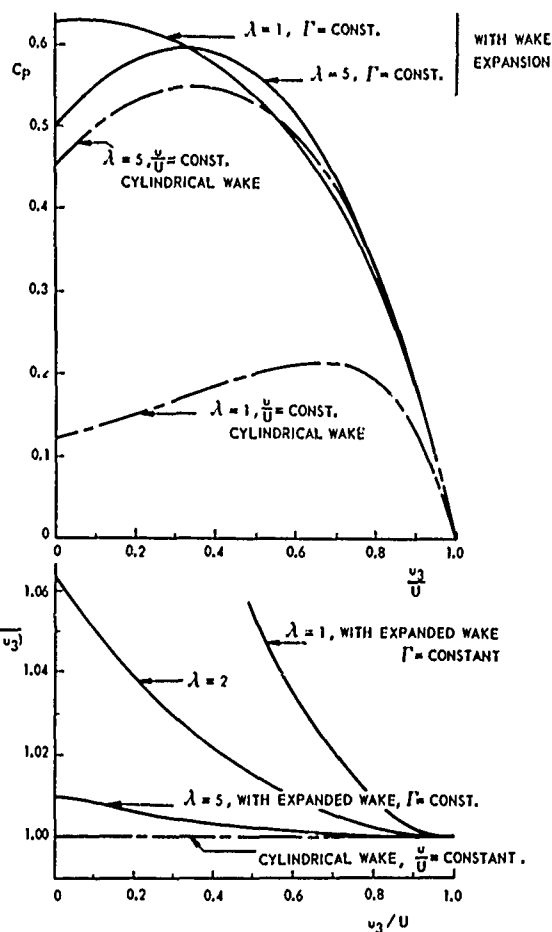


Fig. C.4 Influence of wake expansion. Wake expansion with $\Gamma = \text{constant}$ (see Eqs(C.38a) and (C.39)). Cylindrical wake with $u/U = \text{constant}$ (see Eq.(C.41))

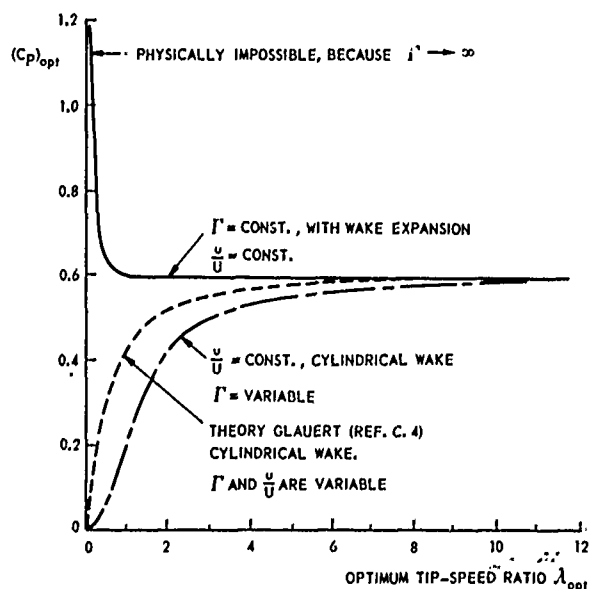


Fig. C.5 The optimum power coefficient as a function of λ , with and without wake expansion (See Eqs(C.38a), (C.39) and (C.41))

APPENDIX D SOME CONSIDERATIONS ABOUT THE ROTOR BLADE SHAPE

D.1 Introduction

In the next Sections, some simple discussions are given concerning the influence of the blade shape of a vertical-axis wind turbine on the blade loading due to centrifugal forces, with the aim to show the advantage of the so-called troposkien blade shape.

Next, the centrifugal loading of a horizontal-axis turbine is discussed and, in a strongly simplified way, the influence of the aerodynamic load is indicated.

D.2 Bending stresses due to centrifugal loading for a drum-type vertical-axis turbine

Consider a vertical-axis turbine with straight blades parallel to the axis of rotation. The radius of the rotor is R_0 and the height is H .

To simplify the calculations, the following assumptions have been made:

- The blade has a constant chord c and a constant thickness ratio t/c .
- The cross-sectional area of the blade construction material is constant along the blade span and, with a factor ϕ , is expressed as ϕtc . The specific mass of the construction material is indicated as ρ_m .

The centrifugal load per unit span at an angular velocity Ω of the rotor can be calculated from

$$F_c/H = \rho_m \phi tc \Omega^2 R_0 .$$

The maximum bending moment in the blade now depends on the blade attachment, which can be indicated by a factor f , thus

$$M_b = f(F_c/H)H^2 = f\rho_m \phi tc \Omega^2 H^2 R_0 .$$

The factor f is equal to $\frac{1}{2}$ if the blade is clamped at one side and free at the other side, f is $1/12$ if the blade is clamped at both sides, and f is $1/8$ if the blade is connected at the tip to the other blades by a horizontal strut and hinged at both sides, etc.

The moment of inertia of the blade cross-section can be expressed by the cross-sectional area and the radius of gyration r_t of the cross-section. The bending resistance is then obtained from this moment of inertia by dividing by $\frac{1}{2}t$, thus

$$W_b = \phi tc r_t^2 / (\frac{1}{2}t) ,$$

where $r_t < \frac{1}{2}t$.

The bending stress is now calculated from

$$\sigma_b = M_b/W_b = \frac{1}{2}f \rho_m (H/r_t)^2 (t/R_0) (\Omega R_0)^2 . \quad (D.1)$$

This formula shows that the bending stress is proportional to the square of the circumferential velocity ΩR_0 and also proportional to the specific mass of the material ρ_m . It can be noticed that $\sigma_b \leq \sigma_{tmax}$, the maximum tensile stress of the material considered, and that the square root of the ratio of σ_{tmax} to the specific mass ρ_m , which has the dimension of a velocity, is a property of the material considered. For aluminum alloy, this material constant is $(\sigma_{tmax}/\rho_m)^{1/2} \approx 420$ m/s.

Eq. (D.1) shows that a given blade construction and blade material sets a limit to the circumferential velocity of the turbine. This equation also shows a kind of similarity rule, viz. if two geometrically similar turbines are taken operating at the same tip-speed ratio λ and wind velocity U (i.e. $\Omega R_0 = \text{constant}$), then the bending stress σ_b is the same for both turbines, irrespective of the size of the turbine.

A final conclusion from the above equation is that, because $r_t < t/2 \ll H$ and often $H \approx 2R_0$, the circumferential velocity of a straight-bladed (drum-type) vertical-axis turbine is severely limited by the allowable bending stress.

D.3 The troposkien blade shape for a vertical-axis turbine

The bending moments in the rotor blades of a vertical-axis turbine caused by the centrifugal forces can be avoided by giving the blades the shape of a rotating rope with zero rigidity, with the end points connected to the axis of rotation.

Consider a steadily rotating curved blade, with a constant mass per unit length (m) along the span of the blade. The shape of the troposkien has to be such, that the variation of the tension force F_n along the blade is in equilibrium with the centrifugal force on a blade element (dF_c , Fig. D.1), in which bending moments in the blade are avoided.

If gravity forces are neglected, from vertical equilibrium, it follows that F_z has to be constant along the span of the blade.

From horizontal equilibrium, it follows that

$$dF_c = (dF_r/dz)dz . \quad (D.2)$$

From the force triangle in Fig. D.1 and the formula for the centrifugal force, the following expressions can be obtained:

$$F_r = -F_z dR/dz ; F_n = F_z [1 + (dR/dz)^2]^{1/2} , \quad (D.3)$$

$$dF_c = \Omega^2 R m [1 + (dR/dz)^2]^{1/2} dz . \quad (D.4)$$

From the Eqs (D.2), (D.3) and (D.4) it follows that

$$m\Omega^2 R [1 + (dR/dz)^2]^{\frac{1}{2}} = -F_z d^2 R / dz^2 \quad (D.5)$$

Because at $z = 0$, $R = R_0$, $dR/dz = 0$ and $d^2 R / dz^2 = -R_k^{-1}$, with R_k the radius of curvature of the troposkien at $z = 0$, it follows that:

$$F_z = +m\Omega^2 R_0 R_k \quad (D.6)$$

and

$$d^2 R / dz^2 = R(R_0 R_k)^{-1} [1 + (dR/dz)^2]^{\frac{1}{2}} \quad (D.7)$$

Integrating with the above boundary conditions gives

$$dz/dR = (2k R_k / R_0) [dF(k, R/R_0) / d(R/R_0)] \quad (D.8)$$

$$H/2R_0 - z/R_0 = 2k(R_k/R_0) F(k, R/R_0) \quad (D.9)$$

with $k^2 = (1 + 4R_k/R_0)^{-1}$,

and $F(k, R/R_0)$ = elliptic integral of first kind.

Choosing a certain radius of curvature R_k leads to a definite height of the rotor, as can be seen from Eq. (D.9) by substituting $z = 0$ and $R/R_0 = 1$.

$$H/2R_0 = 2k(R_k/R_0) K(k) \quad (D.10)$$

with $K(k)$ = complete elliptic integral of first kind.

The minimum value of F_n occurs at $z = 0$ (F_{n0}) and equals F_z Eq. (D.6). The maximum value occurs at the blade root ($R = 0$). From Eqs (D.3) and (D.8), it follows that the ratio of $(F_n)_{\max}$ to F_{n0} is

$$(F_n)_{\max} / F_{n0} = [1 + [4k^2(R_k/R_0)^2]^{-1}]^{\frac{1}{2}} \quad (D.11)$$

The area swept by the rotor blade can be calculated from

$$S_{\text{ref}} = 4R_0^2 \int_0^1 (R/R_0) d(z/R_0) \quad ,$$

what leads to

$$S_{\text{ref}}/R_0^2 = 4(R_k/R_0) \ln[(1+k)/(1-k)] \quad (D.12)$$

It is also interesting to know the blade length s needed to obtain such a swept area S_{ref} . This can be calculated from

$$ds = [1 + (dR/dz)^2]^{\frac{1}{2}} (dz/dR) dR \quad .$$

This can be expressed in complete elliptic integrals of the first (K) and second (E) kind, viz.:

$$s/R_0 = (2/k) [E(k) - [1 - k^2(1 + 2R_k/R_0)] K(k)] \quad (D.13)$$

Some numerical results have been calculated and compiled in Table D.1. If $R_k = 0$, the troposkien degenerates into a folded straight line.

The swept area is connected with the energy extracted from the wind stream, whereas the arc length is connected with the costs of blade construction to obtain such a swept area. The ratio $S_{\text{ref}}/(sR_0)$ is a measure for the "economy" of the shape. It increases with increasing R_k (when $R_k/R_0 \rightarrow \infty$, $S_{\text{ref}}/sR_0 \rightarrow 1.273$), but the corresponding increase in tower height certainly sets a limit to the "optimum" value of S_{ref}/sR_0 .

Denoting the material cross-section of the blade by ϕ_{tc} and the specific mass by ρ_m , the maximum tensile force in the blade can be obtained from the Eqs (D.6) and (D.11) with $m = \rho_m \phi_{tc}$, viz.

$$(F_n)_{\max} = \rho_m \phi_{tc} \Omega^2 R_0^2 (R_k/R_0) [1 + [4k^2(R_k/R_0)^2]^{-1}]^{\frac{1}{2}} \quad ,$$

and the maximum tensile stress can be calculated from

$$\sigma_t = (F_n)_{\max} / \phi_{tc} = \rho_m (\Omega R_0)^2 (R_k/R_0) [1 + [4k^2(R_k/R_0)^2]^{-1}]^{\frac{1}{2}} \quad (D.14)$$

Figure 2.6 shows that a Darrieus turbine can withstand higher circumferential velocities (ΩR_0) than a straight-bladed (drum-type) turbine (see also the Eqs (D.14) and (D.1)).

D.4 Centrifugal stresses in the blades of a horizontal-axis turbine

The centrifugal stresses in the blade of a horizontal-axis turbine can be estimated from some simplifying assumptions, viz. that the relative cross-sectional area of the blade material is constant along the blade span (i.e. $\phi = \text{constant}$; $t/c = \text{constant}$, whereas c varies along the blade span) and that the specific mass of the material is constant along the span ($\rho_m = \text{constant}$).

The centrifugal force in a blade section at radius r can then be calculated from:

$$F_c(r/R_0) = \rho_m \Omega^2 R_0^4 \phi t / c \int_{r/R_0}^1 (c/R_0)^2 (r/R_0) d(r/R_0) \quad (D.15)$$

This integral can be easily evaluated for a blade with linear taper

$$c/R_0 = a - br/R_0, \quad (D.16)$$

which corresponds to a taper ratio

$$TR = c(r/R_0=1)/c(r/R_0=0) = (a-b)/a \quad (D.17)$$

The tensile stress in that cross-section is then easily calculated by dividing through the material cross-section $\phi(t/c)c^2$, thus

$$\sigma_t = \rho_m (\Omega R_0)^2 \frac{\frac{1}{2}a^2(1-x^2) - \frac{2}{3}ab(1-x^3) + \frac{1}{4}b^2(1-x^4)}{a - 2abx + b^2x^2}, \quad (D.18)$$

with $x = r/R_0$.

Figure D.2 shows the spanwise distribution of the tensile stress as a function of the taper ratio (see also Fig. 2.7).

D.5 Possible reduction of bending moments due to the aerodynamic load on the blade of a horizontal-axis turbine

The aerodynamic lift forces on the blades of a horizontal-axis turbine introduce bending moments in the blade sections. When the blade axis is brought out of the plane of rotation (see Fig. D.3), the centrifugal forces create an opposite bending moment, and there might be a possibility to define such a shape of the blade axis, that all bending moments are avoided.

The condition for zero bending moment at each blade section (r_1, x_1) is that the moment due to the aerodynamic load $M_1(r_1)$ is equal and opposite to the moment due to the centrifugal force $M_2(r_1)$, or

$$M_1(r_1) = \int_{r_1}^{R_0} \frac{dN}{dr} (r-r_1) dr = M_2(r_1) = \int_{r_1}^{R_0} \frac{dF}{dr} c (x-x_1) dr$$

for $0 \leq r_1 \leq R_0$.

This condition is difficult to work with; therefore, a slightly different condition is used, viz.

$$dM_1(r_1)/dr_1 = dM_2(r_1)/dr_1,$$

which is, but for a constant (independent of r_1) equivalent with the first condition, as can be seen by integration. This constant has to be zero, because the moment is zero when $r_1 = R_0$.

*When the result for the differentiation of an integral with a parameter is remembered, viz.

$$\frac{d}{dy} \int_{a=f_2(y)}^{b=f_1(y)} f(x,y) dx = \int_a^b \frac{\partial f}{\partial y} dx + f(b,y) \frac{df_1}{dy} - f(a,y) \frac{df_2}{dy},$$

the differentiation of M_1 and M_2 lead to

$$\frac{dM_1}{dr_1} = \int_{r_1}^{R_0} - \frac{\partial r_1}{\partial r_1} \frac{dN}{dr} dr - \left[\frac{dN}{dr} (r-r_1) \right]_{r=r_1} \frac{dr_1}{dr_1} = N(r_1),$$

and

$$\frac{dM_2}{dr_1} = \int_{r_1}^{R_0} - \frac{x_1}{r_1} \frac{dF}{dr} c dr - \left[\frac{dF}{dr} c (x-x_1) \right]_{r=r_1} \frac{dr_1}{dr_1} = \frac{dx_1}{dr_1} F_c(r_1),$$

because $N(R_0) = F_c(R_0) = 0$.

The differential form of the condition for zero bending moments in the blade, neglecting gravity and also neglecting the finite cross-section of the blade, is

$$N(r_1) = (dx_1/dr_1) F_c(r_1),$$

or, written in a more abbreviated form;

$$dx/dr = \tan \gamma = N/F_c \quad (D.19)$$

Such a shape is only feasible if γ remains small, i.e. if the aerodynamic load remains small with respect to the centrifugal forces.

Below, the feasibility will be studied by crudely estimating the aerodynamic and centrifugal forces for an optimally operating wind turbine.

It would be possible to use the theory of Sect. 4.4.2 for the estimation of the aerodynamic load and the corresponding spanwise chord distribution, but a still simpler approach will be followed.

When it is assumed that the induction factor "a" is constant across the entire rotor area, the normal force coefficient for the complete rotor is (cf. Sect. 3.2.1)

$$C_N = N / \frac{1}{2} \rho U^2 \pi R_0^2 = 4a(1-a) ,$$

and the normal force on one blade of a B-bladed rotor is

$$N = (2\pi/B)a(1-a)\rho U^2 R_0^2 . \quad (D.20)$$

Consequently, the normal force on the outer part of the blade between $r/R_0 = 1$ and r/R_0 is then

$$N(r/R_0) = (2\pi/B)a(1-a)\rho U^2 R_0^2 [1 - (r/R_0)^2] . \quad (D.21)$$

The blade chord distribution can be estimated in the following way. The normal force on a blade element $d(r/R_0)$ is, according to the simple momentum estimates of Sect. 3.2.1,

$$dN = (4\pi/B)a(1-a)(UR_0)^2 (r/R_0) d(r/R_0) ,$$

and, according to blade element theory,

$$dN = \frac{1}{2} \rho U_{rel}^2 c_{l1} dr .$$

When the tangential induction factor (a') is neglected (see Sect. 4.4.2), the relative velocity is equal to

$$U_{rel}^2 = (1-a)^2 U^2 + (\Omega r)^2 = U^2 [(1-a)^2 + (\lambda r/R_0)^2] ,$$

and the blade element shows a normal force

$$dN = \frac{1}{2} \rho c_{l1} U^2 R_0^2 [(1-a)^2 + (\lambda r/R_0)^2] (c/R_0) d(r/R_0) .$$

Equating both expressions for dN gives a formula for c/R_0 , viz.

$$c/R_0 = (8\pi/Bc_{l1})a(1-a)\lambda^{-2} (r/R_0) \left[[(1-a)/\lambda]^2 + [r/R_0]^2 \right]^{-1} \quad (D.22)$$

When c_{l1} and "a" are taken constant along the span, a rather simple explicit formula in r/R_0 appears. Comparison with the theory of Glauert (Sect. 4.4.2) shows a surprisingly good agreement, especially at higher values of λ , when "a" is taken to be $\frac{1}{3}$ (Table D.2).

The centrifugal force on the outer part of the blade (between $r/R_0 = 1$ and r/R_0) can now be calculated with the usual assumption of the constant value of ϕ and t/c along the span, thus

$$F_c(r/R_0) = \rho_m \phi (t/c) \Omega^2 R_0^4 \int_{r/R_0}^1 (c/R_0)^2 (r/R_0) d(r/R_0) ,$$

or, with substitution of Eq. (D.22),

$$F_c(r/R_0) = \rho_m \left[(8\pi/Bc_{l1})a(1-a)\lambda^{-2} \right]^2 \phi (t/c) \Omega^2 R_0^4 \int_{r/R_0}^1 y^3 (A^2 + y^2)^{-2} dy , \quad (D.23)$$

with $A = (1-a)/\lambda$ and $y = r/R_0$.

The integral can be evaluated as

$$\frac{1}{2} \left[- \frac{A^2(1-y^2)}{(A^2+1)(A^2+y^2)} + \ln \left(\frac{A^2+1}{A^2+y^2} \right) \right] . \quad (D.24)$$

Returning to Eq. (D.19) and substituting the Eqs (D.21) and (D.23) leads to

$$\frac{d(x/R_0)}{d(r/R_0)} = \tan \gamma = \frac{\rho}{\rho_m} \frac{B(C_{l1})^2(1-y^2)}{16 \phi (t/c) a(1-a)} \left[- \frac{A^2(1-y^2)}{(A^2+1)(A^2+y^2)} + \ln \left[\frac{A^2+1}{A^2+y^2} \right] \right]^{-1} . \quad (D.25)$$

This equation has been numerically evaluated and the result, in the form of the spanwise distribution of γ , is shown in Fig. D.4 with the following values, viz.

$$B = 2, a = 1/3 \text{ (optimum)}, C_{l1} = 1.0, \rho = 1.23 \text{ kg/m}^3 \text{ (air)}, \rho_m = 2750 \text{ kg/m}^3 \text{ (aluminum alloy)}, \\ t/c = 0.12, \lambda = 8 \text{ and } 4, \phi = 0.69 \text{ (solid cross-section) and } 0.20 \text{ (hollow)}.$$

An example of the blade shape is shown in Fig. 2.8 for $\lambda = 8$ and $\phi = 0.20$.

The deflection close to the tip is probably overestimated, because of the neglect of the lift loss close to the tip (tip-correction factor). The deflection angle close to the root is probably underestimated, because of the very large blade chord, which will possibly not be applied in practice.

The hollow blade in this example is still rather heavy (30 % of the cross-section is solid material) and Fig. D.4 shows, that the bending moments can probably not be avoided in a high- λ design with a light-weight construction.

Somewhat surprising and also somewhat misleading is the large influence of λ on the deflection angle, which is caused by two effects, viz.

- The aerodynamic load on the rotor blade of an optimally operating turbine is almost independent of λ (Eq. (D.21)), whereas the centrifugal force depends on the chord length squared, which is strongly

- dependent on λ (Eq. (D.22)).
- The material area factor ϕ is taken to be constant at different λ , but the lower-loaded low- λ blade will certainly show a reduced ϕ compared with a high- λ blade design.

TABLE D.1
Variation of blade geometry and blade loading with varying curvature at the equator plane for a true troposkien

R_k/R_o	$H/2R_o$	S_{ref}/R_o^2	s/R_o	S_{ref}/sR_o	$F_{no}/(m\Omega^2 R_o^2)$	$(F_n)_{max}/(m\Omega^2 R_o^2)$	$(F_n)_{max}/(M\Omega^2 R_o)$
0	0	0	2.0	0	0	0.5	0.2500
0.1	0.3545	0.9912	2.2090	0.1605	0.1	0.6	0.2716
0.2	0.5677	1.5399	2.4119	0.6385	0.2	0.7	0.2902
0.3	0.7358	1.9642	2.6029	0.7546	0.3	0.8	0.3073
0.4	0.8773	2.3209	2.7828	0.8340	0.4	0.9	0.3234
0.5	1.0080	2.6339	2.9524	0.8921	0.5	1.0	0.3387
0.6	1.1139	2.9157	3.1137	0.9364	0.6	1.1	0.3532
0.7	1.2164	3.1740	3.2671	0.9714	0.7	1.2	0.3672
0.8	1.3116	3.4135	3.4137	0.9999	0.8	1.3	0.3808
0.9	1.4003	3.6379	3.5545	1.0235	0.9	1.4	0.3938
1.0	1.4844	3.8497	3.6902	1.0432	1.0	1.5	0.4065
1.5	1.8504	4.7722	4.3059	1.1083	1.5	2.0	0.4645
2.0	2.1565	5.5452	4.8440	1.1447	2.0	2.5	0.5161

R_k = radius of curvature at equator plane (m)
 R_o = maximum radius (m)
 H = height of troposkien blade (m)
 S_{ref} = area swept by the rotating blade (m²)
 s = length of blade (m)
 F_{no} = tension force in blade at equator plane (N)
 $(F_n)_{max}$ = ditto at blade root (N)
 m = mass per unit blade length (kg/m)
 M = ms = total mass of one blade (kg)
 Ω = angular velocity of the rotor (rad./s)

TABLE D.2
Comparison between the optimum blade chord distribution according to Glauert Eq. (4.4.21) with the simplified estimate of Eq. (D.22)

$X = \frac{r}{R_o}$	Glauert $(\lambda BC_1 c/R_o)_{opt.}$	Eq. (D.22)
1	3.367	3.867
2	2.382	2.513
3	1.728	1.774
4	1.338	1.359
5	1.087	1.097
6	.913	.919
7	.787	.791
8	.691	.693
9	.615	.617
10	.555	.556
11	.505	.506
12	.463	.464
13	.428	.428
14	.398	.398
15	.371	.372

Glauert: $(\lambda BC_1 c/R_o)_{opt.} = 8\pi X(1 - \cos \theta)$

with

$$X = \frac{r}{R_o} = \frac{\sin \theta (2 \cos \theta - 1)}{(1 - \cos \theta) (2 \cos \theta + 1)}$$

Eq. (D.22), written in a somewhat different way:

$$(\lambda BC_1 c/R_o)_{opt.} = 8\pi a(1-a)X[(1-a)^2 + X^2]^{-1}$$

with $a = 1/3$.

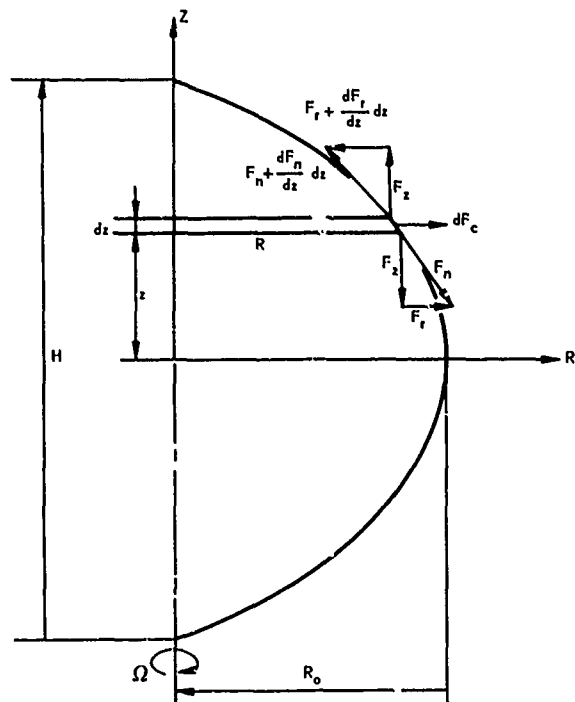


Fig. D.1 Sketch of the troposkien blade shape and nomenclature

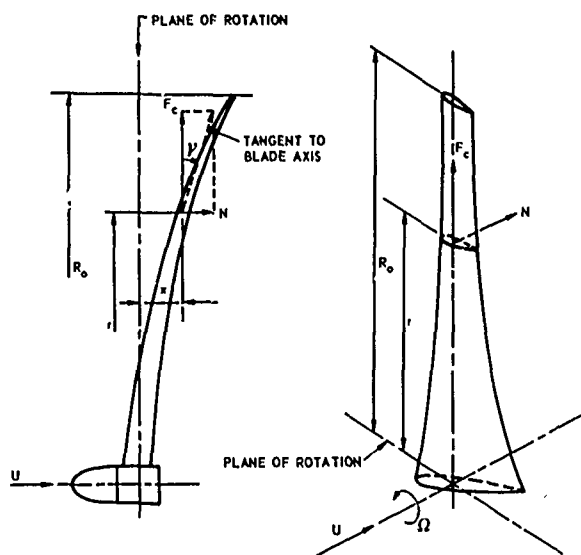


Fig. D.3 Centrifugal and normal force in the blade section; condition of zero bending moment in the blade

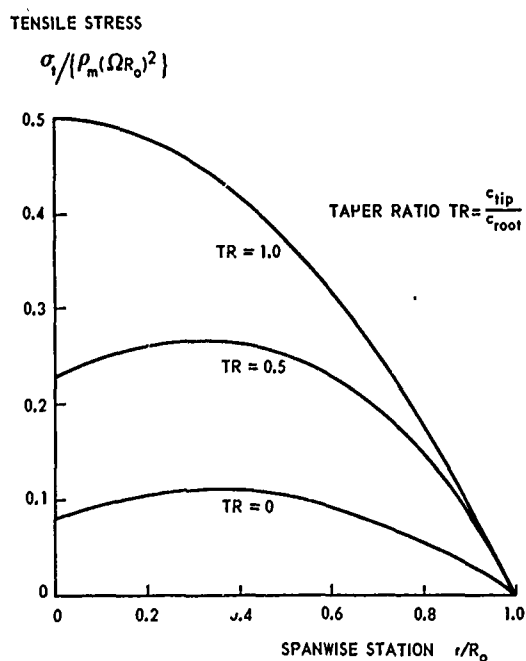


Fig. D.2 Influence of the taper ratio on the stress distribution due to centrifugal forces along the blade span

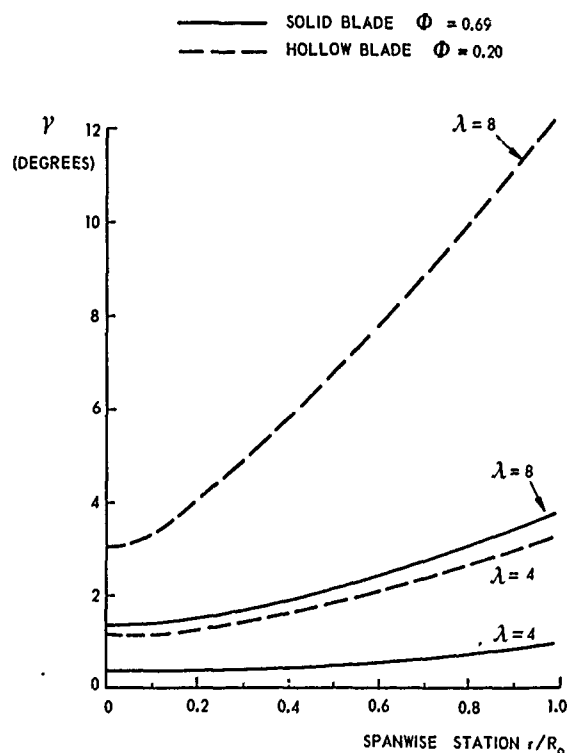


Fig. D.4 Deflection angle of the blade axis of an optimally operating horizontal-axis turbine with zero bending moments in the rotor blade. $B = 2$, $C_1 = 1.0$
 γ is deflection angle of blade axis
 $\rho_m = 2750 \text{ kg/m}^3$, $\rho = 1.23 \text{ kg/m}^3$, $t/c = 0.12$

REPORT DOCUMENTATION PAGE			
1. Recipient's Reference	2. Originator's Reference	3. Further Reference	4. Security Classification of Document
	AGARD-AG-243	ISBN 92-835-1326-6	UNCLASSIFIED
5. Originator	Advisory Group for Aerospace Research and Development North Atlantic Treaty Organization 7 rue Ancelle, 92200 Neuilly sur Seine, France		
6. Title	FLUID DYNAMIC ASPECTS OF WIND ENERGY CONVERSION		
7. Presented at			
8. Author(s)/Editor(s)	O. de Vries		9. Date July 1979
10. Author's/Editor's Address	National Aerospace Laboratory NLR Anthony Fokkerweg 2, 1059 CM Amsterdam, The Netherlands		11. Pages 150
12. Distribution Statement	This document is distributed in accordance with AGARD policies and regulations, which are outlined on the Outside Back Covers of all AGARD publications.		
13. Keywords/Descriptors	<div style="display: flex; justify-content: space-between;"> <div> Fluid dynamics Wind power generation Windmills Wind (meteorology) </div> <div> Turbines Turbulence Wakes </div> </div>		
14. Abstract	<p>A review is made of the fluid dynamic aspects of wind energy conversion. A short survey of the total framework of wind energy conversion is given to bring the fluid dynamics aspect in its proper dimensions. Next, the several wind concentrator concepts are discussed, while the main body of the report is formed by a discussion of the theory of wind-driven turbines, including both the horizontal-axis and the vertical-axis turbines.</p> <p>The report concludes with a survey of inhomogeneous flow and turbulence effects, turbine control and wake interference effects.</p> <p>The AGARDograph has been produced at the request of the Fluid Dynamics Panel of AGARD.</p>		

<p>AGARDograph No. 243 Advisory Group for Aerospace Research and Development, NATO FLUID DYNAMIC ASPECTS OF WIND ENERGY CONVERSION by O. de Vries Published July 1979 150 pages</p> <p>A review is made of the fluid dynamic aspects of wind energy conversion. A short survey of the total framework of wind energy conversion is given to bring the fluid dynamics aspect in its proper dimensions. Next, the several wind concentrator concepts are discussed, while the main body of the report is formed by a discussion of the theory of wind-driven turbines, including both the horizontal-axis and the vertical-axis turbines.</p> <p>P.T.O.</p>	<p>AGARD-AG-243</p> <p>Fluid dynamics Wind power generation Windmills Wind (meteorology) Turbines Turbulence Wakes</p>	<p>AGARDograph No. 243 Advisory Group for Aerospace Research and Development, NATO FLUID DYNAMIC ASPECTS OF WIND ENERGY CONVERSION by O. de Vries Published July 1979 150 pages</p> <p>A review is made of the fluid dynamic aspects of wind energy conversion. A short survey of the total framework of wind energy conversion is given to bring the fluid dynamics aspect in its proper dimensions. Next, the several wind concentrator concepts are discussed, while the main body of the report is formed by a discussion of the theory of wind-driven turbines, including both the horizontal-axis and the vertical-axis turbines.</p> <p>P.T.O.</p>	<p>AGARD-AG-243</p> <p>Fluid dynamics Wind power generation Windmills Wind (meteorology) Turbines Turbulence Wakes</p>
<p>AGARDograph No. 243 Advisory Group for Aerospace Research and Development, NATO FLUID DYNAMIC ASPECTS OF WIND ENERGY CONVERSION by O. de Vries Published July 1979 150 pages</p> <p>A review is made of the fluid dynamic aspects of wind energy conversion. A short survey of the total framework of wind energy conversion is given to bring the fluid dynamics aspect in its proper dimensions. Next, the several wind concentrator concepts are discussed, while the main body of the report is formed by a discussion of the theory of wind-driven turbines, including both the horizontal-axis and the vertical-axis turbines.</p> <p>P.T.O.</p>	<p>AGARD-AG-243</p> <p>Fluid dynamics Wind power generation Windmills Wind (meteorology) Turbines Turbulence Wakes</p>	<p>AGARDograph No. 243 Advisory Group for Aerospace Research and Development, NATO FLUID DYNAMIC ASPECTS OF WIND ENERGY CONVERSION by O. de Vries Published July 1979 150 pages</p> <p>A review is made of the fluid dynamic aspects of wind energy conversion. A short survey of the total framework of wind energy conversion is given to bring the fluid dynamics aspect in its proper dimensions. Next, the several wind concentrator concepts are discussed, while the main body of the report is formed by a discussion of the theory of wind-driven turbines, including both the horizontal-axis and the vertical-axis turbines.</p> <p>P.T.O.</p>	<p>AGARD-AG-243</p> <p>Fluid dynamics Wind power generation Windmills Wind (meteorology) Turbines Turbulence Wakes</p>

<p>The report concludes with a survey of inhomogeneous flow and turbulence effects, turbine control and wake interference effects.</p> <p>The AGARDograph has been produced at the request of the Fluid Dynamics Panel of AGARD.</p> <p>ISBN 92-835-1326-6</p>	<p>The report concludes with a survey of inhomogeneous flow and turbulence effects, turbine control and wake interference effects.</p> <p>The AGARDograph has been produced at the request of the Fluid Dynamics Panel of AGARD.</p> <p>ISBN 92-835-1326-6</p>
<p>The report concludes with a survey of inhomogeneous flow and turbulence effects, turbine control and wake interference effects.</p> <p>The AGARDograph has been produced at the request of the Fluid Dynamics Panel of AGARD.</p> <p>ISBN 92-835-1326-6</p>	<p>The report concludes with a survey of inhomogeneous flow and turbulence effects, turbine control and wake interference effects.</p> <p>The AGARDograph has been produced at the request of the Fluid Dynamics Panel of AGARD.</p> <p>ISBN 92-835-1326-6</p>

B 238

4

AGARD

NATO  OTAN

7 RUE ANCELLE · 92200 NEUILLY-SUR-SEINE

FRANCE

Telephone 745.08.10 · Telex 610176

DISTRIBUTION OF UNCLASSIFIED
AGARD PUBLICATIONS

AGARD does NOT hold stocks of AGARD publications at the above address for general distribution. Initial distribution of AGARD publications is made to AGARD Member Nations through the following National Distribution Centres. Further copies are sometimes available from these Centres, but if not may be purchased in Microfiche or Photocopy form from the Purchase Agencies listed below.

NATIONAL DISTRIBUTION CENTRES

BELGIUM

Coordonnateur AGARD – VSL
Etat-Major de la Force Aérienne
Quartier Reine Elisabeth
Rue d'Evere, 1140 Bruxelles

CANADA

Defence Scientific Information Service
Department of National Defence
Ottawa, Ontario K1A 0Z2

DENMARK

Danish Defence Research Board
Østerbrogades Kaserne
Copenhagen Ø

FRANCE

O.N.E.R.A. (Direction)
29 Avenue de la Division Leclerc
92 Châtillon sous Bagneux

GERMANY

Zentralstelle für Luft- und Raumfahrt-
dokumentation und -information
c/o Fachinformationszentrum Energie,
Physik, Mathematik GmbH
Kernforschungszentrum
7514 Eggenstein-Leopoldshafen 2

GREECE

Hellenic Air Force General Staff
Research and Development Directorate
Hoflagos, Athens, Greece

ICELAND

Director of Aviation
c/o Flugrad
Reykjavik

ITALY

Aeronautica Militare
Ufficio del Delegato Nazionale all'AGARD
3, Piazzale Adenauer
Roma/EUR

LUXEMBOURG

See Belgium

NETHERLANDS

Netherlands Delegation to AGARD
National Aerospace Laboratory, NLR
P.O. Box 126
Delft

NORWAY

Norwegian Defence Research Establishment
Main Library
P.O. Box 25
N-2007 Kjeller

PORTUGAL

Direcção do Serviço de Material
da Força Aérea
Rua da Escola Politécnica 42
Lisboa
Attn: AGARD National Delegate

TURKEY

Department of Research and Development (ARGE)
Ministry of National Defence, Ankara

UNITED KINGDOM

Defence Research Information Centre
Station Square House
St. Mary Cray
Orpington, Kent BR5 3RE

UNITED STATES

National Aeronautics and Space Administration (NASA)
Langley Field, Virginia 23365
Attn: Report Distribution and Storage Unit

THE UNITED STATES NATIONAL DISTRIBUTION CENTRE (NASA) DOES NOT HOLD
STOCKS OF AGARD PUBLICATIONS, AND APPLICATIONS FOR COPIES SHOULD BE MADE
DIRECT TO THE NATIONAL TECHNICAL INFORMATION SERVICE (NTIS) AT THE ADDRESS BELOW.

PURCHASE AGENCIES*Microfiche or Photocopy*

National Technical
Information Service (NTIS)
5285 Port Royal Road
Springfield
Virginia 22161, USA

Microfiche

Space Documentation Service
European Space Agency
10, rue Mario Nikis
75015 Paris, France

Microfiche

Technology Reports
Centre (DTI)
Station Square House
St. Mary Cray
Orpington, Kent BR5 3RF
England

Requests for microfiche or photocopies of AGARD documents should include the AGARD serial number, title, author or editor, and publication date. Requests to NTIS should include the NASA accession report number. Full bibliographical references and abstracts of AGARD publications are given in the following journals:

Scientific and Technical Aerospace Reports (STAR)
published by NASA Scientific and Technical
Information Facility
Post Office Box 8757
Baltimore/Washington International Airport
Maryland 21240, USA

Government Report Announcements (GRA)
published by the National Technical
Information Service, Springfield
Virginia 22161, USA



Printed by Technical Editing and Reproduction Ltd
Harford House, 7-9 Charlotte St, London W1M 1HD

ISBN 92-835-1326-6

AG 243

FLUID DYNAMIC ASPECTS OF WIND ENERGY CONVERSION



E